PHASE EQUILIBRIA OF AQUEOUS ELECTROLYTES UNDER CONFINEMENT: FROM ADSORBED WATER FILMS TO EUTECTIC MELTING ON MARS

Dissertation
Submitted to the University of Hamburg in fulfillment of the requirements for the degree of Doctor of Natural Sciences (Dr. rer. nat)

Department of Chemistry
Faculty of Mathematics, Informatics and Natural Science
University of Hamburg

Shaoheng Wang

Hamburg 2025

1. Reviewer: Prof. Dr. Michael Steiger

2. Reviewer: Prof. Dr. Michael Fröba

Oral defense date: 5th, December, 2025

Publication date: 16th, March, 2026

The present dissertation was carried out in the research group of Prof. Dr. Michael Steiger at the Institute of Inorganic and Applied Chemistry, Department of Chemistry, University of Hamburg, during the period from April 2021 to September 2025.

Acknowledgments

Everything began with a little story from the early days of my bachelor studies: “*We humans can successfully reach the deep space and ocean, but we know little about the water in the glass.*” This simple idea sparked my curiosity and ignited passion to uncover the mysteries of water. During my master studies, I began researching the solubility behavior of aqueous inorganic salts. Later, I was fortunate to pursue this interest more deeply through a fascinating project on confined water, under the guidance of Prof. Michael Steiger over the past four years.

I am deeply grateful for the finical support of the BWFGB project (Freie und Hansestadt Hamburg), Grant No. LFF–FV68 (*Control of the special properties of water in nanopores*), which enable my studies and research at the University of Hamburg. I also sincerely appreciate the University of Hamburg’ travel subsidy, which allowed me to present my findings at several academic conferences.

None of this would have been possible without the supervisor Prof. Michael Steiger. My heartfelt thanks therefore go to him, thank you, Michael, for always listening patiently to my sometimes wild ideas and offering mature, thoughtful feedback. These discussions helped expand my understanding from classic thermodynamics into the nanoscale and interfacial world. I also enjoy our conversations about football and global affairs during the break of science.

I owe a big thanks to my group colleagues. Dr. Amelie Stahlbuhk guided me at the beginning of my studies, and I greatly appreciate our collaborations and discussions on various topics; Tanya Talreja–Muthreja and Markus Dohrmann also offered me essential help, especially with the preparation of porous silica.

I was fortunate to be part of the LFF project, working alongside wonderful collaborators from diverse backgrounds. Preparing presentations for our regular meetings was a challenge, but also a valuable opportunity for growth. As Richard Feynman said, “*If we can't reduce it to a freshman level, we don't really understand it*”. The need to communicate clearly helped me better understand my own work. I’m especially thankful to Prof. Michael Fröba and Prof. Partrick Huber for their insightful feedback, and to Stella Gries for her generous training in atomic force microscopy (AFM).

Beyond the university, I warmly thank Dr. Sebastiaan Godts for his kind assistance with microscopy and his engaging discussions on water vapor sorption. I truly cherished the time in Brussels, made memorable by your hospitality companionship. I must also thank Dr. Dongdong Li, who is the matchmaker of Prof. Steiger and me, and helped become part of the Mars-relevant research community. Your advice during my PhD application, as well as your ongoing support and encouragement, meant the world to me.

A special thank-you goes to my dear friends in Hamburg, Dr. Lingyu Tian, Dr. Wenxi Chen, Ruili Liao, Dr. Cheng Yang, Dr. Lanqian Li, Ting Xu, and many more. Though I can't list everyone here, please know I deeply appreciate the wonderful time we shared. Prof. Hartmut Frank, thank you for the insightful conversations that lifted my mind beyond chemistry. I also thank Yichi Zhang, head of the *Chinesischer Akademikerverein Hamburg* (CAVH). The events you organized not only enriched my life, but also give me the chance to meet new friends.

Mg deepest gratitude goes to my fiancée, Yi Zheng. Your companionship and unwavering support have been instrumental in bringing me to this point in my journey. I'm continually inspired by your beautiful personality. Heartfelt thanks also go to my mother, Suping Wang, your selfless support allowed me to pursue what I like without distraction.

Finally, I would like to thank myself. I am grateful for every choice I have made over the past ten years that shaped who I am today. I may not be the best, but I am becoming the person I aspire to be. I hope this sense of fulfillment endures 20, 30, or 40 years from now, and perhaps even forever.

Shaoheng Wang

Hamburg 2025

Zusammenfassung

Das Phasenverhalten wässriger Salzsysteme spielt eine entscheidende Rolle sowohl in der natürlichen Umwelt als auch in industriellen Anwendungen. Sind diese Systeme auf der Nanoskala eingegrenzt, ergeben sich signifikante Abweichungen von ihrem Verhalten in Bulksystemen, darunter die Erniedrigung von Schmelzpunkten und Deliqueszenzfeuchte (DRH). Diese Phänomene stellen unser klassisches Verständnis von Phasenübergängen zwischen Wasserdampf, wässrigen Lösungen, Eis und Salzen als zentrale Prozesse bei der Solebildung im Marsregolith und den hygroskopischen Eigenschaften von atmosphärischen Aerosolen in Frage. Auf der Nanoskala wird der thermodynamische Zustand einer Lösung nicht nur durch Temperatur und Zusammensetzung bestimmt, sondern auch durch räumliche Einschränkungen und lokale, strukturelle Heterogenitäten. Es ist daher notwendig, klassische thermodynamische Theorien zu erweitern, um nanoskalige Effekte – insbesondere jene, die durch den Kelvin-Effekt und den Laplace-Druck verursacht werden – zu berücksichtigen.

Darüber hinaus haben zahlreiche Studien die Adsorption und Bildung von Wasserfilmen auf Salzoberflächen vor der vollständigen Deliqueszenz beobachtet, die Rolle der Filme bei der gemeinsamen Deliqueszenz von Salzgemischen und bei Fest-Fest-Übergängen in Gegenwart von Wasserdampf ist bislang jedoch wenig untersucht. Diese Dissertation widmet sich daher zwei zentralen Themen: (1) dem Schmelz- und eutektischen Verhalten Mars-relevanter Salzlösungen (Chloride und Perchlorate) in nanoporösen Silica-Materialien und (2) dem Wasserdampfsorptionsverhalten von Salznanopartikeln in Nanoporen sowie von Salzgemischen an den Korngrenzflächen unter Verwendung experimenteller Untersuchungen und thermodynamischer Modellierung.

Die Ergebnisse der durchgeführten experimentellen Untersuchungen zeigen, dass sowohl Schmelzpunkte als auch eutektische Temperaturen in Nanoporen systematisch niedriger sind als in Bulk-Lösungen und mit abnehmender Porengröße weiter abnehmen. Interessanterweise wurden in den untersuchten verdünnten Lösungen keine eutektischen Übergänge beobachtet, was vermutlich auf eine Anreicherung von Ionen in der nicht gefrierenden Grenzschicht zurückzuführen ist, wodurch die Kristallisation des Salzes und eutektische Übergänge im Inneren der Pore verhindert werden. Ähnlich wie bei reinem Wasser verschwinden Phasenübergänge erster Ordnung, wie Gefrieren oder Salzkristallisation, unterhalb einer kritischen Porengröße. Das Pitzer-Ionenwechselwirkungsmodell wurde durch Einbindung der Kelvin-Gleichung und des Laplace-Drucks auf nanoskalige Systeme erweitert. Die modellierten Schmelzpunkte und eutektischen Temperaturen stimmen gut mit den experimentellen Daten überein, wenn geeignete Werte für die Grenzflächenenergie zwischen Kristall und Flüssigkeit (γ_{cl}) verwendet

werden. Die Simulationen deuten zudem darauf hin, dass der Laplace-Druck einen stärkeren Einfluss auf das Löslichkeitsgleichgewicht hat als auf das Schmelzen von Eis, bedingt durch die größere Volumenänderung, die mit dem Auflösen von Salzen einhergeht.

Gleichzeitig zeigten die durchgeführten Messungen der Deliqueszenzfeuchten von Salznanopartikeln in Nanoporen eine deutliche Abnahme der Deliqueszenzfeuchte mit abnehmender Porengröße. Ein typischer Wasserdampfsorptionsprozess verläuft in drei Schritten: Deliqueszenz innerhalb der Pore, durch Krümmung getriebene Porenfüllung und Verdünnung der Lösung. Darüber hinaus wurde beobachtet, dass die gemeinsame Deliqueszenz von Salzgemischen bei einer niedrigeren relativen Luftfeuchtigkeit als die jeweiligen Deliqueszenzfeuchten der Einzelkomponenten durch die Bildung adsorbierter Wasserfilme an den Korngrenzen initiiert wird. Diese Wasserfilme fördern auch Fest-Fest-Phaseumwandlungen zwischen metastabilen und stabilen Salzpaaren, wie es für das quaternäre reziproke System $NaCl + KNO_3 \rightarrow KCl + NaNO_3$ gezeigt ist. Zudem konnte die Deliqueszenz von Calciumchlorid bereits bei 18.5 %, also deutlich unterhalb der DRH von 29.5% der thermodynamisch stabilen Phase ($CaCl_2 \cdot 6H_2O$) beobachtet und auf die Bildung einer metastabilen Hydratphase β-$CaCl_2 \cdot 4H_2O$ zurückgeführt werden.

Zusammenfassend beleuchtet diese Dissertation das multiskalare Phasenverhalten von Salzlösungen in nanokonfinierter Umgebung, indem sie experimentelle Nachweise und thermodynamische Einblicke in eutektisches Schmelzen, Deliqueszenz und Wasserfilmbildung liefert. Die Ergebnisse tragen zu einem besseren Verständnis des Phasenverhaltens wässriger Lösungen unter marsähnlichen sowie unter atmosphärischen Bedingungen bei und bieten einen Rahmen für die Modellierung von Phasengleichgewichten in nanoskaligen Systemen.

Abstract

The phase behavior of aqueous salt systems plays a crucial role in both natural environments and industrial applications. Significant deviations from bulk behavior have been observed when these systems are confined in the nanoscale, including the depression of melting temperatures and deliquescence relative humidities (DRH). These phenomena challenge our classic understanding of phase transitions among water vapor, aqueous solution, ice and salts, key processes relevant to brine formation in Martian regolith and the hygroscopic properties of atmospheric aerosols. At the nanoscale, the thermodynamic state of a solution is governed not only by temperature and composition, but also by spatial confinement and local structural heterogeneities. Furthermore, numerous studies have demonstrated the adsorption and evolution of water film on the salt crystal surface prior to compete deliquescence, but its role in the mutual deliquescence of salt mixtures and in solid–solid transition upon exposure to water vapor is lacking. Therefore, this dissertation primarily addresses two core topics: (1) the melting and eutectic behavior of Mars-relevant salt solutions (chlorides and perchlorates) confined in nanoporous silica, and (2) the water vapor sorption properties of confined salt nanoparticles and salt mixtures, from the perspectives of experimental investigation and thermodynamic modeling.

The calorimeter measurement results on pure water and electrolyte solutions (NaCl, $MgCl_2$, $CaCl_2$, $NaClO_4$, $Mg(ClO_4)_2$, $Ca(ClO_4)_2$, $(NH_4)_2SO_4$) in nanopores reveal that both melting and eutectic temperatures are consistently lower than in bulk solutions, and decrease further with smaller pore size. Notably, eutectic transitions were not observed in dilute solutions for any of the systems studied, likely due to ion accumulation in the interfacial non-freezing layer, which inhibits salt crystallization and eutectic transition within the pore core. Similar to pure water, it was observed that first-order phase transitions such as freezing and salt crystallization disappear below a critical pore size. The Pitzer ion-interaction model was extended to nanoscale systems by incorporating both the Kelvin equation and the Laplace pressure. The modeled melting and eutectic points agree well with the experimental data when appropriate values of crystal–liquid interfacial energies (γ_{cl}) are applied.

In addition, the water vapor sorption experiments conducted at 25 °C revealed that DRH of the investigated salts (KCl, $MgCl_2\cdot 6H_2O$, $CaCl_2\cdot nH_2O$, $NaClO_4\cdot H_2O$, $Mg(ClO_4)_2\cdot 6H_2O$, $Ca(ClO_4)_2\cdot 4H_2O$) in porous silicas show a clear decrease of the values with reducing pore size. A typical water vapor sorption process of the confined salt nanoparticle involves three steps: deliquescence within the pore, curvature-driven pore filling, and dilution of the bulk solution. Additionally, the water vapor sorption isotherms showed that the mutual deliquescence of salt mixtures occur at lower relative humidity (RH) than the DRH of any individual component. Further environmental scanning electron microscope (ESEM) observations indicated that this process is initiated by the formation of adsorbed water film at grain interfaces. These films also facilitate solid–solid transformations between metastable and stable salt pairs, as demonstrated by the quaternary reciprocal system $NaCl + KNO_3 \rightarrow KCl + NaNO_3$, as confirmed by Raman spectroscopy. Moreover, water vapor sorption and Raman data indicated early deliquescence of calcium chloride hydrate at 18.5% RH at 25 °C, below the 29.5% of the thermodynamically stable phase DRH ($CaCl_2 \cdot 6H_2O$), due to formation of the metastable β–$CaCl_2 \cdot 4H_2O$ phase. This transition is enabled by its structural similarity to $CaCl_2 \cdot 2H_2O$.

In summary, this dissertation elucidates the multi-scale phase behavior of salt solutions in confinement, providing experimental evidence and thermodynamic insights into eutectic melting, deliquescence, and water film formation. These findings contribute to a deeper understanding of phase behavior of aqueous solution under Mars-like and atmospheric conditions and offer a framework for modeling phase equilibria in nanoscale environments.

Table of contents

Chapter 1. Introduction

Water, due to its unique fundamental properties (Gallo et al., 2016), ubiquity on earth (Hanslmeier, 2010) and wide-ranging industrial applications (Mauer and Taylor, 2010; Qian et al., 2020), is one of the most intensively studied substances. Its diverse phase behaviors and interactions with dissolved electrolytes are encountered in numerous practical contexts and have attracted many attentions. Notable examples include water harvesting from air (Kim et al., 2017; Kim et al., 2018; Tu et al., 2018; Li et al., 2023), deliquescence of mineral aerosols (Tang et al., 2016), and hydrothermal mineralization (Ruiz−Agudo et al., 2014).

The excellent mobility and solvation capacity of water enable it to act as both solvent and reaction medium in natural and biological systems. Nearly all vital biological processes are facilitated by water, either as solvent or as catalyst. Consequently, liquid water is a prerequisite for life, making it a focal point in planetary science and deep space exploration. On Mars, where the average surface temperature is approximately −70 °C and the atmosphere is predominantly composed of CO_2, water has been detected in the form of polar ice, icy soil, and hydrated salts (Stillman and Grimm, 2011; Jakosky, 2021). Whether liquid water can persist in such a cold and arid environment remains an open question. The presence of solutes significantly alters the structure and properties of water. Dissolved ions disturb the tetrahedral hydrogen bond network of pure water, leading to notable changes in its physical and chemical characteristics, including freezing point depression and vapor pressure lowering, collectively known as the salt effect. The discovery of chlorides and perchlorates in Martian soil by the Pathfinder spacecraft and Phoenix rover suggests the possibility of stable liquid brines, as these salts are highly hygroscopic and substantially lower the freezing point of water (Wänke et al., 2001; Hecht, 2009). Beyond Mars, ice−brine equilibria are also relevant to other icy worlds, such as Enceladus moon and certain cold regions on earth (Starinsky et al., 2003; Collins et al., 2007; Spencer et al., 2013; Glein et al., 2015). On earth, for instance, calcium chloride is widely used as a de−icing agent for snow and ice in winter (Akin et al., 2013), and the freeze−thaw cycles of permafrost significantly influence local hydrology, infrastructure development, and agriculture (Dai et al., 2019; Wang et al., 2023a).

Apart from the ice−brine equilibria, another critical process is the transformation between water vapor and liquid or brine phases, which is driven by fluctuations in atmospheric temperature and humidity. This transformation plays a crucial role in climate change, the water cycle, and has broad implications for the environment and human society. For instance, water uptake and deliquescence of mineral aerosols are key steps in cloud nucleation and also contribute to the production of free radicals (Tang et al., 2016; Wei et al., 2020; Bellouin and Yu, 2022; Dyson et al., 2023). In daily life, phenomena such as the caking and agglomeration of salt grains in kitchen salt

(Li et al., 2016a; Mauer and Taylor, 2010) and the salt crystallization damage in cultural heritage materials (Steiger, 2005) are also largely governed by vapor−liquid phase transitions.

These water−mediated transformations are not limited to open systems, but are also prevalent in nanoconfined space, such as in nanoporous materials used for water harvesting (Li et al., 2023), deliquescent aerosol nanoparticles (Lin et al., 2021), porous soil, and biological tissues (Guiné et al., 2014). The thermodynamic behavior of water in confined systems, particular in porous silica, has been widely studied. Key properties under confinement include the structure of adsorbed water layers (Rother et al., 2022), depression of the melting point (Jähnert et al., 2008), ice stability (Dore, 2000), dielectric constant (Fumagalli et al., 2018), and viscosity (Raviv et al., 2001). The prevailing consensus is that confined water exhibits markedly different properties from bulk water, with systematical shifts in phase boundaries such as freezing point and vapor pressure, an effect known as confinement effect. However, in realistic scenarios like aerosol nanoparticles, permafrost, powder agglomeration, it is the aqueous solution containing various solutes rather than the pure water that should be deeply examined. Despite the importance of these systems, only limited studies have examined the phase behavior and thermodynamic properties of confined aqueous solutions (Meissner et al., 2016; Jantsch et al., 2019), and a comprehensive understanding has yet to be reached. While confinement clearly influences these systems, solution properties also strongly depend on the solute type and concentration.

Given the prevalence of nanoscale salt solution in diverse environments, ranging from Martian soil and aerosol particles to salt grain interfaces, it is crucial to systematically investigate their phase behavior, particular the transitions between gas, liquid, and solid phase. This dissertation focuses on the effect of nanoconfinement on the melting points of salt solutions and deliquescence relative humidity (DRH) of salt particles. Special attention is also given to the role of interfacial water films in initiating mutual deliquescence and solid−solid transformation in salt mixtures upon exposure to water vapor. These investigations offer deeper insights into the formation of liquid brine on the Martian surface and mineralogical evolution via water films under cryogenic environments. Furthermore, by integrating thermodynamic modeling and nanoscale melting points and DRH data, the interfacial energy between liquid and crystalline phases can be quantitatively evaluated.

Chapter 2. Theory

2.1 Martian water chemistry

2.1.1 Remote sensing detection

Mars has long been considered the most Earth−like planet in the solar system, owing to its comparable rotation period, elemental composition, and the presence of a planetary magnetic field (Taylor, 2011). The discovery of water in both polar regions and in the atmosphere of Mars has intensified interest in the planet's potential habitability and its suitability for future human colonization. However, despite these discoveries, the existence of liquid water on the Martian surface remains uncertain, primarily due to the planet's extremely low surface temperature and atmospheric water vapor pressure. Systematic exploration of Martian water began in the 1960s with launch of early spacecraft missions, which collected digitized data using remote sensing instruments and on-site analysis tools (Nazari-Sharabian et al., 2020). These missions provided strong evidence for the presence of extensive polar ice caps (Jakosky and Haberle, 1992; Titus et al., 2003; Bibring et al., 2004; European Space Agency, 2004; Ojha et al., 2015) and trace amounts of water vapor in the Martian atmosphere (Farmer et al., 1977; Smith, 2002). These findings initiate decades of investigation into the Martian water cycle and the potential presence of transient or a stable liquid water phase. The hypothesis that ancient Mars experienced significant hydrogeologic activity, such as lakes, paleo oceans, and large outflow channels like Kasei Valles, is supported by geomorphological evidence (Newsom et al., 1996; Head III et al., 1999; Weitz et al., 2010; Cabrol and Grin, 1999, 2010), the discovery of layered sedimentary deposits (Malin and Edgett, 2000, 2001, 2003; Malin et al., 2006), and the elemental fractionation of certain key species (Dohm et al., 2009). In addition to ice and water vapor, water molecules are also believed to be stored in the crystalline structure of hydrated minerals (Mustard et al., 2008).

In addition to the identification of water ice and atmospheric water vapor, compelling evidence for the possible existence of liquid water on Mars has emerged from both visual observation and *in-situ* measurements. Notably, images captured by the Phoenix's Robotic Arm Camera aboard the Phoenix lander revealed the formation of spheroidal particles on one of the lander leg struts. These particles were observed to grow over time, and their temporal development closely matched fluctuations in near−surface humidity recorded by onboard sensors. Based on this correlation, Rennó et al. (2009) proposed that the particles were droplets of deliquescent brine, formed via the hygroscopic uptake of atmospheric water by perchlorates or similar salts (Rennó et al., 2009). Further support for the transient presence of liquid water comes from thermal and dielectric permittivity data obtained by the Thermal and Electrical Conductivity Probe (TECP) on

Phoenix lander. During the Martian daytime, the dielectric permittivity of the surrounding regolith exhibited noticeable increases, which were interpreted as indicative of the partial melting of salt−rich ice in the shallow subsurface. A similar dielectric anomaly was reported using low-frequency radar data from the Mars Advanced Radar for Subsurface and Ionosphere Sounding (MARSIS) instrument onboard the Mars Express orbiter (Orosei, 2018). Between May 2012 and December 2015, radar reflections obtained from the southern polar region (at approximately 193°E, 81°S) displayed elevated permittivity values consistent with the presence of a subglacial brine layer.

With the continuous explorations of Mars through successive generations of landers and rovers, such as Viking, Sojourner, Spirt, Opportunity, and Phoenix, an increasingly detailed understanding of the Martian surface composition has been established (Clark et al., 1982; Wänke et al., 2001; Gellert et al., 2004; Rieder et al., 2004; Hecht et al., 2009). Of particular interest is the identification of soluble components in Martian regolith, especially halide salts such as chlorides and perchlorates, making the presence of liquid water promising. These salts are of significant astrobiological and geophysical relevance because they can substantially depress the freezing point of water and lower the saturation vapor pressure, thereby facilitating the persistence of liquid brines under Martian surface conditions. The discovery of these hygroscopic salts has shifted scientific attention toward the thermodynamic behavior of cryogenic brines and their stability on Mars. Research efforts, combining remote sensing observation with laboratory simulations, have focused on the dynamic phase transitions among water vapor, brine, and ice−salt mixtures under Mars-relevant environmental conditions, and morphological observation. Key processes of interest include deliquescence and efflorescence, where salts absorb moisture to form liquid solution or crystallize out from solution, as well as freezing and thawing cycles.

2.1.2 Hygroscopic behavior of Mars-relevant salts

Gough and collaborators have conducted a series of experiments to investigate the hygroscopic behavior of chloride and perchlorate salts under Mars-analogous conditions, with a particular focus on their deliquescence and efflorescence behavior at subzero temperatures (Gough et al., 2011, 2014, 2016, 2019; Nuding et al., 2014; Primm et al., 2017; Fernanders et al., 2022). These studies employed Raman spectroscopy coupled with a controlled climate chamber to determine the deliquescence relative humidity (DRH) and efflorescence relative humidity (ERH) for various salts, including NaCl, $MgCl_2·6H_2O$, $CaCl_2·6H_2O$, $NaClO_4·H_2O$, $Mg(ClO_4)_2·6H_2O$, and $Ca(ClO_4)_2·4H_2O$, over a range of low temperatures. In general, the DRH and ERH values were found to be slightly temperature dependent, gradually increasing at lower temperatures. A characteristic hysteresis between the deliquescence and efflorescence was consistently observed due to the nucleation barrier during crystallization. Several notable observations emerged from this body of work.

(1) Extremely low DRH of $Ca(ClO_4)_2 \cdot 4H_2O$: The lowest DRH recorded was approximately 13% for $Ca(ClO_4)_2 \cdot 4H_2O$ at 273 K, which enables liquid phase formation in very arid environment (Nuding et al., 2014). Furthermore, brines containing $Ca(ClO_4)_2$ or $Mg(ClO_4)_2$ were shown to persist in metastable, supersaturated states beyond conventional phase transition thresholds (Nuding et al., 2014; Primm et al., 2017).

(2) Sub-eutectic deliquescence of $NaClO_4 \cdot H_2O$: Deliquescence of $NaClO_4 \cdot H_2O$ was observed at 228 K, which is below the eutectic temperature (236 K) of its aqueous solution, implying that supercooled brine can form through direct water vapor absorption (Gough et al., 2011).

(3) Spectroscopic evidence of hydrate formation: Raman spectra revealed a shift in the symmetric stretching vibration mode (v_1) of perchlorate ion (ClO_4^-) position from 958 cm^{-1} to 946 cm^{-1} (Nuding et al., 2014) and (Gough et al., 2019) at subzero temperature, interpreted as the formation of a novel hydrate. Similar spectral shift from 953 cm^{-1} to 936 cm^{-1} was noted by Fisher et al. (2014). Although early interpretation suggested this to be an octahydrate (Pestova et al., 2005; Nuding et al., 2014), subsequent X–ray diffraction (XRD) confirmed it as a hexahydrate (Hennings et al., 2014). However, the misidentification was propagated across multiple studies, underscoring the importance of cross-validation with structural methods.

(4) Mutual deliquescence in salt mixtures. The mutual deliquescence relative humidity (MDRH) of perchlorate/chloride mixtures was consistently lower than the DRH of their individual components, enhancing the brine-forming potential under Martian humidity conditions. Notably, the MDRH of a $KClO_4$/KCl mixture exceeded the saturation vapor pressure of ice, offering further evidence of supercooled brine formation via vapor condensation (Gough et al., 2014).

It should be emphasized that these DRH and ERH values do not represent true thermodynamic equilibrium, as the experiments involved a relatively rapid humidity change rate (1% RH per minute). Such conditions preclude full equilibrium in water adsorption and phase transitions. Nonetheless, the authors argue that this rate approximates transient humidity changes in the Martian near-surface environment, thereby, offering insights into plausible brine behavior on Mars.

Contemporaneous with experimental investigations into deliquescence, Chevrier and colleagues explored the evaporation dynamics of Mars-relevant brines and examined the influence of kinetic factors on phase transitions between water vapor and liquid brine (Hanley et al., 2012; Chevrier et al., 2009, 2012; Martín-Torres et al., 2015). Their results confirmed that evaporation rates are highly dependent on both temperature and salt concentration, with lower temperature and higher salinity leading to markedly reduced evaporation. Meanwhile, recent studies by Gough et al. (2023) revealed that particle size also plays a critical role in the deliquescence process, where smaller salt grains tend to deliquesce more readily due to their larger surface area to volume ratio. To quantify the thermodynamic stability of brines under Martin conditions, Chevrier and collaborators utilized the FREZCHEM (FREeZing Chemistry) model, an aqueous geochemical code based on Pitzer ion-interaction theory, to simulate phase diagrams and vapor−liquid equilibria of chloride and perchlorate mixtures over a wide temperature range (Chevrier et al., 2022; Slank et al., 2024). A key parameter in their modeling was the mutual relative humidity, which represents the lowest humidity at which a mixture can deliquesce into a stable brine phase. However, their calculated mutual deliquescence humidities often deviated significantly from experimental values reported by Gough et al. (2014). In some cases, FREZCHEM predicted that the mutual deliquescence humidity of the $Mg(ClO_4)_2$−$MgCl_2$ system at 223 K exceeded the saturation vapor pressure of ice, implying that ice would be more stable than the brine under these conditions. This contradicts empirical data showing that the eutectic temperature of a $Mg(ClO_4)_2$ solution is near 210 K, well below 223 K (Chevrier et al., 2022). These inconsistencies are likely attributed to the limited availability of experimental thermodynamic data for binary and ternary salt systems during the model parametrization, resulting in its poor predictive accuracy for multicomponent brines. In addition to equilibrium mode, kinetic aspects of brine formation have also been evaluated. Fischer et al. (2014, 2016) compared the formation rate of $Ca(ClO_4)_2$ via two pathways at −50 °C, deliquescence through water vapor and eutectic melting through direct contact with ice. Their findings suggest that while relative humidity on Mars may reach levels conducive to deliquescence, even approaching 100% (In this Chapter, the relative humidity at subzero temperature, is defined as the vapor pressure relative to the saturated pressure of ice), the process is too slow to occur within a single diurnal cycle. In contrast, eutectic melting upon direct salt contact occurred rapidly and allowed the resulting brine to remain liquid for much of the Martian solar day, provided that sufficient ice was available to counterbalance evaporative loss. Thermodynamically, the chemical potential water vapor at 100% RH is equivalent to that of ice, indicating both should offer similar driving force to brine formation. The observed kinetic disparity thus points to diffusion limitation as a major constraint on deliquescence, in contrast to the more efficient transfer at the ice−salt interface, where direct phase exchange facilitates rapid liquefaction.

2.1.3 Thermodynamic modeling and eutectic melting

Building on the experimental findings that an ice−salt mixture offers a more viable pathway for brine formation on Mars (Fischer, 2014, 2016), a significant body of research has focused on the thermodynamics of freezing equilibria in perchlorate and chloride bearing brines. Notably, many of the relevant binary systems had been well characterized prior to their discovery on Mars due to their relevance in other scientific and industrial applications (Pitzer and Oakes, 1994; Rard and Clegg, 1997; Rard et al., 2000; Wang et al., 1998; Archer and Carter, 2000; Pestova et al., 2005). However, the simultaneous presence of chlorides, sulfates, and perchlorates in the Martian regolith significantly increases the complexity of phase behavior in real systems. Existing binary and even ternary data often prove insufficient to accurately describe the thermodynamic properties of such multicomponent systems, especially those involving perchlorate. This complexity, coupled with the need for wide temperature range applicability (down to 150 K), pose considerable challenges for model development. To address these challenges, several groups have employed thermodynamics modeling approaches based on the Pitzer ion-interaction theory, adapted for low temperature Martian conditions (Marion et al., 2010; Steiger et al., 2011; Toner et al., 2015a; Li et al., 2022). Marion and colleagues (2010) incorporated perchlorate species into the FREZCHEM program by fitting interaction parameters for Na, Mg, and Ca perchlorates. Their simulation of the evaporation and freezing process, based on average wet chemistry data obtained from the Phoenix lander, provided initial insights into element partitioning and crystallization sequences. However, several limitations emerged, such as the absence of the $Ca(ClO_4)_2{\cdot}4H_2O$ phase and the incorrect use of $Mg(ClO_4)_2{\cdot}8H_2O$ instead of $Mg(ClO_4)_2{\cdot}6H_2O$. These issues likely stem from the paucity of the thermodynamic data on perchlorates and multicomponent interactions, leading to unverified or arbitrary ternary mixing parameters in the model. Recognizing these deficiencies, Toner and collaborators undertook a systematic experimental campaign to obtain reliable thermodynamic data on perchlorate bearing systems under sub-zero conditions. Their measurements encompassed solubility, eutectic temperatures, heat capacities, and water activities for a broad set of salts (Toner et al., 2014, 2015a, 2016, 2017a, 2017b, 2018). While initial attempts to integrate these data into FREZCHEM were hampered by structural limitations, such as the model's tendency to overestimate mean activity coefficients, Toner et al. eventually developed a revised Pitzer model independent of FREZCHEM (Toner et al., 2015a). The revised model demonstrated substantially improved agreement with experimental data, particularly in reproducing crystallization sequence and brine behavior at low temperatures. For instance, when applied to simulate brine evolution at the Phoenix landing site, the new model predicted a greater variety of crystalline species than FREZCHEM (Toner et al., 2015b). A key strength of the revised Toner model is the extensive use of heat capacity data to constrain the temperature dependence of the activity coefficients, ensuring its reliability for extrapolations to cryogenic Martian conditions (Toner et al., 2016, 2017a, 2017b). Their investigations also revealed two important phenomena:

(1) Solutions of $Ca(ClO_4)_2$ and $Mg(ClO_4)_2$ exhibit strong supercooling effects. These brines fail to crystalize even at −120 °C, instead transitioning into amorphous glassy states. Notably,

concentrated $Ca(ClO_4)_2$ solutions tend to vitrify unless crystals form early during cooling (Toner et al., 2015a).

(2) The presence of soil modifies both the freezing point and the water activity of perchlorate solutions, and the deviation is also affected by the salt content. Interestingly, differential scanning calorimetry (DSC) experiments have shown that when $Mg(ClO_4)_2$ solutions are embedded in soil under low humidity conditions (RH < 50%), the freezing signal becomes undetectable, possibly due to the inhibited crystallization (Shumway et al., 2021, 2023).

To extend modeling capabilities to ternary and multicomponent systems, Li et al. (2022) contributed additional solubility data for chloride–perchlorate mixtures and developed a mole–fraction based model. Their simulations suggest differential partitioning of ClO_4^- and Cl^- between the solid and liquid phase during the deliquescence and efflorescence, which may explain the observed enrichment of perchlorates in the Mars north polar region (Li et al., 2022)

In summary, the phase equilibria between water vapor, ice, and Mars-relevant brines under cryogenic conditions have been extensively investigated, with particularly significant contributions from Gough et al. and Toner et al. Their systematic experimental and modeling efforts have greatly advanced our understanding of water phase transitions, i.e. vapor to liquid, liquid to ice, and vice versa, under Martian environmental conditions. These studies collectively demonstrate that transient liquid phase is indeed thermodynamically attainable under specific combinations of temperature and relative humidity on Mars (Marion et al., 2010; Gough et al., 2011; Chevrier et al., 2009; Martín–Torres et al., 2015; Toner et al., 2014). However, from a strict thermodynamic standpoint, the permanent existence of liquid brine remains unfavorable. Interestingly, the observed depression in both water activity and freezing point of $Mg(ClO_4)_2$ solution when incorporated into regolith simulants suggests that microscale confinement created by soil grain interfaces can effectively expand the brine stability field. This localized effect may significantly enhance the potential for liquid water on the Martian surface, despite the general environmental hostility to persistent liquid phases.

2.2 Water in nanoconfinement

2.2.1 Water adsorption in confined space

The unique behavior of water in confined environments has been recognized for centuries. Prior to the 17th century, the phenomenon of capillary action was already well–documented and investigated as a special property of water interacting with narrow tubes or porous materials (Boyle, 1660). Entering the 20th century, the scientific exploration of confined water advanced significantly with the development of vapor adsorption studies, particularly in relation to the use of activated charcoal in gas masks for industrial and military applications. Lamb and Coolidge conducted some of the earliest quantitative investigations into water vapor adsorption isotherms of activated charcoal (Lamb and Coolidge, 1920; Coolidge, 1924). They measured the equilibrium vapor pressure of water adsorbed in porous carbon materials and discovered that the adsorbed water remained in a liquid−like state even at temperature below the freezing point. This behavior highlighted the influence of nanoscale confinement on the phase state of water. At that time, research on colloidal systems also contributed to the understanding of confined water. Studies from Foote and Saxton (1916, 1917) and Jones and Gortner (1932) aimed to determine the water content in colloidal substances using two different approaches: gravimetric loss during evaporation and calorimetric heat release during freezing. A consistent discrepancy was observed between the two methods, with the evaporative technique always yielding higher water content than the freezing method. This led to the hypothesis that water in colloidal systems exists in two different structural states, free water and bound (or capillary) water. The bound water, confined within fine pores or interacting with a surface, did not freeze under typical conditions, thereby escaping detection in calorimetric measurements (Foote and Saxton, 1916, 1917).

2.2.2 Freezing and melting behavior of water in nanoscale confinement

These anomalous behavior of water under nanoscale confinement has long intrigued researchers and prompted systematic investigations into its fundamental thermodynamic properties. One of the earliest efforts was carried out by Patrick and Kemper (1937) who reported a significant depression in the melting temperature of water confined within silica gel with calorimetric experiments. They interpreted the abrupt change of heat capacity as indicative of the melting transition, and notably, this depression was found to be independent of the cooling or heating rate (Patrick and Kemper, 1937). This phenomenon was later corroborated by Batchelor and Foster (1944) who used vapor pressure measurements across a range of temperature to detect phase transitions in water within the pores of silica gels. A change in the slope of the vapor pressure−temperature curve signified the occurrence of the liquid−solid phase transition. They observed that water remained in a liquid state down to −65 °C when confined within pores smaller than 2 nm in radius. Utilizing the Clapeyron and Kelvin equations, they derived the ice−water interfacial energy from the extent of melting point depression (Batchelor and Foster, 1944). These early findings also emphasized that freezing and melting transitions in confined water are gradual process, not abrupt, competitive events (Patrick and Kemper, 1937; Hodgson and Mclntosh, 1960). Subsequent work by Antoniou (1964) analyzed the shape of thermal signals and apparent heat capacities to distinguish between bulk−like water in the pore center and nonfreezing adsorbed water near the pore walls. He estimated that the adsorbed nonfreezing water corresponds to approximately three molecular layers, based on the enthalpy of transformation. Moreover, the melting temperature was shown to correlate with pore size, as described by the Clausius−Clapeyron and Kelvin equations. The thermal melting peak shape of confined water closely resembled the pore size distribution profile (Antoniou, 1964). Litvan (1966) quantitatively investigated the role of adsorbed water layer in porous silica and found that phase transitions were not detectable when the water coverage was below 1.6 layers. Similar findings were reported by Rennie and Clifford (1977) who observed that thermal signal disappeared in DSC measurements when only 5% of the pore volume was filled, approximately equivalent to three monolayers. The coexistence of bulk-like water and adsorbed water has also been confirmed by nuclear magnetic resonance (NMR), which differentiates water molecules based on the proton relaxation times (Pearson and Derbyshire, 1973; Rennie and Clifford, 1977). Pearson and Derbyshire (1973) found that below −120 °C, molecular mobility stabilized, and while rapid exchange occurred among adsorbed molecules, exchange between adsorbed and bulk−like water was significantly slower. Overloop and Vangerven (1993) further examined the structure and quantity of nonfreezing water, estimating a layer thickness 2.5−3.0 monolayers. This interfacial water was shown to differ structurally from both bulk water and ice. They also proposed that water molecule clusters may form during early stages of water vapor adsorption before full surface coverage is achieved. Findenegg and colleagues conducted detailed DSC studies on the freezing and melting of water in porous silica, often observing melting curves with three or four peaks. Two of these were attributed to confined and bulk ice melting, while others were linked to transitions in the interfacial layer (Schreiber et al., 2001). By applying the Gibbs−Thomson equation: $T_\mathrm{p} - T_0 = -\frac{2 \times T_0 \times \gamma_\mathrm{cl} \times V_\mathrm{m,w}}{\Delta_\mathrm{m} H \times (r_\mathrm{p} - t)}$, where T_p and T_0 denotes the ice melting temperature in the pore and in bulk, γ_cl is the interfacial energy of ice and water, $V_\mathrm{m,w}$ is the molar volume of water, r_p is the radius of pore, t is the thickness of the non-freezing layer, and $\Delta_\mathrm{m} H$ is the melting enthalpy, they successfully described the relationship between pore size and melting points, estimating a nonfreezing layer thickness of 0.6 nm. (Findenegg et al., 2008; Jähnert et al., 2008). A particular important observation was the disappearance of first−order phase transitions in pores smaller than 2.5 nm (Jähnert et al., 2008). Both freezing and melting enthalpies diminished as pore size decreased, vanishing near this critical diameter. This was interpreted as a consequence of increased structural disorder in confined ice and enhanced short−range order in liquid water, which reduced the free energy difference between two phases and eliminated the latent heat (Seyed−Yazdi et al., 2008; Findenegg et al., 2008). Interestingly, despite the absence of thermal signals in DSC, NMR studies still detected freezing in 2.5 nm pores, suggesting that a larger fraction of molecules in the interfacial layer may skew NMR results toward an ice−like signal (Jähnert et al., 2008).

Morishige and co-workers conducted a comprehensive investigation on the freezing−melting hysteresis of water confined in MCM−41 mesoporous materials (Morishige and Nobuoka, 1997; Morishige and Kawano, 1999; Morishige and Uematsu, 2005). Their results demonstrated that the hysteresis becomes negligibly small as pore size decreases, and the crystalline phase formed within these confined environments is cubic ice (ice Ic), rather than the common hexagonal structure (ice Ih) (Morishige and Nobuoka, 1997; Morishige and Kawano, 1999). Further analysis revealed that cubic ice originates from nanoscale crystallites of hexagonal ice that contain numerous stacking faults. As these defective crystallites grow, they undergo structural rearrangement that favors the formation of the cubic ice (Morishige and Uematsu, 2005). Beyond ice formation, inelastic neutron scattering measurements have provided insight into the structural characteristics of confined water. These studies showed that the structure of confined water more closely resembles that of amorphous ice than crystalline ice (Kittaka et al., 2013; Liu et al., 2006). Erko et al. (2011) performed Raman spectroscopy experiments on water in porous MCM-41 and SBA-15 silica with pore diameters ranging from 2.0 to 8.9 nm. By analyzing the temperature dependent OH stretching spectral region, they identified a confinement induced structural transition. In the weakest confinement condition (8.9 nm), the spectral fingerprint of pore water closely matched that of bulk ice. In contrast, under strong confinement (2.0 nm), the spectral profile resembles that of low−density amorphous ice. Their finding suggests a continuous structural evolution of confined water from bulk−like ice to amorphous−like states as the pore diameter decreases (Erko et al., 2011).

2.2.3 Phase behavior of salt solution in nanoconfinement

Subsequent studies extend the investigation of phase transitions into aqueous salt solution confined within nanoporous materials. Similar to pure water, a significant depression in the freezing and melting points of ice is observed in confined salt solution. These phase transition temperatures are influenced not only by the pore size, but also by the salt concentration. Interestingly, DSC measurements consistently failed to detected eutectic transition in dilute solutions, regardless of the salt type (Aristov et al., 1997; Burba and Janzen, 2015; Koniorczyk and Bednarska, 2019; Jantsch et al., 2019). Koniorczyk and Bednarska (2019) attributed this to the minuscule amount of liquid water still present at the eutectic temperature in dilute NaCl solutions, leading to an undetectable thermal signal. Prause et al. (2020) further demonstrated that eutectic transition in concentrated solution only appeared when the pores were overfilled, and was absent in partially or just filled pores. This was interpreted as a manifestation of glass transition rather than crystallization under strong supercooling. Jantsch et al. (2019) systematically examined the phase transitions of $CaCl_2$ and LiCl solutions in MCM-41 and SBA-15 silica with pore radii ranging from 1.9 nm to 11.1 nm. They found that melting temperature decreases with both decreasing pore size and salt molality. Notably, in the smallest pores, the melting temperature converged to that of pure water, regardless of salt concentration. This behavior is explained by the exclusion of ions from the pore interior, resulting in pure water confinement. To interpret these findings, Jantsch et al. proposed a new variable termed the "effective water activity", which integrates the influence of pressure, solute, and confinement. They supposed that the depression of the melting point under various conditions can be unified under the concept of reduced water activity. Accordingly, if two systems exhibit identical melting temperatures, their effective water activities can be considered equivalent, irrespective of the underlying cause, pressure, salinity, or confinement. Based on this, they developed an empirical relationship linking melting point depression to effective water activity. For salt solutions in confinement, the total water activity was modelled as the product of the bulk solution water activity and that of pure water in the same confined geometry. This framework yielded good agreement with experimental melting point data for $CaCl_2$ and LiCl solutions (Jantsch et al., 2019). Although this approach lacks rigorous thermodynamic justification, it offers valuable insight into the melting behavior of ice in diverse environments. In another study, Meissner et al. (2016) investigated the pore size dependent phase transitions of alkali halide solution using DSC. Their results indicate that eutectic temperature depression depends not only on pore diameter but also on specific salt type. To explain the salt dependent variation, they introduced the concept of *secondary confinement*. During eutectic freezing, salt precipitates as nanocrystal near the pore wall, effectively reducing the accessible pore volume. This localized decrease in effective pore size imposes an additional suppression on the ice melting point. The extent of this secondary confinement is influenced by the number and morphology of salt nanocrystals, resulting in a salt specific signature in eutectic temperature depression. By modifying the Gibbs–Thomson equation to account for the reduced effective pore diameter (excluding the nanocrystal volume), they achieved strong agreement between their theoretical predictions and both their own measurements and those in the literature (Meissner et al., 2016).

One of the primary limitations of the secondary confinement theory proposed by Meissner et al. is its failure to account for cases where the depression of the eutectic temperature in confinement is lower than for pure water, such as in KCl and RbCl solutions. While the secondary confinement hypothesis explains the enhanced melting point depression by considering salt nanocrystal formation near pore walls, it cannot be generalized to all systems. Notably, the eutectic transition is the simultaneous crystallization of ice and salt, rather than a sequential event initiated by salt crystallization that subsequently constrains pore volume. Another important consideration is the eutectic concentration at the eutectic point in confined versus bulk systems. Meissner et al. assumed that the eutectic concentration remains unchanged between these environments due to equilibrium established by ion diffusion. However, thermodynamic modeling by Liu et al. (2016)

challenges this assumption, demonstrating that confinement can significantly alter the eutectic concentration due to interfacial energy effects. Their model which integrates the Gibbs−Thomson and Ostwald−Freundlich equations, captures the combined influence of crystal size of ice and solute on the phase equilibria. Since the eutectic point corresponds to the intersection of the freezing curve of pure water and the solubility curve of salt, its position in confined systems is governed by the relative depression of these curves. The extent of this depression is primarily determined by the interfacial energy between each crystal phase (ice or salt) and solution. When the ice−solution and salt−solution interfacial energies are equal, both liquidus lines shift by the same magnitude, and the eutectic concentration remains constant. Conversely, if the ice−solution interfacial energy is greater, the water freezing line shifts further than the salt solubility line, resulting in reduced eutectic concentration in confinement, and vice versa. Further insight was provided by Malfait et al. (2020), who examined the melting behavior of glycerol−water mixtures in mesoporous silica (Malfait et al., 2020). By combining experimental DSC data with an extended cryogenic model and the Gibbs−Thomson equation, they derived the effective water activity of confined solutions. In their study, the melting points in the smallest pore (r_{p} =1.8 nm) showed no dependence on the bulk water molar fraction, suggesting that the water activity of the confined solution deviates from that of the bulk solution with same composition. This discrepancy was attributed to local concentration heterogeneities at the nanoscale, which cannot be adequately captured by bulk−averaged parameters. The authors proposed that microphase separation within nanoconfined systems may lead to unconventional and non−ideal phase behavior, particularly under strong confinement (Malfait et al., 2020).

In addition to the transformation of an aqueous solution to crystalline phases, vitrification behavior under nanoconfinement have also been extensively investigated. For instance, the glassy transition temperature of LiCl solutions remains largely unaffected within nanopores. However, the concentration range over which vitrification occurs is notably broadened (Longinotti et al., 2019). In contrast, NaCl, typically a poor glass former requiring high pressure for vitrification, exhibits pronounced glass transition under confinement, with both the transition temperature and concentration range influenced by pore size (Zhao et al., 2016). This behavior is likely due to the Laplace pressure induced by the curved liquid interface nanodroplet, mimicking the thermodynamic effect of externally applied pressure in a bulk system.

The deliquescence and water uptake behavior of confined salt particles have also been studied and show marked deviations from bulk behavior (Aristov et al., 1996a, 1996b; Tokarev and Aristov, 1997; Cheng et al., 2015; Talreja−Muthreja et al., 2022). In particular, NaCl exhibits opposite shifts in DRH depending on the physical state of the salt: a shift to higher RH for NaCl nanoparticles and a shift to lower RH for NaCl crystals confined within porous media (Cheng et al., 2015; Talreja–Muthreja et al., 2022). These differences arise from two main confinement aspects: (1) water vapor pressure depression governed by the Kelvin effect, and (2) the solubility modulation due to crystal size and Laplace pressure. Unlike capillary condensation of pure water, which requires a supersaturated vapor environment, the presence of salt in confinement eliminates the nucleation barrier for the liquid phase formation, thereby facilitating deliquescence under lower humidity conditions (Talreja–Muthreja et al., 2022).

Beyond phase equilibria, various other properties of confined solutions have attracted attention, including ice nucleation, ion distribution, and nanoscopic structural organization (Argyris et al., 2010; Barati Farimani and Aluru, 2016; Wang et al., 2023b; Lin et al., 2024). Notably, ions tend to accumulate near the pore walls, resulting in a heterogenous radial distribution within the confined solution (Argyris et al., 2010). This behavior parallels that observed in electrical double layers between bulk electrolytes and charged surfaces (Lima et al., 2008). At the nanoscale, the contribution of this interfacial layer becomes increasingly significant due to its enhanced relative volume, and may be harnessed in emerging technologies such as desalination and enhanced oil recovery (Wang et al., 2018; Fang et al., 2021).

In summary, nanoconfinement induces profound shifts in the phase equilibria of water and aqueous solutions, affecting transitions among gas, liquid, and solid states. These deviations arise from enhanced interfacial interaction and altered thermodynamic conditions at the nanoscale. Importantly, the observed depression in the ice melting point and salt DRH under confinement supports the potential for stable brine phases on the Martian surface, contributing to our understanding of extraterrestrial aqueous environments.

2.3 Interfacial water

2.3.1 Water adsorption on the NaCl crystal surface

Following previous discussions of water vapor adsorption onto pore walls and the associated freezing behaviors in **Section 2.2**, this section focuses on the properties of adsorbed water films on crystal surfaces. Since the mid-20th century, the water adsorption on NaCl surfaces has attracted significant attention due to its impact on various chemical and physical properties of the crystal, such as ductility and electrical conductivity (Otterson, 1963; May and Jayne, 1966). The phenomenon of water adsorption was first reported inadvertently by Craig and Mcintosh (1952), who observed that NaCl particles lost specific surface area exposure to moist air. They attributed this change to particle sintering, which they proposed occurs through a dissolution–recrystallization process facilitated by an adsorbed water film (Craig and Mclntosh, 1952; Papée and Laidler, 1958). Subsequent studies provided molecular-level insight into the nature of the adsorbed water. Price and co-workers, using Infrared spectroscopy, demonstrated that water molecules are adsorbed on cesium halide surfaces via hydrogen bonding, in particular, with surface anions (Price et al., 1958). Based on this, Lad (1968) quantified the amount of adsorbed water and specific surface area of NaCl grains, proposing a molecular model wherein a single water molecule bridges two chloride ion sites through its hydrogen atoms. Barraclough and Hall (1974) further characterized the adsorption process by measuring the isosteric heat of water adsorption, which was found to be close to the enthalpy of water condensation, indicating a strong interaction between water and crystal surface. Complementing this thermodynamic perspective, Hucher et al. (1967) analyzed the superficial conductivity of NaCl crystals and proposed a three-stage adsorption process: initial physisorption of water onto the crystal surface, hydration of the surface Na^+ by adsorbed water molecules, and, eventually, dissolution of the crystal lattice.

2.3.2 Microscopic and spectroscopic investigation of the water adsorption

Since the 1990s, the structure of adsorbed water films and their interaction with crystal surfaces have been extensively investigated using a variety of surface–sensitive spectroscopic techniques, including infrared spectroscopy (IR), ultraviolet photoemission spectroscopy (UPS), X–ray photoelectron spectroscopy (XPS), and electron energy loss spectroscopy (EELS) (Fölsch and Henzler, 1991; Peters and Ewing, 1997a). Atomic force microscopy (AFM) and its advanced derivatives have also been introduced as powerful tools in this field (Dai et al., 1997). In parallel, molecular simulation has been increasingly integrated with experimental approaches to explore the dynamics of water adsorption at the molecular level. Wassermann et al. (1993) demonstrated through molecular simulations that, as the surface coverage approaches approximately 0.5 monolayer, the intermolecular interactions among water molecules become stronger than the interaction with the NaCl substrate. At bilayer coverage, a two-dimensional ice-like structure emerges and is found to be energetically stable. These structural configurations were supported by the optical second harmonic measurement and low-energy electron diffraction patterns. Using infrared spectroscopy, Peters and Ewing (1997a, 1997b) characterized the nature of the adsorbed water film on a NaCl surface. They proposed that the thin water film exhibits a liquid-like behavior as evidenced by the isotropic molecular orientation and an adsorption enthalpy comparable to that of water condensation. By numerically integrating the spectrum over the OH-stretching frequency range (2950−3800 cm^{-1}), the surface water coverage could be quantitatively assessed. At low RH, isolated water molecules adsorb with their oxygen atoms facing the Na^+ ions and oriented perpendicular to the surface. In this region, repulsive dipole interactions prevent hydrogen bonding between neighboring molecules. As the surface coverage increases and reaches a monolayer, additional water molecules are forced to adsorbed at adjacent sites. When the film thickens to two layers, occasional incorporation of ions from surface detects into the water film has been observed (Peters and Ewing, 1997b; Foster and Ewing, 2000). Notably, the infrared spectra of the bilayer water film closely resemble those of a 5 m NaCl solution, suggesting that the adsorbed film behaves as a saturated brine film. Below two layers coverage, the OH-stretching bands (2950–3800 cm^{-1}) shift to lower frequencies as the film grows, indicating enhanced hydrogen bonding among water molecules and reduced interactions with the substrate. Above two layers coverage, the band center stabilizes, indicating the transition to a bulk-like liquid film (Peters and Ewing, 1997a; Foster and Ewing, 2000). AFM and XPS measurements further corroborate a three-stage adsorption−deliquescence process (Dai et al., 1997; Bruzewicz et al., 2011; Verdaguer et al., 2005, 2008; Lin et al., 2021). These studies reveal that a complete monolayer coverage of the NaCl crystal surface is achieved at approximately 35% RH, beyond which ion solvation becomes evident (Dai et al., 1997; Verdaguer et al., 2008). A marked acceleration in water uptake occurs beyond 65% RH, transitioning from layer-by-layer growth to a rapid increase in film thickness at the nanometer scale (Bruzewicz et al., 2011). In summary, the evolution of water adsorption on a NaCl crystal surface can be delineated into three distinct regimes based on relative humidity. Below 35 % RH, water molecules adsorb in isolation. Between 35% and 65% RH, a complete monolayer forms and ion solvation initiates. Above 65% RH, the adsorbed water film behaves like a saturated solution, with enhanced ion mobility and exponentially increasing adsorption rates.

2.3.3 Electrical characterization of the water film

The formation of an adsorbed water film not only initiates the deliquescence of an anhydrous salt, such as NaCl, but also contributes to the formation of salt hydrates. Research conducted by the group of Huinink suggests that salt hydration proceeds through a dissolution−crystallization mechanism, wherein the lower hydrate dissolves into the interfacial water film and subsequently recrystallizes as a higher hydrate (Sögütoglu et al., 2019, 2021). This hypothesis is further supported by conductivity measurement of compacted salt grains (Houben et al., 2022). In particular, the conductivity of a K_2CO_3 tablet was observed to increases with rising relative humidity, with a marked change occurring just below the equilibrium humidity of hydration and formation of $K_2CO_3 \cdot 1.5H_2O$. This abrupt transition was attributed to the formation of a water film at the grain boundaries, enhancing ion mobility within film. In environments with fluctuating humidity, these water films may also promote powder caking (Craig and Mclntosh, 1952; Chen et al., 2018). Under humid conditions, soluble substances partially dissolve into the interfacial water films between the grains. When the environment dries, water evaporation leads to salt crystallization, forming salt bridges that bind particles together, an effect commonly observed in powder technology and food science (Chen et al., 2018). Similarly, Salameh and Mauer proposed that capillary condensation of water at the contact points between crystals can trigger mutual deliquescence in binary mixtures at relative humidities lower than the deliquescence point of the individual components (Salameh and Taylor, 2005; Salameh et al., 2006; Mauer, 2022). Though the direct observation of such interfacial water film remains challenging, their presence offers a physically plausible explanation for these phenomena.

Artemov et al. (2020) constructed a porous structure by compacting single crystalline diamond particles, with pore radii ranging from 2–200 nm as the particle size varied from 5–500 nm. The pore channels of the compacted tablets were saturated with water, and the conductivity of the confined water was measured using broadband dielectric spectroscopy. Their results revealed that the conductivity of confined and interfacial water initially increases with decreasing pore size, reaching a maximum at approximately 2 nm, and then declines as pores become narrower. Confined water was proposed to comprise two components: an interfacial layer and the bulk−like water occupying the pore core. The enhanced conductivity was attributed to the high proton mobility in the interfacial water, with the peak conductivity reaching 0.02 S/cm, five orders of magnitude higher than that of bulk water. Experimental data fitting indicated that the interfacial layer has a thickness of approximately 1 nm. When the pore size drops below 2 nm, the overlapping of opposing interfacial layers results in reduced conductivity, likely due to the confinement effect of both pore walls. Before this, Fumagalli et al. (2018) had developed a precisely defined slit−like nanochannel using hexagonal boron nitride (*h*BN) and graphite, enabling direct measurement of the dielectric constant of confined water within such channels. Their observations reach a good agreement even with different methods, providing further evidence for the distinctive behavior of interfacial water under nanoconfinement.

2.3.3 Premelting water layers on the ice surface

The liquid−like interfacial water film on the surface of ice is another key aspect of confined water research (Kuo et al., 2011; Slater and Michaelides, 2019). The structure and properties of this nonfreezing layer have been extensively characterized using X−ray diffraction (Lied et al., 1994; Suter et al., 2006), AFM (Döppenschmidt and Butt, 2000), various spectroscopic methods (Materer et al., 1995; Wei et al., 2001), and molecular dynamic (MD) simulation (Nada and van der Eerden, 2003; Conde et al., 2008). The thickness of this premelting layer varies from a monolayer to several tens of nanometer, depending on temperature from −100 °C to near the ice melting point (Bartels−Rausch et al., 2014). Recent cryogenic AFM study showed that the ice surface begins to exhibit structural disorder starting around 120 K, suggesting that premelting initiates at crystal detect sites (Hong et al., 2024). Likewise, the stability of monolayer water film on salt crystal surface has been investigated. For NaCl, terrace dissolution begins approximately 145 K (Chen et al., 2014; Peng et al., 2017), which is higher than the onset of premelting on pure ice surface, yet significantly lower than the eutectic temperature of bulk NaCl solution. This observation offers insight into eutectic melting at atomic scale. Analogous to mutual deliquescence in salt mixtures, the eutectic melting in ice−salt systems is likely initiated by the formation of interfacial water film between the ice and salt crystals.

2.4 Water at low temperature

2.4.1 Anomalous properties of the supercooled water and solution

Given that one of the key contexts of this dissertation is the phase equilibrium among salt, ice, aqueous solution, and water vapor in the cryogenic Martian environment, it is essential to introduce the anomalous thermodynamic behavior of water with varying temperature. Unlike most liquid, whose thermodynamic properties such as density, heat capacity, thermal expansion coefficient, and isothermal compressibility change monotonically with temperature, water exhibits unique and non−monotonic behavior. One prominent example is the density maximum at 4 °C, which underlies the well−known phenomenon of ice floating on liquid water (Gallo et al., 2016). This anomaly is generally attributed to the rearrangement of hydrogen bonding networks among water molecules (Speedy and Angell, 1976; Debenedetti and Stanley, 2003; Huang et al., 2009). Over the years, several hypotheses have been proposed over to explain this anomalous behavior (Speedy, 1982; Poole et al., 1992; Poole et al., 1994; Sastry et al., 1996). Despite differences in their proposed phase diagrams for metastable water at low temperatures, a common theme is the existence of two distinct liquid states: low−density liquid water (LDL) and high−density liquid water (HDL) (Soper and Ricci, 2000). Among these models, the second critical point scenario postulates the existence of liquid−liquid critical point (LLCP), which is considered the origin of many of water's anomalies (Mishima and Stanley, 1998; Sciortino et al., 2003). Extending this framework, Poole and collaborators applied molecular dynamic simulations to supercooled salt solution, and found that LLCP behavior can also exist in salt solutions such as LiCl, NaCl, and $NaClO_4$. Interestingly, the LLCP in these systems are located at higher temperatures and lower pressures compared to pure water, implying that the presence of ions shifts the critically region while preserving the essential physics (Corradini et al., 2010; Corradini and Gallo, 2011; Perin and Gallo, 2023; La Francesca and Gallo, 2023)

The multi−temperature equilibria of the water and salt system often extend to temperatures well below the freezing point of pure water, for example, to as low as −50 °C in the case of $CaCl_2$ solution. However, the extension of the ice−liquid water equilibrium to lower temperatures is thermodynamically constrained by the heat capacities of both ice and liquid water (Murphy and Koop, 2005). Due to the limitations imposed by ice nucleation, the heat capacity of water can only be measured down to a certain temperature. Current experimental and simulation studies indicate that water's heat capacities increase with decreasing temperature until it reaches a maximum around 228 K, after which it begins to decline (Pathak et al., 2021; Caupin and Anisimov, 2019). No experimental heat capacity data exist below 228 K due to the of supercooling limit of existing techniques. To model the temperature dependence of equilibria involving ice and supercooled salt solution, it is necessary to extrapolate heat capacity of water beyond the measurable range. However, such extrapolation is inherently uncertain because of the complex and anomalous behavior of water in the deeply supercooled region. The specific heat capacity of aqueous salt solution is further influenced by both temperature and salt concentration. At low concentrations, it typically increases with decreasing temperature, whereas at high concentrations, it decreases monotonically (Toner et al., 2016; Toner et al., 2017a; Toner et al., 2017b). Solutes significant alter the structure and thermodynamic properties of water, and their influence becomes more pronounced in concentrated solutions. As a result, there is currently no consensus on the functional form of water heat capacity in aqueous solution. Researchers therefore adopt different empirical expressions when constructing ion−interaction models to calculate salt−ice phase equilibria (Clegg and Brimblecombe, 1995; Murphy and Koop, 2005; Toner et al., 2015b; Li et al., 2022). The lack of consistency and the empiric nature of these extrapolations can introduce significant uncertainties in modeling low−temperature systems. Nevertheless, in the absence of further experimental data, no superior alternative currently exists.

2.4.2 Glassy transitions of water and salt solutions

In addition to ordinary water freezing and salt crystallization upon cooling, aqueous electrolyte solutions can undergo vitrification, a transition to glassy phase, which has been extensively studied for pure water (Angell and Sare, 1970; Angell, 2002; Ediger et al., 1996). The glass transition temperature of salt solutions is typically higher than that of pure water, and this difference increases with salt concentration (Angell and Sare, 1970). Mars-relevant brines, such as $Ca(ClO_4)_2$ and $Mg(ClO_4)_2$ solutions, are particularly effective glass formers at low temperatures (Tu et al., 2019). While most salt solutions vitrify only under rapid cooling, these perchlorate solutions do not crystalize even under slow cooling. Instead, they form amorphous phases at temperatures as low as −120 °C (Toner et al., 2014). According to the *in-situ* X-ray diffraction and Raman spectroscopy analysis, Tu et al. attributed this unusual phase behavior to ion pair formation and its temperature and concentration dependent dynamics. The strong hydration of the cations (Ca^{2+} or Mg^{2+}) sequesters free water molecules within the hydration shells, inhibiting ice nucleation. Meanwhile, the large anions disrupt the local tetrahedral hydrogen-bonded structure of water, further depressing the freezing. Additionally, their study found a close correspondence between the deliquescence relative humidity of various salts and the eutectic temperatures of their solutions (Tu et al., 2019). This correlation is explained by the shared underlying factor: low water activity, resulting from strong ion−water interactions, which simultaneously lowers both eutectic temperature and deliquescence humidity.

2.4.3 Eutectic transition of ice−salt mixture

The eutectic point represents the lowest temperature at which a salt solution can remain in the liquid state. Therefore, eutectic transitions are expected to be common on the Martian surface wherever brine formation occurs. In a simplified binary phase diagram, the eutectic point corresponds to the intersection of the water freezing curve and the salt dissolution curve, as illustrated in Fig. 2−1. It reflects the convergence of two triple phase equilibria: ice−solution−water vapor and salt−solution−water vapor. Consequently, eutectic melting is a coupled process involving the simultaneous melting of ice and dissolution of salt crystals, as well as the deliquescence of salt through water vapor uptake. This transformation is likely facilitated by the formation of an interfacial water film, either through the premelting of ice or the adsorption of water vapor onto the salt surface. The water film acts as a medium for ion dissolution, forming a thin brine layer that exhibits reduced water activity. This decrease in water activity plays a crucial role in determining both the melting point of ice and the condensation pressure of water vapor (Chen et al., 2014; Peng et al., 2017; Peters and Ewing, 1997a). From a thermodynamic standpoint, it is difficult to definitively distinguish whether melting or deliquescence primarily governs the transformation from solid and gas phase to liquid phase. However, experimental investigations involving $Ca(ClO_4)_2$ in the presence of ice and water vapor suggest that melting is kinetically favored during the formation of liquid brine (Fischer et al., 2014, 2016).

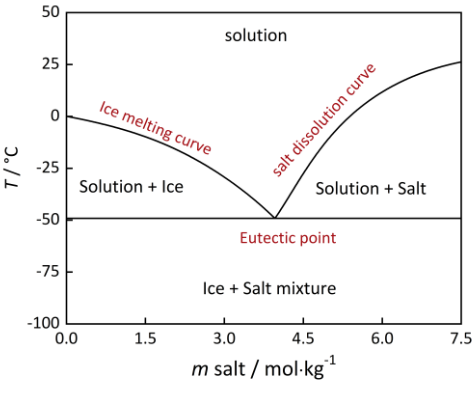

Figure 2−1. Typical binary phase diagram salt solution (in this case for $CaCl_2·6H_2O$).

2.5 Thermodynamic modeling

2.5.1 Pitzer model

The Pitzer model is widely applied in the solutions phase equilibrium studies due to its proven accuracy across broad temperature and concentration ranges (Pitzer and Oakes, 1994; Toner et al., 2015b). In this dissertation, the thermodynamic properties of a bulk system, such as water activity and the activity coefficient of the solute are modelled through Pitzer theory. The equations of the molality-based ion interaction Pitzer model are presented as follows:

Pitzer model equations: The water activity of an electrolyte solution is defined as:

$$\ln a_{\mathrm{w}} = -\left(\frac{\phi}{m_{\mathrm{w}}}\right)\sum_i m_i \tag{2–1}$$

where ϕ is the osmotic coefficient, m_{w} is the molality of water (55.50844 mol·kg^{-1}), m_i is the molality of ion i and the sum covers all solute species. Thus, for a single electrolyte solution we obtain:

$$\ln a_{\mathrm{w}} = -\,\phi \nu m/m_{\mathrm{w}} \tag{2–2}$$

where ν is the total number of ions formed by complete dissociation of the electrolyte (ν=2 in the case of NaCl and ν=3 in the case of $CaCl_2$). In the Pitzer approach the equation for the osmotic coefficient of an electrolyte MX consisting of ν_{M} positive ions of charge z_{M} and ν_{X} negative ions of charge z_{X} is:

$$(\phi - 1) = |z_{\mathrm{M}} z_{\mathrm{X}}| f_{\phi} + 2(\nu_{\mathrm{M}}\nu_{\mathrm{X}}/\nu) m B_{\mathrm{MX}}^{\phi} + 2(\nu_{\mathrm{M}}\nu_{\mathrm{X}})^{3/2}/\nu m^2 C_{\mathrm{MX}}^{\phi} \tag{2–3}$$

In the case of NaCl, $\nu_{\mathrm{M}} = \nu_{\mathrm{X}} = z_{\mathrm{M}} = 1$ and $z_{\mathrm{X}} = -1$; in the case of $CaCl_2$, $\nu_{\mathrm{M}} = 1$, $\nu_{\mathrm{X}} = z_{\mathrm{M}} = 2$ and $z_{\mathrm{X}} = -1$. In equation (2–3) the Debye–Hückel term, f_{ϕ}, for the osmotic coefficient is defined as:

$$f_{\phi} = -A_{\phi}\frac{I^{1/2}}{(1+bI^{1/2})} \tag{2–4}$$

where A_{ϕ} is the Debye–Hückel parameter for the osmotic coefficient, b is a constant (b = 1.2 kg$^{1/2}$·mol$^{-1/2}$) and the ionic strength I is given by:

$$I = \frac{1}{2}\sum_i m_i z_i^2 \tag{2–5}$$

Thus, in the case of NaCl, $I=m$, and for $CaCl_2$, $I=3m$. The second virial coefficient B_{MX}^{ϕ} is ionic strength dependent and is defined as:

$$B_{\mathrm{MX}}^{\phi} = \beta_{\mathrm{MX}}^{(0)} + \beta_{\mathrm{MX}}^{(1)} exp(-\alpha_1 I^{1/2}) + \beta_{\mathrm{MX}}^{(2)} exp(-\alpha_2 I^{1/2}) + \beta_{\mathrm{MX}}^{(3)} exp(-\alpha_3 I^{1/2}) \tag{2–6}$$

where $\beta_{\mathrm{MX}}^{(0)}$, $\beta_{\mathrm{MX}}^{(1)}$, $\beta_{\mathrm{MX}}^{(2)}$, $\beta_{\mathrm{MX}}^{(3)}$ and C_{MX}^{ϕ} are solute-specific interaction parameters for a binary aqueous solution. In the original equations values of α_1=2 kg$^{1/2}$·mol$^{-1/2}$ and α_2=12 kg$^{1/2}$·mol$^{-1/2}$ are fixed and the latter is only used for 2−2 electrolytes such as $CaSO_4$(aq) to avoid the explicit treatment of association equilibria. In the extended set of equations used here (Steiger et al., 2008a), individual values of $\alpha_{\mathrm{MX}}^{(i)}$ are assigned to each electrolyte and the terms in $\alpha_{\mathrm{MX}}^{(2)}, \beta_{\mathrm{MX}}^{(2)}$ and $\alpha_{\mathrm{MX}}^{(3)}, \beta_{\mathrm{MX}}^{(3)}$ are also used for other charge types. In the treatment of $CaCl_2$(aq), it turned out that both parameters $\beta_{\mathrm{MX}}^{(2)}$ and $\beta_{\mathrm{MX}}^{(3)}$ were required to represent the properties of highly concentrated solutions over the full temperature range. In the treatment of NaCl(aq), the only additional parameter was $\beta_{\mathrm{MX}}^{(2)}$, $\beta_{\mathrm{MX}}^{(3)}$ was not required.

The mean activity coefficient $\gamma_\pm$ of a single electrolyte in the ion interaction approach is given by

$$\ln\gamma_{\pm} = |z_{\mathrm{M}}z_{\mathrm{X}}|f_{\gamma} + 2(\nu_{\mathrm{M}}\nu_{\mathrm{X}}/\nu)mB_{\mathrm{MX}}^{\gamma} + 2(\nu_{\mathrm{M}}\nu_{\mathrm{X}})^{3/2}/\nu m^2 C_{\mathrm{MX}}^{\gamma} \tag{2–7}$$

where $C_{\mathrm{MX}}^{\gamma} = 3/2C_{\mathrm{MX}}^{\phi}$ and $B_{\mathrm{MX}}^{\gamma} = B_{\mathrm{MX}} + B_{\mathrm{MX}}^{\phi}$ with

$$B_{\mathrm{MX}} = \beta_{\mathrm{MX}}^{(0)} + \beta_{\mathrm{MX}}^{(1)}g\left(\alpha_1, I^{1/2}\right) + \beta_{\mathrm{MX}}^{(2)}g\left(\alpha_2, I^{1/2}\right) + \beta_{\mathrm{MX}}^{(3)}g\left(\alpha_3, I^{1/2}\right) \tag{2–8}$$

and

$$g\left(\alpha_i I^{1/2}\right) = \frac{2}{\left(\alpha_i I^{1/2}\right)^2}\left[1 - (1 + \alpha_i I^{1/2})\,exp(-\alpha_i I^{1/2})\right] \tag{2–9}$$

The Debye−Hückel term f_γ for the activity coefficient is defined as:

$$f_{\gamma} = -A_{\phi}\left[\frac{I^{1/2}}{(1+bI^{1/2})} + \left(\frac{2}{b}\right)\ln\left(1 + bI^{1/2}\right)\right] \tag{2–10}$$

Using the ion interaction equations to calculate the thermodynamic properties of aqueous solutions of single salts requires values of the ion interaction parameters $\beta_{\mathrm{MX}}^{(0)}, \beta_{\mathrm{MX}}^{(1)}, \beta_{\mathrm{MX}}^{(2)}, \beta_{\mathrm{MX}}^{(3)}$ and C_{MX}^{ϕ} which have to be determined from experimental data. The temperature dependence of the interaction parameters P is obtained from experimental data at different temperatures and is expressed by

$$P(T) = q_1 + q_2(1/T - 1/T_{\mathrm{R}}) + q_3\ln(T/T_{\mathrm{R}}) + q_4(T - T_{\mathrm{R}}) + q_5(T^2 - T_{\mathrm{R}}^2) \tag{2–11}$$

Phase equilibria: For a salt hydrate consisting of ν_{M} cations, ν_{X} anions and n molecules of water, the reaction describing equilibrium between the crystalline solid and its saturated solution is

$$M_{\nu_{\mathrm{M}}}X_{\nu_{\mathrm{X}}} \cdot n\mathrm{H_2O(cr)} \rightleftharpoons \nu_{\mathrm{M}}M^{z+}\mathrm{(aq)} + \nu_{\mathrm{X}}X^{z-}\mathrm{(aq)} + n\mathrm{H_2O(l)} \tag{2–12}$$

In the case of a hydrated solid with n molecules of hydration water, the equilibrium constant of the dissolution reaction, i.e. the thermodynamic solubility product, is thus given by:

$$\ln K_{\mathrm{n}} = \nu_{\mathrm{M}} \ln m_{\mathrm{M}} + \nu_{\mathrm{X}} \ln m_{\mathrm{X}} + \nu_{\mathrm{M}} \ln \gamma_{\mathrm{M}} + \nu_{\mathrm{X}} \ln \gamma_{\mathrm{X}} + n \ln a_{\mathrm{w}} \tag{2–13}$$

where m_{M}, m_{X}, γ_{M} and γ_{X} represent the saturation molalities and activity coefficients of cations M and anions X, respectively, and a_{w} is the water activity in the saturated solution.

At equilibrium, neglecting the very minor influence of the non-ideal behavior of water vapor, the water activity a_{w} of an aqueous solution is given by:

$$a_{\mathrm{w}} = p/p_{\mathrm{w,0}} = \mathrm{RH} \tag{2–14}$$

where p_{w} is the water vapor pressure above the salt solution and $p_{\mathrm{w,0}}$ is the saturation vapor pressure of pure water. At equilibrium, the water activity equals the relative humidity, RH, and the water activity of a saturated solution equals the deliquescence humidity (DRH) of the crystalline solid. This is the relative humidity at which the crystalline salt and its saturated solution are at equilibrium.

Once, the parameters of the ion interaction equations are known, the values of the thermodynamic solubility product (the equilibrium constant of the dissolution reaction) can be calculated from experimental solubility data using Equation (2–13) and the temperature dependence of the logarithmic solubility products can be represented using Equation (2–11).

Additional phase equilibria include the dehydration or decomposition reactions

$$M_{\nu_{\mathrm{M}}}X_{\nu_{\mathrm{X}}} \cdot n_A \mathrm{H_2O(cr)} \rightleftharpoons M_{\nu_{\mathrm{M}}}X_{\nu_{\mathrm{X}}} \cdot n_B \mathrm{H_2O(cr)} + (n_{\mathrm{A}} - n_{\mathrm{B}})\mathrm{H_2O(g)} \tag{2–15}$$

where subscripts A and B refer to the different hydrated forms of a solid. The equilibrium constant K_{AB} for the dehydration reaction is given by:

$$K_{\mathrm{AB}} = p_{\mathrm{w,AB}}/p_{\mathrm{w}}^{\circ} \tag{2–16}$$

where $p_{\mathrm{w,AB}}$ refers to the equilibrium water vapor partial pressure of the hydration–dehydration equilibrium. K_{AB} is also related to the solubility products of the two solids:

$$\ln K_{\mathrm{n_B}} = \ln K_{\mathrm{n_A}} - (n_{\mathrm{A}} - n_{\mathrm{B}}) \ln K_{\mathrm{AB}} \tag{2–17}$$

The Pitzer parameters for $KCl(aq)$, $MgCl_2(aq)$ and $(NH_4)_2SO_4(aq)$ were taken from, Steiger et al., (2008a), Steiger et al. (2011) and Talreja-Muthreja and Steiger (2025), respectively. The parameters for $CaCl_2(aq)$ and $NaCl(aq)$ are presented in Sections A1 and A2, respectively. The model parameters for the binary $NaClO_4$–H_2O system were taken from the molality-based model of Toner et al. (2016). For the binary alkaline earth perchlorate systems $Mg(ClO_4)_2$–H_2O and $Ca(ClO_4)_2$–H_2O the mole fraction based models of Li et al. (2022) were used.

2.5.2 In confinement

In confinement, the melting point depression of pure ice is commonly described by the Gibbs–Thomson equation:

$$\Delta T = (2T_0 \gamma_{\mathrm{cl}} V_{\mathrm{m,s}})/(\Delta_{\mathrm{m}} H(r_{\mathrm{p}} - t)) \qquad (2\text{–}18)$$

where T_0 is the melting temperature of bulk ice (273.15 K), γ_{cl} is the solid–liquid interfacial energy, $V_{\mathrm{m,s}}$ is the molar volume of solid ice, $\Delta_{\mathrm{m}}H$ is the melting enthalpy of ice, r_{p} is the pore radius, and t is the thickness of the non-freezable layer.

However, the Gibbs–Thomson equation is not able to accurately describe the melting behavior of salt solution, as the melting temperature is influenced not only by the pore size but also the solute concentration governing the water activity. To address this limitation, Liu et al. (2017) proposed a hybrid model that combines the Ostwald–Freundlich and Gibbs–Thomson equations to better predict the phase behavior of confined glycerol solution. In nanopores, the temperature depression of the ice melting point is primarily attributed to the increased importance of the curvature of the solid–liquid interface. The solid–solution and the liquid–vapor interfaces are schematically illustrated in Fig. 2–2 for both unsaturated and fully saturated conditions within pores.

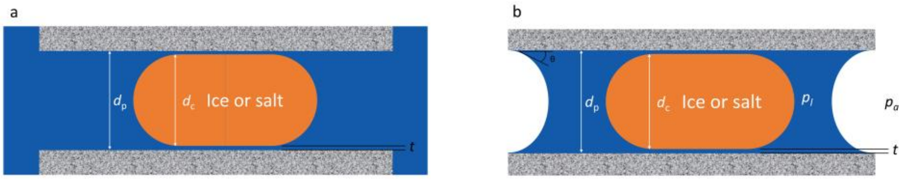

Figure 2–2. Schematic illustration of the solid–liquid interface of confined solution and crystal. (a): saturated pore; (b): partial pore filling.

In the calorimeter measurements carried out in this dissertation, the nanoporous silica was completely saturated with solution, and excess bulk solution exists outside the pores, as illustrated Fig. 2–2a. While the confined solution initially forms a flat interface with the adjacent bulk solution, this interface will become unstable upon crystallization during freezing. As a result, the geometry shifts and the initial melt in the nanopore forms a concave interface similar to that shown in Fig. 2–2b. Thermodynamically, the main difference between the two conditions illustrated in Fig. 2–2 lies in the presence or absence of a curved liquid–vapor interface, which results in a pressure drop. In this study, we compare phase equilibrium shifts under both scenarios: one considering the solute effect described by Pitzer theory, the Kelvin effect, and the

Laplace pressure induced by the curved solution−vapor interface, in the following referred to as the PKL model (Pitzer theory, Kelvin effect, and Laplace pressure), and, second, neglecting Laplace pressure, marked as PK model (Pitzer theory and Kelvin effect).

In the over-filled pore, as shown in Fig. 2−2a, the chemical potential of an ice nanocrystal with a hemispherical solid−liquid interface is modified by an additional interfacial energy term:

$$\mu_{\mathrm{ice},r} = \mu_{\mathrm{ice},\infty} + \gamma_{\mathrm{cl}} 2V_{\mathrm{m,w}}/r_{\mathrm{c}} \qquad (2-19)$$

Where $\mu_{\mathrm{ice},r}$ and $\mu_{\mathrm{ice},\infty}$ are the chemical potentials of an ice nanocrystal and the bulk crystal, respectively, γ_{cl} is the interfacial energy of the ice−solution interface, $V_{\mathrm{m,w}}$ is the partial molar volume of ice, and r_{c} is the radius of the nanocrystal, which is assumed to be isotropic. It is worth mentioning that the nanocrystal radius is not exactly equivalent to the pore radius due to the presence of a solution film between the ice and the pore wall (Desarnaud, 2016). In our calculation, we adopted a film thickness t = 0.6 nm, which is consistent with the typical thickness of the non-freezing water layer at the ice−silica interface.

If the pore is not fully saturated with solution, as shown in Fig. 2−2b, the liquid−vapor interface forms a concave meniscus. For complete wetting (θ = 0°), which is assumed for the aqueous solution in silica materials, the Laplace pressure is given by:

$$\Delta p = p_{\mathrm{l}} - p_{\mathrm{a}} = 2\gamma_{\mathrm{lv}}/r_{\mathrm{lv}} \qquad (2-20)$$

where p_{l} and p_{a} are pressure in the liquid and the ambient pressure, respectively, and γ_{lv} is the liquid−vapor interfacial energy. r_{lv} is the radius of the curvature of the liquid−vapor interface, calculated as the pore radius minus the thickness of the non-freezing layer ($r_{\mathrm{p}} - t$).

The influence of Laplace pressure on the chemical potential of ice is given by:

$$\mu_{\mathrm{ice,r}} = \mu_{\mathrm{ice},\infty} - \frac{\Delta\bar{V}^{\circ}}{\mathrm{R}T}\Delta p + \frac{\Delta\bar{K}^{\circ}}{2\mathrm{R}T}(\Delta p)^2 \qquad (2-21)$$

Where R is the universal gas constant, T is the absolute temperature, and Δp is the Laplace pressure. $\Delta\bar{V}^{\circ}$ and $\Delta\bar{K}^{\circ}$ are the changes in molar volume and molar compressibility, respectively, during the melting process. Considering the small deviations between the standard pressure and that in the confinement, its influence on compressibility is very small and was neglected in this model.

By combining the Equations (2−19) and (2−21), the chemical potential of ice in the partially−filled nanopores can be expressed as:

$$\mu_{\mathrm{ice,r}} = \mu_{\mathrm{ice},\infty} + \gamma_{\mathrm{cl,ice}} \frac{2V_{\mathrm{m,c}}}{r_{\mathrm{cl}}} - \frac{\Delta\bar{V}^{\circ}}{\mathrm{R}T}\Delta p + \frac{\Delta\bar{K}^{\circ}}{2\mathrm{R}T}(\Delta p)^2 \qquad (2-22)$$

The chemical potential of bulk water is given by

$$\mu_{\mathrm{water}} = \overset{\circ}{\mu}_{\mathrm{water},\infty} + \mathrm{R}T\ln a_{\mathrm{w}} \tag{2–23}$$

Where $\overset{\circ}{\mu}_{\mathrm{water},\infty}$ is the standard chemical potential of bulk water and a_{w} is the water activity of the salt solution. The melting equilibrium of ice in the PKL model can be calculated combining Equations (2–22) and (2–23), whereas in PK model, it is determined by Equations (2–19) and (2–23).

For the equilibrium between a salt nanocrystal and the surrounding solution, both the curvature effect and pressure shift influence solubility. For a spherical solid, the solubility product is corrected using the Ostwald–Freundlich equation (Steiger, 2005)

$$\ln K_{\mathrm{r}}^{\circ} = \ln K_{\infty}^{\circ} + \gamma_{\mathrm{cl}}\,(2V_{\mathrm{m,c}})/(\mathrm{R}Tr_{\mathrm{c}}) \tag{2–24}$$

where $\ln K_{r}^{\circ}$ and $\ln K_{\infty}^{\circ}$ are the thermodynamic solubility products at standard pressure (0.1 MPa) for the nanocrystal with radius of r_{c} and the bulk crystal, respectively; γ_{cl} is the crystal–solution interfacial energy, $V_{\mathrm{m,c}}$ is the molar volume of the crystal, and $r_{\mathrm{c}} = r_{\mathrm{p}} - t$ accounts for the exclusion of the solution film (thickness t) from the crystal radius.

The pressure dependence of the solubility product of the bulk crystal is described by Millero (1982):

$$\ln K_{\infty}^{p} = \ln K_{\infty}^{\circ} - \frac{\Delta\bar{V}^{\circ}}{\mathrm{R}T}\Delta p + \frac{\Delta\bar{K}^{\circ}}{2\mathrm{R}T}(\Delta p)^{2} \tag{2–25}$$

where $\ln K_{\infty}^{p}$ and $\ln K_{\infty}^{\circ}$ are the solubility product of the bulk crystal at 0.1 MPa and at elevated pressure p. Similar with the ice melting in the pore, the compressibility change in the dissolution process is neglected.

By combining Equations (2–24) and (2–25), the solubility product of a nanocrystal in an unsaturated pore under pressure p is given by

$$\ln K_{\mathrm{r}}^{p} = \ln K_{\infty}^{\circ} + \gamma_{\mathrm{cl}}\frac{2V_{\mathrm{m,c}}}{\mathrm{R}Tr_{\mathrm{c}}} - \frac{\Delta\bar{V}^{\circ}}{\mathrm{R}T}\Delta p + \frac{\Delta\bar{K}^{\circ}}{2\mathrm{R}T}(\Delta p)^{2} \tag{2–26}$$

The solubility equilibrium in PKL model can be calculated using Equation (2–26), whereas in PK model, it is determined by Equation (2–24).

The chemical potential of water vapor (μ_{g}) and of liquid water (μ_{l}) in the confined solution are given by:

$$\mu_{\mathrm{g}} = \overset{\circ}{\mu}_{\mathrm{g}} + \mathrm{R}T\ln\,(p_{\mathrm{w}}/p^{\circ}) \tag{2–27}$$

$$\mu_{\mathrm{l}} = \mu^{\circ}_{\mathrm{l},\infty} + 2\gamma_{\mathrm{lv}}\bar{V}_{\mathrm{w}}/(r_{\mathrm{lv}}\mathrm{R}T) + \mathrm{R}T\ln a_{\mathrm{w}} \qquad (2\text{–}28)$$

Where μ°_{g} and $\mu^{\circ}_{\mathrm{l},\infty}$ are the standard potentials of water vapor and pure liquid water, respectively at p° = 0.1 MPa.

Combining Equations (2–27) and (2–28), the relative vapor pressure of an aqueous solution in a nanopore can be expressed by

$$\ln(p_{\mathrm{w}}/p_{\mathrm{w,sat}}) = 2\gamma_{\mathrm{lv}}\bar{V}_{\mathrm{w}}/(r_{\mathrm{lv}}\mathrm{R}T) + \ln a_{\mathrm{w}} \qquad (2\text{–}29)$$

The deliquescence equilibrium in PKL model can be calculated combining Equations (2–26) and (2–29), whereas in PK model, it is determined by Equations (2–24) and (2–29).

According to Equations (2–22), (2–26), and (2–29), the crystal–solution interfacial energy γ_{cl}, surface tension γ_{lv}, and the $\Delta V_{\mathrm{m}}^{\circ}$ are primary factors influencing the equilibrium shift in the pores at a given size. The interfacial energy between ice and water (γ_{cl}) has been extensively studied with various methods, including measurements of ice crystal growth rates, observations of grain–boundary grooves shape, analysis of supercooling behavior, and deductions based on ice nucleation theory (Fernandez and Barduhn, 1967; Ketcham and Hobbs, 1969; Coriell et al., 1971; Jones, 1973; Hardy, 1977; Hillig, 1998). These studies suggest that γ_{cl} decreases with temperature, a trend also observed for other materials (Jian et al., 2012; Němec, 2013; Baidakov et al., 2013). In aqueous system, this decline reflects the increased formation of tetrahedral water cluster in the supercooling region.

In contrast, the interfacial energy between ice and salt solutions (γ_{cl}) has been less thoroughly investigated, though it is generally predicted to be higher than that of pure ice–water due to the increased structure disparity between the liquid and ice phase. Apart from the temperature, γ_{cl} is also affected by the crystal size at the nanoscale, typically increasing as crystal size decreases (Jiang and Lu, 2008). In the experiments of this dissertation, melting at low temperatures occur exclusively in nanopores, where melting temperature correlates closely with pore size. This suggests that both positive and negative effects on γ_{cl}, caused respectively by reduced crystal size and lower temperature act simultaneously over the temperature range studied, complicating the determination of the temperature dependence of γ_{cl}. Thus far, the quantitative relationship between interfacial energy and variables such as temperature, crystal size, and solution composition remain unresolved. The variation in molality of saturated solutions also affect the interfacial energy at the ice–solution or salt–solution boundary. This effect arises from the structural divergence in the interfacial region, resulting from the change in ion hydration, water orientation, and local ordering at the salt–solution interface. Consequently, a constant value of γ_{cl}

(covering the interfacial energies between ice–water, ice–solution, and salt–solution) is assumed in the present calculations, which is regarded as an approximation due to the lack of reliable data.

2.5.3 Confinement effect on the ice melting and solubility equilibrium

According to the previous introduction, the origin of confinement effects on solubility arises from two primary contributions, the influence of Laplace pressure and the crystal size on the solubility. Due to the concave curvature of the confined liquid–gas interface, the negative Laplace pressure in the nanopores decreases the chemical potential of the solid, resulting in a salting–out effect that tends to lower solubility. On the contrary, the crystal–solution interfacial energy term increases the chemical potential of the solid phase, leading to the considerably salting–in effect that enhances solubility. The net influence on solubility depends on which of these two opposing effects predominates for a given system. For NaCl, the influence of Kelvin effect and Laplace pressure on solubility was quantified using the PKL model as a function of pore size. As demonstrated in Fig. 2–3, the salting–out effect arising from negative Laplace pressure becomes increasingly pronounced as pore size decreases, as indicated by the filled orange circles. In contrast, the crystal size effect exhibits a more complex dependence: it is not only controlled by the pore size but also highly sensitive to crystal–solution interfacial energy (γ_{cl}). The green and red squares show the variations of γ_{cl} in affecting the solubility changes in confinement. The net influence of Kelvin effect and Laplace pressure leads to a reduction in NaCl solubility (red circle) when the interfacial energy γ_{cl} is 20 mJ·m^{-2} (red square). However, when γ_{cl} is increased to 75 mJ·m^{-2} (green square), the salting–in effect becomes dominant, leading to the net increase in solubility (green circles). This behavior highlights the sensitivity of confined solubility equilibria to γ_{cl}. Talreja–Muthreja et al. (2022) analyzed the γ_{cl} for the NaCl–solution interface by interpreting experimental deliquescence relative humidities (DRH) of NaCl nanocrystals. They reported a range of γ_{cl} values from 25.6–88 mJ·m^{-2} at 25 °C. This broad variability underscores the challenge in precisely determining γ_{cl} due to the scarcity of direct measurements.

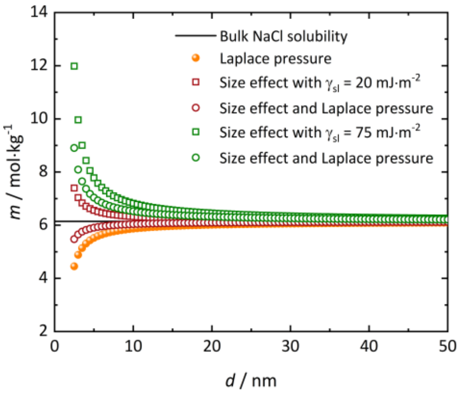

Figure 2–3. Influence of crystal size, Laplace pressure, and crystal–solution interfacial energy (γ_{cl}) on the solubility of NaCl at 25 °C in nanopore.

Chapter 3. Motivation and Tasks

This dissertation aims to investigate the lowest temperatures and relative humidities under which Mars-relevant salt brines can remain stable, with particular focus on chlorides and perchlorates. In addition, the freezing and melting behavior of common atmospheric aerosol solutions, such as sodium chloride and ammonium sulfate, under nanoconfinement is analyzed to gain insight into the interactions between water and nanoscale aerosol particles. Furthermore, the ubiquitous water films at the surface or interface of grains, generated by capillary condensation or water molecule adsorption, play a crucial role in the phase transitions of salts or their mixtures, including processes such as hydration, caking, and mutual deliquescence. To explore these phenomena, two quaternary reciprocal systems (Na^+–K^+–Cl^-–NO_3^-//H_2O and Na^+–NH_4^+–Cl^-–SO_4^{2-}//H_2O) are studied, with particular emphasis on the formation and evolution of solution films during phase transitions.

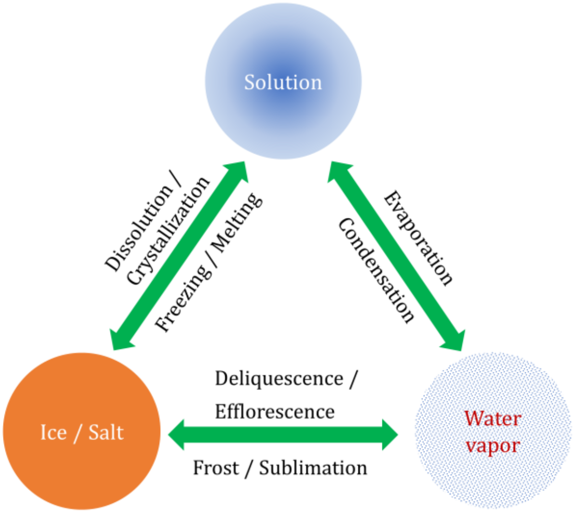

Figure 3–1. The phase equilibria among the water vapor, solution, and crystalline phase.

Overall, the phase transitions of electrolyte solutions, as illustrated in Fig. 3–1, and their anomalous behavior under nanoconfinement (in nanoporous silica) is systematically investigated using calorimetry, water vapor sorption analysis, Raman spectroscopy, and environmental scanning electron microscopy (ESEM). The experimental objectives of each Chapter are summarized as follows.

Chapter 4: This Chapter presents a detailed account of the synthesis and characterization of the porous materials, MCM-41 and SBA-15. It also outlines the experimental techniques and parameters applied throughout in this dissertation.

Chapter 5: An anomalously low DRH (18.5% at 25 °C) for $CaCl_2 \cdot nH_2O$, significantly lower than the widely accepted value of 28.5%, was reported in some literature studies. To elucidate this anomaly, water vapor sorption and Raman spectroscopy are employed to identify the corresponding solid phase associated with the 18.5% DRH and to explore the underlying mechanism behind this metastable transition.

Chapter 6: In order to interpret the absence of eutectic transitions in confined dilute solutions, it is proposed that ion accumulation in interfacial nonfreezing layers near the pore walls leads to the ion scarcity in the pore core, thus, inhibiting salt crystallization and eutectic transitions. A series of calorimetric experiments to systematically investigate the effects of salt concentration, pore size, and pore filling degree, which are the factors determining the ion content within pores, on the appearance of eutectic transitions under confinement are presented.

Chapter 7: The freezing and melting process of Mars-relevant salt solutions (NaCl, $MgCl_2$, $CaCl_2$, $NaClO_4$, $Mg(ClO_4)_2$, and $Ca(ClO_4)_2$) and of $(NH_4)_2SO_4$ solutions with atmospheric relevance in SBA-15 and MCM-41 nanopores are investigated calorimetrically. The effects of salt concentration on melting points and the influence of pore size on the depression of the melting and eutectic points under nanoconfinement are analyzed. The absence of first-order phase transitions in smaller pores are also discussed. In addition, the DRHs of Mars-relevant salts (KCl, $CaCl_2 \cdot nH_2O$, $MgCl_2 \cdot 6H_2O$, $Ca(ClO_4)_2 \cdot 4H_2O$, $Mg(ClO_4)_2 \cdot 6H_2O$, $NaClO_4 \cdot H_2O$) under nanoconfinement measured using water vapor sorption at 25 °C are presented. The influence of pore size on the DRHs and water vapor sorption isotherms of SBA-15−KCl composites is analyzed.

Chapter 8: A thermodynamic model combining Pitzer theory, Kelvin equation, and Laplace pressure is employed to simulate the phase equilibria of salt solutions within nanoconfinement. The model predicts key properties, including the melting temperature of ice, the eutectic melting temperature of ice−salt mixtures, and the DRHs of salt crystals within nanoporous silica. Interfacial energies of ice−solution and salt−solution are derived from the experimental melting temperature data, and their influence on the phase equilibria is analyzed. Finally, the model's limitations, which is caused by uncertainties in extrapolated thermodynamic properties at low temperature and supersaturation, are critically evaluated.

Chapter 9: Water film formed by adsorption or capillary condensation on salt particle surfaces are thought to initiate the deliquescence of NaCl. In this Chapter, the mutual deliquescence of a NaCl−KCl mixture is investigated via water vapor sorption and ESEM observations. It is proposed that water film formation at the contact points of two crystals facilitates mutual deliquescence at humidities lower than the DRHs of the individual salts. Moreover, the role of water films in the transformation from the metastable $NaNO_3$−KCl salt pair to the stable NaCl−KNO_3 pair within the Na^+−Cl^-−K^+−NO_3^-//H_2O quaternary reciprocal system as explored using water vapor sorption, *in-*

situ Raman spectroscopy, and ESEM are presented. Additionally, the behavior of an analogous atmospheric aerosol system $Na^+–NH_4^+–Cl^-–SO_4^{2-}//H_2O$ examined with water vapor sorption analysis is reported.

Chapter 10. Several conclusions regarding the phase behavior of aqueous electrolytes under nanoconfinement, as well as critical role of interfacial water films during phase transition, will be drawn. In addition, the potential applications of these process in various fields, such as planetary science and atmospheric chemistry, are discussed.

Chapter 4. Materials and Methods

This Chapter provides a brief overview of the materials and primary experimental techniques employed in this dissertation. The salts used in all experiments were obtained from commercial sources and used as received, without further purifications. In contrast, the mesoporous silicas, MCM-41 and SBA-15, are synthesized in the laboratory according to established protocols reported in the literature.

4.1 Materials

The salts used in all experimental investigations, including the calorimetry, water vapor sorption analysis, and Raman spectroscopy are summarized in Table 4−1.

Table 4−1. Commercial salts used in this dissertation.

Material	Purity	Source
$NaCl$	> 99.5%	Roth
KCl	> 99.5%	Roth
NH_4Cl	> 99.8%	Merck
$MgCl_2·6H_2O$	> 99%	Roth
$CaCl_2·2H_2O$	> 99%	Merck
$CaCl_2·6H_2O$	> 98%	Roth
$NaClO_4$	> 98%	Sigma
$Mg(ClO_4)_2·6H_2O$	> 99.5%	Sigma
$Ca(ClO_4)_2·4H_2O$	> 99%	Sigma
$NaNO_3$	> 99.5%	Roth
KNO_3	> 99.5%	Roth
Na_2SO_4	> 99%	Roth
$(NH_4)_2SO_4$	> 99.5%	Merck

SBA-15 was synthesized following the method reported by Zhao et al. (1998). In a typical synthesis, 6.4 g of the triblock copolymer Pluronic P-123 ($EO_{20}PO_{70}EO_{20}$, $M_w = 5800$, Aldrich) was dissolved in a solution containing 38 g of HCl (37 wt%, VWR International) and 194 g of deionized water. The solution was stirred until it became homogeneous and transparent. Subsequently, 13.8

g of tetraethoxysilane (TEOS, Aldrich) was added as the silica precursor, and the mixture was stirred vigorously for 24 hours at 35 °C. The resulting milky suspension was then subjected to hydrothermal treatment at a temperature ranging from 60 to 140 °C for a duration between 24 and 48 hours.

Preparation of mesostructured cellular foam (MCF) and larger-pore SBA-15 (d > 10nm) was conducted following a similar procedure, differing only by the addition of a swelling agent (*n*-hexane, 1,3,5-trimethylbenzene, or 3,3′,5,5′-Tetramethylbenzidine, TMB) to the solution after P-123 dissolution. After cooling to room temperature, the colloidal solution was filtered, washed with deionized water, and dried under ambient conditions. Finally, to remove P-123 and TMB, the powders were calcined in air by heating from room temperature to 550 °C and maintaining that temperature for 6 hours. Similarly, MCM-41 was synthesized following the method reported by Kresge et al. (1992).

Following a drying pretreatment at 200 °C for a duration of 24 h, the porosity of the mesoporous materials was characterized through nitrogen physical adsorption measurements conducted at 77 K (Quantachrome Quadrasorb-SI-MP and Quadrasorb evo). The mean pore diameter, total pore volume, and surface area were calculated from the desorption branch using the non-local density functional theory (NLDFT) method, specifically tailored for cylindrical pore geometries. The results are visually represented in Fig. 4−1 and summarized in Table 4−2.

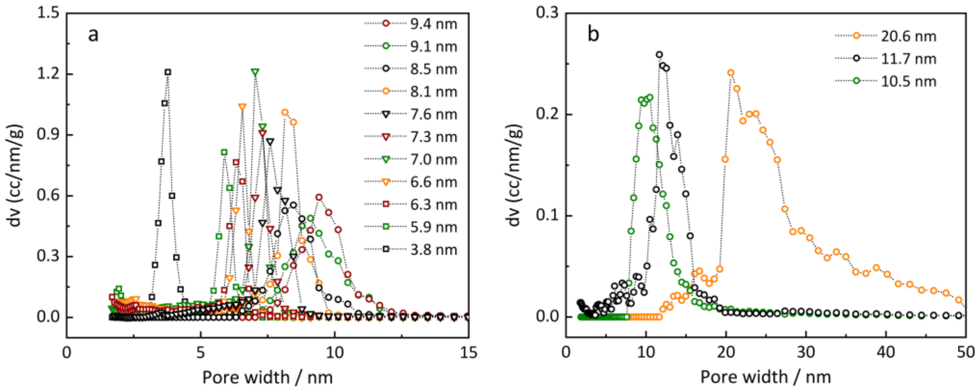

Figure 4−1. Pore size distributions of synthetic porous materials, MCM-41 (3.8 nm), SBA-15 (5−10 nm), and MCF (10.5, 11.7, and 20.6 nm).

Table 4−2. Summary of synthesis and characterization for ordered mesoporous silica materials.

Sample	Pore size d/ nm	Specific volume V_{pore} /cm^3·g^{-1}	Specific surface area m^2·g^{-1}	Temperature T / °C	Time t / h	Swelling agent
MCM-41	3.8	0.834	758	150	48	
SBA-15	5.9	0.708	905	60	24	
SBA-15	6.3	0.833	854	80	24	
SBA-15	6.6	0.880	875	80	24	
SBA-15	7.0	1.121	834	100	24	
SBA-15	7.3	0.939	628	100	30	
SBA-15	7.6	1.104	605	120	24	
SBA-15	8.1	1.149	570	120	64	
SBA-15	8.5	1.047	484	140	24	
SBA-15	9.1	1.086	463	140	30	
SBA-15	9.4	1.215	490	140	36	
SBA-15[a]	10.5	1.076	370	–	–	
SBA-15	11.7	1.254	452	140	24	*n*−hexane
MCF[a]	20.6	2.709	423	14	72	TMB

a: materials were obtained from Talreja−Muthreja et al., 2022

4.2 Methods

First−order phase transitions, such as freezing or melting of water and crystallization or dissolution of salt are typically accompanied by heat. Hence, differential scanning calorimetry is therefore used to detect the temperature at which these thermal events occur during cooling and heating cycles, corresponding to the solid−liquid phase transitions between salt, ice and their solutions. Water vapor sorption analysis is another key technique, well−studied for examining the hygroscopic behavior of electrolytes upon exposure to atmospheric moisture. Additionally, it can be used to characterize the porosity of porous materials. In this study, water vapor sorption is utilized to determine the deliquescence relative humidity (DRH) of salts under both bulk and confined conditions. While the calorimetry and water vapor sorption are effective for identifying phase boundaries, based on temperature or humidity, they do not provide direct insights into the nature of identity of the solid and liquid phases involved. To address this limitation, Raman spectroscopy is used to monitor phase evolution and to identify specific solid or liquid species during temperature or humidity changes. Moreover, phase transformations are often accompanied by changes in the morphology of material surfaces, which can reveal information about the kinetics of transition at the microscale. To capture these processes in real time, environmental scanning electron microscopy (ESEM) is applied, particularly to observe mutual deliquescence in salt mixtures. Elemental changes associated with phase transformations are further analyzed using energy dispersive X–ray spectroscopy (EDX).

4.2.1 Calorimetry

Thermal analysis and calorimetry are widely employed to investigate processes and materials properties, such as phase transition enthalpies, heat capacities, thermal expansivity, and other thermophysical changes, all of which are associated with heat generation or absorption. The results obtained from thermal analytical and calorimetric techniques can be influenced by both operational parameters (e.g., heating rate, atmosphere, pressure) and sample characteristics (e.g., mass, geometrical shape, structure). A wide variety of calorimeter designs exist, differing in their principles of measurement, yet all are fundamentally aimed at measuring heat or heat flow rates (Gallagher and Brown, 1998).

Among these, differential measurement methods are commonly used. In such approaches, the quantity of interest is measured relative to a reference under identical experimental conditions. Differential scanning calorimetry, for example, records the difference in the heat flow between a sample and an inert reference as both are subjected to controlled temperature changes. This technique offers two main advantages: (1). The differential signal can be significantly amplified, enhancing the sensitivity to subtle variation by suppressing the high baseline signal. (2). External disturbances that affect both the sample and reference systems tend to cancel out, improving measurement accuracy by minimizing systematic errors.

In a power-compensating DSC, the sample and reference materials are placed in two separate small furnaces, each equipped with its own heating element and temperature sensor. During the measurement, a control loop continuously adjusts the heating power to each furnace in order to minimize the temperature difference between the two. A proportional controller is typically used for this purpose, maintaining a small but measurable residual temperature difference between the sample and reference. When the system is thermally symmetric, this residual temperature difference is directly proportional to the difference in heating powers supplied between the sample and reference or from thermal event in the samples, such as endothermic or exothermic phase transitions. The additional power required to compensate for these effects, and thus maintain thermal balance, is directly proportional to the difference in heat flow rates. In this way, the instrument can quantify the heat flow associated with a thermal event in the sample. The DSC output signal is recorded as a heat flow rate (typically in W or mW), with positive values corresponding to exothermic processes (e.g., crystallization, freezing) and negative values indicating endothermic processes (e.g., melting, evaporation).

The calorimeter used in this dissertation is the BT 2.15 model from SETARAM KEP Technologies. It offers high sensitivity with a temperature resolution of ± 0.01 °C and a heat flow resolution of 0.01 ± mW. The instrument operates over a broad temperature range from 200 °C to −150 °C, and is equipped with a liquid nitrogen cooling system for sub-ambient temperature control. The device supports a wide range of heating rates (0.01 to 1 $K \cdot min^{-1}$), while the cooling rate is typically below 0.1 $K \cdot min^{-1}$ under standard nitrogen flow. To achieve higher cooling rates (e.g., 0.2 $K \cdot min^{-1}$ or above), manual adjustment of the liquid nitrogen flow is required. In this study, calorimetric measurements were mainly conducted to determine the freezing and melting points of salt solutions in both bulk and confined phase. To ensure thermal equilibrium during the phase transitions, a temperature ramp rate of 0.1 $K \cdot min^{-1}$ was employed during both cooling and heating cycles. For bulk solution measurements, an empty tube was used as reference, while for confined solution measurement, the reference contained the same amount porous silica. A representative example of the freezing and melting behavior of pure water is shown in Fig. 4−2.

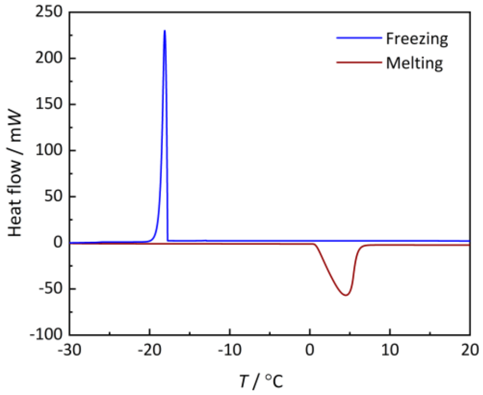

Figure 4−2. Freezing and melting curves of pure water.

The exothermic peak observed during cooling (blue curve) corresponds to the freezing of water, while the endothermic peak during heating (red curve) is associated with the melting of ice. The temperature delay in the exothermic peak reflect the nuclei barrier for ice formation. In contrast to the sharp freezing peak, the melting peak is broader, likely due to the gradual heat transfer from the outer surface to the core of the ice crystal. This contrast in peak shapes underscores the fast nucleation and crystal growth during freezing and the diffusion-limited melting process in heating.

4.2.2 Water vapor sorption

Physical sorption analysis is a widely employed technique for characterizing material porosity, as the resulting sorption isotherms are significantly sensitive to pore shape and size distribution (Thommes et al., 2006). Given the ubiquity of atmospheric water vapor and its high reactivity with many materials, understanding moisture-induced changes in material properties is essential across various disciplines, including food technology, pharmaceutical production, and construction materials (Stahlbuhk and Steiger, 2025a). Research in these fields primarily focuses on how materials respond to water adsorption or desorption, such as the caking of salts or sugars, volume expansion of hygroscopic drug components, and the salt crystallization damage in built heritage. These phenomena represent a complex sequence of process, ranging from the initial adsorption of water molecules to deliquescence and capillary condensation.

The instrument employed in this dissertation is the SPSx−1μ multi-sample dynamic moisture sorption analyzer, manufactured by ProUmid GmbH & Co. KG. This fully automated system determines sorption and desorption isotherms as well as sorption kinetics over a wide range of temperature and relative humidities using a gravimetric method. It measures mass change over time in samples maintained under precisely controlled conditions of temperature and relative humidity, with mass change occurring due to either water uptake from the air or water release from the sample. The relationship between the equilibrium moisture content of a sample and the relative humidity at a given temperature is referred to as the water vapor sorption isotherm, which reflects moisture−induced structural changes typically indicated by abrupt, or transient variations in sample mass. A typical water vapor sorption isotherm for a 9.1 nm porous SBA-15 silica is shown in Fig. 4−3.

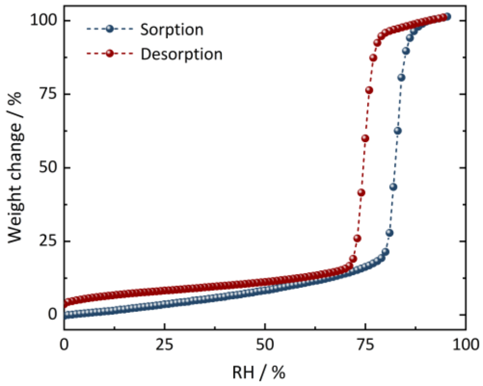

Figure 4−3. Water vapor sorption and desorption in 9.1 nm SBA-15 at 25 °C.

Each experiment allows for the simultaneous analysis of up to 23 samples, with sample mass ranging from 10 mg to 22 g. The system offers a temperature range of 5 °C to 60 °C with accuracy of ± 0.1 °C, and a humidity range from 0% to 95% RH with accuracy of 0.5%. The SPSx−1μ provides high-precision gravimetric measurements with a resolution of 1 μg and a reproducibility of better than ± 2 μg. All measurements presented in this study, including those of bulk salts, empty porous materials, and salt nanoparticles under confinement, were conducted at 25 °C within a humidity range of 0% to 95% RH

4.2.3 Raman spectroscopy

Scattering is a fundamental phenomenon widely observed in nature. When an incident particle strikes a target along a specific direction, its trajectory, and in some cases, its energy and be altered due to interactions with the target, leading to scattering (Zhang, 2012). In the 20th century, researchers began to focus on the energy shift, or more precisely, the change in wavelength of the scattered light relative to the incident light. In light scattering experiments, this wavelength shift is commonly expressed in terms of wavenumber (in cm^{-1}), which is the reciprocal of the wavelength. Based on the magnitude of the energy change, light scattering is typically categorized into three types:

1. Rayleigh scattering, where the energy change is less than 10^{-5} cm^{-1}.
2. Brillouin scattering, first observed by Léon Brillouin in 1922, involves energy shifts on the order pf 0.1 cm^{-1} (Brillouin, 1922).
3. Raman scattering, discovered by C.V. Raman in 1928, exhibits energy shifts larger than 1 cm^{-1} (Raman and Krishnan, 1928).

If the wavelength of the scattered light remains unchanged compared to the incident light, the process is referred to as elastic scattering. In contrast, if the scattered light exhibits a different wavelength, it is known as inelastic scattering. The energy change associated with Rayleigh scattering, Stokes Raman scattering, and Anti-Stokes Raman scattering are schematically illustrated in Fig. 4–4.

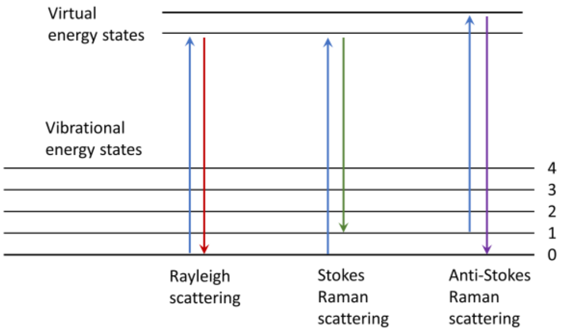

Figure 4–4. Energy-level diagram showing the states involved in Raman spectra.

In this dissertation, Raman spectra were recorded using a Senterra Raman dispersive microscope (Bruker Optics GmbH, Germany), which is equipped with an automated Raman frequency calibration system (SurCal technology) and a CCD detector. The excitation laser operated at a wavelength of 532 nm. Temperature control was achieved using a THMS600 heating/cooling stage (Linkam Scientific Instrument, UK), while humidity control was provided by an MHG32 humidity generator (ProUmid GmbH, Germany), enabling precise regulation of environmental conditions. The system allows for a temperature range is from −100 °C to 500 °C and a relative humidity range is from 0 to 85% RH. To be specific, Raman spectroscopy was employed to characterize the moisture-induced phase transformations and deliquescence of calcium chloride hydrates, with a focus on the anomalous metastable deliquescence behavior at 25 °C. Additionally, *in-situ* Raman experiments were conducted to investigate the phase behavior of $Ca(ClO_4)_2{\cdot}nH_2O$, $(NH_4)_2SO_4$ and their aqueous solutions under cryogenic conditions.

4.2.4 Environment scanning electron microscope

Scanning electron microscopes (SEMs) operate on principles similar to those of optical microscopes but a focused beam of electrons instead of visible light is used to image the samples and gather information about their structure and composition. Electron microscopy was developed to overcome the limitations of light microscopy, which are constrained by the physics of light. In contrast, SEM offers significantly higher magnifications and greater resolving power than a light microscope, enabling the observation of features at the nanoscale, including molecular level structure. In SEM operation, a beam of electrons is generated by an electron source and then accelerated toward the specimen using a positive electrical potential. The beam is confined and focused through metal apertures and magnetic lenses to form a thin, focused, monochromatic stream of electrons. As this beam interacts with the atoms on the surface of the sample, it generates various signals, including secondary electrons, backscattered electrons, and characteristic X-rays. These signals provide information on the surface topography, elemental composition, and electrical properties of the samples. The resulting signals are detected and processed to construct high-resolution images of the sample (Kannan, 2018).

A typical scanning electron microscope (SEM) system consists of several core components:

- an electron source;
- lenses and apertures for beam shaping
- coils for rastering (scanning) the beam across sample;
- control electronics and high-voltage power supplies;
- a deflector/acquisition system for collecting and processing the signal information;
- a display monitor;
- a vacuum system for the electron column and sample chamber.

Maintaining a high vacuum environment (typically in the range of 10^{-3} to 10^{-5} Pa) is essential for two reasons:

- To prevent contamination of the electron source;
- To avoid scattering of the electrons by atmospheric particles, which would reduce the resolution.

While the region around the electron source and much of the electron column are kept under high vacuum to preserve the unscattered trajectories of the primary electrons, environmental SEM (ESEM) allows for a relatively higher pressure in the sample chamber. This enables the observation of samples in the presence of water vapor, crucial for humidity-sensitive materials (Stokes, 2008).

The chemical composition of a sample can be characterized via X-ray spectroscopy. When high-energy incident electrons interact with the inner-shell electrons of the sample atoms, an inner shell electron may be ejected, ionizing the atom. An out-shell electron then transitions into the vacancy, releasing energy in the form of a characteristic X-rays, corresponding to the energy difference between the two shells. These X-rays have discrete energy levels, unique to each element, resulting in a spectrum with identifiable peaks. The technique used to detect and analyze these X-rays is called energy dispersive X-ray spectroscopy (EDX or EDS).

In this dissertation, environmental scanning electron microscopy coupled with energy-dispersive X-ray spectroscopy (ESEM-EDX) is employed using the EVO system (Carl Zeiss Microscopy GmbH). This method enables the *in-situ* observation of mutual deliquescence and solid–solid transformations in salt mixtures. Because these processes occur at relatively low humidity at lower temperatures, all measurements were conducted at 3 °C under controlled relative humidity conditions ranging from 0% to 85% RH, ensuring stable imaging conditions while maintaining appropriate water vapor presence in the chamber

Chapter 5. Hydration and deliquescence behavior of calcium chloride hydrates

Deliquescence represents a three-phase equilibrium between water vapor, liquid, and solid phase. Therefore, the deliquescence relative humidity (DRH) can also be determined by measuring the water activity of saturated solutions. As depicted in a calculated phase diagram of $CaCl_2$–H_2O in Fig. 5−1 (details shown in the Section A1 of Appendix), it depends on the temperature which solid phase is stable in the solid–liquid equilibrium and, thus, undergoes deliquescence. For example, at temperatures > 319 K, $CaCl_2{\cdot}2H_2O$ and $CaCl_2{\cdot}H_2O$ are thermodynamically stable. Between 303 K and 319 K, α−$CaCl_2{\cdot}4H_2O$ is the stable phase, and below 303 K is the hexahydrate. The latter temperature limit corresponds to the incongruent melting of $CaCl_2{\cdot}6H_2O$ and crystallization of α−$CaCl_2{\cdot}4H_2O$. The model calculated value of 302.69 K agrees nicely with a literature value of 302.85 K (Voigt, 2015).

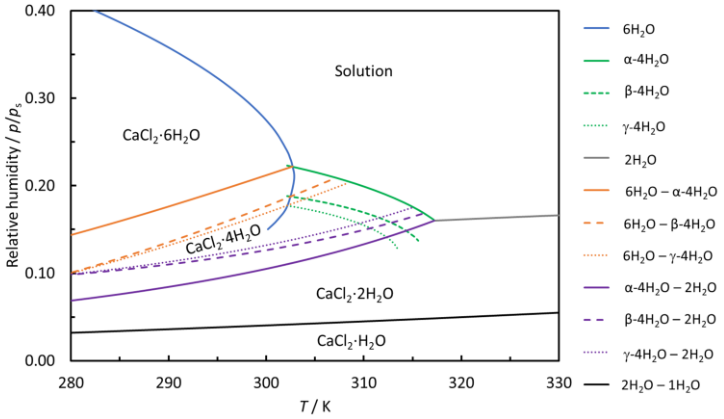

Figure 5−1. Phase diagram of the $CaCl_2$–H_2O system (details provided in the Section A1 of Appendix). The solid blue, green, and grey curves denote deliquescence of $CaCl_2{\cdot}6H_2O$, α−$CaCl_2{\cdot}4H_2O$, and $CaCl_2{\cdot}2H_2O$, respectively; the solid black, purple, and orange curves denote the hydration of $1H_2O$ to $2H_2O$, $2H_2O$ to α−$4H_2O$, and α−$4H_2O$ to $CaCl_2{\cdot}6H_2O$, respectively; the green dashed and dotted curves denote the deliquescence of β−$CaCl_2{\cdot}4H_2O$ and γ−$CaCl_2{\cdot}4H_2O$ respectively; the purple dashed and dotted curves denote the hydration of $2H_2O$ to β−$4H_2O$ and $2H_2O$ to γ−$4H_2O$, respectively; the orange dashed and dotted curves denote the hydration of β−$4H_2O$ to $6H_2O$ and γ−$4H_2O$ to $6H_2O$, respectively; phase boundaries to the lower hydrates ($CaCl_2{\cdot}1/3H_2O$ and $CaCl_2$) are not shown as these phases are not formed under the conditions of the experiments in this work.

In general, in the absence of kinetic hindrance, going from a dry to a humid environment at room temperature, the expected transitions proceed from $CaCl_2{\cdot}H_2O$ to $CaCl_2{\cdot}2H_2O$, α−$CaCl_2{\cdot}4H_2O$, and $CaCl_2{\cdot}6H_2O$, followed by deliquescence of the latter. Except for the stable hydrates, there are two metastable $CaCl_2{\cdot}4H_2O$ phases, named β−$CaCl_2{\cdot}4H_2O$ and γ−$CaCl_2{\cdot}4H_2O$, respectively, as shown in the phase diagram (Fig. 5−1, and more details shown in the Fig. A1−1 of Appendix). Both polymorphs are metastable due to their higher solubility than the stable α−polymorph with the solubility of γ−$CaCl_2{\cdot}4H_2O$ exceeding that of β−$CaCl_2{\cdot}4H_2O$ by about 0.3–0.7 $mol{\cdot}kg^{-1}$. Therefore, the saturation vapor pressures of the metastable phases are lower (19.3% RH and 18.3% RH at 298.15 K for β−$CaCl_2{\cdot}4H_2O$ and γ−$CaCl_2{\cdot}4H_2O$, respectively) than of the α−polymorph (22.9 % RH at 298.15 K).

Numerous data on the vapor pressures of solutions saturated with $CaCl_2{\cdot}6H_2O$ have been reported (summarized in Table A1−3 of Appendix) and the most reliable value at 298.15 K can be derived from the best available water activity data (Rard and Clegg, 1997). With a solubility of 7.33 ± 0.06 $mol{\cdot}kg^{-1}$ (see Section A1.3 of Appendix), this yields 29.1 ± 0.4%. The direct water vapor sorption measurement with $CaCl_2{\cdot}6H_2O$ reported by Guo et al. (2019), yielded a deliquescence humidity of 28.5% RH at 298.15 K, which is in line with other data from Table A1−3 of Appendix. It is noteworthy that they also observed deliquescence occurring at 18.5% RH in some of their experiments, which they assigned to the DRH of metastable $CaCl_2{\cdot}2H_2O$ that did not undergo hydration to either $CaCl_2{\cdot}4H_2O$ or $CaCl_2{\cdot}6H_2O$. However, as our calculated phase diagram (Fig. 5−1) shows, the observed DRH at 18.5% is closer to the saturation vapor pressure of β−$CaCl_2{\cdot}4H_2O$ (19.4%) or γ−$CaCl_2{\cdot}4H_2O$ (18.5%) solution, rather than that of $CaCl_2{\cdot}2H_2O$ (14.6%). In fact, Gough et al. observed the direct deliquescence of $CaCl_2{\cdot}2H_2O$ using Raman microscopy, however, their study was carried out at very low temperatures (223–273 K) and may not apply to higher temperatures (Gough et al., 2016). These divergent results underline the complexity of the hydration process in the $CaCl_2$–H_2O system and suggest that not all observed transitions follow the predicted thermodynamic equilibria.

In this study, water vapor sorption analysis and *in-situ* Raman spectroscopy were conducted to address the unexpected transitions upon hydration and to investigate the hydration and deliquescence behavior of $CaCl_2{\cdot}nH_2O$. The water vapor sorption isotherms at 298.15 K for calcium chloride hydrates ($CaCl_2{\cdot}2H_2O$ and $CaCl_2{\cdot}6H_2O$), that were dehydrated at room temperature in dry air or by thermal drying, are presented. Subsequently, the phases present in certain humidity ranges during the hydration process as identified using Raman spectroscopy are reported. Finally, an explanation for the observed metastable transition pathways is proposed based on the experimental results of water vapor sorption and Raman spectroscopy.

5.1 Experiments

Water vapor sorption measurements were conducted using an SPSx−1μ moisture sorption analyzer (ProUmid GmbH, Germany). The isotherms were recorded at 298.15 K (0.1 MPa) with a 1% increment in relative humidity within the range of 0–95%. Equilibrium was considered to be achieved when the weight change was less than 0.045 wt.% over 4 hours. It is important to note that a 48−hour drying pretreatment at different temperatures in a dry nitrogen gas flow (nominal RH of 0%) was applied initially to dehydrate the samples. Three experiments were conducted with the following starting materials and drying conditions: SPS−1: $CaCl_2{\cdot}2H_2O$ with drying at 333.15 K and 0% RH (hereafter referred to as thermal drying); SPS−2: $CaCl_2{\cdot}6H_2O$ with thermal drying; SPS−3: $CaCl_2{\cdot}6H_2O$ with drying at 298.15 K and 0% RH (hereafter referred to as isothermal drying). The different drying temperatures were selected as they led to large differences in the rehydration pathways.

Raman spectra were recorded using a Senterra Raman dispersive microscope (Bruker Optics GmbH, Germany) equipped with an automated Raman frequency calibration system (SurCal technology) and a CCD detector. The device includes a BX 51 microscope with Plan M 10× and LMPlanFL N 20× lenses (Olympus, Germany). The laser was operated at a wavelength of 532 nm (frequency−doubled Nd: YAG laser) at 20 mW with an integration time of 5 second. Spectra were collected by summing up ten spectra at the same spot in the range of 1520−3700 cm^{-1} (co−addition mode). A THMS600 stage (Linkam Scientific Instrument, UK) was used for temperature and RH control. An airflow with controlled RH at a rate of 500 $mL{\cdot}min^{-1}$ was provided by a humidity generator MHG32 (ProUmid GmbH, Germany) yielding sufficiently large gas exchange rates and a constant RH in the THMS600 stage. In order to achieve comparable results with the SPS experiments, all Raman measurements were conducted at 298.15 K, and the following three experiments were performed: Raman−1: Drying of $CaCl_2{\cdot}2H_2O$ at 333.15 K and 0% RH in the Linkam chamber (thermal drying) and collection of Raman spectra after drying and during rehydration at 5%, 12%, 15%, 18%, 20% and 24% RH, respectively. Raman−2: After recording a spectrum of $CaCl_2{\cdot}6H_2O$ initially the sample was dehydrated at room temperature (r.t.) and decreasing RH. Spectra were measured at 15%, 12%, and 5% RH, with a final 20−hour hold time at 5% RH. During hydration, Raman spectra were collected at 16.5%, 18%, and 27% RH, respectively. Raman−3: After recording a spectrum of $CaCl_2{\cdot}6H_2O$, the sample was dried at 333.15 K and 0% RH for 10 hours. Then, spectra were recorded at 0%, 8%, 15%, and 25% RH, respectively, during hydration. The experimental conditions during the dehydration−rehydration experiments 1−3 can been found in Table 5−1. Listed are the temperatures, relative humidities, hold times and the phases detected in the respective Raman spectra and micrographs. The spectra are shown in Fig. 5−5 (experiment Raman−1), Fig. 5−8a (Raman−2) and Fig. 5−8b (Raman−3).

Table 5−1. Details of the experiments performed with Raman microscopy.

Starting material	T / K	RH/%	Detected phases	Hold time/h
Raman−1:	333.15	<10	$CaCl_2 \cdot H_2O$	12
$CaCl_2 \cdot 2H_2O$	298.15	5	$CaCl_2 \cdot H_2O$ and $CaCl_2 \cdot 2H_2O$	0.5
(Fig. 5−6, Fig. 5−7)	298.15	12	$CaCl_2 \cdot 2H_2O$	1
	298.15	15	$CaCl_2 \cdot 2H_2O$	1
	298.15	18	β−$CaCl_2 \cdot 4H_2O$	1
	298.15	20	β−$CaCl_2 \cdot 4H_2O$ and solution	1
	298.15	24	β−$CaCl_2 \cdot 4H_2O$ and solution	0.5
Raman−2:	298.15	30	$CaCl_2 \cdot 6H_2O$	0.5
$CaCl_2 \cdot 6H_2O$	298.15	15	$CaCl_2 \cdot 6H_2O$	48
(Fig. 5−8a, Fig. 5−9)	298.15	12	α−$CaCl_2 \cdot 4H_2O$	24
	298.15	5	$CaCl_2 \cdot 2H_2O$	22
	298.15	16.5	α−$CaCl_2 \cdot 4H_2O$ and $CaCl_2 \cdot 2H_2O$	6
	298.15	18	α−$CaCl_2 \cdot 4H_2O$ and solution	60
	298.15	27	$CaCl_2 \cdot 6H_2O$	24
Raman−3:	298.15	0	$CaCl_2 \cdot 6H_2O$	10
$CaCl_2 \cdot 6H_2O$	333.15	0		10
(Fig. 5−8b, Fig. 5−10)	298.15	0	$CaCl_2 \cdot H_2O$ and $CaCl_2 \cdot 2H_2O$	1
	298.15	8	$CaCl_2 \cdot 2H_2O$	2
	298.15	15	β−$CaCl_2 \cdot 4H_2O$	24
	298.15	25	β−$CaCl_2 \cdot 4H_2O$ and solution	4

X−ray diffraction analysis was carried out with a powder diffractometer (PANalytical MPD X'Pert, The Netherlands) with Cu−Kα−radiation (generated at 450 kV and 400 mA, scanning ranges from 6 to 70° 2θ). Samples were covered with a thin Kapton polyimide film to prevent contact with moisture. Two samples were investigated: XRD−1: $CaCl_2 \cdot 2H_2O$ dried at 333.15 K (thermal drying). XRD−2: $CaCl_2 \cdot 2H_2O$, initially dried at 333.15 K, then stored in an environmental chamber at 15% RH and room temperature (293.15–298.15 K) for 24 hours.

The standard uncertainties of the humidity and temperature sensors used in all experiments are u = 1% RH and u = 0.1 K. Table 5−2 provides a summary of the experiments, all carried out at 0.1 MPa.

Table 5−2. Overview on the starting materials and conditions in the water vapor sorption, Raman and XRD experiments.

Starting material	Drying conditions before hydration	Experiment
$CaCl_2 \cdot 2H_2O$	333.15 K and 0% RH	SPS−1
$CaCl_2 \cdot 6H_2O$	333.15 K and 0% RH	SPS−2
$CaCl_2 \cdot 6H_2O$	298.15 K and 0% RH	SPS−3
$CaCl_2 \cdot 2H_2O$	333.15 K and 0% RH	Raman−1
$CaCl_2 \cdot 6H_2O$	333.15 K and 0% RH	Raman−2
$CaCl_2 \cdot 6H_2O$	298.15 K and 0% RH	Raman−3
$CaCl_2 \cdot 2H_2O$	333.15 K and < 10% RH	XRD−1
$CaCl_2 \cdot 2H_2O$	333.15 K and < 10% RH (hydration at 298.15 K and 15% RH)	XRD−2

5.2 Results and Discussion

5.2.1 Water vapor sorption and hydration

The water vapor sorption data at 298.15 K, starting from dehydrated $CaCl_2 \cdot 2H_2O$ (SPS−1) and $CaCl_2 \cdot 6H_2O$ (SPS−2), are presented in Fig. 5−2. In both measurements, two hydration steps at 4.5 ± 0.5% and 11.5 ± 0.5% RH can be observed. A third step at 18.5 ± 0.5% is followed by continuous water uptake with increasing RH indicating the onset of deliquescence and subsequent dilution of the solution. It should be mentioned that the initial water content of the sample before hydration was not exactly defined due to the thermal drying at the beginning. According to the phase diagram shown in Fig. 5−1, $CaCl_2 \cdot H_2O$ is stable at very low humidity, while $CaCl_2 \cdot 2H_2O$, $\alpha-CaCl_2 \cdot 4H_2O$ and $CaCl_2 \cdot 6H_2O$ are stable in the humidity ranges of 4–10% RH, 10–20.5 %RH, and 20.5–29% RH, respectively. When comparing the increase of the number of moles of water per mole of $CaCl_2$ (n_w/n_s) in the first (at 4.5%) and the second step (at 11.5%) in Fig. 5−2a ($CaCl_2 \cdot 2H_2O$ starting material), it can be observed that the water content involved in the second step is approximately twice as high as in the first one. This is in accordance with the hydration from $CaCl_2 \cdot H_2O$ to $CaCl_2 \cdot 2H_2O$ and, subsequently, from $CaCl_2 \cdot 2H_2O$ to $CaCl_2 \cdot 4H_2O$. Therefore, $CaCl_2 \cdot H_2O$ is confirmed as the initial state after dehydration as presented in Fig. 5−2. The theoretical hydration steps and the water uptake (n_w/n_s) of the solution at higher humidities calculated with our model are in good agreement with the experimental data, except for the deliquescence which is predicted at 29.5% RH by the model but is observed at 18.5% already.

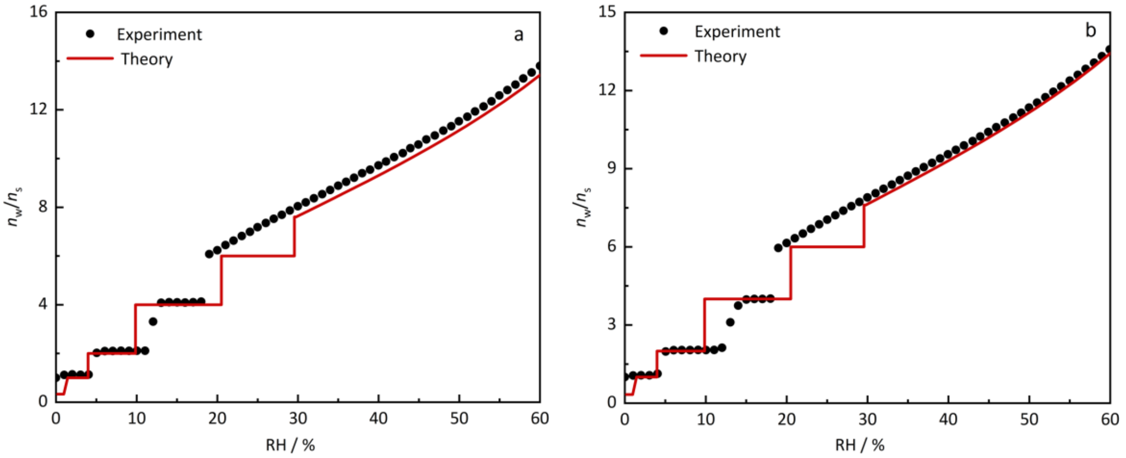

Figure 5–2. Water vapor sorption measurements starting from $CaCl_2·2H_2O$ (a, SPS–1) and $CaCl_2·6H_2O$ (b, SPS–2), plotted as the ratio of moles of water per moles of salt n_w/n_s versus RH.

This observation of the direct deliquescence at 18.5% RH instead of the expected hydration to the hexahydrate at 20.5% RH and subsequent deliquescence at 29.5% RH as given in the phase diagram in Fig. 5–1, is very interesting. Hence, the absence of the last hydration step in the sorption measurement from tetrahydrate to hexahydrate shifts the deliquescence reaction from 29.5% RH down to 18.5% RH. This result is also reported in some experiments of Guo et al. (2019), which they attributed to the direct deliquescence of $CaCl_2·2H_2O$. In the following section, a detailed investigation including a combination of Raman spectroscopy and X–ray diffraction experiments is presented to further address this issue.

5.2.2 Raman spectroscopy experiments

For the different hydrates of $CaCl_2$, the vibrational modes of water molecules are influenced by the structure of the hydrates. Table 5–3 provides an overview of the characteristic peak positions for $CaCl_2·nH_2O$ (n = 2, 4, 6) in the O–H stretching region as reported in the literature (Uriarte et al., 2015; Baumgartner and Bakker, 2009). Unfortunately, no data are available for $CaCl_2·H_2O$ and β–$CaCl_2·4H_2O$. As discussed below, the spectrum of $CaCl_2·H_2O$ was measured in this study and the main Raman modes are also listed in Table 5–3. Attempts to collect a spectrum of pure β–$CaCl_2·4H_2O$ were unsuccessful.

Table 5–3. Characteristic peaks of H_2O vibrational modes (stretching region) in $CaCl_2 \cdot nH_2O$ Raman spectra at room temperature (Uriarte et al., 2015; Baumgartner and Bakker, 2009).

Hydrates	Stretching modes / cm^{-1}	Source
$CaCl_2 \cdot 6H_2O$	3245, 3430	Uriarte et al., 2015; Baumgartner and Bakker, 2009
α–$CaCl_2 \cdot 4H_2O$	3511, 3435, 3400, 3242	Uriarte et al., 2015; Baumgartner and Bakker, 2009
γ–$CaCl_2 \cdot 4H_2O$*	3435	Baumgartner and Bakker, 2009
$CaCl_2 \cdot 2H_2O$	3486, 3452, 3216	Uriarte et al., 2015; Baumgartner and Bakker, 2009
$CaCl_2 \cdot H_2O$	3428, 3394	this work

* at 246 K

Hydration starting from dehydrated $CaCl_2 \cdot 2H_2O$ (experiment Raman–1): To start with a pure phase, $CaCl_2 \cdot 2H_2O$ was dried at 333.15 K for 24 hours before the hydration experiment was started. After thermal drying, the presence of $CaCl_2 \cdot H_2O$ was confirmed by X–ray diffraction (XRD–1, Fig. 5–3a), which is also in agreement with the analysis based on the water vapor sorption curve presented in Section 5.2.1. The very broad peak between 10°–30° 2θ in the diffraction pattern is attributed to the amorphous protective material used to avoid moisture uptake during the measurement. Using the same drying conditions in the Linkam chamber, a Raman spectrum was recorded yielding two major peaks in the O–H stretching region (OHS) at 3394^{-1} and 3428 cm^{-1} which are assigned to $CaCl_2 \cdot H_2O$. The spectrum of the monohydrate in the OHS is shown in comparison to the starting phase ($CaCl_2 \cdot 2H_2O$) in Fig. 5–4, the full spectrum is provided in the Fig. 5–5.

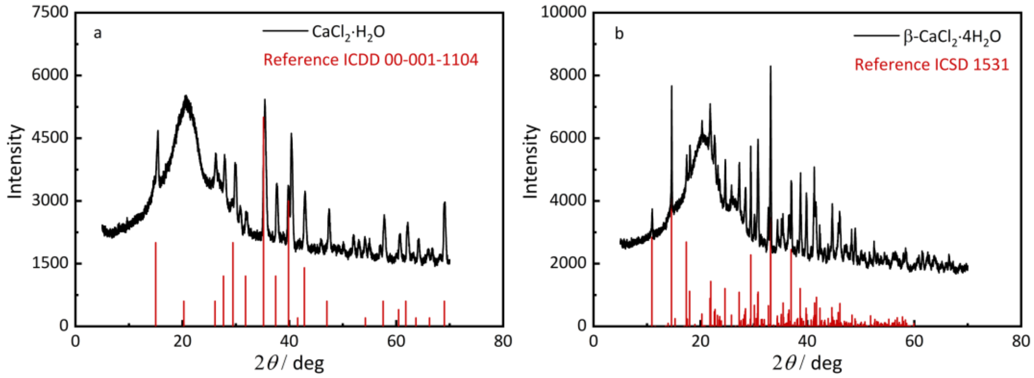

Figure 5–3. XRD patterns of calcium chloride hydrates and reference patterns for $CaCl_2 \cdot H_2O$ (Hanawalt et al., 1938) and β–$CaCl_2 \cdot 4H_2O$ (Leclaire and Borel, 1978).

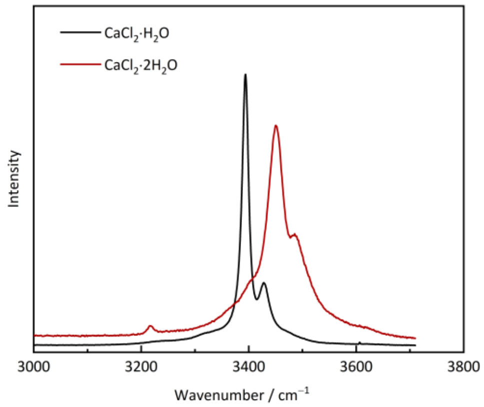

Figure 5−4. Raman spectra in the OHS of $CaCl_2·2H_2O$ and its dehydration product $CaCl_2·H_2O$.

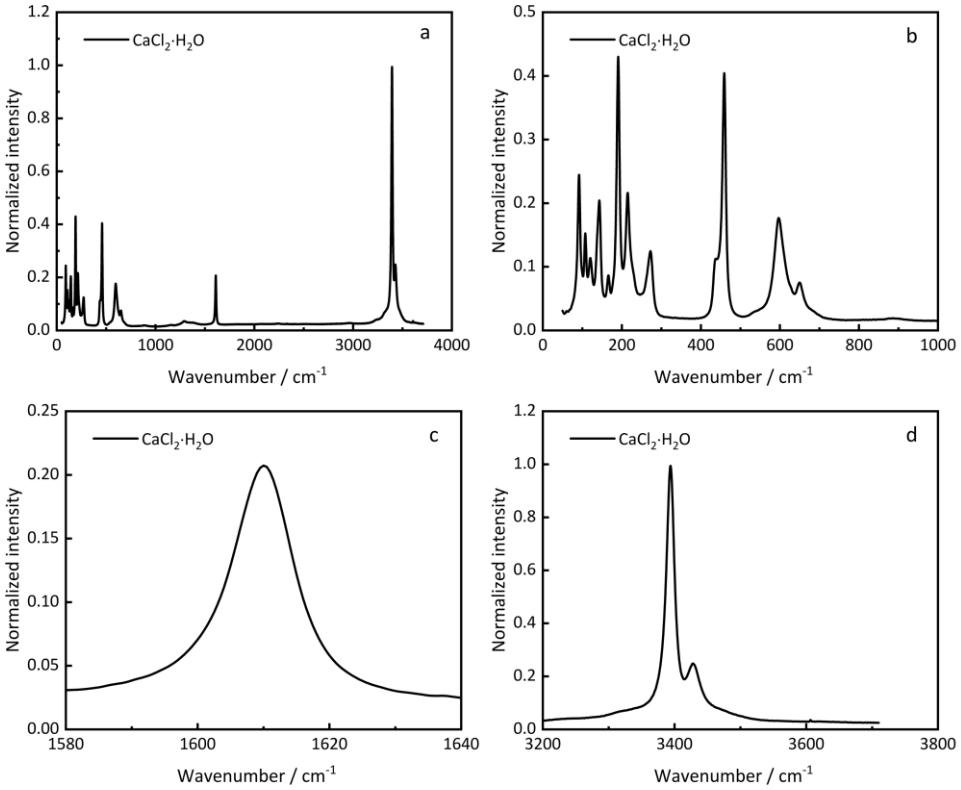

Figure 5−5. Raman spectrum of $CaCl_2·H_2O$ at 298.15 K; full spectrum range (a), low wave number range (b) and H_2O bending (c) and stretching modes (d).

The Raman spectra collected during the rehydration of dehydrated $CaCl_2·2H_2O$ are shown in Fig. 5−6. The first spectrum recorded at 5 % RH, which is close to the phase boundary between monohydrate and dihydrate, exhibits four peaks in the stretching region at 3394, 3218, 3452, and 3484 cm^{-1}. All peaks of $CaCl_2·2H_2O$ listed in Table 5−3 are present in this spectrum and the additional strong peak at 3394 cm^{-1} belongs to the monohydrate suggesting that at least a partial transformation from monohydrate to dihydrate already occurred at 5% RH. The spectra taken at 12% and15 % RH closely match both the reference spectrum from the literature (Uriarte et al., 2015) and the spectrum of the starting phase $CaCl_2·2H_2O$ shown in Fig. 5−4, thus, confirming that the transition from monohydrate to dihydrate is complete.

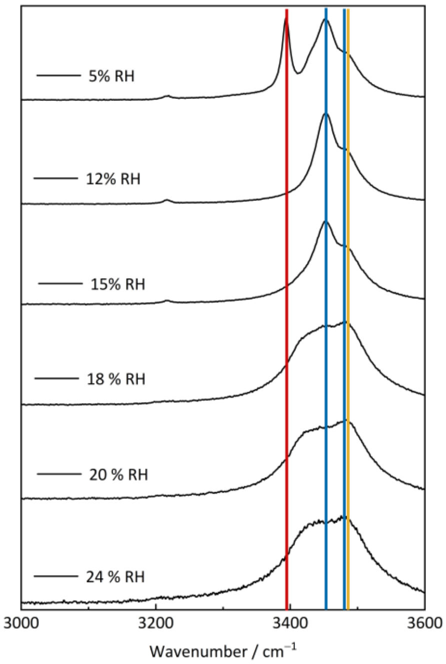

Figure 5–6. Raman spectra in the OHS recorded during the rehydration of dehydrated $CaCl_2 \cdot 2H_2O$ (experiment Raman–1). Red line: $CaCl_2 \cdot H_2O$; blue lines: $CaCl_2 \cdot 2H_2O$; yellow line: attributed to β–$CaCl_2 \cdot 4H_2O$.

Within the range 10–20.5% RH, α–$CaCl_2 \cdot 4H_2O$ is the thermodynamically stable phase. However, the spectrum recorded at 18% RH does not correspond to either α–$CaCl_2 \cdot 4H_2O$ nor γ–$CaCl_2 \cdot 4H_2O$ (cf. Table 5–3 and Fig. 5–6). Approaching the stability field of $CaCl_2 \cdot 6H_2O$, a liquid film was observed on the crystal surface in the Raman microscope at 20% RH, as the micrographs shown in Fig. 5–7, while the expected transition from α–$CaCl_2 \cdot 4H_2O$ to $CaCl_2 \cdot 6H_2O$ did not occur. The liquid film formation continued upon further humidity increase until the dissolution of the crystal was complete at 24% RH, as the micrographs shown in Fig. 5–7. Surprisingly, the hexahydrate could not be detected throughout the entire hydration process from monohydrate to deliquescence. This result is in line with the hydration sequence observed in the water vapor sorption curve, but contradicts the expected equilibrium transition pathway.

To clarify this phenomenon, the phase that corresponds to the spectrum recorded at 18% RH and deliquescence at 24% RH was investigated more closely. For that purpose, a sample of $CaCl_2 \cdot 2H_2O$, initially dried at 333.15 K, was stored at 15% RH for 24 hours and the resulting product was characterized by X–ray diffraction (XRD–2). The resulting XRD pattern (Fig. 5–3b) shows agreement with the reference pattern of β–$CaCl_2 \cdot 4H_2O$ (Leclaire and Borel, 1978), but not with the patterns of the stable α–polymorph (Leclaire and Borel, 1979) or the metastable γ–$CaCl_2 \cdot 4H_2O$ (Leclaire et al., 1980). Therefore, the Raman peak located at 3483 cm^{-1} (yellow line in Fig. 5–6) was assigned to β–$CaCl_2 \cdot 4H_2O$.

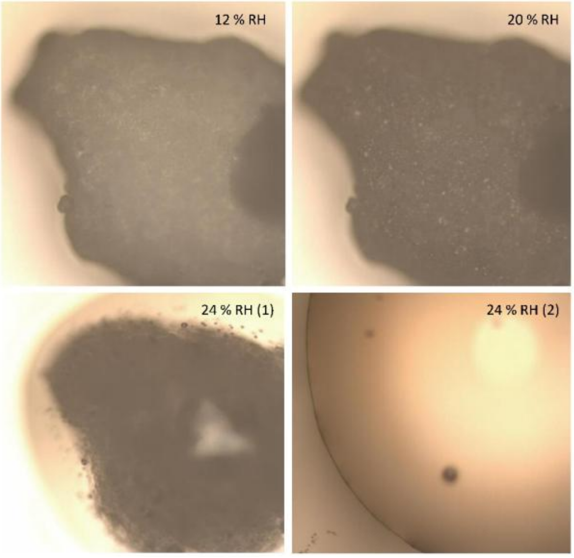

Figure 5−7. Micrographs taken before and after deliquescence in experiment Raman−1. The darkening observed upon increasing the RH from 12 % ($CaCl_2 \cdot 2H_2O$) to 20 % (presumably β−$CaCl_2 \cdot 4H_2O$) is an indication of the formation of a liquid film on the crystal surface; the two micrographs at 24 % show how the deliquescence process proceeds.

Hydration starting from dehydrated $CaCl_2 \cdot 6H_2O$ (experiments Raman−2 and Raman−3): The dehydration and rehydration of $CaCl_2 \cdot 6H_2O$ were also investigated using Raman spectroscopy. First, the $CaCl_2 \cdot 6H_2O$ starting material was dehydrated isothermally at 298.15 K by stepwise decreasing the RH to 5 %. Spectra were recorded at 15%, 12%, and 5% RH, respectively. The results are shown in Fig. 5−8a, corresponding micrographs can be found in the Fig. 5−9. Initially, the identity of $CaCl_2 \cdot 6H_2O$ as starting material was confirmed. Upon decreasing the RH to 15% RH, i.e. below the transition equilibrium RH (20%) of $CaCl_2 \cdot 6H_2O$ to α−$CaCl_2 \cdot 4H_2O$, the spectrum did not change. As the humidity was further reduced to 12% RH, the dehydration to α−$CaCl_2 \cdot 4H_2O$ was observed followed by the formation of $CaCl_2 \cdot 2H_2O$ at 5% RH with 22 hours holding time. Thus, apart from a slightly delayed dissociation of the hexahydrate, the dehydration followed the expected pathway (Fig. 5−1).

In the subsequent rehydration, a mixture of $CaCl_2 \cdot 2H_2O$ and α−$CaCl_2 \cdot 4H_2O$ was obtained at 16.5% RH and the transition was complete at 18% RH. Eventually, the hydration of the tetrahydrate to the initial phase $CaCl_2 \cdot 6H_2O$ was observed at 27% RH. The first spectrum recorded at 27% RH (spectrum 1), still includes bands of α−$CaCl_2 \cdot 4H_2O$ indicating that the hydration from tetrahydrate to hexahydrate was still not complete. Only after 24 h, pure hexahydrate (second spectrum at 27% RH in Fig. 5−8b) was obtained. While these observations agree with the equilibrium pathway according to the phase diagram (Fig. 5−1), they differ from the Raman measurements starting from thermally dehydrated $CaCl_2 \cdot 2H_2O$ (Raman−1, Fig. 5−6) and the water vapor sorption results with thermally dehydrated $CaCl_2 \cdot 6H_2O$ and $CaCl_2 \cdot 2H_2O$ (SPS−1 and

SPS−2, Fig. 5−2). The only difference between the measurements is the absence of thermal drying in experiment Raman−2, probably leading to a different composition of the dehydrated samples.

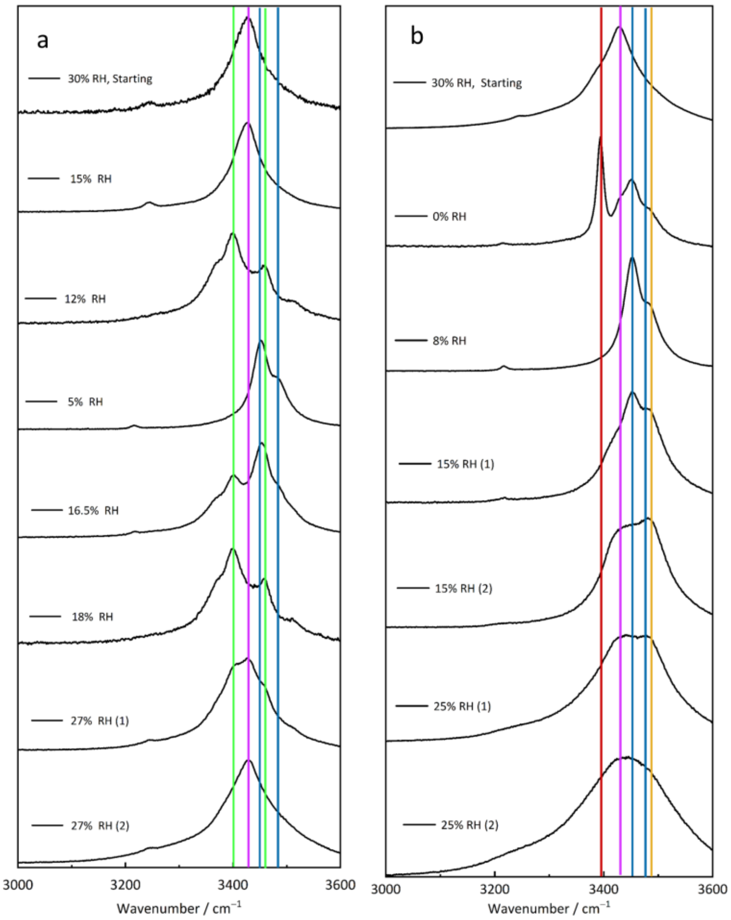

Figure 5−8. Raman spectra in the OHS recorded during dehydration and rehydration of $CaCl_2{\cdot}6H_2O$ at 298.15 K. (a) Raman−2 and (b) experiment Raman−3. Green lines: α−$CaCl_2{\cdot}4H_2O$; purple line: $CaCl_2{\cdot}6H_2O$; blue lines: $CaCl_2{\cdot}2H_2O$; red line: $CaCl_2{\cdot}H_2O$; yellow line: β−$CaCl_2{\cdot}4H_2O$.

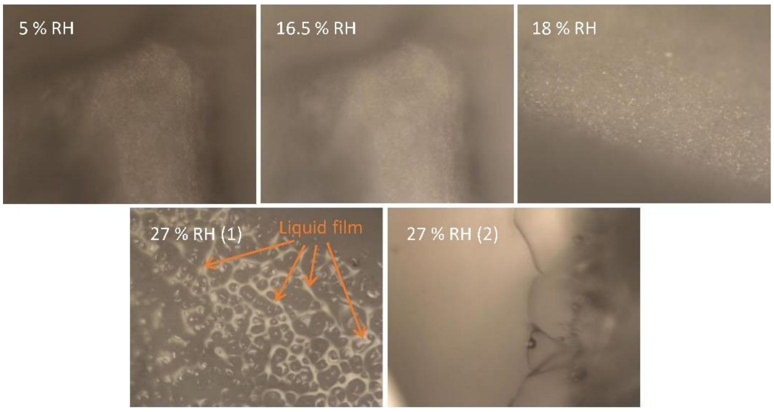

Figure 5−9. Micrographs taken during the rehydration of isothermally dehydrated $CaCl_2{\cdot}6H_2O$ in experiment Raman−2; the solids identified by Raman spectroscopy are $CaCl_2{\cdot}2H_2O$ (5 %), a mixture of $CaCl_2{\cdot}2H_2O$ and α−$CaCl_2{\cdot}4H_2O$ (16.5 %), α−$CaCl_2{\cdot}4H_2O$ (18 %) and $CaCl_2{\cdot}6H_2O$ (27 %); the micrographs reveal the presence of a liquid film at 27 % (as exemplarily indicated by the arrows) indicating deliquescence of α−$CaCl_2{\cdot}4H_2O$ and formation of $CaCl_2{\cdot}6H_2O$ which is the only phase detected in the second spectrum at 27 % RH (lower right micrograph).

To resolve these contradictory results, experiment Raman−3 was performed which included thermal drying at 333.15 K in dry air before hydration (cf. Table 5−1). The spectra are shown in Fig. 5−8b and the corresponding micrographs in the Fig. 5−10. The first spectrum confirms that the starting material was $CaCl_2·6H_2O$. After thermal drying, the spectrum at 0% is almost identical to that at 5% RH in Fig. 5−6 (Raman−1), except for a small deviation in the relative intensities of the peaks at 3394 and 3252 cm^{-1}, thus, revealing a mixture of $CaCl_2·H_2O$ and $CaCl_2·2H_2O$. This mixture transforms to $CaCl_2·2H_2O$ at 8% RH. It is evident that in contrast to the previous hydration experiment (Raman−2, Fig. 5−8a), metastable β−$CaCl_2·4H_2O$ was formed at 15% RH and deliquescence occurred between 15% and 25% RH. Qualitatively, this agrees with the water vapor sorption curves (Fig. 5−2) and the observation in experiment Raman−1 (Fig. 5−6), even though deliquescence occurred at a lower RH in the latter experiments (18−20%). Regarding this discrepancy, it should be mentioned that these Raman experiments were not designed in a way that would allow the determination of precise thermodynamic transition humidities. Nonetheless, with the identification of β−$CaCl_2·4H_2O$, the unexpected appearance of two different deliquescence humidities, one below 20% RH and another one close to 30%, can be explained by the Raman experiments. While the latter RH represents the DRH of $CaCl_2·6H_2O$, the lower value can be attributed to the deliquescence of β−$CaCl_2·4H_2O$, and not to the deliquescence of $CaCl_2·2H_2O$ as proposed by Guo et al. (2019).

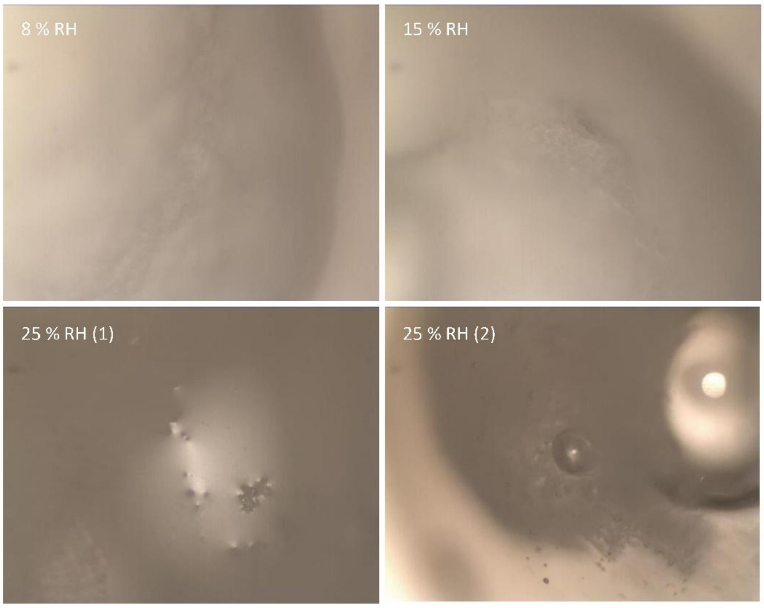

Figure 5−10. Micrographs taken during the rehydration of thermally dehydrated $CaCl_2·6H_2O$ in experiment Raman−3; the solids identified by Raman spectroscopy are $CaCl_2·2H_2O$ (8 %), β−$CaCl_2·4H_2O$ (15 %) and β−$CaCl_2·4H_2O$ and solution (25 %), thus, deliquescence occurring between 15 and 25 % RH.

As mentioned previously, in the investigation of Guo et al. (2019) the water vapor sorption measurements were conducted after initial isothermal drying at 298.15 K similar to experiment Raman−2 in this work. In their experiments, both deliquescence at 28.5% RH and at 18.5% RH were observed, which is consistent with the results of experiments Raman−2 and 3. The presence of α−$CaCl_2·4H_2O$ seems to be the key factor. In the case of its presence, deliquescence occurs at 28.5% RH after hydration to $CaCl_2·6H_2O$; in its absence, deliquescence occurs directly from β−$CaCl_2·4H_2O$ without transition to $CaCl_2·6H_2O$. The kinetics of dehydration and hydration are influenced by various factors, such as temperature, particle size, shape, and moisture diffusion. Therefore, different dehydration products may have been formed in the experiments of Guo et al. (2019), even though all materials were dried under isothermal conditions. In experiment Raman−3, the thermal drying represents a more drastic treatment that allows the dehydration reaction to proceed further, compared with the isothermal drying in experiment Raman−2. This assumption is also confirmed by an additional water vapor sorption measurement SPS−3, as shown in the Fig. 5−11, including initial isothermal drying at 298.15 K and 0% RH, but no heating step before rehydration. In this experiment, the deliquescence was indeed observed close to 30% RH, which again reinforces the assumption that the conditions during the drying step decisively influence the hydration sequence.

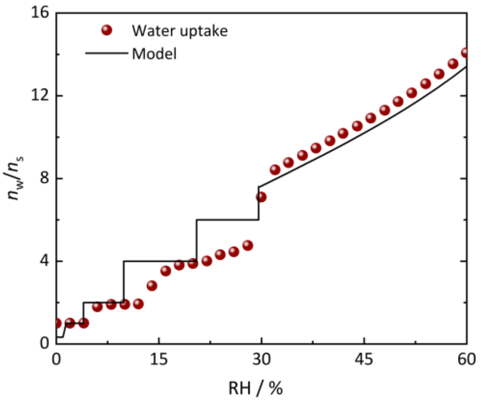

Figure 5−11. Water vapor sorption of dehydrated $CaCl_2·6H_2O$ at 298.15 K (dehydration at 298.15 K and low RH).

In the experiments with isothermal drying, e.g. Raman−2 and SPS−3, as shown in the schematic diagram in Fig. 5−12, the phase transitions in the crystal core become slow due to the increased moisture diffusion path length when the surface is completely covered with the lower hydrate. Then, if the reaction time is insufficient, it is likely that the dehydration reaction does not proceed to completion. Remaining nuclei of the higher hydrates, i.e. α−$CaCl_2·4H_2O$ or $CaCl_2·6H_2O$ may then act as seeds during the subsequent rehydration process, preventing the metastable transition to β−$CaCl_2·4H_2O$. In comparison, in the experiments with thermal drying, e.g. Raman−1, Raman−3, SPS−1, and SPS−2, the higher temperature promotes the dehydration reactions resulting in complete dehydration to the lower hydrates ($CaCl_2·H_2O$ or $CaCl_2·2H_2O$). In addition, the temperature of thermal drying (333.15 K) is above the incongruent melting temperature of α−$CaCl_2·4H_2O$. The value of 317.22 K calculated with the present model (Section A1.1 of Appendix) is in excellent agreement with an experimental value determined recently (317.45 K) (Ushak et al., 2016). Moreover, even if the incongruent melting process is incomplete, the metastable congruent melting temperature at 319.3 K provides an absolute stability limit excluding the presence of α−$CaCl_2·4H_2O$ nuclei after thermal drying. In this case, metastable β−$CaCl_2·4H_2O$ can be formed and its deliquescence will be observed subsequently.

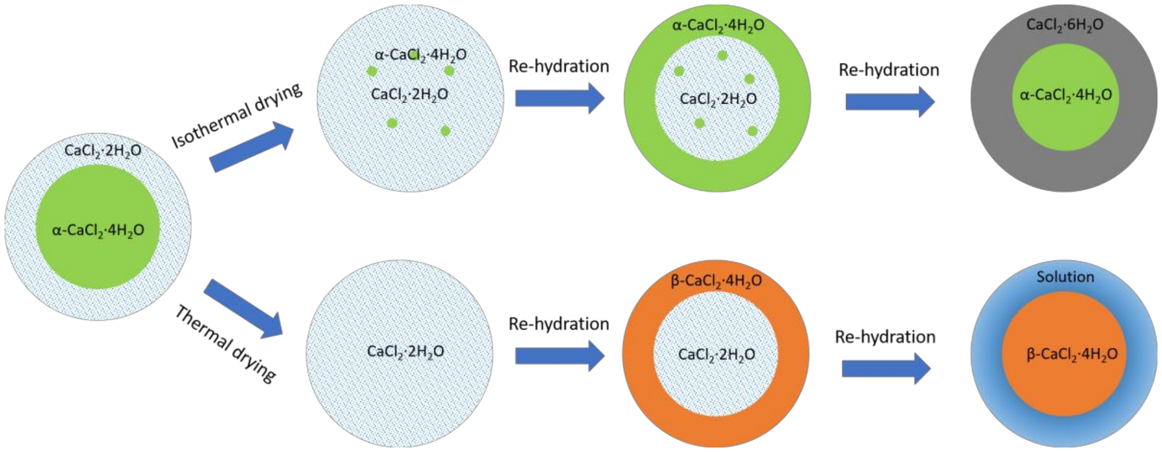

Figure 5−12. Schematic diagram of dehydration and rehydration between $CaCl_2·2H_2O$ and $CaCl_2·4H_2O$.

5.2.3 Metastable transition

Metastable transitions are commonly observed in systems involving freezing and crystallization due to nucleation hysteresis (Steiger and Voigt, 2019). To find a possible explanation for the presence of metastable β−$CaCl_2·4H_2O$ instead of thermodynamically stable α−$CaCl_2·4H_2O$ and thus the deviation of the equilibrium pathway observed in experiment Raman−1, the lattice structures of the different calcium chloride hydrates (Table 5−4) are discussed. $CaCl_2·2H_2O$ exhibits a highly symmetrical orthorhombic structure, followed by β−$CaCl_2·4H_2O$ (monoclinic), and α−$CaCl_2·4H_2O$ (triclinic) having the lowest symmetry. It is assumed that more similar structures are more likely to undergo solid−solid transformations due to the lower barrier for the formation of the new phase. As shown in Fig. 5−13, $CaCl_2·2H_2O$ has a hexacoordinated octahedral structure with the central calcium ion being surrounded by four chloride ions and two water molecules. In α−$CaCl_2·4H_2O$, the coordination number is seven with four water molecules and three chloride ions surrounding the calcium ion. In the lattice cell of β−$CaCl_2·4H_2O$, both hexacoordinated and heptacoordinated cations coexist, linked via bridging chloride ions. The cell may thus be considered as an intermediate structure that is more similar to $CaCl_2·2H_2O$ than the α−$CaCl_2·4H_2O$ structure. For example, the square planar coordination of the calcium cation with chloride in $CaCl_2·2H_2O$ is maintained in the structure of the β−polymorph. Thus, the formation of metastable β−$CaCl_2·4H_2O$ is more likely than the formation of the stable hydration product (α−$CaCl_2·4H_2O$). It should be noted that the formation of the β−polymorph also follows Ostwald's rule (Ostwald, 1987) which was explained on the basis of both thermodynamic and structural considerations (Threlfall, 2003). In the present study, the formation of the metastable polymorph has a structural basis. The β–polymorph forms easier due to its structural similarity to the educt phase $CaCl_2·2H_2O$.

Table 5–4. Lattice structures of $CaCl_2·nH_2O$ (Leclaire and Borel, 1977a; Leclaire and Borel, 1977b; Leclaire and Borel, 1978; Leclaire and Borel, 1979)

Hydrate	Crystal system
$CaCl_2·2H_2O$	Orthorhombic
α–$CaCl_2·4H_2O$	Triclinic
β–$CaCl_2·4H_2O$	Monoclinic
γ–$CaCl_2·4H_2O$	Monoclinic
$CaCl_2·6H_2O$	Hexagonal

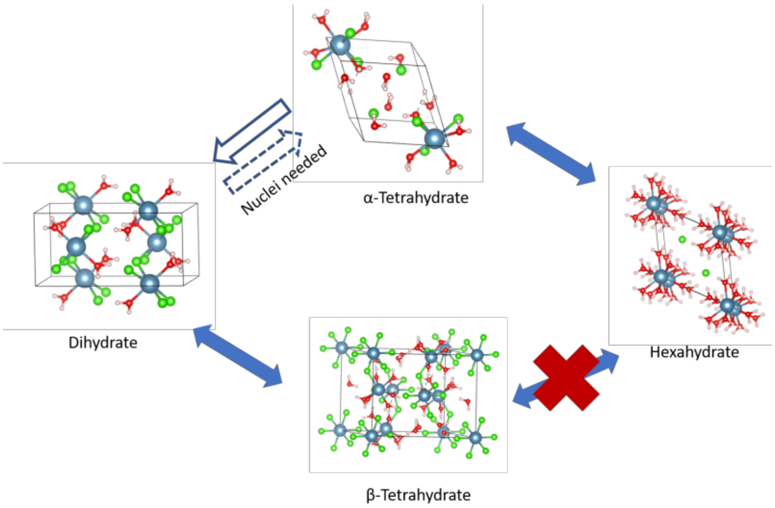

Figure 5–13. Lattice structures and hydration–dehydration pathways of $CaCl_2·nH_2O$ (figures produced in VESTA (Momma and Izumi, 2011).

Once the formation of the metastable β–$CaCl_2·4H_2O$ is understood, the missing hydration step to $CaCl_2·6H_2O$ has to be addressed next. When the relative humidity approaches the DRH, a continuous liquid film on the crystal surface, likely a saturated solution, acts as the catalyst reducing the nucleation barrier for the formation of a liquid (Finlayson–Pitts, 2003; Ewing, 2005; Ewing, 2006; Bruzewicz et al., 2011; Lin et al., 2021). Such a solution film has also been proposed as an intermediate state in the hydration of a salt (Sögütoglu et al., 2019; Sögütoglu et al., 2021) and the presence of such a film with increased ion mobility during the hydration of K_2CO_3 was recently detected by impedance spectroscopy (Houben et al., 2022). The initial nanoscale thin film grows to a macroscopic solution film as the humidity reaches and exceeds the DRH of the lower hydrate, which was observed in the hydration of Na_2SO_4 and $MgSO_4$ (Linnow et al., 2014; Steiger et al., 2008b). This macroscopic solution film also appears during the transition from α−$CaCl_2·4H_2O$ to $CaCl_2·6H_2O$ in experiment Raman−2 (shown in Fig. 5−9). The presence of the macroscopic solution film promotes the rate of the hydration reaction and the stable higher hydrate at the respective humidity crystallizes from solution. However, in the case of β−$CaCl_2·4H_2O$, its solubility at 298.15 K is 9.49 mol·kg^{-1}, equivalent to 5.85 moles of water per mole of salt. Thus, the amount of water in the saturated β−$CaCl_2·4H_2O$ solution film is not sufficient to allow the complete precipitation of the hexahydrate and might inhibit the hydration to $CaCl_2·6H_2O$. In contrast, the solubility of α−$CaCl_2·4H_2O$ is 8.57 mol·kg^{-1}, or 6.48 water molecules per mole of salt, so the formation of the hexahydrate is not hindered.

5.3. Conclusions

In this study, the hydration and deliquescence behavior of the $CaCl_2$ hydrates at 298.15 K was investigated using water vapor sorption analysis and Raman spectroscopy. The results reveal two possible hydration pathways leading to deliquescence: First, an equilibrium pathway in which, starting from $CaCl_2·2H_2O$, water uptake leads to two hydration steps and the formation of α−$CaCl_2·4H_2O$ and $CaCl_2·6H_2O$ which, eventually, undergoes deliquescence at 29% RH. Second, a metastable pathway in which the hydration of $CaCl_2·2H_2O$ leads to metastable β−$CaCl_2·4H_2O$ which undergoes deliquescence at 18.5% RH. This metastable transition may be favored because the lattice structure of metastable β−$CaCl_2·4H_2O$ is more similar to the structure of $CaCl_2·2H_2O$ than is the structure of the stable polymorph α−$CaCl_2·4H_2O$. In addition, the higher solubility of β−$CaCl_2·4H_2O$ leads to less than six water molecules per mole of salt and impedes the precipitation of the hexahydrate from a solution supersaturated with respect to this phase.

The present results also show that the formation of β−$CaCl_2·4H_2O$ strongly depends on the conditions during the dehydration of $CaCl_2·6H_2O$. Only if the dehydration products, i.e. $CaCl_2·2H_2O$ or $CaCl_2·H_2O$, do not contain any residual nuclei of α−$CaCl_2·4H_2O$, the metastable β−tetrahydrate can form during rehydration. Notably, the conditions during thermal dehydration seem to be favorable for the formation of the metastable β−tetrahydrate. Therefore, the present results are particularly important for applications with thermal dehydration of $CaCl_2·6H_2O$ such as in thermochemical heat storage. In such applications, the formation of β−$CaCl_2·4H_2O$ is very likely leading to a significantly lower deliquescence relative humidity than for $CaCl_2·6H_2O$. Deliquescence and the formation of solutions are major issues in thermochemical heat storage applications (Donkers et al., 2017). On the other hand, on Mars, if this metastable transition still applies to low temperatures, the metastable pathway would expand the stable humidity range of the liquid phase, and the existence of a calcium chloride solution on such a cold and dry planet is more likely. In natural environments on Earth, complete hydration or dehydration is unlikely due to climate fluctuations, slow reaction rates and the highly hygroscopic nature of calcium chloride.

Hence, the observed metastable pathway is not expected, but deliquescence at 29.1% RH at 298.15 K instead.

Chapter 6. Missing eutectic transition in the electrolyte solutions in confinement

The eutectic point represents the lowest temperature at which a liquid solution remains thermodynamically stable, and marks the beginning of melting in a salt−ice mixture. In confinement, the eutectic point in electrolyte solutions is significantly shifted to lower temperatures (Meissner et al., 2016). Consequently, eutectic melting is considered the most plausible mechanism for the presence of liquid water on Mars. Theoretically, the eutectic transition should occur in all salt solutions, regardless the solute type or concentration. However, under confinement, this transition was only observed in concentrated solutions but absent in the dilute solutions in the previous studies (Aristov et al., 1997; Koniorczyk and Bednarska, 2019). To date, this anomalous behavior lacks a clear and comprehensive explanation. This phenomenon is apparently similar to the nonfreezing behavior observed in pure water within pores smaller than 2.5 nm or under partial filling conditions, attributed to the strong interaction of water molecules with the pore wall (Overloop and Vangerven, 1993; Jähnert et al., 2008; Pearson and Derbyshire, 1974; Rennie and Clifford, 1977; Morishige and Nobuoka, 1997; Morishige and Kawano, 1999). Meissner et al., (2016) proposed that ions crystallize as extremely small nanocrystals within the interfacial layer producing a secondary confinement effect on the remaining solution. Argyris et al. (2010) using molecular dynamics simulation, found strong accumulation of dissolved ions in the interfacial layer of silica nanopores. In this perspective, ions can be categorized based on their spatial distribution: interfacial ions located near the pore wall and bulk like ions in the core of the pore.

It is well−established that the water molecules are unable to freeze within an interfacial layer of about 0.6 nm thickness (Jähnert et al., 2008). Ion crystallization in this region is likely inhibited as well. Consequently, the eutectic transition can only occur in the core of the pore solution and only if the accumulation of ions in the interfacial layer leaves a sufficient amount of ions in the core. The total amount of ions is influenced by three factors: salt concentration, pore volume, and pore filling degree. These factors directly determine the existence of bulk like ions in the core, which results in the eutectic transition. In this study, systematic calorimetric measurements were conducted to investigate the effects of salt concentration, pore size, and pore filling degree on the eutectic transition in nanoporous silica. The results confirm the strong adsorption and accumulation of ions within the nonfreezing interfacial layer, meaning that no bulk like ions are present in the core, thus, impeding the eutectic transition. Only if the interfacial layer is saturated, the eutectic transition in dilute solutions can be observed.

6.1 Experiments

The samples were prepared by impregnation of a weighted mass of the silica material (approximately 50 mg) with an appropriate amount of solution ($CaCl_2$ or NaCl) in a mortar. Grinding facilitated the formation of a homogeneous mixture of the liquid and the porous material. The filling degree was estimated by the ratio of the solution volume and the pore volume of the respective material. Calorimetric measurements were conducted using a Setaram BT 2.15 calorimeter in DSC mode with very low cooling and heating rates of 0.1 $K \cdot min^{-1}$ (to avoid kinetic influences) with a 3 hour hold time at the lowest temperature. The working temperature range depends on the intrinsic properties of salt and pore size, spanning from –100 °C to 25 °C for $CaCl_2$ solutions and from –80 °C to 25 °C for NaCl solutions.

6.2 Results and Discussion

6.2.1 Eutectic Transition in Bulk and in Confined Solutions

The freezing or melting of a salt solution is more complex than that of pure water as it involves a phase separation of both ice and salt crystals from the solution. As shown in Fig. 6−1a for a solution with a concentration lower than the eutectic concentration (solution A), the freezing process begins with the crystallization of ice at the freezing temperature (point B). Upon further cooling, ice crystallization continues and the concentration in the remaining solution increases until the eutectic point is reached. The solution is now also saturated with the salt and further cooling causes the simultaneous crystallization of both solids. The reverse process starts with the eutectic melting. In case of the frozen solution A, the salt dissolves completely in the eutectic melt, and upon further heating, ice melting continues until point B is reached.

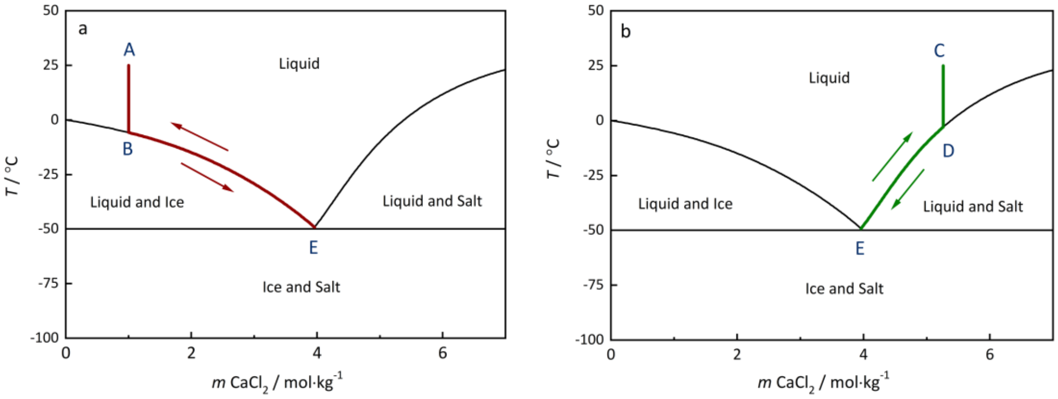

Figure 6−1. Equilibrium freezing and melting pathways of bulk $CaCl_2$ solutions. Red lines: Starting from solution A with a concentration lower than the eutectic concentration. Green lines: Starting from solution C (concentration higher than eutectic concentration). Solid lines are freezing temperatures and solubilities of $CaCl_2 \cdot 6H_2O$ calculated with the model of Wang et al. (2024) which is based on critically evaluated freezing temperatures and solubilities.

The freezing and melting process of a solution with a concentration higher than the eutectic concentration (solution C) is illustrated in Fig. 6−1b. In this case, the process starts with the crystallization of the crystalline salt (point D). Upon further cooling, the salt crystallizes continuously until the eutectic point is reached below which both solids crystallize (point E). The melting process of this mixture starts with complete ice melting at the eutectic temperature and partial dissolution of the salt. During subsequent heating, dissolution of the salt continues until point D is reached. A similar diagram for the phase transition pathway for NaCl solutions is shown in Fig. 6−2.

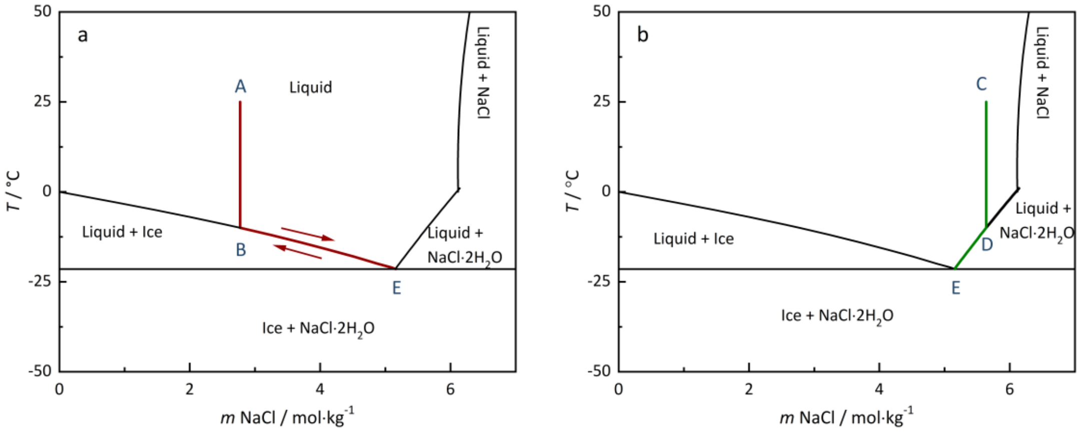

Figure 6−2. Equilibrium freezing and melting pathways of bulk NaCl solutions. (a) Starting from solution A with a concentration lower than the eutectic concentration. (b) Starting from solution C (concentration higher than eutectic concentration). Solid lines are freezing temperatures and solubilities of $NaCl·2H_2O$ and NaCl calculated with Pitzer model (the parameters are provided in Section A2 of the Appendix), which is based on critically evaluated freezing temperatures and solubilities.

A typical thermogram of a DSC heating scan of a frozen bulk 0.4 m $CaCl_2$ solution yields two endothermic signals (Peaks 1 and 2) as illustrated in Fig. 6−3a. Peak 1 corresponds to the eutectic melting of the solid mixture of $CaCl_2·6H_2O$ and ice at the eutectic temperature –50 °C (corresponding to point E in Fig. 6−1a). Peak 2 represents the temperature at which ice melting is complete (corresponding to point B in Fig. 6−1a). This latter transition is termed the ice melting temperature in the following discussion to distinguish it clearly from the eutectic point. It should be noted, however, that the eutectic melting Peak 1 represents a transition at a single temperature, thus, yielding a sharp peak. The peak width in a bulk solution is controlled essentially by the properties of the calorimeter and the heating rate. In confinement, the shape of the eutectic melting peak is controlled by the pore size distribution (Jähnet et al., 2008). In contrast, the ice melting Peak 2 represents the continuous process of ice melting along the line EB in Fig. 6−1a, starting right above the eutectic temperature and extending to the endpoint B, the temperature of which depends on the solution composition.

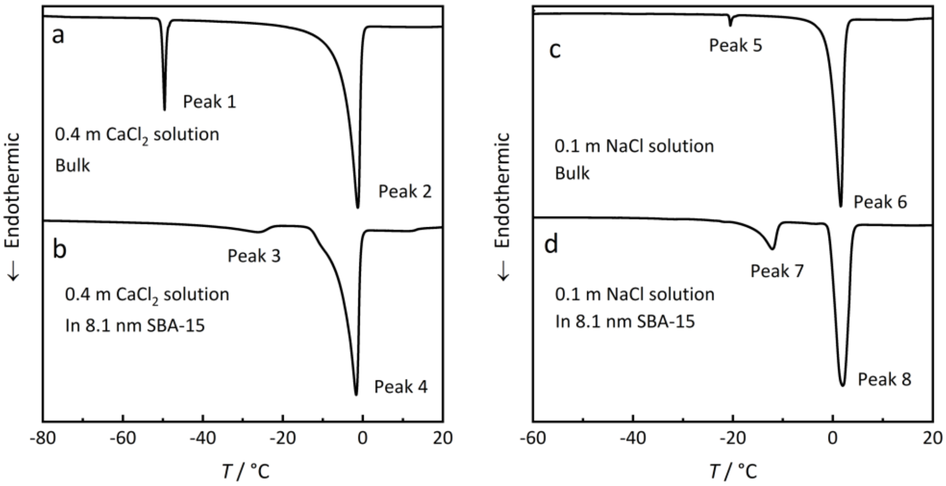

Figure 6−3. Melting curves of dilute $CaCl_2$ (0.4 m) (a and b) and NaCl (0.1 m) solutions (c and d) both in bulk and in 8.1 nm SBA-15 (overfilling 150%); the total amount of solution was the same in the bulk measurement and in the experiment in confinement.

DSC scanning of the same amount of the 0.4 m $CaCl_2$ solution in an 8.1 nm SBA-15 sample with 150% filling degree are shown in Fig. 6−3b. The overfilled confined solution also exhibits two thermal signals (Peak 3 and Peak 4) during the melting process. The higher temperature signal Peak 4 closely aligns with Peak 2 of Fig. 6−3a, representing the melting of bulk ice in the salt solution. However, compared to the Peak 1 (bulk eutectic point), Peak 3 is shifted significantly to higher temperature. This suggests that Peak 3 reflects the ice melting within the pore rather than the eutectic transitions, which are expected at −50 °C for the bulk solution (Peak 1) and at lower temperature in pore as discussed below.

Similar results are observed in measurements with a dilute 0.1 m NaCl solution in bulk and in confinement (Figs. 6−3c and 6−3d). Peaks 5 and 6 represent the eutectic transition and the continuous ice melting, respectively, in the bulk solution, while the Peaks 7 and 8 correspond to ice melting occurring in the bulk and within the pore, respectively. Thus, in both experiments with rather dilute solutions, no signal of a eutectic transition is observed. Since the total amount of the $CaCl_2$ and NaCl solutions were the same in the bulk and in confinement, these findings clearly confirm that the absence of a detectable eutectic transition in confined dilute solutions is a real effect rather than an experimental artifact due to limited sensitivity of the calorimetric measurement as suggested in a previous investigation (Koniorczyk and Bednarska, 2019).

6.2.2 Influence of salt concentration

The absence of the eutectic melting signal is only observed with dilute electrolyte solutions. In contrast, it is well known that more concentrated solutions yield eutectic melting signals that are shifted to lower temperature than the respective bulk eutectics (Meissner et al., 2016; Jantsch et al., 2019; Prause et al., 2020; Aristov et al., 1997). Figure 6−4 presents a systematic investigation of the influence of solution concentration on the melting curves of frozen $CaCl_2$ (Fig. 6–4a) and NaCl (Fig. 6–4b) solutions in SBA-15 with pore sizes 9.4 nm and 8.5 nm, respectively. To ensure complete pore impregnation, all host materials were treated with a solution volume of 150% of the pore volume, resulting in composites that include both bulk and confined solutions. Consequently, the melting curves incorporate phase transition signals from the bulk phases (indicated by blue arrows and blue dashed lines) and the confined solutions (indicated by red arrows and blue dashed lines).

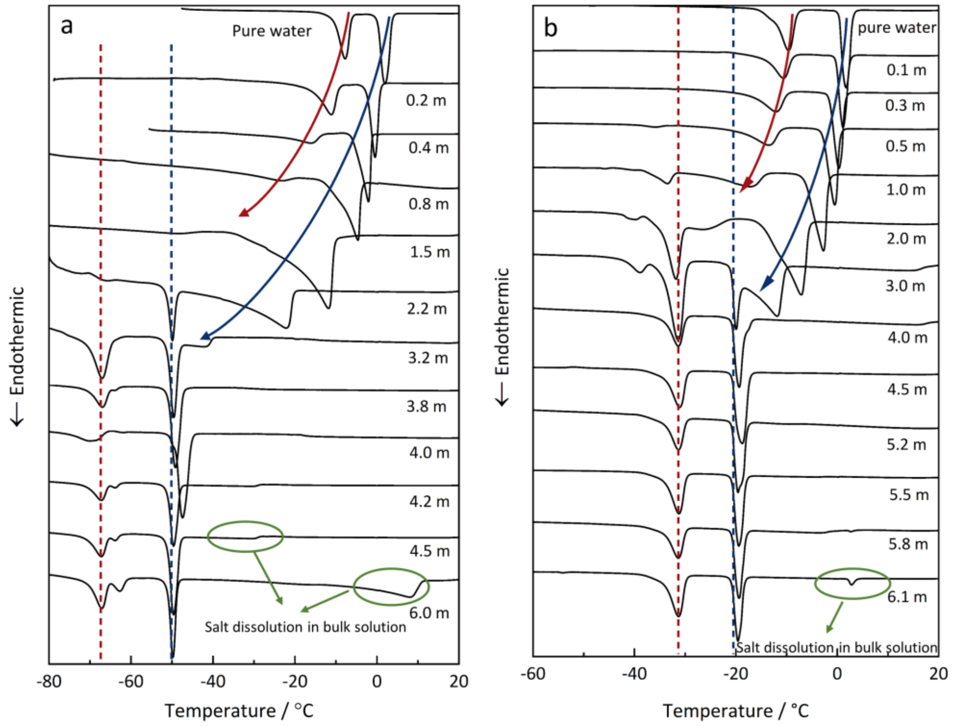

Figure 6–4. The melting curves of $CaCl_2$ solutions (a) in 9.4 nm SBA-15 with molalities 0–6.0 m and NaCl solutions (b) in 8.5 nm SBA-15 silica with molalities 0–6.1 m (overfilling 150%). The dashed red line and blue lines indicate in-pore and bulk eutectic points, respectively; Red and blue arrows are drawn to guide the eyes along the endpoints of the ice melting in pore and in bulk, respectively.

The influence of salt concentration on the melting process of the frozen $CaCl_2$ and NaCl solutions follows a similar pattern with distinct behavior observed in both the low and the high concentration regions. For $CaCl_2$, the melting curves for concentrations at 1.5 m and below show only two endothermic peaks, corresponding to the ice melting in the bulk phase and in the confined solution. The temperature of both peaks decreases with increasing concentration as illustrated by the blue and red arrows in Fig. 6–4a. The temperature decrease illustrated by the arrows reflects the influence of concentration on the ice melting temperature as shown in Fig. 6–1a. The shift between the ice melting temperatures in pore (red arrow) and in the bulk (blue arrow) reflects the decrease in the melting temperatures due to the limited size of the ice crystals in confinement. Notably, no eutectic transition is detected in either bulk phase or in the confined solution at these concentrations.

At high concentrations (2.2 m and above), two endothermic peaks at approximately −67 °C (dashed red line) and −50 °C (dashed blue line) indicate eutectic melting in confinement and in the bulk, respectively. It should be noted that the bulk eutectic temperature is represented by the peak onset temperature in DSC while the eutectic temperature in confinement is better represented by the peak maximum (Jähnet et al., 2008). A significant depression of the eutectic melting temperature due to the confinement effect is evident, independent of salt concentration. The smaller peaks (illustrated by the green circles in Fig. 6−4a) above the bulk eutectic temperature correspond to continuous salt dissolution which follows the pathway illustrated in Fig. 6−1b (along line ED) at concentrations above the eutectic concentration (e.g., 4.5 m and 6.0 m in Fig. 6−4a). Overall, the salt concentration, which primarily controls the total amount of ions in the pore, has a significant impact on the appearance of the eutectic transitions.

It is notable that the ice melting peak of the confined solutions does not appear in the thermograms. This absence is attributed to ion diffusion and exchange between solutions inside and outside of the pore during the freezing process, thus, leading to salt fractionation and a final ice–salt mixture composition in the pores that matches the eutectic composition (Meissner et al., 2016). If crystallization in the bulk solution starts with the precipitation of ice (i.e., at concentrations below the eutectic as in Fig. 6−1a), there is a rapid increase in concentration resulting in inward diffusion. If, on the other hand, crystallization starts with the precipitation of $CaCl_2 \cdot 6H_2O$, the concentration decreases resulting in diffusion outward. In either case, the concentration within the pore approaches the eutectic concentration. As a result, thermal signals of ice melting or salt dissolution within the confined solutions do not appear. As shown in Fig. 6−5, cooling a solution at composition A, the freezing point of the bulk solution outside the pore is reached at point B. The segment BE represents a continuous freezing process in which ice crystallizes out from the bulk solution. This crystallization leads to an increase of the salt concentration in the remaining liquid. The resulting concentration gradient triggers diffusion of ions which are transported into the pore. Due to ongoing ice precipitation outside and diffusion inwards, the salt concentrations continuously approaches the eutectic composition both in the external solution and within the pore and ice formation occurs exclusively in the bulk during this initial stage. As temperature and salt molality shifts to point E, the eutectic point of the bulk solution is reached, where both ice and salt begin to crystallize simultaneously in the bulk phase. At this stage, the salt concentration in the confined solution equals the eutectic concentration of the bulk. In confinement, due to the limited crystal sizes, both the freezing curves and the solubility curve of the salt are shifted to lower temperatures as shown by the two dotted lines.

There intersection is the eutectic point F within the pore. Thus, upon decreasing the temperature from the bulk eutectic temperature E to the eutectic temperature F within the pore, eutectic crystallization also occurs in the pore, involving the simultaneous formation of ice and salt. Consequently, the salt-to-ice ratio in the pore at this point (i.e., eutectic composition) differs significantly from the initial composition of the solution.

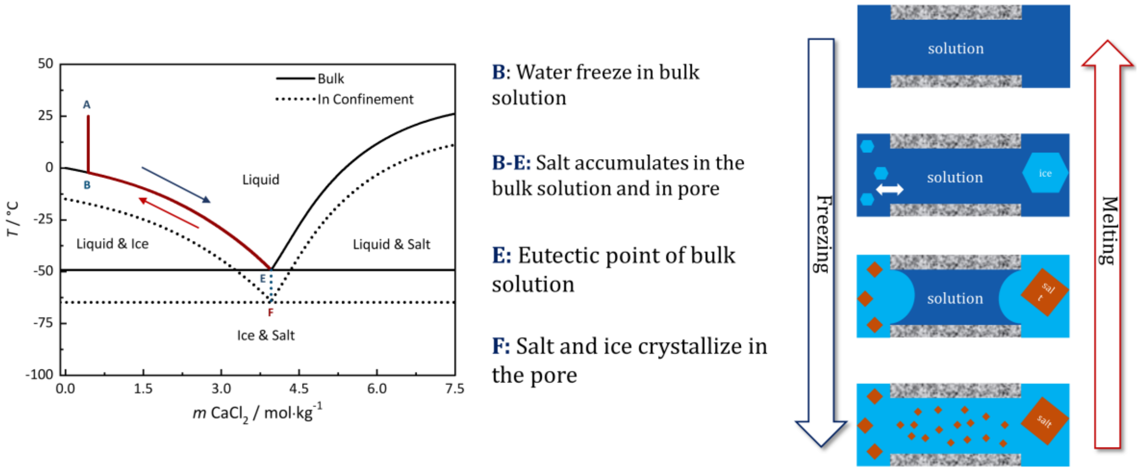

Figure 6–5. Freezing pathway of the salt solution within the overfilled pores. This diagram indicates that the final ice–salt mixture in the pore is as same as the eutectic concentration, resulting in the absence of ice melting behavior in the pore.

During the reverse melting process, liquefaction begins in the pore at point F, corresponding to the complete eutectic melting of the salt–ice eutectic mixture within the pore, leaving no residual solid in the confined space. As the temperature further increases, eutectic melting in the bulk solution occurs at point E, followed by continuous ice melting along path EB, which is complete at point B.

This melting process results in three distinct thermal events: (1) the eutectic melting in the pore, (2) eutectic melting in the bulk phase, and (3) ice melting in the bulk phase, which corresponds to three peaks in the thermograms observed in the melting curves of solutions with higher concentrations (but below the eutectic molality), e.g. the 3.2 m $CaCl_2$ solution and the 3.0 m NaCl solution, respectively, shown in Fig. 6–4. Notably, due to the exchange of water molecular and ions between the pore and the bulk, the continuous ice melting process (following line BE) is not observed within the confined space. For initial concentrations above the eutectic composition, the freezing process starts with the precipitation of salt resulting in a decreasing concentration a diffusion outward. However, also in this case, the concentration approaches the eutectic both in pore and in the bulk. Apart from the two eutectic signals, the third thermal signal represents then the continuous dissolution of the salt as illustrated in Fig. 6–4 for the very concentrated solutions (4.5 m and 6 m $CaCl_2$ and 6.1 m NaCl).

Similarly, eutectic transitions are observed only in concentrated NaCl solutions and are absent in dilute solutions, as shown in Fig. 6−4b. The molality threshold for the absence of the eutectic transition in confined NaCl solutions (≤ 0.5 m) is notably lower than in case of $CaCl_2$ (≤ 2.2 m), indicating a stronger influence of confinement on the phase behavior of the $CaCl_2$ solution. This disparity is likely due to the stronger interaction between the ions and the pore wall. It is well established that that the highly polarized silica-solution interface is negatively charged, primarily resulting from the deprotonation of the silanol group upon contact with solutions (Salis et al., 2010; Yang et al., 2020). The deprotonation equilibrium and the surface charge density are affected by both pH and salt concentration. According to the classic Poisson-Boltzmann (PB) theory, this results in the formation of an electrical double layer (EDL) characterized by counterion accumulation and co−ion depletion (Israelachvili, 2011). Ion enrichment near the interface has been well investigated by Monte Carlo and molecular dynamics simulation, showing significant ion accumulation within a layer of approximately 1 nm from the pore wall (Argyris et al., 2010; Freund, 2002; Qiao and Aluru, 2003; Yang et al., 2002; Wang et al., 2023b).

Based on these insights, we propose that ion accumulation in the interfacial layer at the pore walls, where the first-order phase transition disappears, leads to significant depletion of ions in the core solution resulting in the absence of the eutectic transition. The ion enrichment behavior is likely sensitive to the ionic charge, as the electrostatic attraction between the negatively charged pore wall and a bivalent cation (Ca^{2+}) is stronger than with a monovalent cation (Na^{+}). This stronger interaction leads to a higher capacity for divalent ions to accumulate in the interfacial layer, thereby explaining why the eutectic transition in confined $CaCl_2$ solutions occurs only at higher concentrations compared to NaCl.

In the present experiments with dilute solutions, the limited number of ions is insufficient to saturate the interfacial layer. Thus, all available ions are consumed completely leading to the absence of salt crystallization and eutectic transition. In contrast, in the more concentrated solutions, there is sufficient supply of ions to saturate the interfacial layer and the excess bulk−like ions in the core solution crystallize at the eutectic point.

6.2.3 Influence of pore filling degree and pore size

The key factor influencing the phase behavior of the confined solution is thus the total amount of ions present, rather than the apparent salt concentration. In addition to the initial concentration, the total reservoir of dissolved ions is also controlled by both pore size and the degree of pore filling. Figure 6−6 illustrates the heat flow curves during melting of frozen $CaCl_2$ and NaCl solutions in SBA-15 and MCF silica with different pore size and overfilling degree. Red and black curves represent DSC scans with and without detection of the eutectic transition, respectively. As shown in Fig. 6−6a for 8.5 nm pores impregnated with an 0.8 m $CaCl_2$ solution at pore filling degrees of 150%, 450%, and 750%, the in−pore eutectic transition is observed only in the 750% overfilled sample but not in the other two samples. A similar effect of pore filling degree on the eutectic transition is also obvious in the NaCl samples as shown in Fig. 6−6e. The bulk solution connected to the pores serves as a reservoir ensuring supply with a sufficient amount of ions to fill the interfacial layer while still maintaining a sufficiently high concentration in the core to observe the eutectic transition. A few experiments were carried out with dilute NaCl solutions and pore fillings below 100%. The resulting DSC scans revealed only a single broad ice melting peak and, as expected, no signal for the eutectic transition. Therefore, further experiments with low pore fillings were not conducted.

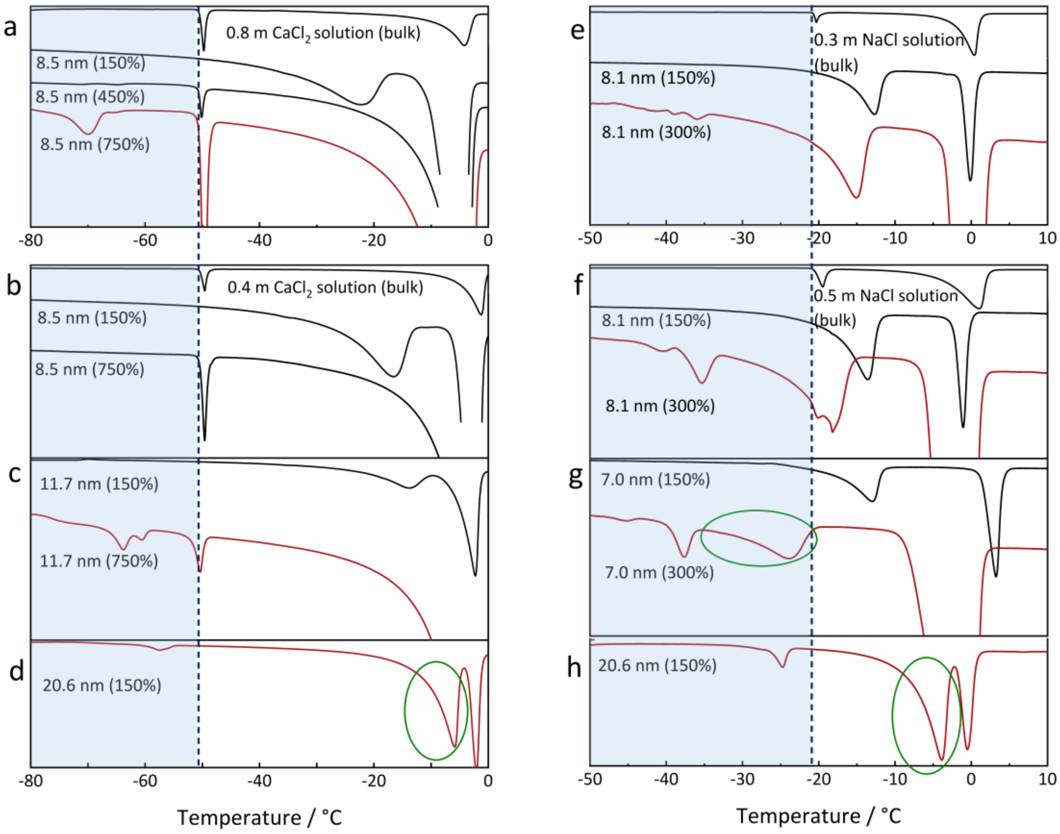

Figure 6−6. Heat flow curves during melting of $CaCl_2$−H_2O (a–d) and NaCl−H_2O (e–h) in SBA-15 silica (7.0–11.7 nm) and a siliceous mesostructured cellular foam (MCF, 20.6 nm) with different pore sizes and pore filling degrees (150%–750%).Vertical dashed lines: the bulk eutectic points; blue areas: the regions where the signal of the eutectic transition in the confined solution is expected; red and black curves: measured thermograms with and without detection of the eutectic transition, respectively.

Finally, alongside with salt concentration and pore filling degree, pore size is the third factor affecting the total amount of salt in the confined solution. Figures 6−6b to 6−6d compare the melting curves for different pore sizes at constant pore filling degree. At 150% pore filling, the eutectic transition occurs only in the 20.6 nm pore and is absent in the smaller pores (11.7 nm and 8.5 nm). At 750% pore filling, the eutectic transition is observed in the 11.7 nm but not in the

8.5 nm pore. Similar behavior is shown for NaCl solutions in Figs. 6−6f to 6−6h. Notably, in some cases where a peak for the eutectic transition in the pore is observed (indicated by the red curves), the expected eutectic melting signal of bulk solution did not appear. Instead, signals (marked with green circles) are detected at temperature deviating from the bulk eutectic point, as seen in Figs. 6−6d, 6−6g, and 6−6h. As illustrated in Fig. 6−1, ice melting in the salt solution is a continuous process over a temperature range, typically producing a broad thermal peak. In contrast, the eutectic transition take place at a fixed temperature and is characterized by a sharp, distinct peak. Therefore, these unidentified signals are assigned to the ice melting in the confined salt solution, as their broad profiles, as discussed before, are characteristic of gradual thermal events, such as ice melting above the eutectic in the electrolyte solutions. This indicates that the final ice–salt mixture composition within the pore has a lower salt content than the bulk eutectic mixture, even if all ions diffuse into the pore from the bulk solution.

6.2.4 Ion accumulation in the pore

To further analyze the ion enrichment in the interfacial layer semi−quantitively, the concentration of $CaCl_2$ in this region was calculated based on the following assumptions: (1) the thickness of the interfacial layer is 0.6 nm, consistent with that of pure water, (2) the density in this region is same as in the core solution, (3) all ions accumulate in the interfacial layer, leaving the pore core devoid of ions, and, (4) the total capacity of this layer is limited and the average concentration does not exceed the eutectic molality of 4 m. Given the cylindrical geometry of SBA-15, the volume fraction of the interfacial layer can be expressed by the following equation

$$f_{\mathrm{V}} = \frac{V_i}{V_{\mathrm{P}}} = 1 - \left(\frac{r_{\mathrm{p}}-t}{r}\right)^2 \tag{6–1}$$

where V_{i} is the volume of the interfacial layer, V_{P} is the pore volume, r_{p} is the pore radius and t is thickness of the interfacial layer, assumed to be 0.6 nm.

Assuming that all ions preferentially accumulate within the interfacial layer, the local salt molality m_{i} in this region can be estimated by:

$$m_i = \frac{m_0}{f_{\mathrm{V}}} \tag{6–2}$$

where m_0 is the starting molality of the salt solution, i.e., the molality averaged over the entire pore volume.

The calculated results, shown in Fig. 6−7a, display the volume fractions of the interfacial layer (black curve) and the core (grey curve) as a function of pore diameter. The decrease in the volume fraction of the core solution with decreasing pore size results in a diminished influence of bulk–like ions in the core on the overall properties of the system making the interfacial ions predominant for pore sizes below 4 nm (the intersection of black and grey curves). In such small pores and at low to moderate concentrations, the interfacial layer remains unsaturated even after collecting all ions from the core solution. The dashed lines represent the interfacial layer concentration as a function of pore size at specific initial solution molalities and 100% pore filling. The intersections of the dashed lines with the blue area boundary, thus, the maximum concentration in the interfacial layer, marked by red, blue and green circles, yield the threshold pore sizes at which the interfacial layer just reaches saturation at the given initial molalities. At this moment in time, all ions are consumed to fill up the interfacial layer and the core consists of pure water. For a 0.4 m $CaCl_2$ solution, the threshold pore size is 23.5 nm in reasonable agreement with our measurements for the 20.6 nm pore size.

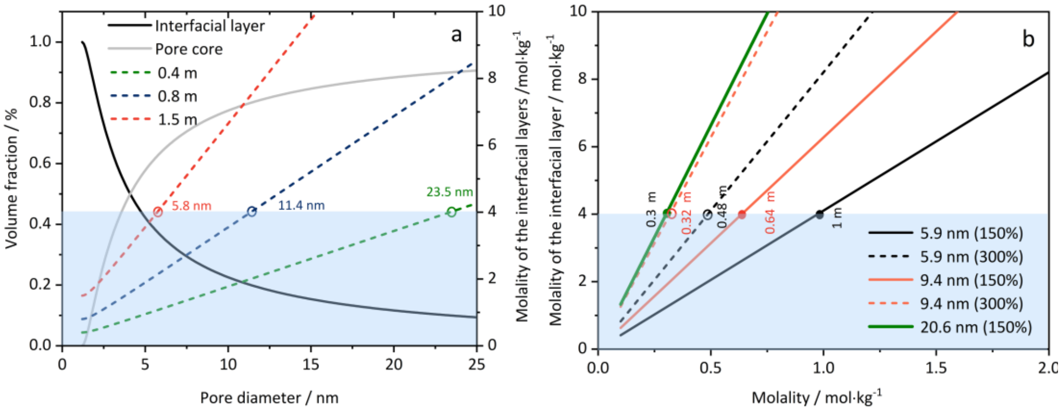

Figure 6–7. (a) Volume fractions of the interfacial layer (solid black curve) and the core (solid grey curve), concentration in the interfacial layer for initial molalities of 0.4 m (dashed green curve), 0.8 m (dashed blue curve), and 1.5 m (dashed orange curve). (b) Salt concentrations in the interfacial layer for pore sizes of 5.9 nm (solid black line: 150% pore filling and dashed black line: 300% pore filling), 9.4 nm (solid orange line: 150% pore filling and dashed orange line: 300% pore filling), and 20.6 nm (solid green line: 150% pore filling). Blue area: the unsaturated interfacial layer region (concentration in the interfacial layer below eutectic).

Figure 6–7b illustrates the relationship between the concentration in the interfacial layer and the initial salt molality for fixed pore sizes and pore fillings. The minimum concentrations at which the interfacial layer reaches saturation at these pore sizes and pore fillings are marked by the green, orange, and black symbols at the upper boundary of the blue area. Only if the initial concentration exceeds these values, dissolved ions remain in the core solution. For example, the limiting concentrations are 0.3 m and 0.64 m for 20.6 nm and 9.4 nm pores at 150% filling, respectively. An increase in the pore filling degree promotes the saturation of the interfacial layer even at low concentration as shown in Fig. 6–6b for two different pore sizes (open and filled symbols in Fig. 6–7b).

The role of the interfacial layer in the freezing process of dilute solutions within nanopores is illustrated schematically in Fig. 6–8. In a confined solution with a limited reservoir of dissolved ions, such as in a small pore, at low concentration, or at low pore overfilling, the ions are exclusively present within the unsaturated interfacial layer and the core of the pore consists of pure water (or an extremely dilute solution). Thus, only ice crystallizes in the core resulting in the absence of a eutectic transition (Fig. 6–8a). Conversely, in confined solutions with a sufficiently large reservoir of ions which can be achieved by larger pore sizes, higher concentrations or larger overfilling, as shown in Figs. 6–8b, c, d, the interfacial layer becomes fully saturated and an excess of ions remains in the core solution resulting in the eutectic transition within the core of a nanopore.

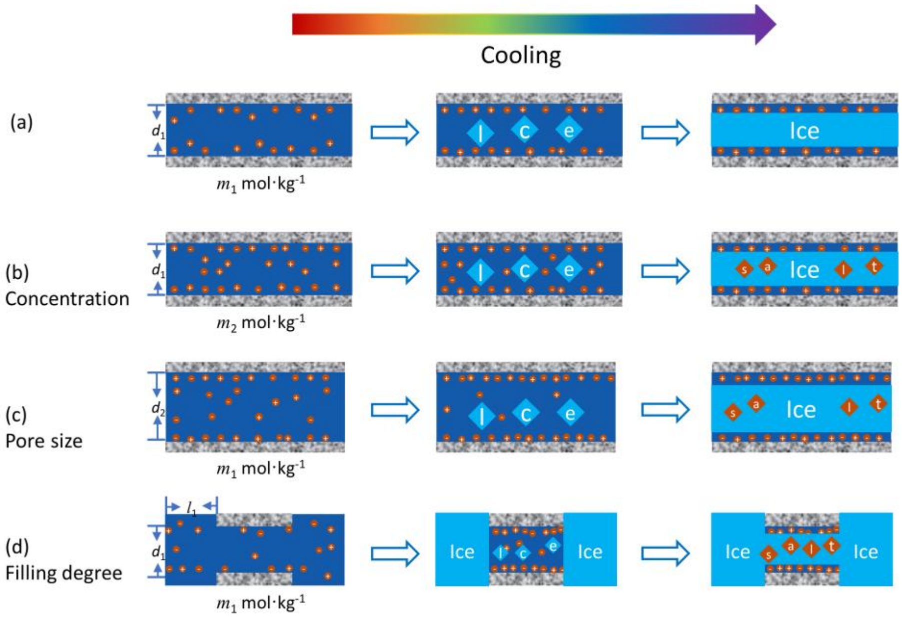

Figure 6–8. Schematic illustration of the freezing of electrolyte solutions in pores. Absence of a eutectic at very low concentrations (a) and formation of a eutectic at larger concentration (b), by increasing the pore size (c) or at larger overfilling (d). Pore sizes: $d_2 > d_1$; concentrations: $m_2 > m_1$.

6.3 Conclusion

In summary, anomalous phase behavior of $CaCl_2$ and NaCl solutions in nanoconfinement was observed, specifically, the absence of a eutectic transition at low concentrations. This study is the first to report how the eutectic transition of confined dilute solutions is controlled by concentration, pore size and pore filling degree. The findings suggest that strong ordering and preferential enrichment of dissolved ions in the interfacial layer and the resulting depletion of ions in the core solution results in the absence of salt crystallization. Formation of crystalline salt and the eutectic transition only occur when bulk–like ions remain in the core solution, thus, if the interfacial layer is fully saturated. The saturation of the interfacial layer depends on the total ion content, which is determined by three factors: salt concentration, pore size, and pore filling degree. The measurements presented in this work provide solid experimental evidence for the strong accumulation of dissolved ions in the interfacial layer. Furthermore, the temperature depression of the ice melting and eutectic point of electrolytes in nanopores and its pore size dependence are worth further quantitative analysis, as they are significantly affected by the ice–solution interfacial energy (Steiger, 2006). This discussion will be extended in a subsequent paper that integrates experimental results with a thermodynamic model. Ion diffusion from the bulk solution into the confined space holds potential for practical applications, such as desalination and enhancing oil recovery (Wang et al., 2018; Fang et al., 2021). Their findings provide experimental evidence supporting our interpretation of ion accumulation in the interfacial layer and ion exchange between the solution inside and outside the pore.

Chapter 7. Phase equilibria of aqueous electrolytes in porous silicas

Numerous studies have been conducted to investigate the phase transformations among water vapor, liquid solution, ice, and salts by fluctuations in temperature and vapor pressure. These studies have demonstrated that chlorides, perchlorates, and their mixtures significantly broaden the stability range of the liquid phase (Gough et al., 2011, 2014; Primm et al., 2017). It has been suggested that perchlorate brines can temporarily form on the Martian surface during daytime, either through melting of ice−salt mixtures or the deliquescence of salt particles (Nuding et al., 2014; Toner et al., 2015a). However, whether such brine can persist under Martian conditions remains still uncertain.

Recent studies have indicated that the liquefaction threshold of water is significantly lowered in nanopores compared to the bulk phase (Jähnert et al., 2008). Given that Martian regolith is a natural porous medium with pore sizes ranging from nanometer to micrometer, confinement effects become highly relevant. Magnesium perchlorate solutions mixing with soil have been found to exhibit a eutectic temperature lower than those of the bulk solution (Shumway et al., 2021, 2023). Similarly, salt−soil mixtures are expected to undergo deliquescence at lower humidites. These confinement-induced modifications to the phase behavior of salt solutions further enhance the likelihood of the stable presence of liquid water on Mars.

On the other hand, atmospheric aerosol nanoparticles, including NaCl and $(NH_4)_2SO_4$, also display unique phase behavior compared to their bulk counterparts. Previous studies conducted by my colleague Tanya Talreja-Muthreja have investigated the deliquescence of NaCl and $(NH_4)_2SO_4$ nanoparticles in porous silicas (Talreja-Muthreja et al., 2022; Talreja-Muthreja and Steiger, in preparation). Building on this work, the present Chapter also includes experiments on the melting behavior of NaCl and $(NH_4)_2SO_4$ solutions under nanoscale confinement.

In this Chapter, porous silica materials (SBA-15 and MCM-41) were employed to create confined environments for the salt solutions and crystals. The deliquescence relative humidities (DRH), melting points, and eutectic points of several salts in confinement were investigated through calorimetry and water vapor sorption analysis. Additionally, Raman spectroscopy was utilized to monitor and identify the phase transformations over the investigated temperature range.

7.1 Experiments

Calorimetry: Porous materials were impregnated with pure water or salt solutions (NaCl, $MgCl_2$, $CaCl_2$, $NaClO_4$, $Mg(ClO_4)_2$, $Ca(ClO_4)_2$, and $(NH_4)_2SO_4$) at varying concentrations. To prevent the inhibition of water freezing and salt crystallization in unsaturated pores (Prause et al., 2019), the solution to pore volume ratio was maintained approximately 150% of the total pore volume of host materials ($V_{\mathrm{sol}} = V_{\mathrm{pore}} \times w_{\mathrm{host}} \times 1.5$). The thermal behavior of the confined solutions during freezing and melting was measured using a calorimeter, with a scanning rate of 0.1 $\mathrm{K \cdot min^{-1}}$ for both cooling and heating cycles. The temperature scanning begins at 25 °C and proceeds down to a final temperature between −50 °C to −150 °C, depending on the specific sample, for example, −50 °C for pure water and −150 °C for $Ca(ClO_4)_2$ solution.

Water vapor sorption analysis: To ensure complete loading of the solution into the pores, two−solvent method (Prause et al., 2019) was employed in the preparation of porous silica salt composites (PSSC). The porous silicas, with pore sizes ranging from 3.8–20.6 nm, were pre-dried at 200 °C for 48 hours to remove any adsorbed water molecules. After cooling to room temperature in the desiccator, a specific amount of solution, calculated based on the pore volume and the amount of host material ($V_{\mathrm{sol}} = V_{\mathrm{pore}} \times w_{\mathrm{host}} \times 0.95$), was added to approximately 200 mg porous silica. The concentration of the chlorides (KCl, $MgCl_2$, and $CaCl_2$), perchlorates ($NaClO_4$, $Mg(ClO_4)_2$, and $Ca(ClO_4)_2$), and $(NH_4)_2SO_4$ solutions are listed in the Table 7−1.

Table 7−1. Salt concentrations applied in the preparation of porous silica−salt composites.

Salt	KCl	$MgCl_2$	$CaCl_2$	$NaClO_4$	$Mg(ClO_4)_2$	$Ca(ClO_4)_2$	$(NH_4)_2SO_4$
m / $\mathrm{mol \cdot kg^{-1}}$	4.2	2.8	4.0	9.8	3.4	4.2	5.0

The pore filling degree was kept below 95% to avoid the presence of bulk solution outside the pores. The porous silica with aqueous solution was then dispersed in 5 mL *n*-hexane, and the milky mixture was shaken for 2 hours to ensure efficient mixing. Afterward, the silica−aqueous solution suspension was obtained by slow evaporation of the *n*-hexane at room temperature. Finally, the sample PSSCs were dried at 200 °C to constant weight.

After cooling to room temperature in a desiccator containing a silica gel drying agent, the dehydrated PSSCs were transferred to the water vapor analyzer (SPSx−1µ, ProUmid GmbH, Germany). The water vapor sorption data of approximate 50 mg PSSC samples were collected under controlled humidity conditions at 25 °C, with the relative humidity incremented by 1% over a range from 0% to 95%. At each humidity step, sorption equilibrium was considered achieved when the weigh change within 30 mins was less than 1.5%, with a maximum allowable time of 50 hours per step. Prior to each measurement, the PSSC samples were dried at 60 °C under a pure nitrogen atmosphere to remove any adsorbed water accumulated during sample preparation.

Raman spectroscopy: Raman spectra were recorded using a Senterra Raman dispersive microscope (Bruker Optics GmbH, Germany) equipped with an automated Raman frequency calibration system (SurCal technology) and a CCD detector. The system was coupled with a BX51 microscope fitted with Plan M 10× and LMPlanFL N 20× lenses (Olympus, Germany). The laser was operated at a wavelength of 532 nm (frequency doubled Nd:YAG laser) at 20 mW, with an integration time of 5 seconds per acquisition. Spectra were collected by summing up ten spectra at the same spot, covering the range from 1520–3700 cm^{-1} (co–addition mode). Temperature and relative humidity were controlled using a THMS600 stage (Linkam Scientific Instrument, UK). A continuous airflow with controlled RH at a rate of 500 mL·min^{-1} was provided by a humidity generator (MHG32, ProUmid GmbH, Germany), ensuring sufficiently rapid gas exchange rates and maintaining stable RH conditions inside the THMS600 stage. Liquid nitrogen was utilized to achieve sub–zero temperatures during the Raman spectroscopy measurements, with a cooling rate of 2 °C·min^{-1}. The spectra of $Ca(ClO_4)_2·4H_2O$, a $Ca(ClO_4)_2$ solution, $(NH_4)_2·SO_4$(cr), and an $(NH_4)_2·SO_4$ solution was examined over a temperature range from 25 °C to −100 °C to investigate their phase behavior under cryogenic conditions.

7.2 Results and Discussion

To better understand the phase behavior of salt solution under varying temperature and humidity, the bulk phase diagrams for all the measured binary salt solution are presented in Fig. 7–1.

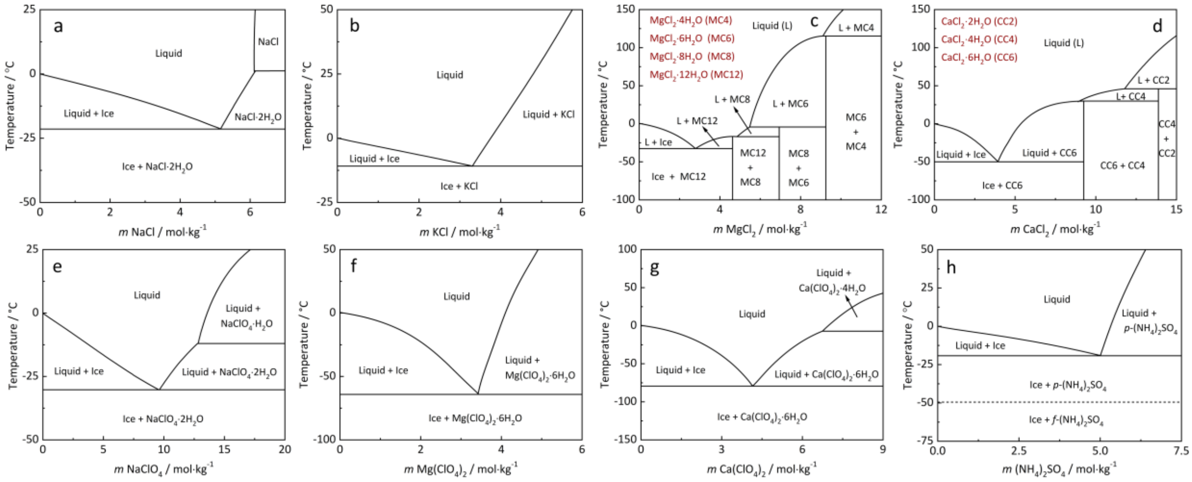

Figure 7–1. Phase diagram of the salt (NaCl, KCl, $MgCl_2$, $CaCl_2$, $NaClO_4$, $Mg(ClO_4)_2$, $Ca(ClO_4)_2$, and $(NH_4)_2SO_4$) + water systems, obtained by ion-interaction thermodynamic models. The configuration and parameters of the Pitzer model for the binary systems, NaCl–H_2O and $CaCl_2$–H_2O are presented in Section A1 and A2 of Appendix. The parameters of KCl–H_2O, $MgCl_2$–H_2O, and $(NH_4)_2SO_4$–H_2O have been reported in previous publications of our research group (Steiger et al, 2008a; Steiger et al., 2011; Talreja–Muthreja and Steiger, 2025), and the model parameters for the binary $NaClO_4$–H_2O system were taken from the molality-based model of Toner et al. (2016). For the binary alkaline earth perchlorate systems $Mg(ClO_4)_2$–H_2O and $Ca(ClO_4)_2$–H_2O, the mole fraction based models of Li et al. (2022) were used.

These diagrams illustrate the equilibrium solid phase during eutectic freezing and deliquescence transitions. Specifically, the salt corresponding to the eutectic points are $NaCl·2H_2O$, KCl, $MgCl_2·12H_2O$, $CaCl_2·6H_2O$, $NaClO_4·2H_2O$, $Mg(ClO_4)_2·6H_2O$, $Ca(ClO_4)_2·6H_2O$, and p-$(NH_4)_2SO_4$. For deliquescence at 25 °C, the corresponding salts are KCl, $MgCl_2·6H_2O$, $CaCl_2·6H_2O$, $NaClO_4·H_2O$, $Mg(ClO_4)_2·6H_2O$, and $Ca(ClO_4)_2·4H_2O$.

7.2.1 Melting behavior of pure water in confinement

Freezing and melting isotherms of ice in 8.1 nm SBA-15 as well as the melting isotherms of ice confined within porous silica materials with pore size ranging from 3.8–20.6 nm, are presented in Fig. 7−2a and Fig. 7−2b, respectively.

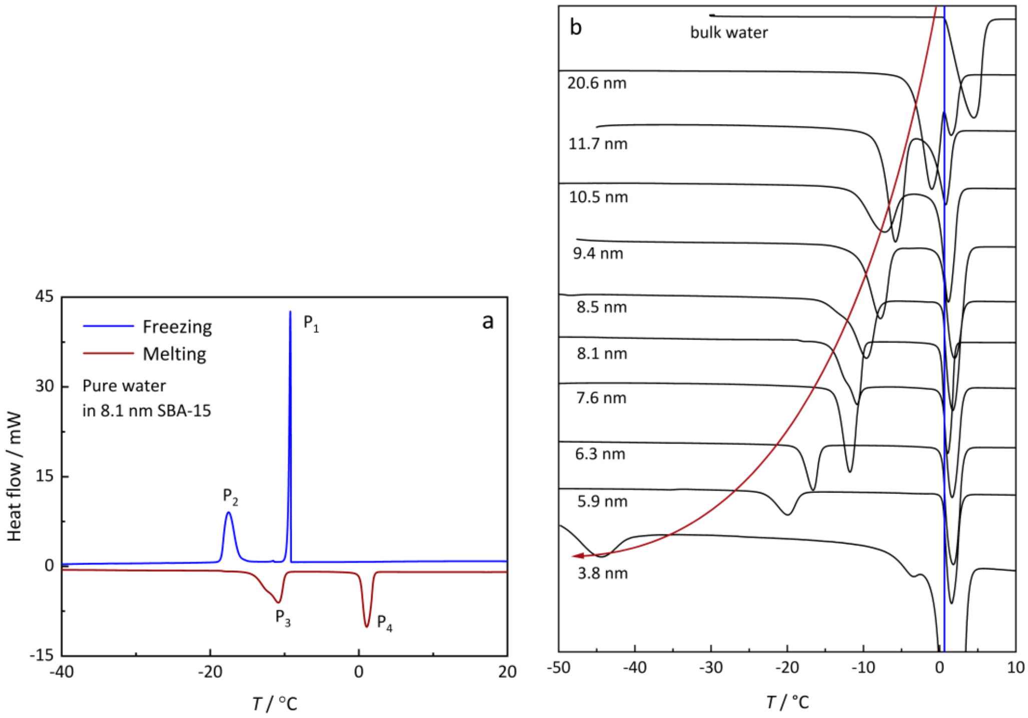

Figure 7−2. (a): Freezing and melting curves of ice in 8.1 nm SBA-15; (b): Melting curves of ice confined within nanopores of various diameters.

As described previously, all host materials were impregnated with excess solution, resulting in the formation of ice in both bulk phase and within the nanopores. Figure 7−2a shows two signals in both freezing (blue) and melting (red) curves, corresponding to phase transitions occurring in bulk phase (P_1 and P_4) and within the confined space (P_2 and P_3), respectively. Compared with the melting curve, the consistent shift of the observed transition to lower temperatures during the freezing process is attributed to the presence of a nucleation barrier, which delays the onset of ice formation. The melting point of bulk water was determined by the onset temperature of the endothermic peak, while for confined water, the peak maximum was used. This distinction arises because the shape of the melting peak for confined water is strongly influenced by the pore size distribution of host material, and the peak maximum corresponds to the most probable pore size as shown by Jähnert et al. (2008). In the thermograms of Fig. 7−2b, the peaks at higher temperature, labelled by the blue line, corresponds to the melting of bulk ice. These peaks consistently onset at approximately 0 °C and are independent of pore size. In contrast, the peaks on the left shift to lower temperatures as the pore diameter decreases, reflecting the stronger confinement effects in smaller pores.

The essence of the confinement effect lies in the influence of the interfacial molecules on the thermodynamic behavior of the entire system. Due to the loss of chemical bonding in the outward direction, the interfacial layers exhibit distinct thermodynamic properties compared to the interior (bulk−like) molecules. Therefore, a bulk material can be regarded as a combination of an interfacial layer and a bulk−like core. As illustrated in Fig. 7−3, the volume fraction of the interfacial molecules is negligible with only 0.24% for the large particle (e.g., 1 μm) but increases significantly as the particle size approaches the nanometer scale, reaching approximately 12% for a 20 nm particle and 42% for a 5 nm particle. This increase in the fraction of interfacial molecules leads to divergence in thermodynamic properties between nanoconfined systems and bulk phase.

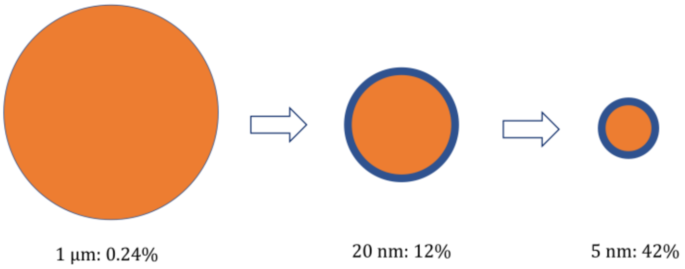

Figure 7−3. The volume fraction of an interfacial layer of thickness 0.6 nm (blue layer) in spherical particles with diameters 1 μm, 20 nm, and 5 nm.

In the experiments of this dissertation, ice melting signals were observed for all porous silica samples with pore size ranging from 3.8 nm to 20.6 nm. However, literature reports (Yoshida et al., 2008; Jähnert et al., 2008; Findenegg et al., 2008) indicate that when the pore size drops below approximately 2.5 nm, freezing and melting peaks are no longer detectable by differential scanning calorimetry (DSC). Furthermore, both melting enthalpy and the thermal hysteresis between freezing and melting decreases with decreasing pore size, eventually approaching to zero when extrapolated to around 2.8 nm (Kittaka, 2006; Findenegg et al., 2008). This loss of enthalpy and hysteresis is interpreted as evidence for the disappearance of first−order phase transition under extreme confinement (Findenegg et al., 2008). Furthermore, the suppressed freezing and melting transitions reflect the structural similarity between the liquid and solid phases of water within smaller pores at low temperatures. Interestingly, nuclear magnetic resonance (NMR) spin–echo measurements still reveal a transition from low to high water mobility even in pores as small as 2.5 nm, suggesting a form of melting despite the absence of a detectable thermal signal (Jähnert et al., 2008). This phenomenon is attributed to the dominant contribution of interfacial water molecules, which exhibit slower dynamics than the bulk–like core water but do not produce a conventional calorimetric signal.

7.2.2 Melting behavior of the frozen NaCl and CaCl₂ solution in confinement

In the Fig. 6–4 (Chapter 6), we presented the melting curves of the frozen NaCl and $CaCl_2$ solutions in porous silica at various initial concentrations. Here, their melting and eutectic points are compiled in the phase diagram of Fig. 7–4.

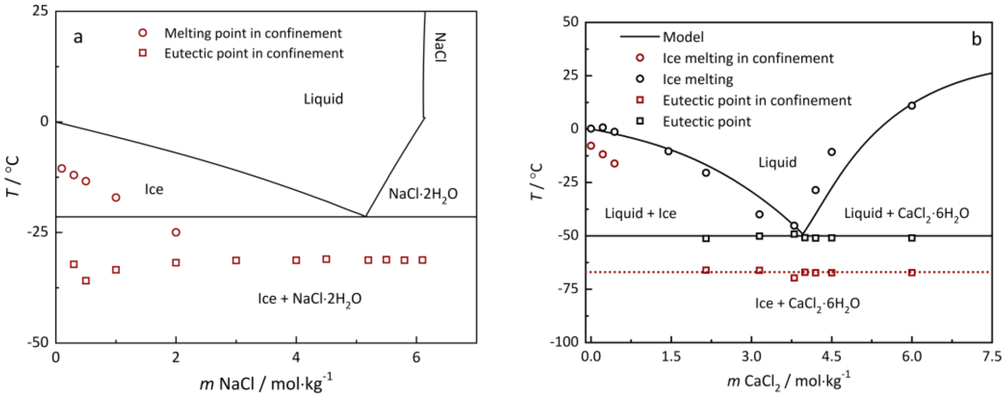

Figure 7–4. (a): Phase diagram of NaCl solution and its melting eutectic points in 8.5 nm SBA-15; (b): Phase diagram of $CaCl_2$ solution and its melting eutectic points in 9.4 nm SBA-15. peak maximum of the thermal signals was used to determine the melting and eutectic temperatures confined solutions, while the offset and onset of the thermal signals were used to determine the melting point and eutectic in the bulk solution.

For both systems, the confined solutions exhibit a clear downward shift in both melting and eutectic points relative its bulk phases. As expected, the depression of the eutectic temperatures in the nanopores is independent of concentration, underscoring the impact of confinement on the phase behavior of electrolyte solutions. As discussed in Chapter 6, the absence of a eutectic transition in dilute solutions can be explained by the redistribution of ions between the intra-pore and extra-pore solutions. This diffusion, coupled with the preferential accumulation of ions in the interfacial layer near the pore wall, alters the local composition and effectively suppress the eutectic crystallization pathway.

7.2.3 Eutectic points of frozen salt (NaCl, NaClO₄, MgCl₂, and CaCl₂) solutions in confinement

This study aims to investigate the lowest temperature at which liquid water or brine solutions can stably exist, which corresponds to the eutectic point. Thus, the confinement effect on eutectic transition of salt solution was examined more closely. Figure 7–5 presents the melting curves of 5.2 m NaCl and 9 m $NaClO_4$ solutions (bulk eutectic concentration) in silica materials of varying pore sizes. As with pure water, the eutectic point in the bulk phase is determined by the onset temperature of the melting peak, whereas for the confined solutions, the peak maximum is used due to peak broadening caused by the pore size distribution. As illustrated by the blue dashed lines in Fig. 7–5, the endothermic peaks at −20 °C correspond to bulk eutectic melting of NaCl solutions, whereas the bulk eutectic temperature of bulk $NaClO_4$ solution is observed at −33 °C. In both systems, additional peaks at temperatures lower than the bulk eutectic point, indicated by the red arrows, represent eutectic transitions occurring within nanopores. Similar with the phase behavior of confined pure water, the eutectic temperature decreases with decreasing pore diameter, and no eutectic transition is not detected in the pore of 3.8 nm. This absence is most likely attributable to the severe spatial constraints imposed on nucleation and subsequent crystal growth in such confined geometries.

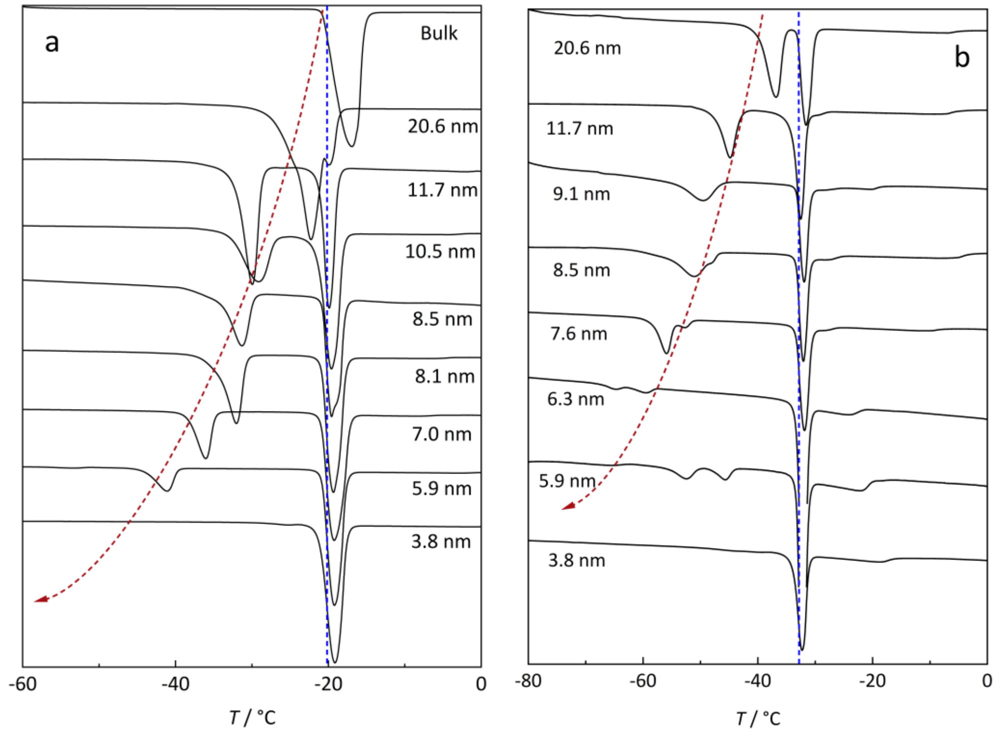

Figure 7–5. Melting curves of NaCl (a) and $NaClO_4$ (b) solutions confined within nanopores of various diameters, the corresponding solid phases at eutectic point are ice–$NaCl{\cdot}2H_2O$ and ice–$NaClO_4{\cdot}2H_2O$, respectively. Red dashed arrows: visual guide indicating the eutectic points in nanopores; blue dashed lines: eutectic points of the corresponding bulk solutions.

Comparing the melting temperatures in Fig. 7–2b and Fig. 7–5, the presence of NaCl and $NaClO_4$ enables the liquid phase to persist at lower temperature. This is because ion hydration destroys the local tetrahedral structure of cold water, which is a prerequisite for ice nucleation (Tu et al., 2019). Clearly, nanoconfinement also significantly affects the eutectic transition, a coupled process of ice formation and salt crystallization. An exception is observed in the 3.8 nm pore, where no thermal signals were detected below the bulk eutectic temperature. Only the bulk eutectic peak at −20 °C appears, indicating the absence of a first–order phase transition within the confined solution. This aligns with observed behavior of pure water in the literature, where freezing and melting transitions disappear below 2.5 nm pore diameters (Jähnert et al., 2008), though the critical threshold is slightly higher in the saline system. Molecular dynamics simulation by Chen et al. (2024) showed that the structure of dissolved ions in the saturated aqueous nanodroplet closely resembles the crystal structure of NaCl nanoparticles, with convergence occurring at 0.51 nm (Chen et al., 2024). This highlights the blurring of the boundary between liquid and crystalline phase at sub−nanometer scale. In this study, the extremely low temperatures further restrict molecules mobility and diffusion, inhibiting the occurrence of crystallization.

The pore size dependence of eutectic temperatures of $CaCl_2$ and $MgCl_2$ solutions is shown in Fig. 7−6. In both systems, the eutectic temperature decreases with decreasing pore size. Notably, eutectic transitions are no longer observed for $CaCl_2$ in the 5.9 nm pores and for $MgCl_2$ and the 3.8 nm pores, indicating a lower critical pore size for eutectic crystallization in the confined phase. An anomalous result is observed in the $MgCl_2$ solution in 11.7 nm SBA-15. In this case, the eutectic transition signal from the bulk phase is absent. Instead, a higher−temperature endothermic peak appears, likely corresponding to ice melting or salt dissolution within the pores (marked by the orange circle in Fig. 7−6b). This suggests that nearly all ions have aggregated and crystallized inside the pore, leaving insufficient salt in bulk phase to form a eutectic mixture. This behavior is likely influenced by strong supercooling during the freezing process. Supporting this interpretation, the corresponding freezing curve in Fig. 7−7a display a strong exothermic peak at −57 °C and a weaker peak at −51 °C corresponding to the eutectic freezing in the pore and in bulk phase, respectively, which are lower than the eutectic melting points of both bulk and confined solutions. This indicates the ice and salt crystallized simultaneously in both environments, rather than undergoing sequential crystallization as typically expected. The rapid freezing dynamics complicates the prediction of final salt distribution between bulk and confined phases. However, the thermal signature suggests that only a small amount, if any, of salt remained in the bulk phase.

In smaller pores, such as 5.9 nm SBA-15 for $CaCl_2$ solutions, the melting behavior closely resembles that of NaCl solution confined within 3.8 nm MCM-41, with only a single endothermic peak near the eutectic temperature of the bulk solution and a missing signal for the in-pore eutectic transition. This means that the missing eutectic is not only observed in dilute solutions and intermediate pore sizes but also in concentrated solutions and small pores. Similar observation was reported in the literature for other systems (Jantsch et al., 2019; Malfait et al., 2020).

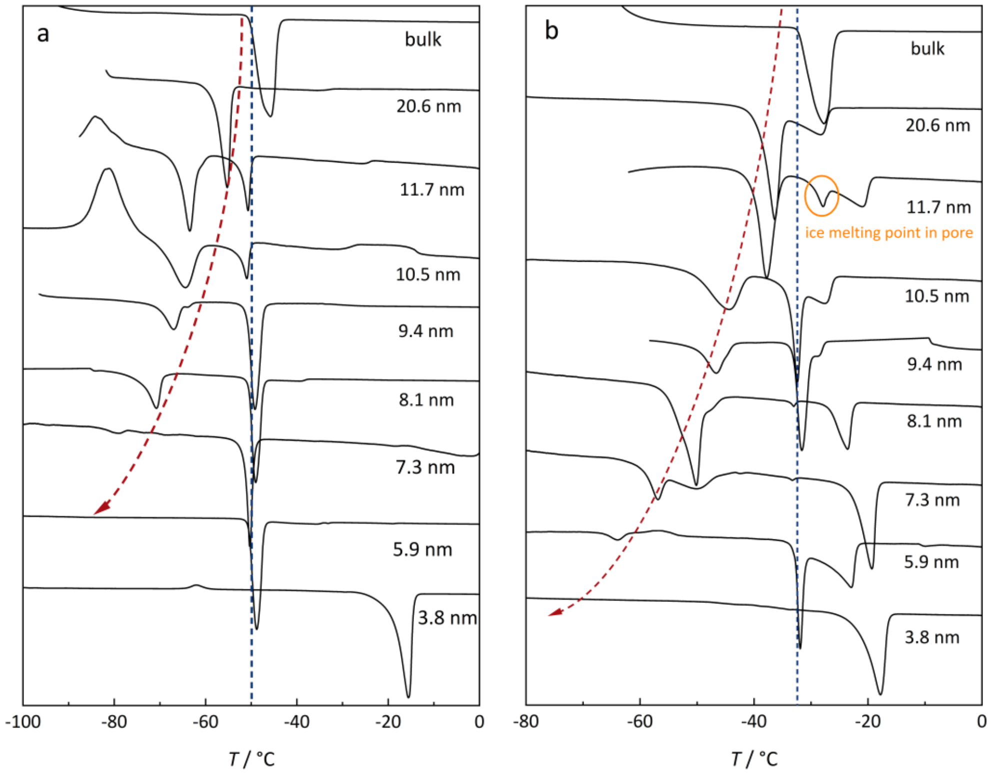

Figure 7–6. (a): Melting curves of a 4 m $CaCl_2$ solution confined in nanoporous silica of various pore size, the corresponding solid phases at eutectic point are ice and $CaCl_2{\cdot}6H_2O$; (b): Melting curves of a 2.8 m $MgCl_2$ solution under similar confinement conditions, the corresponding solid phases at eutectic point are ice and $MgCl_2{\cdot}12H_2O$. Red dashed arrows: visual guide indicating the eutectic points of $MgCl_2$ and $CaCl_2$ solutions in nanopores; blue dashed lines: eutectic points of the corresponding bulk solutions.

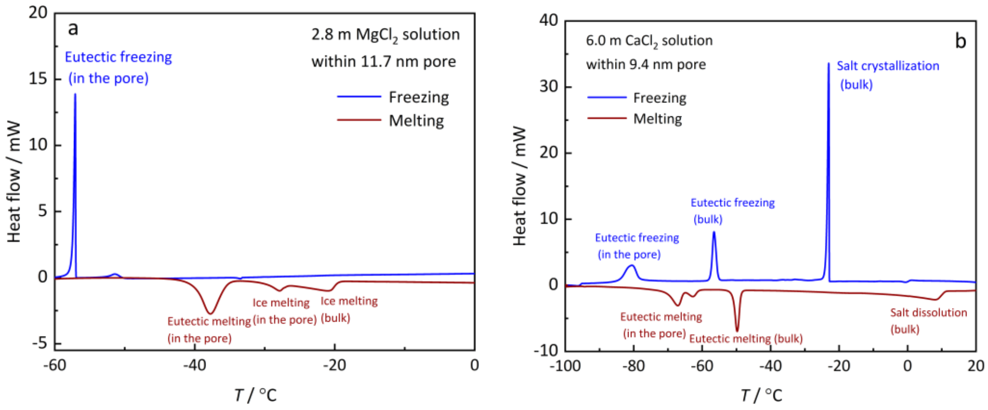

Figure 7–7. (a): Freezing curve of a 2.8 m $MgCl_2$ solution within 11.7 nm SBA-15; (b): Freezing and melting isotherms of a 6.0 m $CaCl_2$ solution within 9.4 nm SBA-15.

To assess the specific ion effect on phase behavior under confinement, Figure 7–8a compares the eutectic points of various salt solutions confined within 3.8–20.6 nm pores. In all systems, the eutectic temperatures decrease with decreasing pore size and are consistently lower than the melting point of pure water in pores of the same size. Notably, bulk $NaClO_4$ and $MgCl_2$ solutions exhibit similar eutectic melting temperatures (–33.3 °C and –32.0 °C, respectively), and their confined eutectic points are also comparable, as indicated by the blue and red squares. Figure 7–

8b summarizes the depression of the eutectic melting points (ΔT), defined as the difference between eutectic temperatures in bulk ($T_{\mathrm{m,bulk}}$) and in confinement (T_{m}), against pore size. While there is only a slight dependence on salt type for the same pore size, a clear trend still emerges for ΔT: H_2O < NaCl < $MgCl_2$/$NaClO_4$ < $CaCl_2$. This sequence indicates that salts with lower bulk eutectic points experience larger temperature depression when confined. Moreover, the minimum pore size at which a eutectic signal is detectable depends on the salt: 3.8 nm for NaCl, 5.9 nm for $MgCl_2$ and $NaClO_4$, and 7.3 nm for $CaCl_2$. Although the bulk eutectic points of these salts differ significantly, from −20 °C for NaCl to approximately −50 °C for $CaCl_2$, the lowest eutectic temperature reached in confinement converges between −60 °C and −70 °C.

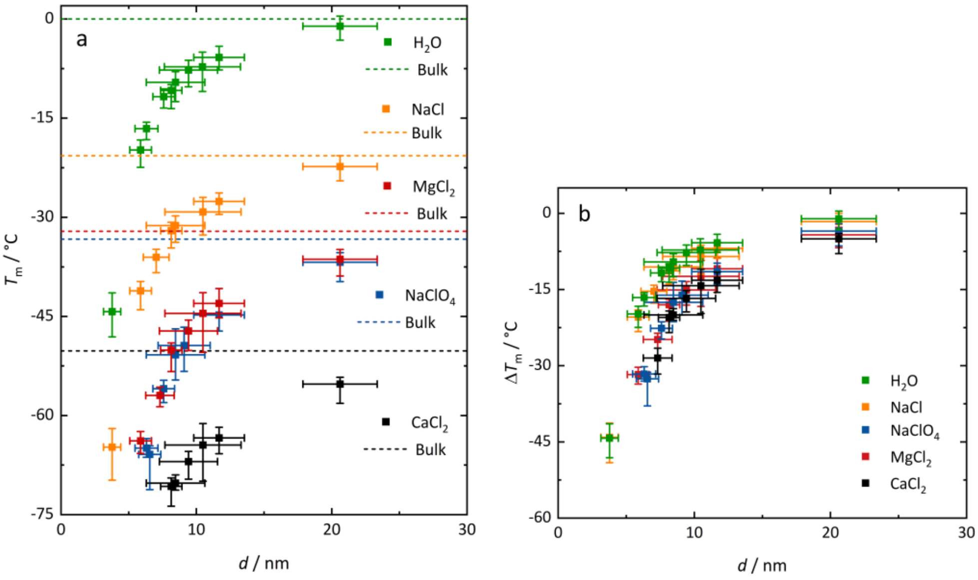

Figure 7–8. (a) Influence of pore size on the melting point of pure water and the eutectic points of salt solutions (NaCl, $MgCl_2$, $NaClO_4$, and $CaCl_2$); (b) temperature depression $\Delta T_{\mathrm{m}} = T_{\mathrm{m,bulk}} - T_{\mathrm{m}}$ of the melting and eutectic points (T_{m}) (right). Dashed line: the ice melting or eutectic points in bulk phase. The error bar of d represents the pore size distribution range of the host materials, while the error bar of T_{m} or ΔT_{m} denotes the difference between peak maximum and either the onset temperature (lower limit) or the offset temperature (upper limit) of the melting peak.

To date, no comprehensive theory fully accounts for the unique phase behavior of salt solutions under strong confinement. Here, we propose three possible interpretations for the observed suppression of eutectic transitions in small pores.

(1) **Convergence of interfacial layers:** It is well established that a nonfreezing water layer (approximately 0.6 nm thick) exists near the pore wall, exhibiting structural and thermodynamic behavior distinctly different from bulk-like water in the pore center. (Antoniou, 1964; Rennie and Clifford, 1977; Overloop and Vangerven, 1993; Jähnert et al., 2008). In salt solutions, this layer is likely thicker due to the presence of hydrated ions, ion pairs, and solvent–solute interactions. As pore size decreases, the two interfacial layers can overlap, effectively eliminating the bulk-like region and thus suppressing both

water freezing and salt crystallization, resulting in the missing of water freezing and salt crystallization, as illustrated in Fig. 7−9a. Supporting this, Wang et al. (2023b) observed a relatively homogenous radial ion distribution in 4 m $CaCl_2$ solutions within 4 nm MCM-41 using neutron scattering and Monte Carlo simulation, challenging the widely accepted electric double layer theory (Argyris et al., 2010; Israelachvili, 2011). However, the threshold pore sizes (3.8 nm and 5.9 nm for $MgCl_2$ and $CaCl_2$, respectively) are still too large to be fully explained by the overlap of interfacial layers alone, making this explanation insufficient on its own.

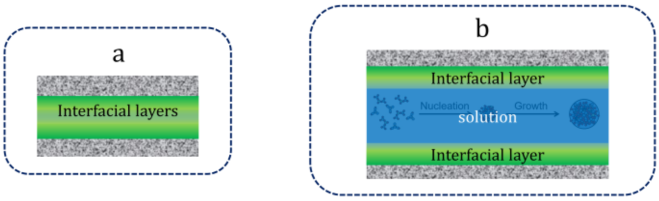

Figure 7−9. (a): The convergence of two interfacial layers within confined space disrupting the formation of a eutectic structure; (b): the spatial restriction within small pores suppresses the nucleation of eutectic phase.

(2) **Spatial restriction of nucleation**: Both ice formation and salt crystallization are nucleation-controlled process requiring the overcoming of an energy barrier. Classical nucleation theory describes a three-step pathway: initial monomer or cluster formation, diffusion, and growth to a stably nucleus (Mullin, 2001; Thanh et al., 2014). Transient nanocrystals may form but dissolve quickly unless they reach a critical size. Since nanocrystals have higher solubilities than their bulk counterparts, stable nuclei can only form when the surrounding solution is sufficiently supersaturated. For example, ice nuclei typically consist of approximately 100 molecules. Hydrated salt crystals, having more complex structures, may require even significantly larger nuclei. In confined space, as depicted in Fig. 7−9b, the available volume in the pore core may be insufficient to accommodate such nuclei, particularly for the hydrated salts like $CaCl_2{\cdot}6H_2O$. Thus, even without interfacial layer overlap, nucleation may be physically inhibited, preventing first−order phase transitions in pores below the critical size.

(3) **Transition into an amorphous phase**: An alternative explanation is that confined salt solutions do not crystallize due to spatial restriction or interfacial effects, but instead bypass crystallization entirely by undergoing a glass transition. Solution normally transforming into an amorphous solid during rapid cooling. The behavior of amorphous ice has been extensively studied, leading to a metastable phase diagram that includes supercooled water, amorphous (glassy) phases, and the so-called "no−man's land", where homogenous nucleation and crystallization become kinetically unfavorable (Angell, 2002). For pure water, the glass transition temperature at ambient pressure is

approximately −133 °C (Angell, 2002), significantly lower than the minimum melting points −70 °C observed in our confined salt solution systems. However, dissolved ions can significantly elevate the glass transition temperature depending on ion type and concentration. For example, bulk solutions of $CaCl_2$ and $MgCl_2$ solution, can exhibit glass transition temperatures as high as −110 °C and −100 °C, respectively, at high concentrations (Angell and Sare, 1970), as presented in Fig. 7−10. The influence of confinement on the glass transition of salt solutions is less well investigated and has not yet reached consistent conclusions. Available results from the literature show a weak confinement effect on the LiCl solution glass transition, but profound negative impact on that of NaCl solutions (Zhao et al., 2016; Longinotti et al., 2019). Hence, we take the glass transition temperature in confinement as the same as that of the bulk $CaCl_2$ and $MgCl_2$ solutions. Concerning the more pronounced supercooling effect in nanopores, as indicated by the freezing and melting curves of Fig. 7−7, it is logically that the supercooled brine can easily reach −100 °C if their melting temperature is below −70 °C and the direct transformation to an amorphous solid may be possible even in a slow cooling process. Supercooled pure water in a 2 nm mesoporous silica was proposed to form the low−density amorphous (LDA) ice (Erko et al., 2011). They analyzed the shift in the spectral position of the tetrahedral water cluster and the full width at half maximum (FWHM) in the Raman spectrum of water confined within pores ranging from 2.0 nm to 8.9 nm at multiple temperatures. It was found that the temperature dependence curve of bulk water locates in the extension of crystalline ice, and progressively shifts to the LDA ice with the decrease of pore size. It suddenly jumps to the extension of LDA ice curve in 2.0 nm pore. The presence of amorphous ice in strong confinement might be contributed to the missing of first−order phase transition, either for water or salt solution.

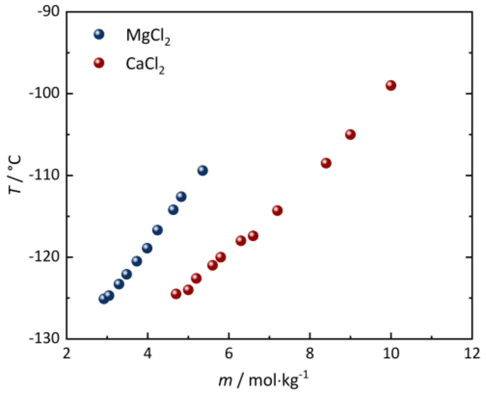

Figure 7−10. Glass transition temperatures of bulk $CaCl_2$ and $MgCl_2$ solutions as a function of salt concentration (data from Angel and Sare, 1970).

Combination of the influence of concentration and pore size: Previously, we discussed the influence of spatial confinement on the eutectic temperatures of various salt solutions and found that the temperature depression caused by confinement shows no clear ion-specific effects despite their bulk eutectic temperatures spanning a wide range. In this section, we extend the investigation by incorporating the role of salt concentration, focusing on its combined effect with pore size on the melting behavior of confined salt solutions. Figure 7−11 presents the melting curves of $CaCl_2$ solutions with molalities 0.4 m and 0.8 m, respectively, confined in pores with diameters ranging from 5.9–20.6 nm. Overall, the two sets of data exhibit consistent trends. Specifically, for pore sizes below 11.7 nm only two endothermic peaks are observed in each melting curve, one at higher temperature corresponding to the melting point of the bulk solution (indicated by the blue lines), and one at a lower temperature corresponding to the melting in confinement (indicated by red arrows). Notably, the eutectic transition peak is only observed in the 20.6 nm pore and the bulk solution. It is completely absent in the smaller pores for both concentrations. These results underscore that both pore size and salt concentration influence the phase behavior of confined solutions and that a critical combination of these parameters is required for eutectic crystallization to occur.

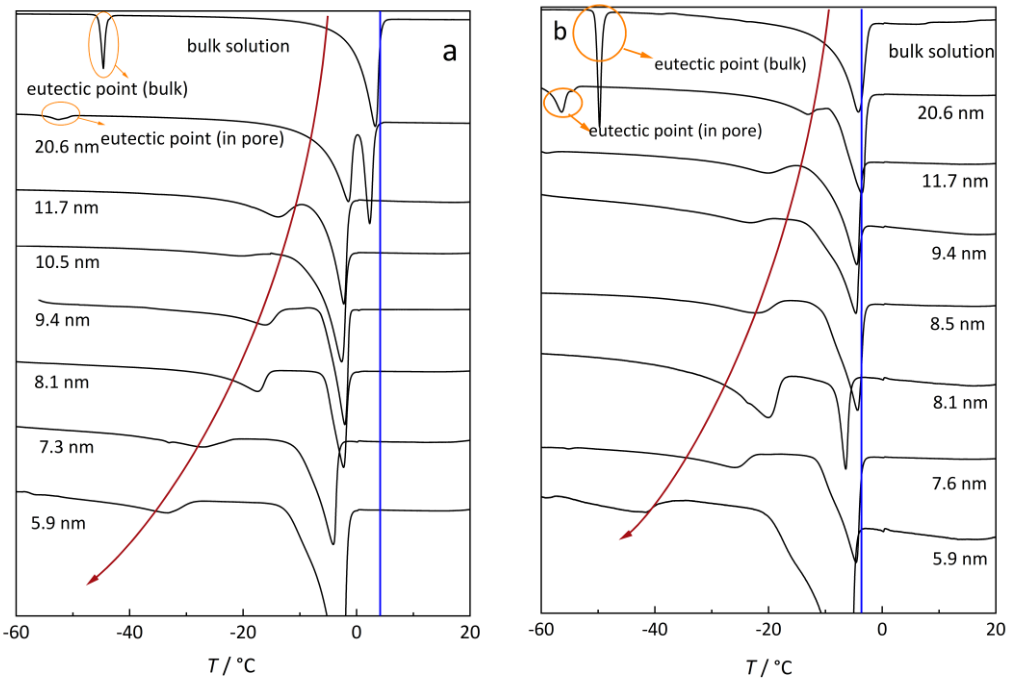

Figure 7−11. Melting curves of $CaCl_2$ solution with molalities 0.4 m (a) and 0.8 m (b) confined in mesoporous silica with pore diameters ranging from 5.9 nm to 20.6 nm. The red arrows indicate the melting points of ice within confined $CaCl_2$ solutions, while the blue line marks the melting point of ice in the corresponding bulk $CaCl_2$ solution.

The melting points of the confined 0.4 m and 0.8 m solutions are plotted in Fig. 7−12a, alongside the size dependent eutectic points measured at 4.0 m. As shown, the ice melting points of the confined solutions decrease with decreasing pore size, consistent with the trend observed for eutectic points. Notably, even in the smallest pores, the ice melting point remains significantly higher than the eutectic temperature of the bulk solution, indicating that salt molality exerts a stronger influence on the melting point than confinement alone. The temperature depressions due to confinement, plotted as a function of pore size in Fig. 7−12b, further emphasize the concentration effect that higher salt molality results in greater temperature depression.

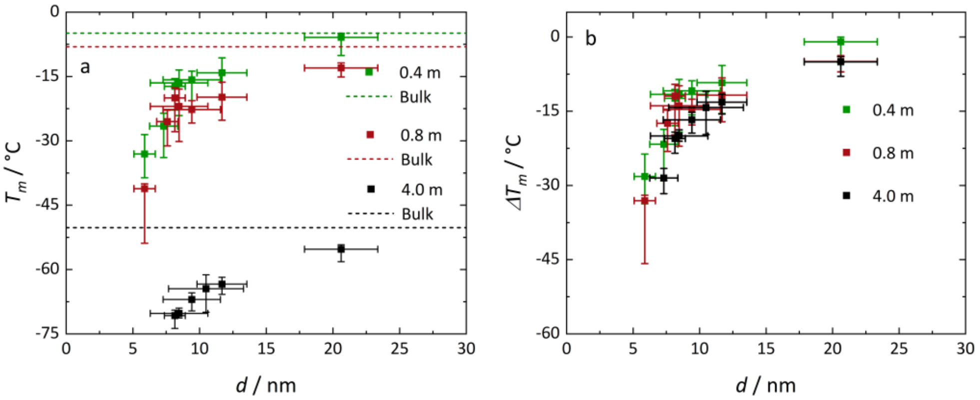

Figure 7−12. (a): Influence of pore size on the ice melting temperature in $CaCl_2$ solutions; (b): Temperature depression caused by confinement effects. Dashed line: meting/eutectic points of ice in bulk $CaCl_2$ solutions. The error bar of d represents the pore size distribution range of the host materials, while the error bar of T_m or ΔT_m denotes the difference between peak maximum and either the onset temperature (lower limit) or the offset temperature (upper limit) of the melting peak.

The origin of this effect likely stems from changes in the interfacial energy between ice and salt solution. Previously, we attributed the confinement-induced thermodynamic property changes to the unique behavior of interfacial molecules. This influence on chemical equilibria can be described by the thermodynamic variable interfacial energy (γ), which is sensitive to both temperature and salt molality. Theoretically, lower temperatures and lower concentrations of dissolved electrolytes favor the stability of tetrahedral water clusters, resulting in structural similarity between ice and the surrounding solution. Consequently, the interfacial energy of ice and solution is relatively low in dilute solution. According to the Gibbs−Thomson equation, higher interfacial energy leads to greater melting point depression, which aligns to the observed concentration−dependent temperature depression(ΔT_m) in Fig. 7−12b.

7.2.4 Freezing and melting behavior of $Ca(ClO_4)_2$ and $Mg(ClO_4)_2$ solutions in confinement

Raman spectra of calcium perchlorate solutions and its solid hydrates: Perchlorate solutions are known to be effective glass formers, readily transitioning to a glassy state at low temperature even under slow cooling conditions (Tu et al., 2019). As shown in Fig. 7−13a, the freezing and melting isotherms of a 0.5 m $Ca(ClO_4)_2$ solution exhibit only the thermal signals associated with water freezing and melting. In contrast, the eutectic transition signal is not observed at the expected temperature of approximately −75 °C. Initially, it was speculated that ice formation in this dilute solution might serve as a nucleation site to trigger the eutectic crystallization. However, the experimental results demonstrate that ice alone is insufficient to initiate the simultaneous crystallization of both ice and salt. Hence, the eutectic solution is likely to transform to a glassy phase instead of crystallization. However, the eutectic transition was clearly observed in the calorimetric measurement of the wet solid phase of $Ca(ClO_4)_2$ and its saturated solution, as illustrated in Fig. 7−13b. Peaks P_1 and P_2 are likely associated with the crystallization of two distinct hydrates: $Ca(ClO_4)_2{\cdot}4H_2O$ and $Ca(ClO_4)_2{\cdot}6H_2O$, respectively, while peak P_3 corresponds to the eutectic freezing. Due to the difficulty in nucleation, the induced-time of calcium perchlorate crystallization is longer than expected, resting in the eutectic freezing occurring in the heating cycle. Upon further melting, the eutectic melting is observed at −74.8 °C (P_4) followed by the completion of the dissolution of the crystalline salt marked by P_5. These results indicate that the presence of crystalline calcium perchlorate hydrates can successfully trigger eutectic crystallization. In contrast, the absence of such a transition in the 0.5 m $Ca(ClO_4)_2$ solution suggests that the nucleation barrier for $Ca(ClO_4)_2{\cdot}6H_2O$ is higher than that for ice.

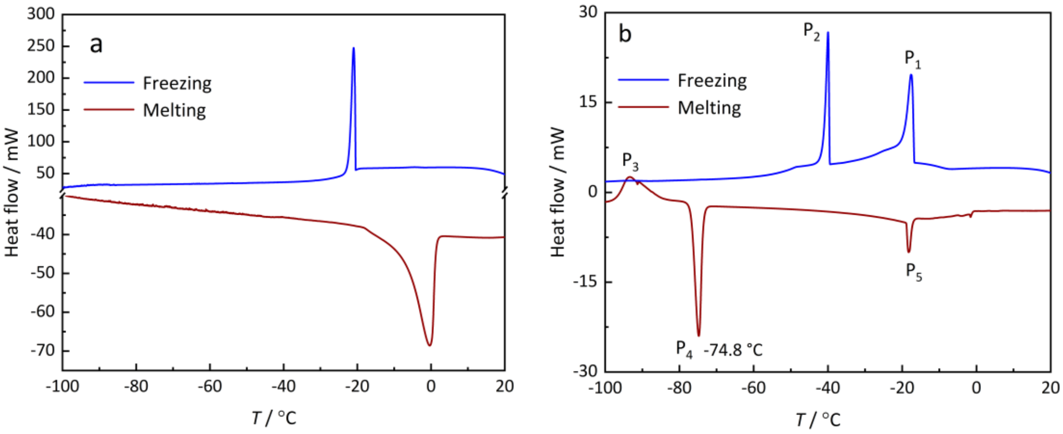

Figure 7−13. Freezing and melting curves of the 0.5 m $Ca(ClO_4)_2$ solution (a) and saturated (at 25 °C) $Ca(ClO_4)_2$ solution (b).

To further investigate the phase behavior during the cooling process, a series of temperature−dependent Raman spectroscopy experiments were conducted on $Ca(ClO_4)_2{\cdot}4H_2O$ and $Ca(ClO_4)_2$ solutions. As indicated in Fig. 7−14, there is only a slight change in the ClO_4^- vibration mode of $Ca(ClO_4)_2{\cdot}4H_2O$ from 951 cm^{-1} at 20 °C to 952 cm^{-1} at −100 °C. In the O−H stretching region (3000−3750 cm^{-1}), significant spectral changes occur below −40 °C, where three new peaks emerge at 3440, 3514, and 3629 cm^{-1}, consistent with previously reported low−temperature spectra (Fisher et al., 2014). As shown in Fig. 7−15a, the crystal morphology of $Ca(ClO_4)_2{\cdot}4H_2O$ remains unchanged with decreasing temperature, maintaining a flat crystal surface. The spectra of 2.5 m and 6.3 m $Ca(ClO_4)_2$ solutions at various temperatures are displayed in Fig. 7−16 and Fig. 7−17, respectively. Compared with $Ca(ClO_4)_2{\cdot}4H_2O$, the ClO_4^- vibration mode in the solution phase appears at lower wavenumber (935 cm⁻¹), shifting slightly to (936 cm⁻¹) upon the crystallization of a calcium perchlorate hydrate at low temperatures. In the O−H stretching region 3000−3750 cm⁻¹, both solutions exert a distinct set of Raman peaks at low temperature at 3380, 3454, 3478, 3518, and 3544 cm⁻¹, respectively. The latter four peaks correspond closely to those of $Ca(ClO_4)_2{\cdot}4H_2O$ though with different relative intensity, while the 3380 cm⁻¹ peak is unique and indicative of a different hydrate form. Notably, the peaks at 3608 and 3629 cm⁻¹ observed in $Ca(ClO_4)_2{\cdot}4H_2O$ are absent in the spectra of the solutions, further confirming that the formed hydrate is not the tetrahydrate. Therefore, the observed spectral features support the formation of $Ca(ClO_4)_2{\cdot}6H_2O$, which has been suggested in previous studies (Hennings et al., 2014; Fisher et al., 2014; Li et al., 2022).

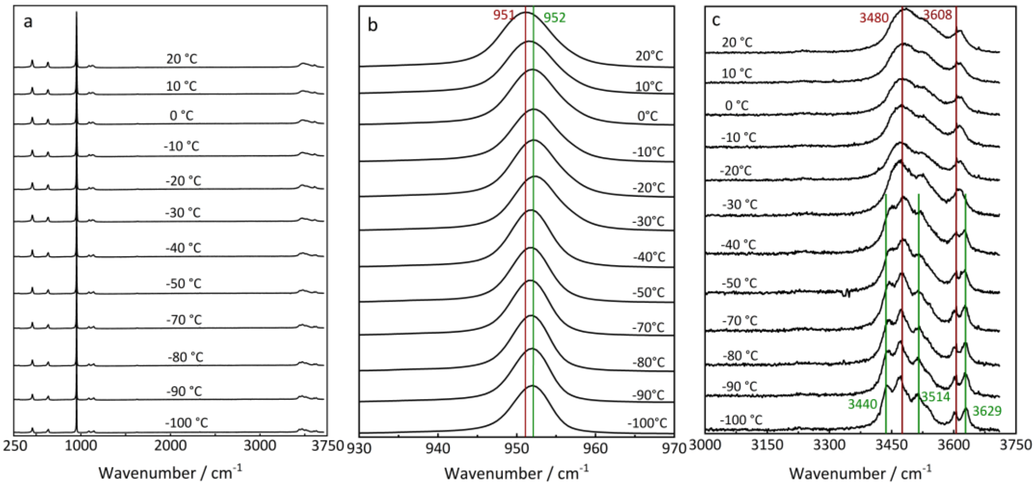

Figure 7−14. Temperature-dependent Raman spectra of $Ca(ClO_4)_2{\cdot}4H_2O$ collected over a temperature range from −100 °C to 20 °C. (a): Full spectral range: (b): Expanded view of the ClO_4^- symmetric stretching region; (c): Expanded view of the O−H stretching region, highlighting changes in hydrogen bonding environments.

As the micrographs in Fig. 7−15b show, crystallization in the 2.5 m $Ca(ClO_4)_2$ solution begins between −50 °C and −60 °C, consistent with the spectral features presented in Fig. 7−16. Interestingly, the characteristic Raman peak of ice at approximately 3150 cm⁻¹ is absent in the spectrum of this solution, despite its concentration being below the eutectic concentration. This absence is likely due to partial evaporation during the measurements, which could increase the salt concentration to above the eutectic composition, potentially reaching the solubility limit. In contrast, in the 6.3 m solution, the crystallization of $Ca(ClO_4)_2{\cdot}6H_2O$ appears near 0 °C, as illustrated in Fig. 7−15c and Fig. 7−17. At this temperature, the Raman spectrum exhibits a single prominent O−H stretching peak at 3544 cm⁻¹. This behavior indicates that, similar to $Ca(ClO_4)_2{\cdot}4H_2O$, $Ca(ClO_4)_2{\cdot}6H_2O$ exhibits distinct spectral characteristics at room temperature, suggesting a structural transformation or reorganization of hydrate upon cooling.

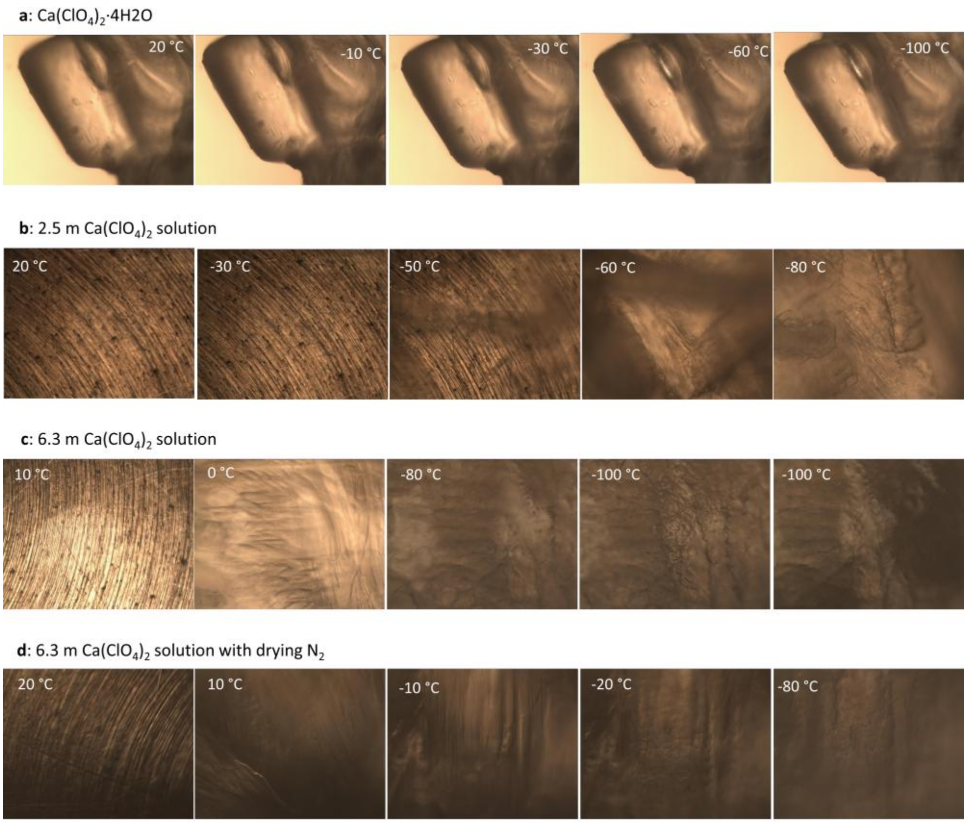

Figure 7−15. Raman micrographs of $Ca(ClO_4)_2{\cdot}4H_2O$ (a) and $Ca(ClO_4)_2$ solutions (b–d) over a temperature range from −100 °C to 20 °C.

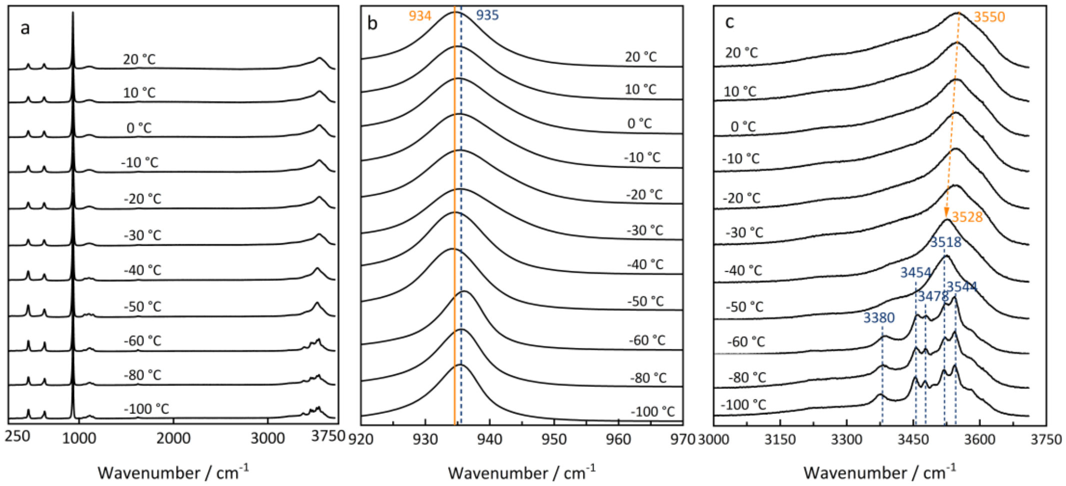

Figure 7−16. Temperature-dependent Raman spectra of a 2.5 m $Ca(ClO_4)_2$ solution collected over a temperature range from −100 °C to 20 °C. (a): Full spectral range: (b): Expanded view of the ClO_4^- symmetric stretching region; (c): Expanded view of the O−H stretching region, highlighting changes in hydrogen bonding environments.

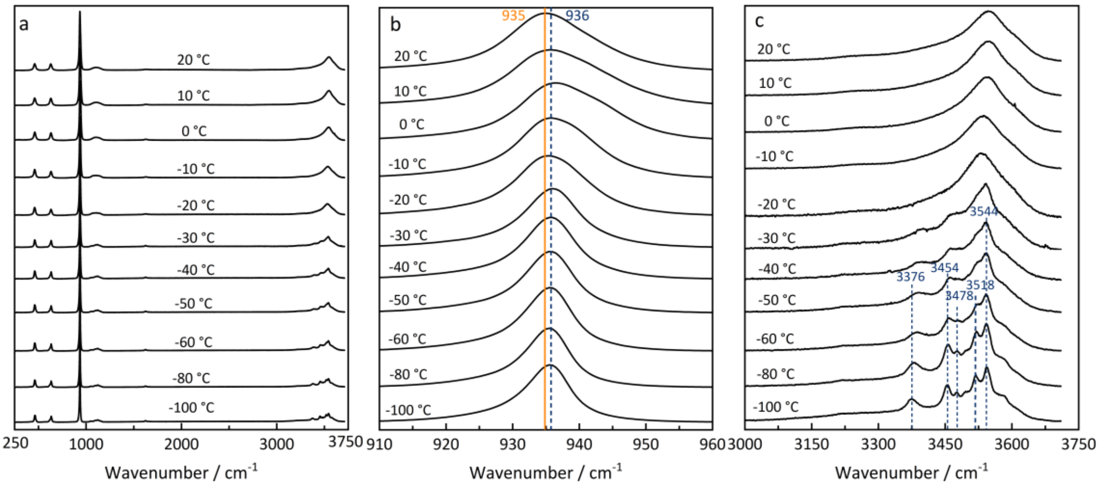

Figure 7−17. Temperature-dependent Raman spectra of a 6.3 m $Ca(ClO_4)_2$ solution collected over a temperature range from −100 °C to 20 °C. (a): Full spectral range: (b): Expanded view of the ClO_4^- symmetric stretching region; (c): Expanded view of the O−H stretching region, highlighting changes in hydrogen bonding environments.

In separate Raman measurements with the 6.3 m of $Ca(ClO_4)_2$ solution, a constant flow of dry N_2 was introduced throughout the cooling process. This setup promoted gradual evaporation, resulting in an increase of solute concentration and crystallization at higher temperature. As shown in the micrographs in Fig. 7−15d, salt crystallization now begins at approximately 10 °C, in agreement with the spectrum presented in Fig. 7−18. Upon crystallization, the ClO_4^- vibration mode shifts from 935 cm^{-1} to higher wavenumber, accompanied by the emergence of two shoulders at 3480 and 3608 cm^{-1} in the O−H stretching region. These spectral changes signify the formation of $Ca(ClO_4)_2{\cdot}4H_2O$. At −10 °C, the spectrum fully transitions to that characteristic of the tetrahydrate, with the ClO_4^- peak shifting to 952 cm^{-1} and the O−H stretching region (3000−3750 cm^{-1}) exhibiting all the signature features of $Ca(ClO_4)_2{\cdot}4H_2O$.

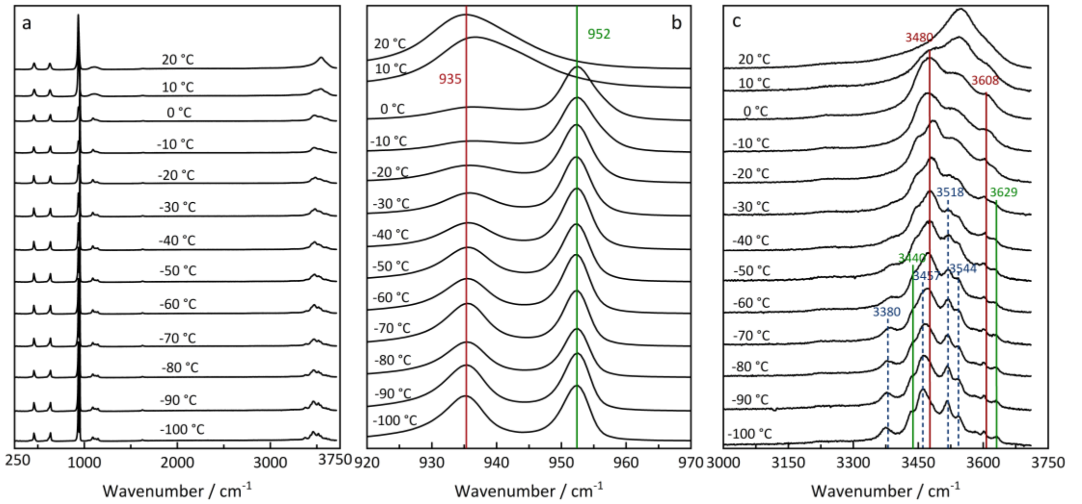

Figure 7−18. Temperature-dependent Raman spectra of a 6.3 m $Ca(ClO_4)_2$ solution exposed to dry N_2 atmosphere, collected over a temperature range from −100 °C to 20 °C. (a): Full spectral range: (b): Expanded view of the ClO_4^- symmetric stretching region; (c): Expanded view of the O−H stretching region, highlighting changes in hydrogen bonding environments.

Notably, the Raman peak (Fig. 7−18b) at 935 cm^{-1} reappears below −30 °C and increases in intensity as the temperature decreases. Concurrently, characteristic peaks of $Ca(ClO_4)_2{\cdot}6H_2O$ appear in the O−H stretching region, particularly the distinct peak at 3380 cm^{-1}. This spectral evolution indicates a transformation from $Ca(ClO_4)_2{\cdot}4H_2O$ to $Ca(ClO_4)_2{\cdot}6H_2O$, while the persistent presence of the 952 cm^{-1} suggests that the transition is incomplete. Supporting this, the morphological changes captured in Fig. 7−15d, from flat surfaces at 10 °C to pleated crystals at −80 °C, further reflecting the hydrate phase transition.

It is also noteworthy that the expected Raman signal for ice, near 3150 cm^{-1}, was not detected in any of the solution samples, including both 2.5 m and 6.3 m concentrations. This is surprising, given that the theoretical eutectic point of $Ca(ClO_4)_2$ solution (−75 °C) falls within in our investigated temperature ranges (−100 °C to 20 °C). In principle, the precipitation of $Ca(ClO_4)_2{\cdot}6H_2O$ could serve as a nucleation site to trigger eutectic crystallization and overcome the nucleation barrier for ice. However, no such eutectic transition was observed in the Raman experiments. As a result, the solution appears to remain in a supercooled state, with no detectable ice crystallization. While the coexistence of salt crystals and a supercooled solution seems thermodynamically inconsistent, an alternative explanation could involve complete evaporation of water during the cooling process, leaving only hydrates behind. Nevertheless, distinguishing whether liquid water persists at −100 °C remains challenging, as neither Raman spectral nor optical micrographs provide definitive evidence.

Calorimetric thermogram of $Ca(ClO_4)_2$ and $Mg(ClO_4)_2$ solutions: The calorimetric measurements of $Mg(ClO_4)_2$ solutions are presented in Fig. 7−19. As shown in Fig. 7−19a, the freezing curve of the 0.5 m bulk solution displays only one exothermic peak, corresponding to the freezing of water (ice formation). Interestingly, an additional exothermic signal appears at −67 °C in the melting curve, which is attributed to delayed eutectic freezing. This is followed by an endothermic peak at −57 °C, corresponding to the eutectic melting of $Mg(ClO_4)_2{\cdot}6H_2O$ in bulk solution. Theoretically, the eutectic freezing should occur during the cooling cycle. However, its appearance in the heating cycle implies that the nucleation of $Mg(ClO_4)_2{\cdot}6H_2O$ is kinetically hindered and requires a longer induction time than expected. A similar delay in eutectic freezing was observed in the measurements of the 4.2 m solution, as shown in Fig. 7−19b. Further insights into the phase behavior of the 4.2 m $Mg(ClO_4)_2$ solution in porous silica are shown in Fig. 7−19c and Fig. 7−19d. The eutectic transition temperature shifts to −63 °C in 20.6 nm pore and is further depressed to −73 °C in a 10.4 nm pore, indicating that confinement enhances supercooling and suppresses eutectic crystallization temperature.

In comparison to $Ca(ClO_4)_2$ thermogram in Fig. 7−13, eutectic transitions were clearly detected in the calorimeter measurements of both bulk and confined $Mg(ClO_4)_2$ solutions, although, notably, the eutectic freezing anomalously appeared during the heating cycle. This delayed crystallization highlights the strong supercooling tendency of perchlorate solutions, which renders the transition to the crystalline phase highly unpredictable. In more confined systems with smaller pore sizes, the calorimetric signals expected for eutectic transitions in $Mg(ClO_4)_2$ solutions were absent, further emphasizing the experimental challenge of capturing eutectic events in the two systems. To address this limitation, the melting temperatures of ice in less concentrated $Ca(ClO_4)_2$ and $Mg(ClO_4)_2$ solutions confined within nanopores were instead measured, as they typically remain detectable despite confinement. These melting points offer an alternative route to estimate the influence of confinement on the phase equilibria of perchlorate solutions.

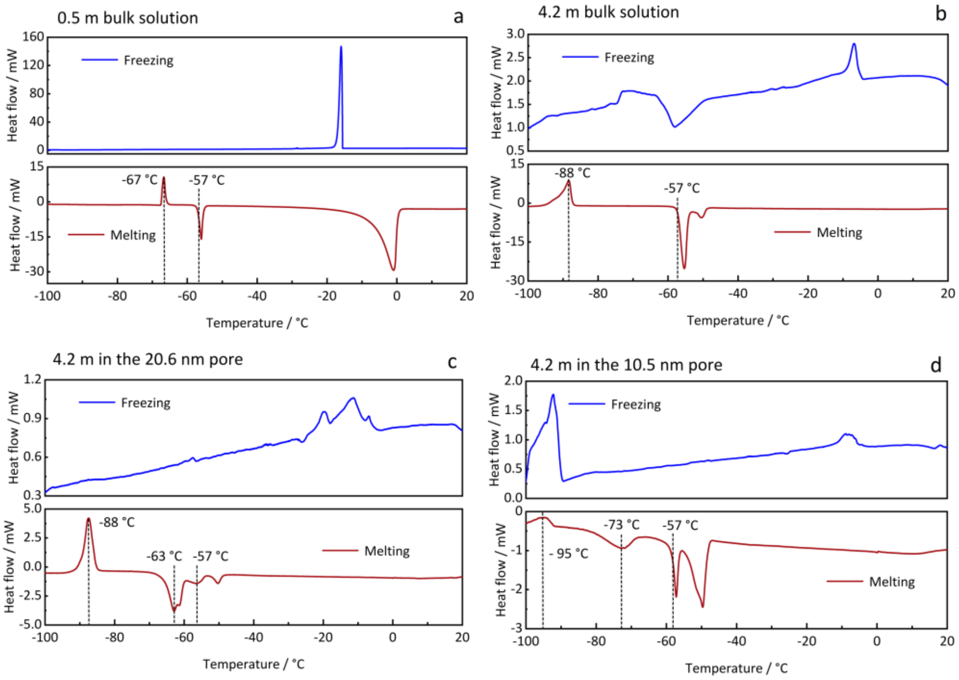

Figure 7−19. Freezing and melting curves of the $Mg(ClO_4)_2$ solutions in bulk and confinement.

The melting curves of the $Ca(ClO_4)_2$ solutions with molalities ranging from 0.1 to 2.0 m in nanopores with diameters of 5.9, 7.6, and 9.1 nm are presented in Fig. 7−20, while corresponding measurements for confined $Mg(ClO_4)_2$ solutions are shown in Fig. 7−21. In both systems, the ice melting points exhibit a downward trend with increasing salt concentration and decreasing pore size, as highlighted by the red and blue arrows in these figures. Notably, in the smallest pores (shown in Figs. 7–20a and 7–21a), the range of concentrations where ice melting is detectable becomes significantly narrower. This observation suggests that strong confinement not only lowers the melting temperature but also increasingly inhibits ice nucleation, making it more difficult for ice to form under high salinity and nanoscale confinement.

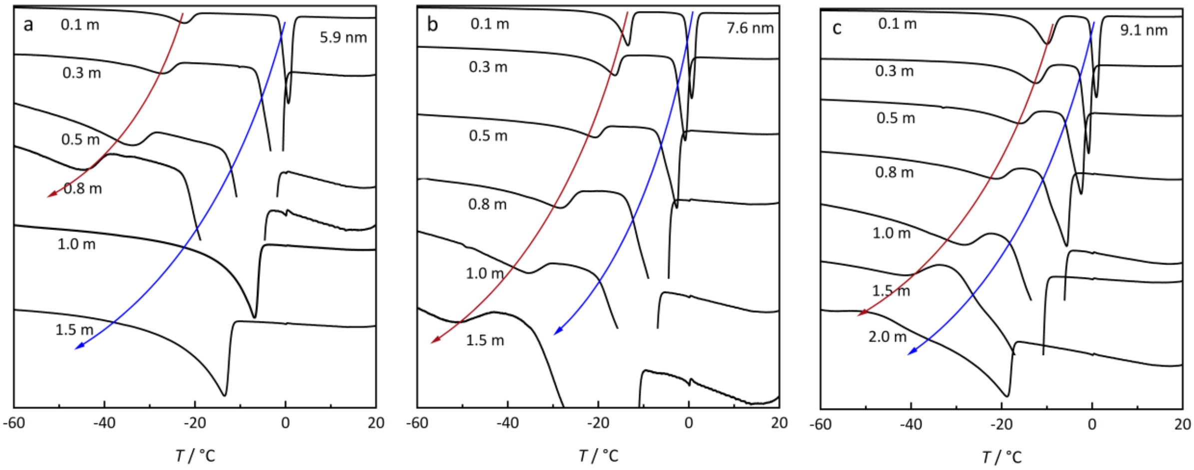

Figure 7−20. Melting curves of the $Ca(ClO_4)_2$ solutions confined in nanopores (5.9 nm, 7.6 nm, and 9.1 nm) at various concentrations. Red arrows: visual guides indicating the ice melting points of $Ca(ClO_4)_2$ solution in nanopores; blue arrows: visual guides for the ice melting points in bulk $Ca(ClO_4)_2$ solutions.

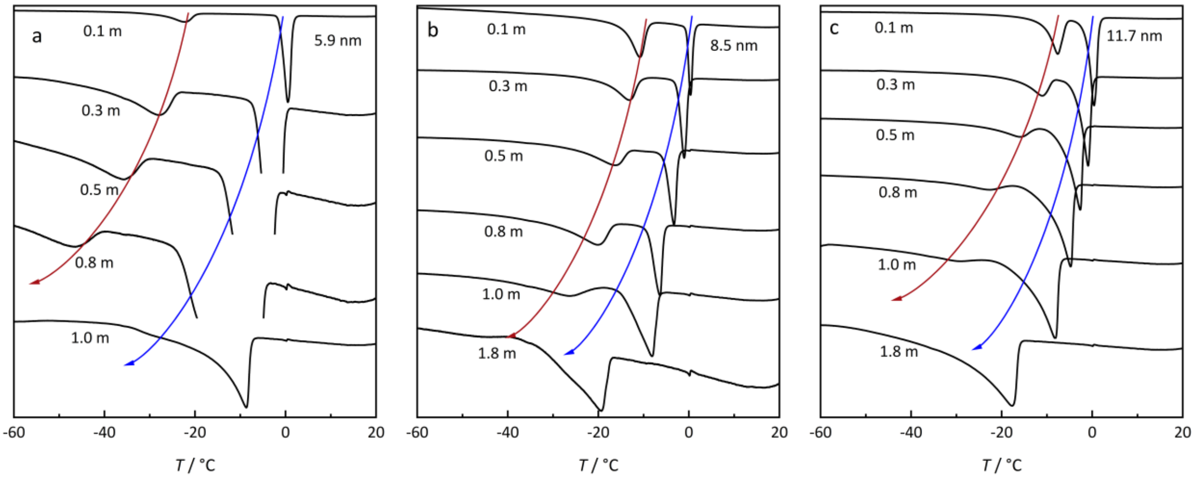

Figure 7−21. Melting curves of the $Mg(ClO_4)_2$ solutions confined in nanopores (5.9 nm, 8.5 nm, and 11.7 nm) at various concentrations. Red arrows: visual guides indicating the ice melting points of $Mg(ClO_4)_2$ solution in nanopores; blue arrows: visual guides for the ice melting points in bulk Mg $(ClO_4)_2$ solutions.

The measured ice melting points of $Ca(ClO_4)_2$ and $Mg(ClO_4)_2$ solutions are summarized in Fig. 7−22a and Fig. 7−22b. For both salts, the melting points of bulk solutions align well with published phase diagrams (Li et al., 2022). In the case of $Ca(ClO_4)_2$, the melting points systematically decrease with decreasing pore size, indicating a consistent confinement effect. In contrast, the melting points of $Mg(ClO_4)_2$ solutions in 11.7 nm and 8.5 nm pores nearly overlap and even intersect, suggesting a less pronounced size dependence. As shown in Fig. 7−21, the endothermic peaks for confined $Mg(ClO_4)_2$ solutions are notably broad (highlighted by red arrows), leading to a greater uncertainty in identifying the exact melting temperatures. This broadness likely masks any subtle melting point variations between different size pores. Additionally, the eutectic point for bulk $Mg(ClO_4)_2$ solutions observed in our calorimetric experiments (Fig. 7−19a and b) is −57 °C, obviously higher than the −63 °C predicted by the thermodynamic model of Li et al. (2022). This discrepancy stems from the modeling parameters being derived primarily from freezing points and solubility data reported by Pestova et al. (2005) and Toner et al. (2015b), where the eutectic point was not directly measured. Instead, these authors inferred the liquid–solid phase boundaries based on visual observation of ice or salt crystallization. Consequently, the eutectic point at −63 °C is an extrapolated intersection of regressed melting and solubility data, rather than an experimentally verified thermodynamic equilibrium point. As their criterion for the equilibrium is the presence of a crystalline phase, which may be affected by nucleation hysteresis, their result is not a realistic reflection of the thermodynamic equilibrium. On the other hand, the visual method is significantly influenced by the subjective factor of the observer. In fact, Stillman and Grimm (2011) have pointed out that the data from Pestova et al. significantly overestimated the eutectic point due to pronounced supercooling. They determined the eutectic temperature of $Mg(ClO_4)_2$ solution to be 216 K (−57 °C) using both calorimetry and electric permittivity measurement, with the transition point clearly observed during heating. Given the consistency and reproducibility of our calorimetric results and the results reported by Stillman and Grimm, we consider −57 °C to be the true eutectic temperature of $Mg(ClO_4)_2(aq)$.

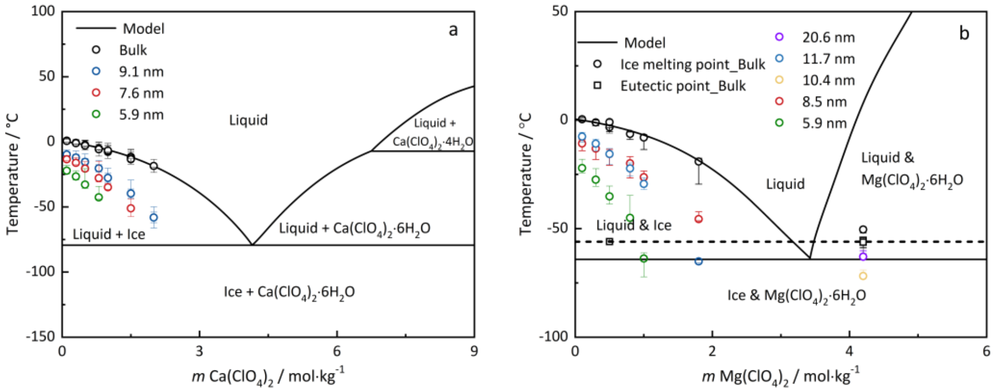

Figure 7–22. Ice melting points of $Ca(ClO_4)_2$ (a) and $Mg(ClO_4)_2$ (b) solutions confined within in the nanoporous silica. Black curves: phase boundaries calculated using thermodynamic model of Li et al. (2022). The error of temperature denotes the difference between the peak maximum and either the onset temperature (lower limit) or the offset temperature (upper limit) of the melting peak.

Despite acknowledging these discrepancies, Toner et al. (2015b) did not question their estimate of the eutectic temperature. Instead, they attributed the higher experimental value to the possible formation of an unidentified $Mg(ClO_4)_2$ hydrate while arguing that the addition of crystalline particles mitigates supercooling and facilitates phase transitions. Though this may apply to many systems, our data suggest this may not be the case for perchlorate solutions. As shown in both the calorimetric data (Fig. 7–13) and the Raman spectra (Fig. 7–15), the presence of ice or salt precipitates did not successfully initiate the eutectic transition in $Ca(ClO_4)_2$ solutions, pointing to a more complex nucleation behavior.

7.2.5 Melting behavior of frozen $(NH_4)_2SO_4$ solutions in confinement

The thermodynamic properties and phase behavior of aqueous $(NH_4)_2SO_4$ solutions has been recently extensively reviewed (Talreja-Muthreja and Steiger, 2025). Available literature data of eutectic temperatures cover a range of −18 °C to −19 °C, the model of Talreja-Muthreja and Steiger (2025) based on the freezing temperature and solubility curves yields −19 °C. The stable solid phase in this temperature range is paraelectric $(NH_4)_2SO_4$. Below −50 °C, a transition to a ferroelectric phase is observed. This polymorphic transition has been thoroughly investigated using spectroscopic methods, diffraction methods and differential scanning calorimetry (Torrie et al., 1972; Carter, 1976; Kwon and Kim, 1990; Bertram et al., 2007; Malec et al., 2018). A detailed phase diagram can be seen shown in Fig. 7–1.

Raman spectra of $(NH_4)_2SO_4$ and its aqueous solution: Herein, *in-situ* Raman spectroscopy was employed to investigate the phase behavior of $(NH_4)_2SO_4$ and its aqueous solutions. Figure 7–23 presents the Raman spectra of solid $(NH_4)_2SO_4$ recorded over the temperature range from −80 °C to 20 °C, focusing on four spectral regions, 420–480 cm^{-1}, 600–630 cm^{-1}, 960–990 cm^{-1}, and 2800–3600 cm^{-1}. At temperature above −50 °C, the peak positions of the SO_4^{2-} vibration modes march well with those reported for paraelectric $(NH_4)_2SO_4$ in the literature (Dong et al., 2007). Below −50 °C, a blue shift of approximately 6 cm^{-1} in the v_2–SO_4^{2-} mode (from 451.5 to 457.5 cm^{-1}), and a red shift of 3 cm^{-1} in the v_1–SO_4^{2-} mode below −60 °C (from 975.5 to 972.5 cm^{-1}) are observed. These spectral shifts are highlighted in the pink and green spectra of Fig. 7–23. Furthermore, a red shift in the NH_4^+ vibration band (2800–3600 cm^{-1}) occurs at low temperatures. The emergence of these spectral features around −60 °C, near the known polymorphic transition temperature, is attributed to the formation of ferroelectric $(NH_4)_2SO_4$.

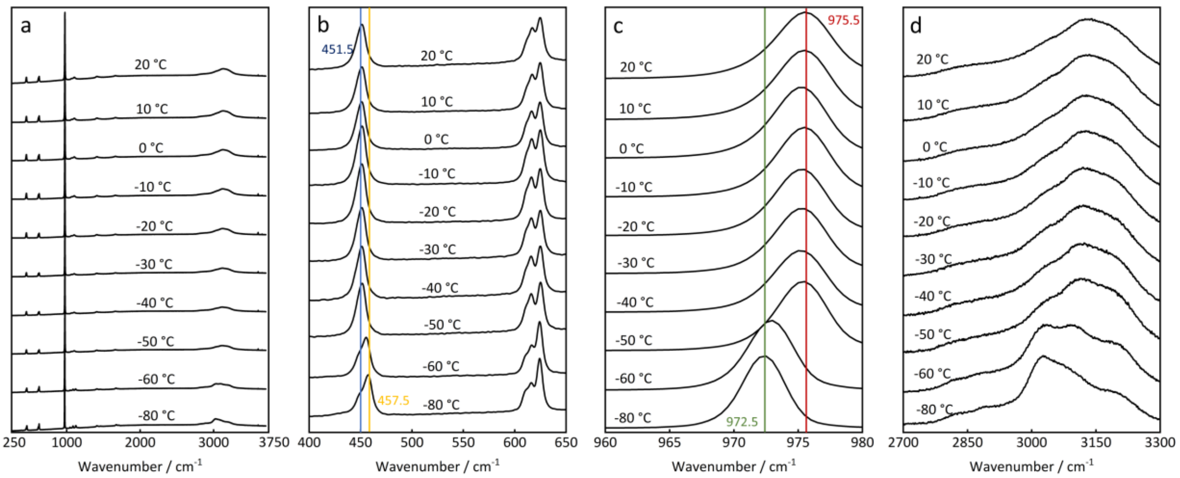

Figure 7–23. Raman spectra of $(NH_4)_2SO_4$ crystal during cooling from 20 °C to −80 °C.

The Raman spectra of the 6.0 m $(NH_4)_2SO_4$ solution, collected during the cooling (from 20 °C to −80 °C) and subsequent heating (from −80 °C to 20 °C), are shown in Fig. 7–24 and Fig. 7–25, respectively. The spectra of the v_1–SO_4^{2-} mode (960–990 cm^{-1}) in Fig. 7–24c illustrate the phase evolution of the solution throughout the cooling process, including the crystallization of paraelectric $(NH_4)_2SO_4$ from the solution and its subsequent transformation into the ferroelectric phase. At 20 °C, the v_1–SO_4^{2-} band of the aqueous solution appears at a slightly higher wavenumber compared to the corresponding peak of paraelectric $(NH_4)_2SO_4$, as shown by the black curve in Fig. 7–24c. Upon cooling, this band splits into two distinct features: a lower wavenumber peak corresponds to the crystallization of paraelectric $(NH_4)_2SO_4$, while the higher wavenumber peak arises from the SO_4^{2-}(aq) in the residual solution. The latter undergoes a progressive blue shift as temperature decreases, attributed to the decrease in solubility and molality of $(NH_4)_2SO_4$ (Dong et al., 2007). The disappearance of the higher wavenumber solution peak at −50 °C suggests eutectic freezing and complete solidification of the solution. This transition temperature is significantly lower than the known eutectic point of $(NH_4)_2SO_4$ solution, likely due to delayed nucleation. Further blue shift observed below −60 °C is indicative of the polymorphic transition from the paraelectric to the ferroelectric phase. Similar changes in peak positions and profiles are evident in other spectral regions (425–475 cm^{-1} and 2800–3600 cm^{-1}), aligning with these two temperature markers.

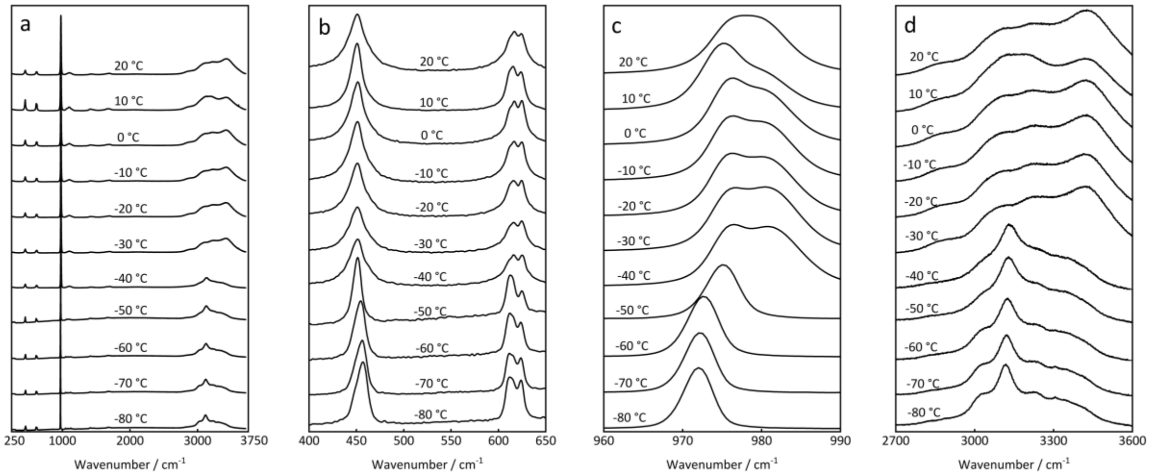

Figure 7–24. Raman spectra of 6 m $(NH_4)_2SO_4$ solution during cooling from 20 °C to –80 °C.

During the subsequent heating process (Fig. 7–25), the polymorphic transition is again observed between −60 °C and −50 °C, consistent with the cooling cycle. However, unlike in the cooling spectra, a distinct bimodal feature in the 960–990 cm^{-1} range is not evident. Instead, the spectra show a dominant peak at the lower wavenumber with a shoulder at higher wavenumber, which becomes apparent at −20 °C and above, which is close to the eutectic melting point. This higher–wavenumber shoulder is attributed to the v_1–SO_4^{2-} vibrational mode of $(NH_4)_2SO_4$ in the liquid phase, suggesting the reappearance of the aqueous component upon melting.

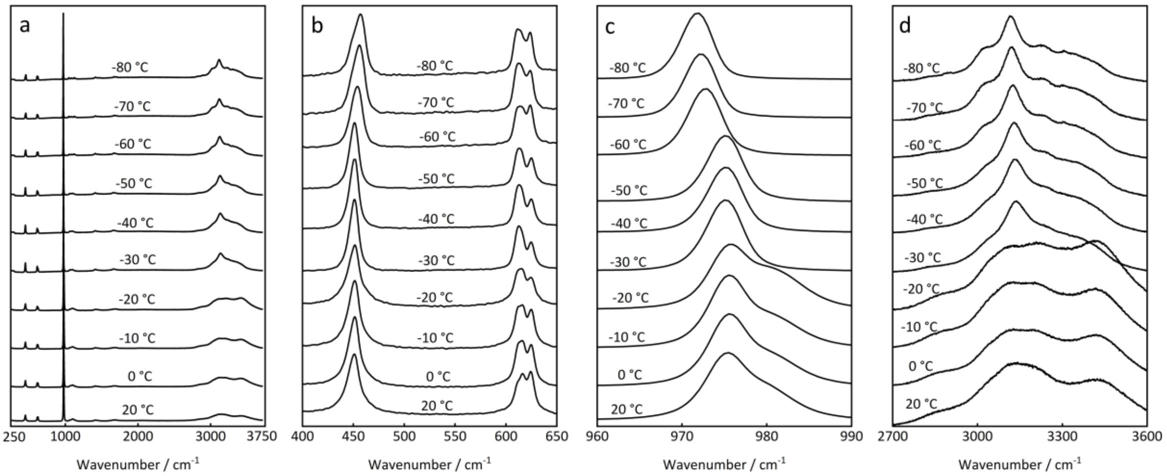

Figure 7−25. Raman spectra during heating of a frozen 6 m $(NH_4)_2SO_4$ solution from −80 °C to 20 °C.

Phase transitions of $(NH_4)_2SO_4$ solutions in confinement: The phase behavior of $(NH_4)_2SO_4$ solutions confined in porous silicas was investigated to elucidate the effects of salt concentration and pore size on the ice melting and eutectic transitions. Figure 7−26a presents the melting curves of $(NH_4)_2SO_4$ solutions with concentrations ranging from 0.1 to 6.0 m confined within 6.3 nm SBA-15. Similar to the results previously observed for NaCl and $CaCl_2$ solutions, only two endothermic peaks are detected in the dilute concentration region (below 1.5 m), corresponding to the melting of ice in the pore and in the bulk phase, indicated by red and blue arrows, respectively. Notably, the expected eutectic melting transition at −19 °C is absent in this dilute regime, likely due to the ion accumulation in the interfacial nonfreezing layer, which hinders salt crystallization (Chapter 6, Wang and Steiger, 2025). At higher concentrations, three endothermic signals appear at or below the bulk eutectic temperature, replacing the ice melting signal from the pores. These are marked by dashed lines in blue (−18.5 °C), red (−41.5 °C), and green (−49 °C), corresponding to the eutectic melting in the bulk phase, eutectic melting within the pore, and the paraelectric to ferroelectric phase transition, respectively. The absence of the endothermic signal at −49 °C in the dilute solutions confirms that $(NH_4)_2SO_4$ crystallization does not occur in these systems.

Figure 7−26b and Figure 7−26c display the melting curves of 3 m and 5 m $(NH_4)_2SO_4$ solutions confined in pore of sizes ranging from 5.9 nm to 20.6 nm. These results clearly demonstrate that the eutectic melting temperature within the pores is lower than that of the corresponding bulk solution and decreases systematically with decreasing pore size, as indicated by the red arrows. In contrast, the temperature associated with the polymorphic transition temperature remains invariant across different pore size, as shown by the green dashed lines. In addition to the three thermal events, one or two additional endothermic peaks are observed between the eutectic and polymorphic transition temperatures. These features are tentatively attributed to the crystallization and melting of the ferroelectric polymorph within the confined environment.

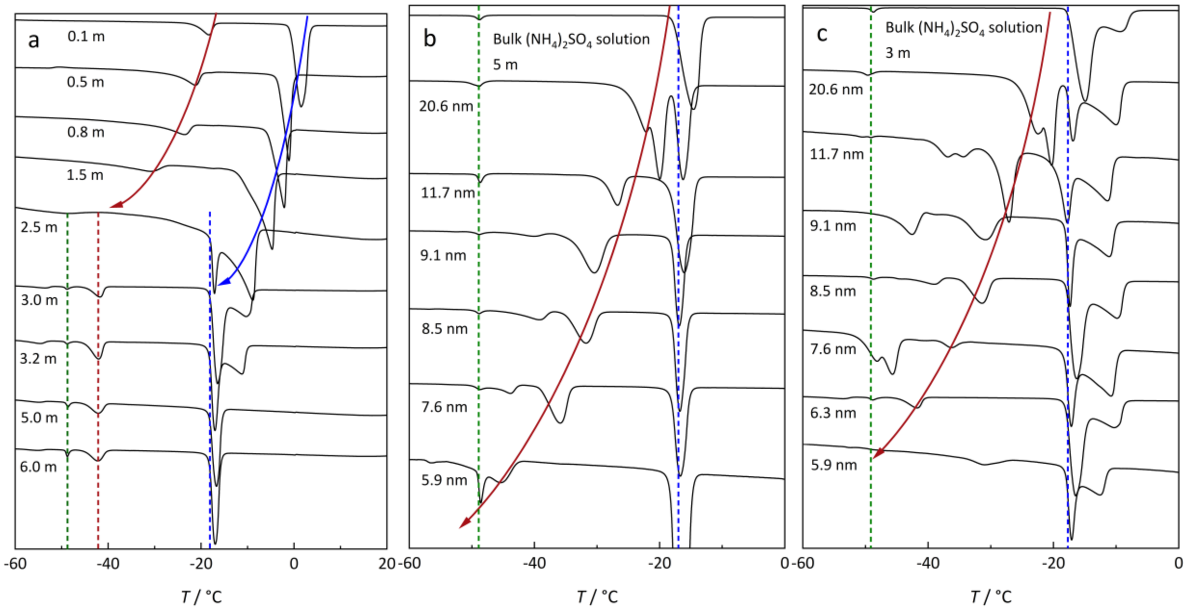

Figure 7−26. (a): Melting curves of $(NH_4)_2SO_4$ solutions within 6.3 nm pore over a concentration range from 0.1 m to 6.0 m; (b): melting curves of 5 m $(NH_4)_2SO_4$ solution in porous silica with pore size ranging from 5.9 to 20.6 nm; (c): melting curves of 3 m $(NH_4)_2SO_4$ solution under the same pore size conditions. Red arrows indicate the decrease in eutectic melting temperature with decreasing pore size; vertical dashed blue, red and green lines represent bulk eutectic, in-pore eutectic and polymorphic transition temperatures

7.2.6 Water vapor sorption of salt nanoparticles in confinement

Water adsorption on salt surfaces and in porous silica: Gas condensation in capillaries or the bulk phase is delayed due to the nucleation barrier associated with the formation of the liquid phase, whereas liquid desorption typically proceeds via an equilibrium process (Thommes et al., 2006; Thommes et al., 2015), as illustrated in Fig. 7−27a. However, this behavior changes in the case of water vapor condensation on a salt crystal surface. As shown in Fig. 7−27b, an equilibrium transition step appears in the sorption curve, corresponding to the relative humidity (RH) at which the water activity equals that of a saturated salt solution at a given temperature. In contrast, during desorption, efflorescence occurs at a significantly lower RH. This hysteresis arises from the nucleation barrier associated with salt crystallization during water evaporation. Remarkably, the presence of the salt alters the kinetics of water vapor sorption and condensation, effectively eliminating the nucleation barrier typically required for water liquification. According to classic adsorption theory, water molecules can be absorbed onto the surface of a pore wall or a salt crystal even at the humidity below the condensation point. This occurs because solid−liquid interfacial energy is smaller than that of the solid−gas interface, making adsorption energetically favorable. This initial sorption behavior in Fig. 7−27b is evident in the gradual increase of the sorption curve prior to condensation. The thickness of the water layer adsorbed within porous SBA-15 silica was estimated based on the measured water uptake, pore diameter, and pore volume. In this calculation, the density of confined water was assumed to be equal to that of bulk water 0.997 g·cm^{-3} (Wagner and Pruß, 2002), and the diameter of a water molecule is 3 Å (Marcus, 2003). The thickness of the adsorbed water layer is given by the following equation:

$$t = r_{\mathrm{p}} - \sqrt{\left(V_{\mathrm{p}} - \frac{w_{\mathrm{t}}}{\rho}\right)/\pi}$$

where t is the thickness of the adsorbed water layer, r_{p} is the pore radius, V_{p} is the pore volume, w_{t} is the mass of adsorbed water, ρ is the density of water at 25 °C.

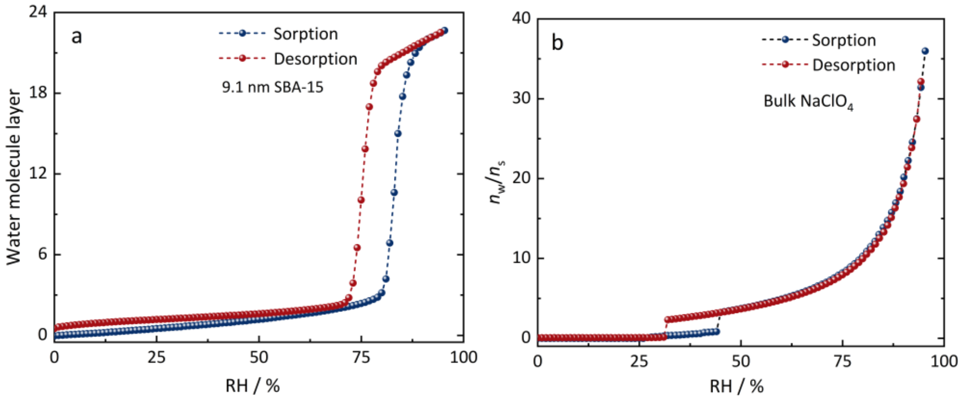

Figure 7–27. Water vapor sorption and desorption isotherms for 9.1 nm mesoporous silica SBA-15 (a) and bulk NaClO$_4$ (b).

As illustrated in the green shaded region of Fig. 7–28a, the adsorbed water layer reaches an approximate thickness of four molecular layers at the onset of condensation. In contrast, during the reversed desorption process (Fig. 7–28b), water layer recedes to a thickness of around three molecular layers at the offset of the evaporation. The observed thicker adsorbed water layer prior to condensation is likely related to the formation of liquid like nuclei, as a thicker water layer more closely resembles the structure of bulk three-dimensional liquid water. This transitional layer may facilitate the nucleation required for capillary condensation within the confined geometry.

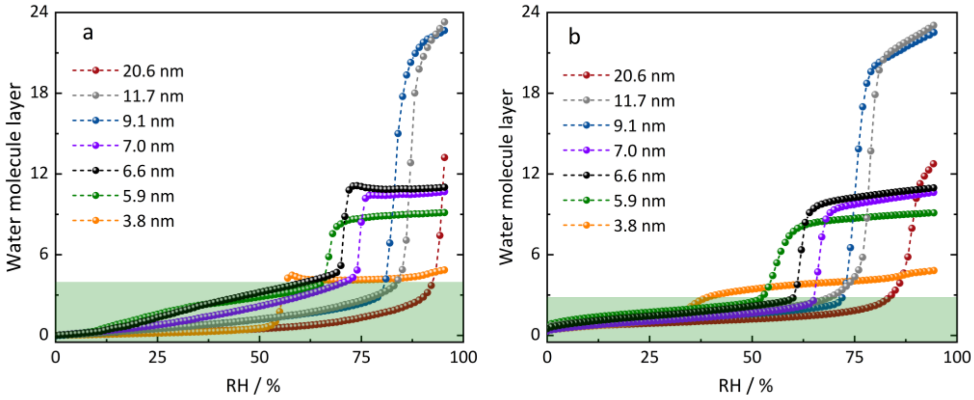

Figure 7–28. Water vapor sorption (a) and desorption (b) isotherms for the porous silicas (see Table 4–2 and Figure 4–1) with the diameter ranging from 3.8 nm to 20.6 nm.

A similar phenomenon has been reported during the pre-deliquescence of NaCl (Ewing, 2004), indicating that the onset of abrupt water uptake (deliquescence), occurs once approximately three molecule layers of water have accumulated on the surface. At this stage, the interfacial driving force for adsorption diminishes, as the solid surface is largely screened by the adsorbed water layers. Instead, the adsorption process becomes increasingly governed by the rising chemical potential of water vapor as it approaches the saturation pressure. In porous silica, capillary condensation occurs at a RH higher than the thermodynamic equilibrium due to the nucleation barrier associated with liquid formation in confined geometry. In contrast, on salt crystal surfaces, the pre–adsorbed water layers gradually evolve into a brine film as the salt begins to dissolve. This leads to the formation of three-dimensional hydrated ion clusters (Peters and Ewing, 1997a, 1997b), as schematically illustrated in Fig. 7−29. These hydrated clusters act as the structure templates that promote further water adsorption onto the salt surface. Consequently, the continued water uptake on salt surface beyond this point resembles the dilution of an extremely concentrated aqueous solution, rather than the classical liquid nucleation process. This mechanism effectively bypasses the nucleation barrier typically required for capillary condensation.

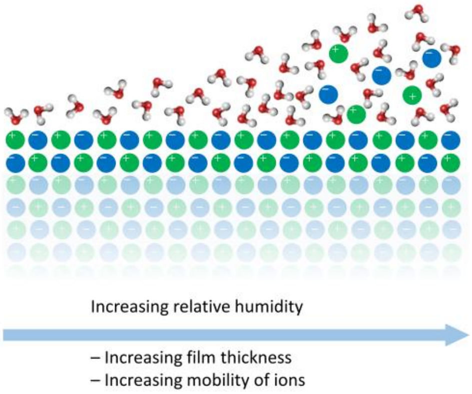

Figure 7−29. Schematic diagram of water adsorption on a salt crystal surface.

Deliquescence relative humidity (DRH) of chlorides in confinement: The water vapor sorption isotherms of chloride nanoparticles confined in porous silica are presented in Fig. 7−30. The ratio of the number of moles of water per mole of salt, n_w/n_s, was calculated by dividing the measured amount of adsorbed water by the amount of salt in each porous silica–salt composite (PSSC) sample. During water vapor sorption measurements, partial dehydration of the sample in the drying step removes some hydrated or adsorbed water, producing an initial negative value in the n_w/n_s water vapor sorption curve. As indicated by the vertical blue line, the DRHs of KCl, $MgCl_2{\cdot}6H_2O$, and β−$CaCl_2{\cdot}4H_2O$ (as clarified in Chapter 5) are 83%, 32%, and 19%, respectively, which are consistent with previously reported values in the literature (Greenspan, 1977; Guo et al., 2019; Wang and Steiger, 2025). $MgCl_2$ hydrates from $MgCl_2{\cdot}2H_2O$ to $MgCl_2{\cdot}6H_2O$ prior to deliquescence, consistent with literature reports (Hamze et al., 2024). $CaCl_2$ sequentially forms $CaCl_2{\cdot}H_2O$, $CaCl_2{\cdot}2H_2O$, and $\beta{-}CaCl_2{\cdot}4H_2O$, as described in Chapter 5. Different from the clear deliquescence step of bulk salt, the DRHs in confined systems fall within a humidity range as the pore size distribution of the host materials. Herein, we define the DRHs in the pore as the average of the onset and offset of the deliquescence humidities, which were determined at the relative humidity where an abrupt change in the slope of sorption isotherms occurs, as marked by the green dashed line. Overall, the DRHs of chlorides are lower in confinement compared to their bulk counterparts, and the deviation becomes more pronounced with decreasing pore size.

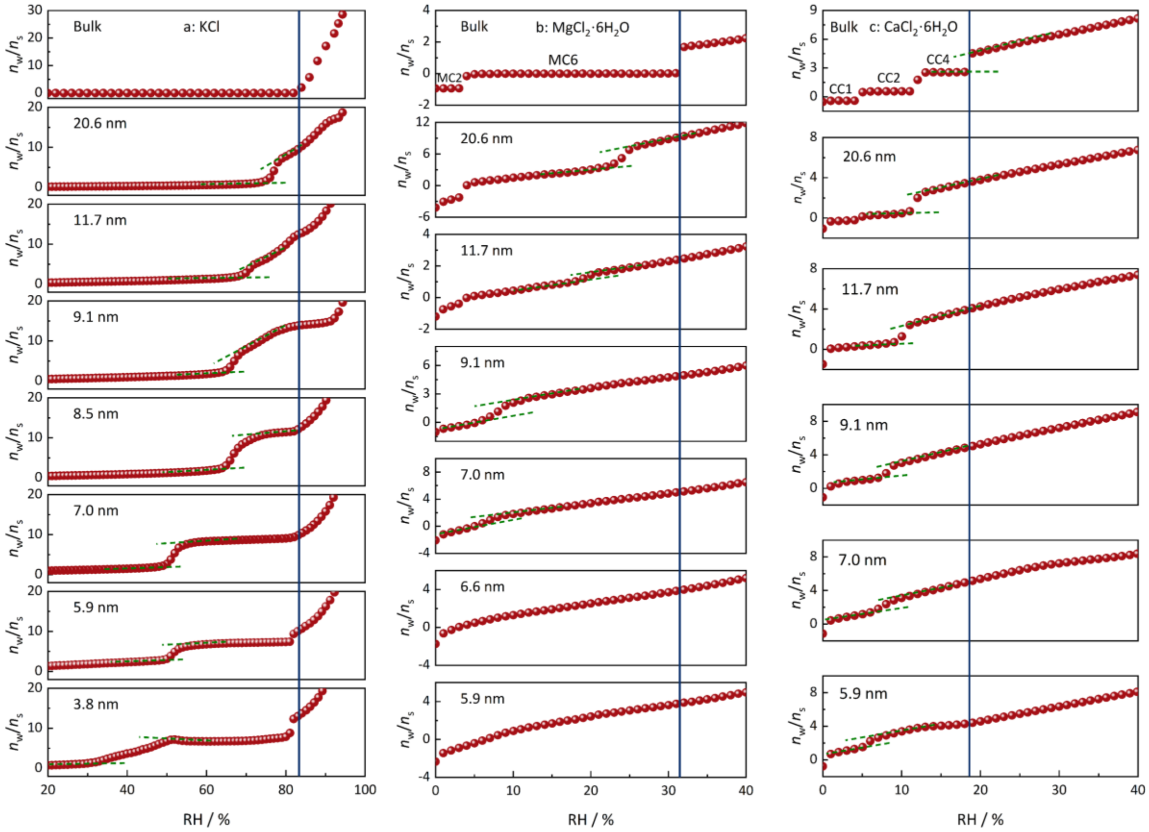

Figure 7−30. Water vapor sorption isotherms of chloride salt particles (KCl, $MgCl_2{\cdot}nH_2O$, and $CaCl_2{\cdot}nH_2O$) confined in porous silica with pore size ranging from 3.8 nm to 20.6 nm, compared to bulk salt crystals. Blue line: deliquescence relative humidity of the corresponding bulk salts (KCl, $MgCl_2{\cdot}6H_2O$, and $\beta{-}CaCl_2{\cdot}4H_2O$).

The sorption curve of KCl is continuous due to its lack of hydrate formation. In contrast, salts capable of forming multiple hydrates, such as $MgCl_2{\cdot}nH_2O$ and $CaCl_2{\cdot}nH_2O$, exhibit stepwise adsorption associated with successive hydration transitions prior to deliquescence. These hydration and deliquescence steps are distinctly observed in larger pores (e.g., 20.6 nm), closely resembling bulk behavior. However, in smaller pores, the sorption curves become smoother, and the characteristic steps become less distinguishable. A notable feature is the first step occurring near 1% RH. For KCl, this step shows a gradual increase, probably reflecting the water adsorption on the pore wall. While $CaCl_2$ displays an abrupt rise, with $MgCl_2$ exhibiting intermediate behavior. Given the absence of clear transition steps in small pores, the sharp uptake is likely attributed to the complex behavior of water adsorption on the pore wall and potential salt hydration reaction.

For an anhydrous salt, such as KCl, the solid phase in equilibrium during deliquescence under confinement matches that of the bulk. However, for salts forming hydrates, such as $CaCl_2{\cdot}nH_2O$, confinement may favor deliquescence from lower hydrate states. For example, as shown in Fig. 7−31, the phase diagram of $CaCl_2$–H_2O is expected to exhibit a downward shift in the pore (red curve) relative to the bulk system (bulk curve). This shift also alters the stability range of the hydrates. At 25 °C, $CaCl_2{\cdot}4H_2O$ or $CaCl_2{\cdot}2H_2O$ is likely to be the thermodynamically stable phase within the pore, in contrast to the $CaCl_2{\cdot}6H_2O$ in the bulk system. Moreover, $CaCl_2{\cdot}nH_2O$ undergoes deliquescence in nanopores at RHs below 13%, as shown in Fig. 7−30. This humidity threshold corresponds to the bulk phase transition from $CaCl_2{\cdot}2H_2O$ to $CaCl_2{\cdot}4H_2O$, thereby suggesting that, under confinement, $CaCl_2{\cdot}2H_2O$ deliquesces directly without undergoing hydration to $CaCl_2{\cdot}4H_2O$.

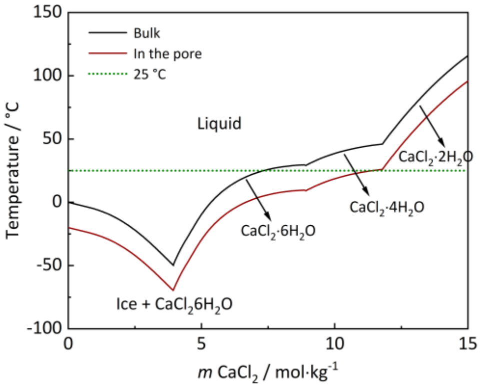

Figure 7−31. Phase diagram of $CaCl_2$–H_2O system both in bulk behavior (black curve) and its corresponding expected behavior under confinement (red curve).

The shape of the water vapor sorption isotherms for KCl in porous silica differs notably from those of $MgCl_2$ and $CaCl_2$. A pronounced second sorption step at approximately 80% RH for KCl in 5.9 nm and 3.8 nm pores suggests the deliquescence of bulk crystal, rather than a gradual dilution of saturated solution, which is a continuous process, as indicated in larger pores such as 7.0 nm, and 8.5 nm pores. This is originated from the imperfect impregnation during sample preparation, leaving bulk salt crystallizing outside the pores. In the pores below 9 nm, sorption curves display two distinct steps with a plateau in between, indicating a three-stage process: (1) deliquescence and dilution within the pore, (2) curvature filling, and (3) overflow and dilution of bulk solution, as interpreted in Fig. 7−32a. The shape of the first step, corresponding to the deliquescence of confined KCl nanoparticle, is influenced by the pore size distribution of the host material. Deliquescence occurs first in the smallest pores and later in larger pores, therefore, there water uptake does not follow a sharp step function as in the bulk, but rather exhibits a continuous increase over a range of relative humidities. Notably, the majority of the pores were filled during deliquescence, since the initial salt loading is based on concentrated KCl solution (4.2 m). The observed downward shift in the DRH for KCl in confined space is governed by two aspects (Talreja-Muthreja et al., 2022): (1) changes in solubility at the nanoscale and (2) the reduction in water vapor pressure due to the curvature of the liquid–vapor interface, given by Kelvin equation $\ln(\frac{p}{p^{\circ}}) = \ln a_{\mathrm{w}} - \frac{2\times V_{\mathrm{m}}^{\circ}\times\gamma_{\mathrm{lv}}\times cos\theta}{r_{\mathrm{k}}\times \mathrm{R}\times T}$ and $r_{\mathrm{k}} = (r_{\mathrm{p}} - t)/\cos\theta$, where r_{k} is the radius of curvature of the solution, r_{p} is the pore radius, t is the thickness of non-freezing layer (0.6 nm), and θ is the angle between solution interface and pore wall, as shown in Fig. 7–32b. The former is predominantly controlled by crystal size and the salt–liquid interfacial energy(γ_{cl}), while the latter is influenced by pore size, the solution–vapor surface tension (γ_{lv}), and the angle between the salt solution curvature and the pore wall (θ). During the initial deliquescence step (step ① in Fig. 7–32a). In the second stage, a plateau in water uptake isotherm is observed, suggesting that only minimal additional water is adsorbed while the vapor pressure increasing substantially from 60% to 80% RH. This minimal uptake slightly dilutes the saturated solution, but the resulting volumetric expansion efficiently contributes to filling within the pores. This is associated with an increase of in the angle between the curvature and pore wall, as illustrated by step ② in Fig. 7–32a.

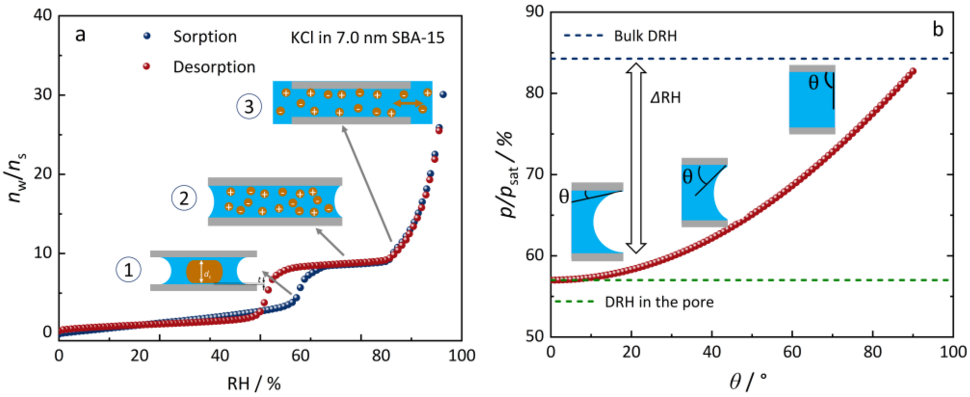

Figure 7–32. (a): Water vapor sorption isotherms of KCl in 7.0 nm porous silica; (b): Influence of contact angle on the water vapor pressure of KCl solution under same confined condition. θ is the angle between the salt solution curvature and pore wall.

Figure 7–32b shows the water vapor pressure of a saturated KCl solution as a function of the angle of solution curvature and pore wall in porous silica, overlaid with the RH range corresponding to the plateau observed in the sorption isotherm in Fig. 7–32a. This comparison indicates that the variation in water vapor pressure during the second stages is not only driven by the dilution of the KCl solution, but also by changes in the angle between the solution and the pore wall. As the radius of curvature approaches infinity, the water vapor pressure approaches to the DRH of bulk KCl, suggesting that the pore becomes completely filled with solution. The slight deviation between the blue dash line and red curve in Fig. 7–32b is likely due to the minor solubility difference KCl nanoparticle and the bulk crystal. In the third stage, continued water adsorption leads to volumetric expansion of the confined solution, which begins to overflow from the pores. The RH at which this overflow initiates aligns with the DRH of bulk KCl. At this point, water adsorption involves dilution of both the confined and the external bulk solution, as illustrated in step ③ of Fig. 7−32a. Notably, the sorption and desorption curves fully overlap in the third stage (RH > 80%), indicating that crystallization of KCl in the bulk solution does not occur. In contrast, the hysteresis observed in the first stage (50−60% RH) during desorption is indicative of salt crystallization within the pore.

The water vapor sorption behavior of perchlorates is shown in Fig. 7−33. The DRHs of the bulk $NaClO_4 \cdot H_2O$, $Mg(ClO_4)_2 \cdot 6H_2O$, and $Ca(ClO_4)_2 \cdot 4H_2O$ are 45%, 40%, and 16%, respectively, as indicated by the blue lines, in agreement with literature values (Jia et al., 2018; Gu et al., 2017).

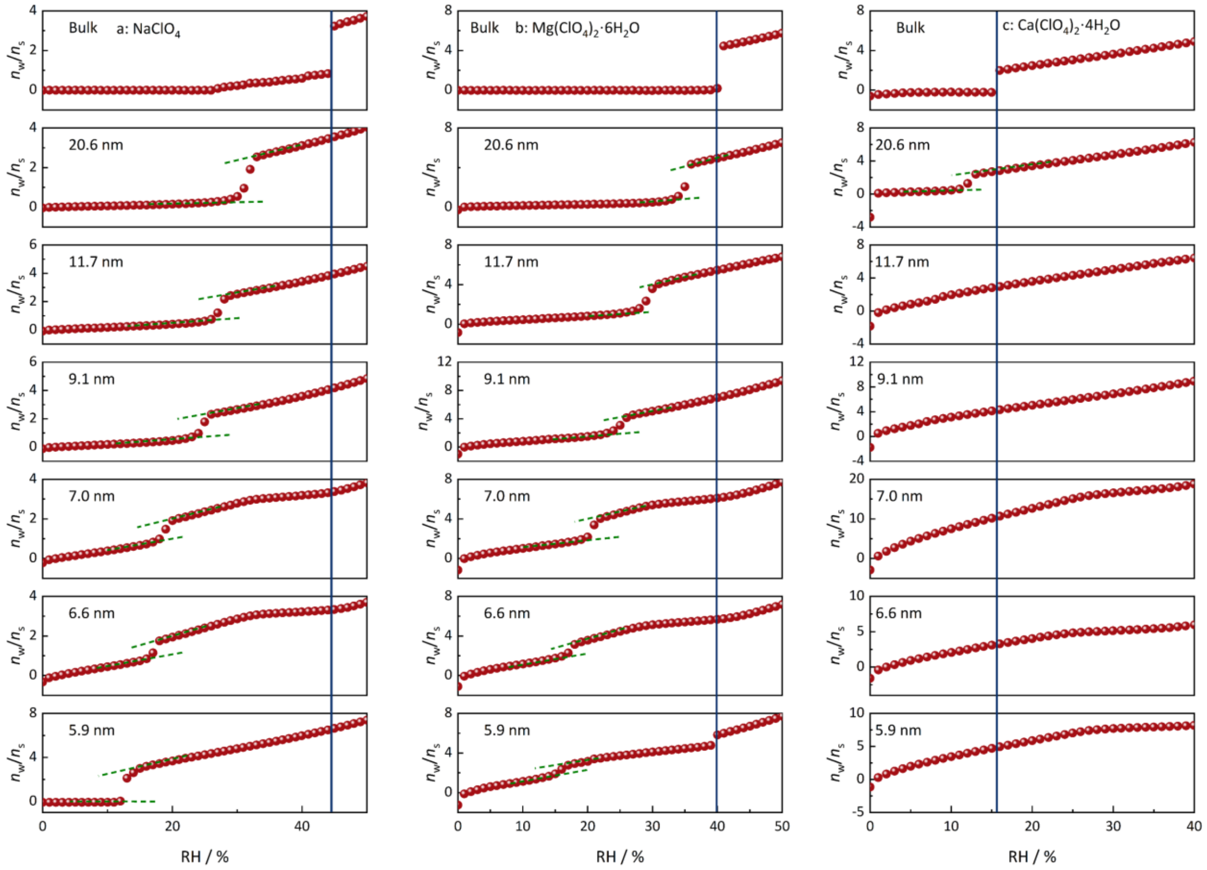

Figure 7−33. Water vapor sorption isotherms of chloride salt particles ($NaClO_4 \cdot H_2O$, $Mg(ClO_4)_2 \cdot 6H_2O$, and $Ca(ClO_4)_2 \cdot 4H_2O$) confined in porous silica with pore size ranging from 3.8 nm to 20.6 nm, compared to bulk salt crystals. Blue line: deliquescence relative humidity of the corresponding bulk salts ($NaClO_4 \cdot H_2O$, $Mg(ClO_4)_2 \cdot 6H_2O$, and $Ca(ClO_4)_2 \cdot 4H_2O$).

In porous silica, the DRHs of $NaClO_4 \cdot H_2O$ and $Mg(ClO_4)_2 \cdot 6H_2O$, determined as the average of the onset and offset of the deliquescence humidities (marked by two green dashed lines), systematically decrease with decreasing pore size. However, for $Ca(ClO_4)_2 \cdot 4H_2O$, the deliquescence transition is only observed in 20.6 nm pores but absent in pores smaller than 11.8 nm. Considering that the extremely low DRH of bulk $Ca(ClO_4)_2{\cdot}4H_2O$ (18%), the continuous water uptake in the pores arises from a combination of water adsorption on the pore walls, deliquescence of $Ca(ClO_4)_2{\cdot}4H_2O$, and subsequent dilution. The overlap of these process makes it difficult distinguish a distinct deliquescence step.

Figure 7−34a summarizes the DRHs of both chlorides and perchlorates confined in porous silica. In all cases, the DRHs in confinement are lower than those in the bulk phase (indicated by dashed line) and show a decreasing trend with the reduced pore diameter. This pore−size−dependent suppression of DRH is more pronounced for salts with higher bulk DRH. For example, the weakly hygroscopic KCl exhibits a steeper DRH−pore size dependence compared to the strongly hydroscopic $CaCl_2$. The DRH differences between bulk and confined salts are presented in Fig. 7−34b, revealing a general correlation: salts with higher bulk DRHs tend to exhibit greater DRH depression in confinement.

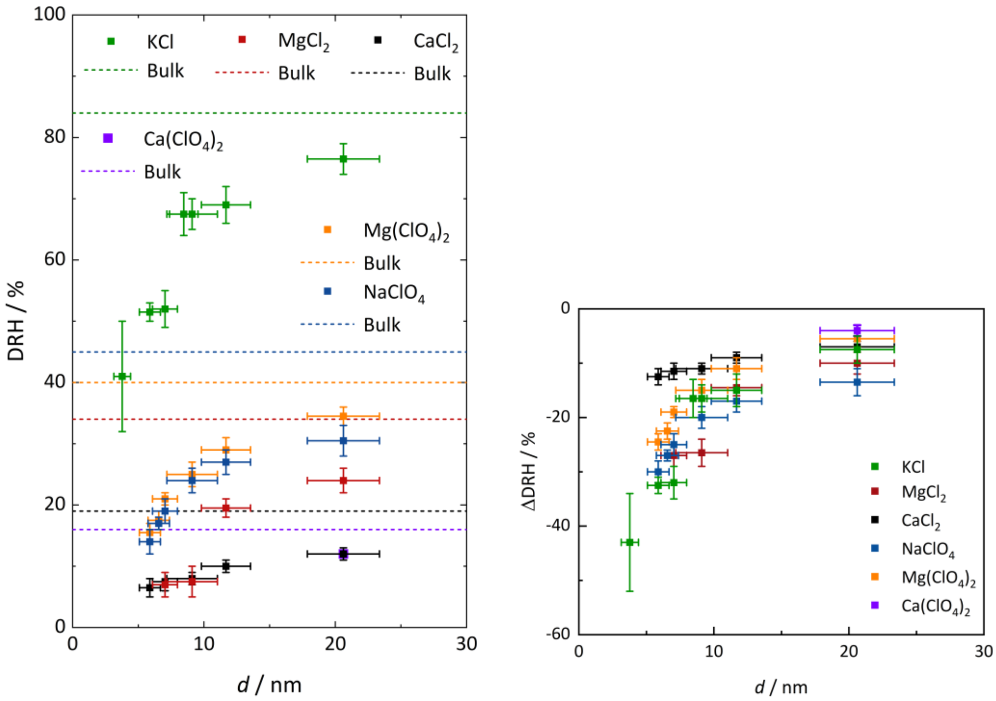

Figure 7−34. (a): DRHs of chlorides (KCl, $MgCl_2{\cdot}6H_2O$, and $CaCl_2{\cdot}nH_2O$ (β−$CaCl_2{\cdot}4H_2O$ or $CaCl_2{\cdot}2H_2O$)) and perchlorates ($NaClO_4{\cdot}H_2O$, $Mg(ClO_4)_2{\cdot}6H_2O$, and $Ca(ClO_4)_2{\cdot}4H_2O$) nanoparticles confined in porous silica with pore size ranging from 3.8 nm to 20.6 nm and their bulk counterparts. (b): difference of DRHs between the confined and bulk phases. The error bar of d represents the pore size distribution range of the host materials, while the error bar of DRH or ΔDRH denotes the deviation between average value and either the onset DRH (lower limit) or the offset DRH (upper limit) of the water vapor sorption isotherm.

7.3 Conclusions

The melting and eutectic points of Mars-relevant salt solutions, NaCl, $MgCl_2$, $CaCl_2$, $NaClO_4$, $Mg(ClO_4)_2$, $Ca(ClO_4)_2$, and the main constituent of atmospheric aerosols $(NH_4)_2SO_4$ confined in porous silica matrices were investigated using calorimetry and Raman spectroscopy. In addition, the hygroscopic behavior and DRHs of these salt systems in confinement were examined using water vapor sorption measurements. The influence of solute molality and pore size on the phase transition temperature and humidity were systematically explored. The major findings are summarized below:

(1) Melting behavior of ice in nanopores

The melting temperature of ice in nanopores is significantly depressed relative to the bulk phase, with melting points reaching as low as −45 °C in pores with diameters as small as 3.8 nm. In the solutions, the melting temperature of ice is influenced by both pore size and solute molality.

(2) Eutectic transition of confined salt solutions

Eutectic points of salt solutions (NaCl, $MgCl_2$, $CaCl_2$, $NaClO_4$, $(NH_4)_2SO_4$) are independent of salt concentration but decrease with decreasing pore size. Eutectic transitions are absent in dilute solutions and small pores. The critical concentration and pore size at the which eutectic transition occurs depend on salt type. Across all investigated brines, the lowest detected eutectic melting temperatures in nanopore locate between −60 °C and −70 °C.

(3) Solid−solid transformation at low temperature

The formation of $Ca(ClO_4)_2{\cdot}6H_2O$ and of ferroelectric $(NH_4)_2SO_4$ in aqueous solution at low temperatures was confirmed by Raman spectroscopy, with observed transition temperatures consistent with previously reported data.

(4) Three−stage water sorption of confined KCl

Water adsorption of KCl nanoparticle in porous silica contains three stages: 1. initial gradual growth by adsorption, deliquescence, and subsequent dilution; 2. the plateau after deliquescence, suggesting the filling of the solution−gas interface curvature; 3. the final water uptake above the DRH of bulk crystal, denoting the overflow of the confined solution and the dilution of bulk solution. The minimal water uptake during the second stage leads to an increase of solution−gas curvature radius and the angle at the solution−pore wall interface, resulting in the increase of water vapor pressure.

(5) Influence of hydration on the deliquescence of confined salt

For an anhydrous salt, such as KCl, the solid phase in equilibrium during deliquescence under confinement matches that of the bulk. However, for salts forming hydrates, such as $CaCl_2{\cdot}nH_2O$, confinement may favor deliquescence from lower hydrate states.

(6) Size dependent deliquescence process

The DRHs of salt nanoparticles in the porous silica are consistently lower than those of bulk counterparts, and further decrease with decreasing pore size. Unlike the sharp deliquescence observed in bulk salts, confined salts exhibit smoother sorption transitions, reflecting the pore size distribution in the host material.

In summary, these investigations into the phase behavior of water and salts in the confined space deepen our understanding of the wet properties of saline soils on the Martian surface. While the stable, long-term presence of bulk water remains improbable, nanoconfinement markedly broadens the liquid-phase domain through mechanism such as eutectic melting and deliquescence. Importantly, the recurrent formation of nanoscale brines and films under such conditions is not only plausible but also likely to influence geochemical reactions and mineral evolution on Mars. These findings underscore the critical role of confinement effect in shaping aqueous process on planetary surface, thereby offering new perspectives for interpreting the hydrological and mineralogical evolution of Mars.

Chapter 8. Thermodynamic modeling of the phase equilibria of confined salt solutions

Thermodynamic modeling has been extensively employed to calculate phase equilibria among ice, salts, aqueous solutions, and water vapor in environmental and geochemical studies (Wexler and Clegg, 2002; Marion et al., 2010; Gough et al., 2011). Phase transitions driven by fluctuations in temperature and humidity, such as deliquescence, ice melting, and salt dissolution, are effectively described using models based Pitzer theory (Pitzer, 1991), e.g., Toner et al. (2015b) and Li et al. (2022). To enhance model accuracy under low temperature and low vapor pressure conditions relevant to extraterrestrial environments like Mars, substantial thermodynamic datasets have been experimentally obtained and adopted into the model parameterization schemes (Nuding et al., 2014; Toner et al., 2015a; Li et al., 2022).

Under confinement, an expansion of the liquid stability region for water and aqueous solutions has been observed (Cheng et al., 2015; Meissner et al., 2016; Jantsch et al., 2019). Several frameworks, including Gibbs–Thomson and Ostwald–Freundlich equations, have been extended to describe the phase behavior of aqueous solutions confined within nanopores (Meissner et al., 2016; Liu et al., 2017). These models highlight the critical role of solute and interfacial energy in shifting equilibrium conditions, thereby providing a theoretical basis for understanding the altered solubility and phase transition behavior under nanoscale confinement. In this Chapter, we integrate Pitzer model with pore size dependent effects to develop PKL and PK frameworks, which are employed to simulate the phase behavior of salt solutions, including NaCl, KCl, $MgCl_2$, $CaCl_2$, $NaClO_4$, $Mg(ClO_4)_2$, $Ca(ClO_4)_2$, and $(NH_4)_2SO_4$ under nanoconfinement. Specifically, we examine the melting and eutectic points, as well as the deliquescence relative humidities (DRH), of these systems.

8.1 Surface tension and apparent molar volume

8.1.1 Surface tension and molar volume of pure water

As introduced in Section 2.5, the phase equilibria of salt solutions in nanopores are primarily govened by the crystal–solution interfacial energy γ_{cl}, surface tension γ_{lv}, and the $\Delta V_{\mathrm{m}}^{\circ}$. The temperature dependence of the vapor–liquid surface tension (γ_{lv}) is given by the equation from IAPWS (2014; Hrubý et al., 2014):

$$\gamma_{\mathrm{lv}} = \mathrm{B}\tau^{\mu}(1 + \mathrm{b}\tau) \qquad (8\text{–}1)$$

Where $\tau = 1 - T/T_c$, $T_c = 647.096$ K, $\mu = 1.256$, $B = 235.8$ mN·m⁻¹, and $b = -0.625$. The calculated water surface tension is presented in Fig. 8−1a.

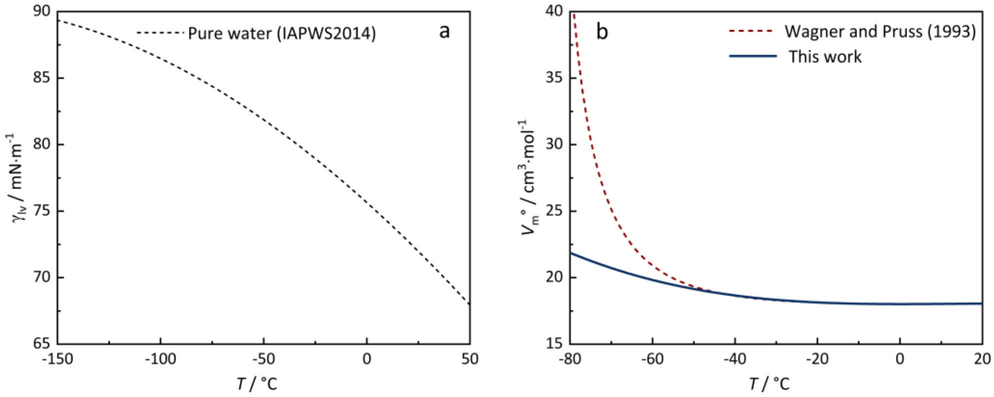

Figure 8−1. Surface tension and molar volume of pure water at low temperatures.

The molar volume of pure water ($V_{m,w}$) can be derived from the density calculated using the IAPWS equation (Wagner and Pruss, 1993). However, when extrapolated to temperatures as low as −80 °C, the values become unrealistic as the IAPWS formulation is only valid in the temperature range from 273.15 to 647.10 K. Due to the homogeneous ice nucleation limit, obtaining reliable experiment data in the sub-zero temperature range remains highly challenging. Consequently, extrapolating Wagner and Pruss's equation into this regime is largely empirical and introduces significant uncertainty. This deviation is illustrated by the red dashed curve in Fig. 8−1b. To overcome this limitation, we performed a polynomial fitting using the IAPWS data within the temperature range of 233.15 to 298.15 K. The resulting curve exhibits a smooth upward trend in the low−temperature region, shown as the blue curve in Fig. 8−1b. The fitted polynomial function is given as:

$$V_{m,w} = a_1 + a_2(T - T_0) + a_3(T - T_0)^2 + a_4(T - T_0)^3 \tag{8–2}$$

where T is the absolute temperature, T_0 = 273.15 K, a_1 = 18.016 cm^3·mol^{-1}, a_2 = −2.1957×10^{-4} cm^3·mol^{-1}, a_3 = 1.8426×10^{-4} cm^3·mol^{-1}, a_4 = −4.5884×10^{-6} cm^3·mol^{-1}.

8.1.2 Liquid–vapor surface tension of salt solutions

It was found that, at low to moderate concentrations, the liquid–vapor surface tension of salt solutions follows a linearly increase with concentration (Henry et al., 2007; Dutcher et al., 2010; Talreja–Muthreja et al., 2022). In this work, experimental data of surface tension differences of solution and pure water ($\gamma_{lv} - \gamma_{lv,w}$) from the available literature were fitted using the linear function (8−3).

$$\gamma_{lv} - \gamma_{lv,w} = a_1 m + a_2 m^2 \tag{8–3}$$

where *m* is the molality of the solute. In case of $NaClO_4$, $Mg(ClO_4)_2$, and $Ca(ClO_4)_2$, Henry et al. (2007) reported linear equation in terms of molar concentration (c in $mol\cdot L^{-1}$). However, in terms of molality, surface energies calculated with their equations are longer linear. Therefore, a quadratic polynomial equation had to be used the coefficients of which are also listed in Table 8–1. Then, calculated surface tension using both expressions are identical in the entire temperature range from −100 °C to 25 °C, as shown in Figs. 8–2 and 8–3. This model are essentially only described by the temperature dependence of the surface energy of pure water ($\gamma_{lv,w}$), and the coefficients listed in the Table 8–1 are all independent of temperature.

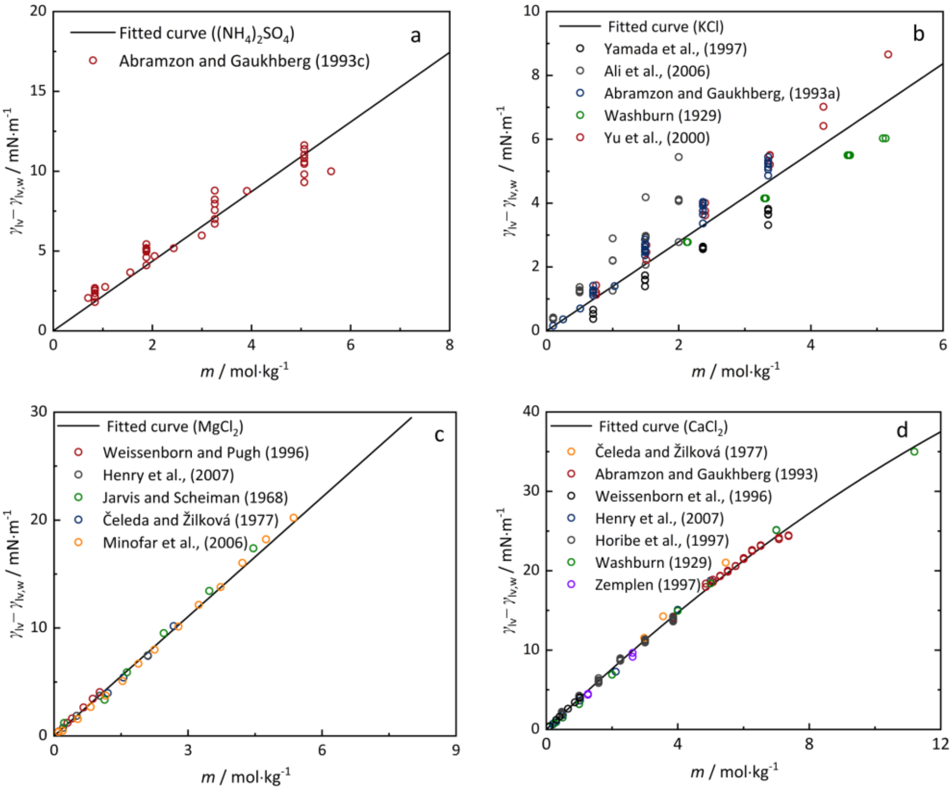

Figure 8–2. Comparison between the fitted results (black curves) and experimental data for the surface tension difference ($\gamma_{lv} - \gamma_{lv,w}$) between chloride salt solutions and pure water.

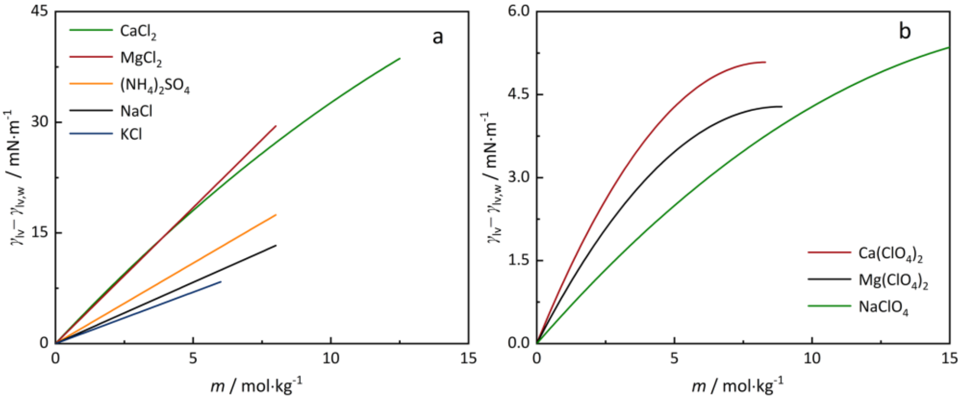

Figure 8–3. Calculated surface tension differences ($\gamma_{lv} - \gamma_{lv,w}$) between salt solutions and pure water calculated using the present model with coefficients listed in Table 8–1.

Table 8−1. The fitted parameters and data sources for the surface tension of pure water and salt solutions

Salt	**a_1** $\mathrm{mN{\cdot}m^{-1}{\cdot}mol^{-1}}$	**a_2** $\mathrm{mN{\cdot}m^{-1}{\cdot}mol^{-2}}$	
$(NH_4)_2SO_4$	2.1807		Abramzon and Gaukhberg (1993a)
NaCl	1.66		Talreja−Muthreja et al. (2022)
KCl	1.3945		Abramzon and Gaukhberg (1993b), Yamada et al. (1997), Yu et al. (2000), Ali et al. (2006), Washburn (1929)
$MgCl_2$	3.6864		Čeleda and Žilková (1977), Weissenborn and Pugh (1996), Henry et al. (2007), Jarvis and Scheiman (1968), Minofar et al. (2006)
$CaCl_2$	3.9594	-6.95×10^{-2}	Zemplén (1907), Washburn (1929), Čeleda and Žilková (1977), Horibe et al. (1997), Weissenborn and Pugh (1996), Henry et al. (2007), Abramzon and Gaukhberg, (1993c)
$NaClO_4$	0.5671	-1.4195×10^{-2}	Henry et al. (2007)
$Mg(ClO_4)_2$	0.9653	-5.438×10^{-2}	Henry et al. (2007)
$Ca(ClO_4)_2$	1.2235	-7.363×10^{-2}	Henry et al. (2007)

8.1.3 Apparent molar volume at infinite dilute solution

The apparent molar volume in infinite dilute solutions (V_m°) of various salts have been previously evaluated, with their temperature dependence expressed using an empiric equation (Krumgalz et al., 2000), as shown by the red curves in Fig. 8−4. However, direct extrapolation of these expression to sub−zero temperatures leads to unphysical results, such as anomalously high values for $MgCl_2$ or negative values for NaCl and KCl (Fig. 8−4). These discrepancies arise from the fact that the model of Krumgalz et al. (2000) is based on experimental data at temperatures above the freezing point of water (indicated by the green regions in the Fig. 8−4). To enable a physically more reasonable extension to lower temperatures, the data of Krumgalz et al. were refitted using the following polynomial expression:

$$V_\mathrm{m}^\circ = a_1 + a_2(T - T_0) + a_3(T - T_0)^2 + a_4(T - T_0)^3 \tag{8−4}$$

The fitted parameters for NaCl, KCl, $MgCl_2$, $CaCl_2$, and $(NH_4)_2SO_4$ are listed in Table 8–2, and the calculated curves are presented in Fig. 8–4 and Fig. 8–5. The $NaClO_4$ and $Mg(ClO_4)_2$ parameters were derived from experimental data reported from literature (Hnedkovsky et al., 2021; Caro et al., 2020). The apparent molar volume of $Ca(ClO_4)_2$ was estimated using the relation

$$V_\mathrm{m}^\circ(\mathrm{Ca(ClO_4)_2}) = V_\mathrm{m}^\circ(\mathrm{CaCl_2}) + 2\,V_\mathrm{m}^\circ(\mathrm{NaClO_4}) - 2\,V_\mathrm{m}^\circ(\mathrm{NaCl}) \tag{8–5}$$

This approach ensures continuity and physical plausibility in the low–temperature region relevant for phase behavior modeling.

Table 8–2. The fitted parameters and data sources for the molar volume of pure water and the apparent molar volumes of salts at infinite dilute solution

Salt	a_1 $\mathrm{cm^3{\cdot}mol^{-1}}$	a_2 $\mathrm{cm^3{\cdot}mol^{-1}{\cdot}K^{-1}}$	a_3 $\mathrm{cm^3{\cdot}mol^{-1}{\cdot}K^{-2}}$	a_4 $\mathrm{cm^3{\cdot}mol^{-1}{\cdot}K^{-3}}$	$T^{(1)}$ / K	Source
NaCl	1.4088×10^{1}	1.2520×10^{-1}	-1.1922×10^{-3}		278.15–368.15	Krumgalz et al. (2000)
KCl	2.4758×10^{1}	1.0697×10^{-1}	-9.9987×10^{-4}		288.15–368.15	Krumgalz et al. (2000)
$MgCl_2$	1.1919×10^{1}	1.0584×10^{-1}	-7.4513×10^{-4}		288.15–313.15	Krumgalz et al. (2000)
$CaCl_2$	1.5381×10^{1}	1.2148×10^{-1}	-1.1067×10^{-3}	-7.3410×10^{-6}	288.15–328.15	Krumgalz et al. (2000)
$NaClO_4$	3.7059×10^{1}	2.7162×10^{-1}	-1.4685×10^{-3}		293.15–343.15	Hnedkovsky and Hefter (2021)
$Mg(ClO_4)_2$	5.9057×10^{1}	3.8329×10^{-1}	-0.0025×10^{-3}		293.15–343.15	Caro et al. (2020)
$(NH_4)_2SO_4$	4.4248×10^{1}	3.5135×10^{-1}	-4.4310×10^{-3}		273.15–333.15	Clegg and Wexler (2011)
H_2O	1.8017×10^{1}	-2.5719×10^{-4}	1.8426×10^{-4}	-4.5884×10^{-6}	233.15–298.15	Wagner and Pruss (1993)

(1) Temperature range of the data used in fit

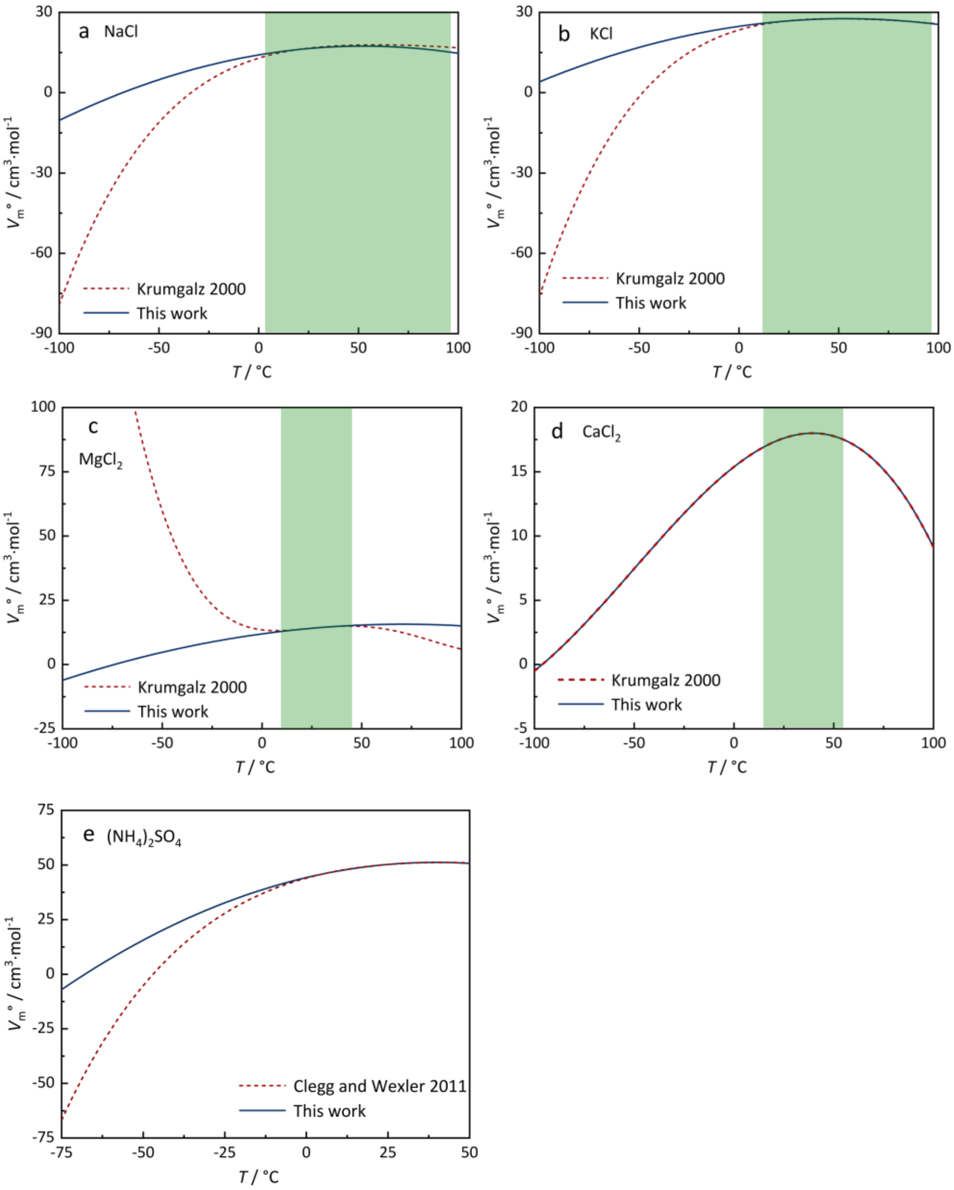

Figure 8–4. Comparison of the fitted results (blue curves) with literature–reported values (red curves) for the apparent molar volume in infinite dilute solutions (V_m°) over a range of temperatures.

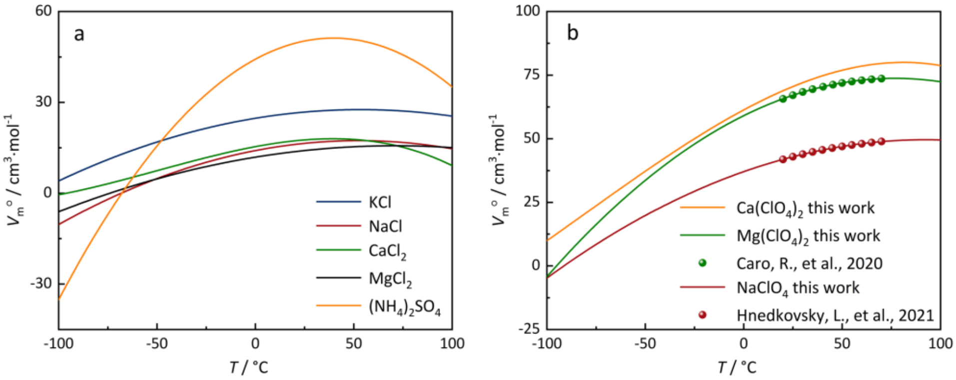

Figure 8–5. Apparent molar volume in infinite dilution (V_m°) of selected salt solutions (NaCl, KCl, MgCl$_2$, CaCl$_2$, (NH$_4$)$_2$SO$_4$, NaClO$_4$, Mg(ClO$_4$)$_2$, and Ca(ClO$_4$)$_2$) as a function of temperature.

8.2 Phase equilibria of salt solutions in confinement

8.2.1 Ice melting and eutectic points

The PKL (less-filled pore with Laplace pressure) and PK (over-filled pore without Laplace pressure) models, which have been introduced in Section 2.5, were applied to calculate the melting behavior of confined water and chloride solutions, respectively. Figure 8−6 shows the comparison of predicted ice melting temperatures in nanopores using PKL (green region) and PK model (orange region) with constant ice−water interfacial energy (γ_{cl}). It is clear that the PKL modelled values are systematically higher than those obtained from PK model, and the lower boundary of green region (γ_{cl} = 30 mJ·m^{-2}) closely approaches the upper boundary of the orange region (γ_{cl} = 20 mJ·m^{-2}). The difference in melting temperature predicted by PKL and PK models (green and orange regions) indicate that Laplace pressure plays a significant role in the melting behavior of confined ice.

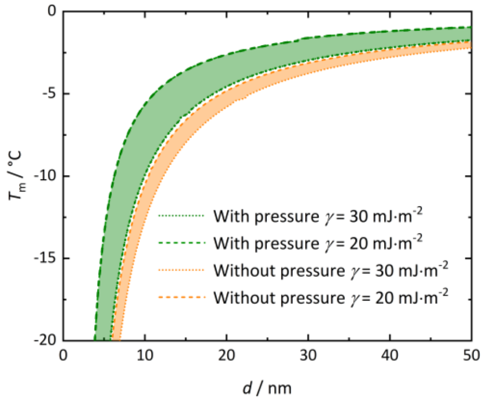

Figure 8−6. Calculated ice melting temperature of the confined water as a function of pore radius, green area represents results obtained with PKL model, orange region corresponds to calculations with PK model.

Ice melting temperatures in the confined pure water, as well as NaCl (5.2 m), $MgCl_2$ (2.8 m), and $CaCl_2$ (4.0 m) solutions at concentrations corresponding to their bulk eutectic points, were first calculated with the PK model, and the results are depicted in Fig. 8−7a and compared with the experimental data. For each system, three different values of crystal−liquid interfacial energy (γ_{cl}) were used in these calculations, and the results are depicted as dotted, solid, and dashed curves.

For all systems investigated, the experimental data align well with the dotted curve in larger pores, corresponding to smaller value of γ_{cl}. As pore size decreases, the experimental data progressively shift toward the dashed curves, which represents larger γ_{cl} value. The influence of salt molality is minimized in these comparisons, as all samples were prepared at eutectic concentration. The shaded regions in Fig. 8−7a encompass the majority of the experiment data points, indicating that γ_{cl} likely varies within this range as a function of both temperature and crystal size. Accordingly, an estimated γ_{cl} value was determined as the average between the minimum and maximum used in the PK model calculations, yielding values of 20, 20, 25, and 30 mJ·m^{-2} for H_2O, NaCl, $MgCl_2$, and $CaCl_2$, respectively, as shown by the solid lines. Moreover, Fig. 8−7b presents the calculated melting and eutectic temperatures using PKL model with three γ_{cl} values. The optimal interfacial energies ice−liquid for the pure water, NaCl, $MgCl_2$, and $CaCl_2$ solutions are consistently 25 mJ·m^{-2}.

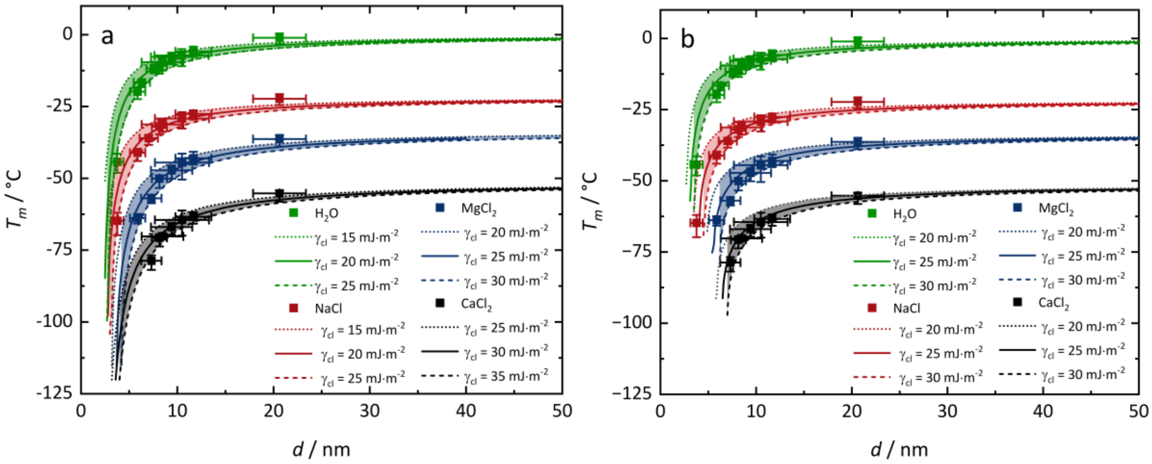

Figure 8−7. Comparison of experimental data and calculated results using different values of crystal−liquid interfacial energy (γ_{cl}). Ice melting point and eutectic points in pure water and in NaCl (5.2 m), $MgCl_2$ (2.8 m), and $CaCl_2$ (4.0 m) solutions confined within nanopores ranging from 3.8 to 20.6 nm; dotted, solid, and dashed lines represent calculated results using low, average, and high γ_{cl} values, respectively. (a): PK model; (b): PKL model. The error bar of d represents the pore size distribution range of the host materials, while the error bar of T_m denotes the difference between peak maximum and either the onset temperature (lower limit) or the offset temperature (upper limit) of the melting peak.

8.2.2 Phase equilibria of $CaCl_2$ solutions in confinement

Figure 8−8 shows a comparison between the melting temperatures of $CaCl_2$ solutions at eutectic concentration (4.0 m) and a lower molality (0.4 m). Across full pore size range, the melting points of 0.4 m solution are consistently lower than those of the eutectic concentration. Nevertheless, the trend with respect to γ_{cl} remains consistent: experimental values match calculations using lower γ_{cl} in larger pores and higher γ_{cl} in smaller pores. This similarity suggests that salt molality has only a minor effect on γ_{cl}. Although both the temperature and concentration influence the interfacial energy, the calculated results for the 0.4 m $CaCl_2$ solutions show good agreement when a constant value from the 4.0 m solution is applied. Accordingly, the estimated γ_{cl} value of the ice−$CaCl_2$ solution can be reasonably used for constructing the phase diagram across the entire concentration range.

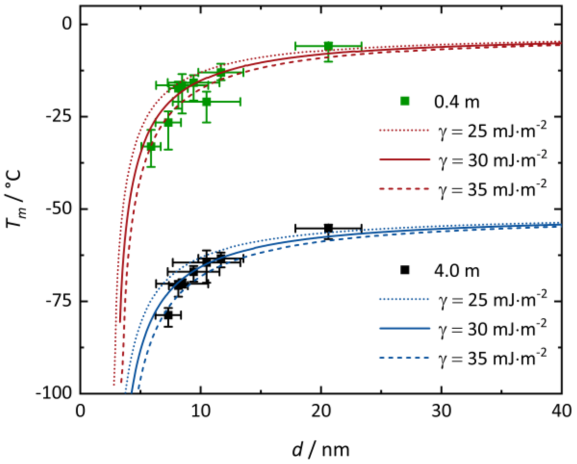

Figure 8–8. Melting points of $CaCl_2$ solutions at two concentrations (0.4 m and 4.0 m) confined within nanopores ranging from 3.8 to 20.6 nm, comparison of experimental results with curves calculated using PK model with different values of γ_{cl}. The error bar of d represents the pore size distribution range of the host materials, while the error bar of T_m denotes the difference between peak maximum and either the onset temperature (lower limit) or the offset temperature (upper limit) of the melting peak.

The melting temperatures of $CaCl_2$ solution in 9.4 nm SBA–15 calculated using PK (γ_{cl} = 30 mJ·m^{-2}), and the results are presented in Fig. 8–9. Compared to the phase diagram of the bulk solution, a significant depression of the melting point is observed in the confined system. The black squares represent the experimental melting points determined from the calorimetry thermograms of $CaCl_2$ solutions in 9.4 nm SBA–15 (as shown in Fig. 6–4a).

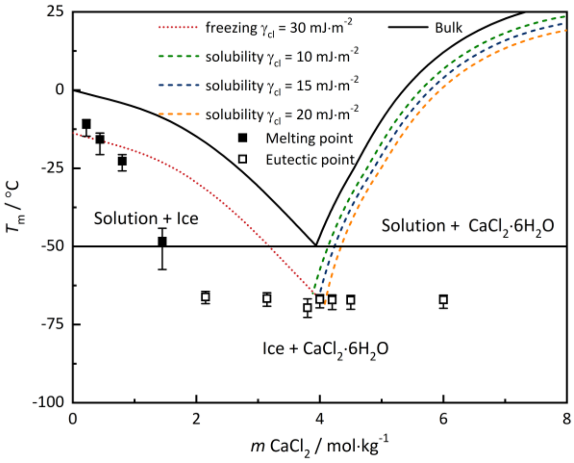

Figure 8–9. Calculated phase diagram of the $CaCl_2$–H_2O system in bulk and 9.4 nm pores with PK model; error bar of T_m denotes the difference between peak maximum and either the onset temperature (lower limit) or the offset temperature (upper limit) of the melting peak.

In the low concentration region, the experimental data align well with the calculated ice melting equilibrium curve, marked as red dotted line. Since the eutectic point corresponds to the intersection of ice melting and solubility curves, it represents an equilibrium state involving both ice melting and salt dissolution. To estimate the interfacial energy between the salt crystal and the solution (γ_{cl}), three values were used in the solubility equilibrium calculations, shown as the green, blue, and orange dashed curves. The intersection point of dotted melting curve and the blue dashed solubility curve closely matches the measured eutectic points in 9.4 nm SBA–15, suggesting that an interfacial energy of 15 mJ·m^{-2} for the $CaCl_2 \cdot 6H_2O$–solution interface is appropriate in the framework of PK model.

Using the determined interfacial energies γ_{cl} = 30 mJ·m^{-2} for the ice–liquid interface and γ_{cl} = 15 mJ·m^{-2} for the salt–liquid interface, the equilibria of the $CaCl_2$–H_2O system were calculated for the pores with diameters of 6, 10, and 16 nm using PK model. The results are presented in Fig. 8–10. It is indicated that the liquid phase region expands as pore size decreases. Notably, the melting curves exhibit a more pronounced downward shift compared to solubility curves. This disparity arises because the interfacial energy governing the ice–solution boundary is significantly different from that of the salt–solution interface, leading to a stronger suppression of the melting transition relative to the dissolution equilibrium. This asymmetric behavior causes the eutectic point to shift toward lower salt concentration in smaller pores, which contrasts with the fixed eutectic composition assumption proposed in a previous study (Meissner et al., 2016). The deviation in eutectic concentration also accounts for the appearance of the small additional endothermal peak between the bulk and the confined eutectic transitions (seen in Fig. 6–4a). These signals likely arise from solute redistribution during freezing. As freezing progresses, the liquid phase confined within the pore reaches a same composition with the bulk eutectic mixture. However, as shown in Fig. 8–10, the actual salt molality at the confined eutectic point is slightly higher the that of bulk phase, implying the presence of excess salt in the pore.

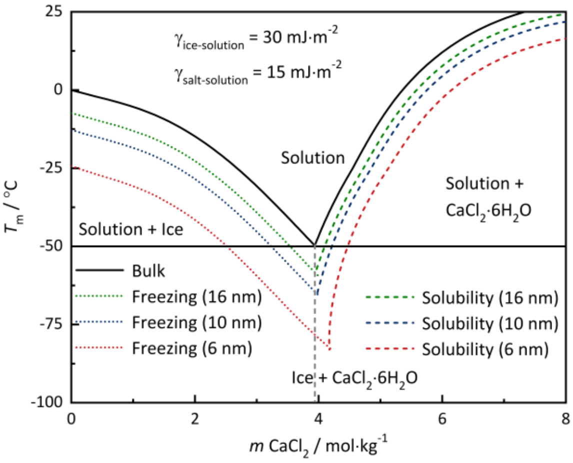

Figure 8–10. Calculated phase diagram of the $CaCl_2$–H_2O system confined within 6 nm, 10 nm, and 16 nm pores with the PK model.

8.2.3 Phase equilibria of NaCl solutions in confinement

The phase diagram of the NaCl–H_2O system for both the bulk solution and the confined solution in 8.5 nm SBA-15 are calcualted using PK model, and the results are presented in Fig. 8–11.

Evidently, the ice–solution phase boundary shift to lower temperatures within the 8.5 nm pore, and the experimenal melting points are systematically lower than the calculated ice melting curve (blue dottted curve). This deviation higlight the inherent drawback of applying a constant γ_{cl} to the while concentration and temperature domin, as interfacial energy is in reality dependent on both variables. As shown in Fig. 8–11, the interfacial energy between $NaCl_2 \cdot 2H_2O$ and solution (γ_{cl}) was determined to be 20 $mJ \cdot m^{-2}$ by adjusting the $NaCl_2 \cdot 2H_2O$ solubility curve (orange dashed line) such that its intersection with the ice melting curves coincides with the experimentally observed eutectic temperature. NaCl–solution interfacial energy (γ_{cl} = 25.6 $mJ \cdot m^{-2}$) is taken from the previous study of our group (Talreja–Muthreja et al., 2022). The calculated solubility curve of NaCl (green dashed line) intersects with that of $NaCl_2 \cdot 2H_2O$ at lower temperature and higher concentration, which is consistent with our analysis on the Fig. 7–31. This shift of the phase boundary originates from the asymmetric expansion of the different hydrates due to their distinct interfacial energies, highlighting how confinement amplifies the disparity between hydrate stability fields compared to the bulk system.

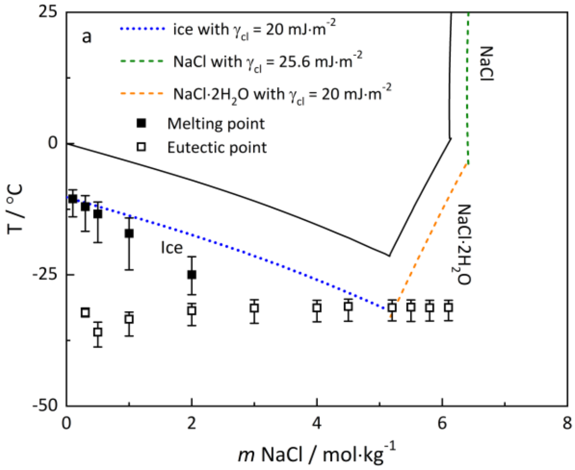

Figure 8–11. Calculated phase diagrams of the $NaCl-H_2O$ system for the bulk and for the solution confined in an 8.5 nm SBA–15, obtained using the PK model; error bar of T_m denotes the difference between peak maximum and either the onset temperature (lower limit) or the offset temperature (upper limit) of the melting peak.

8.2.4 Phase equilibria of $(NH_4)_2SO_4$ solutions in confinement

The size dependence of the eutectic points of an $(NH_4)_2SO_4$ solution was calculated using the PK model with three different values of the ice–solution interfacial energy. The calculated eutectic points (5 m) were then compared with the experimental data, as shown in Fig. 8–12. The result indicates an optimal value of γ_{cl} = 25 $mJ \cdot m^{-2}$ for ice, as presented by the black solid curve. This interfacial energy value was subsequently applied to calculate the phase equilibria calculation of $(NH_4)_2SO_4$ solution confined within 6.3 nm pore, as presented in Fig. 8–12b. The interfacial energy between an $(NH_4)_2SO_4$ crystal and its saturated solution was determined by adjusting the solubility curve (green dotted line) to intersect with the calculated ice curve (red dotted line) at experimental eutectic temperature. The resulting interfacial energy value was 20 mJ·m^{-2}.

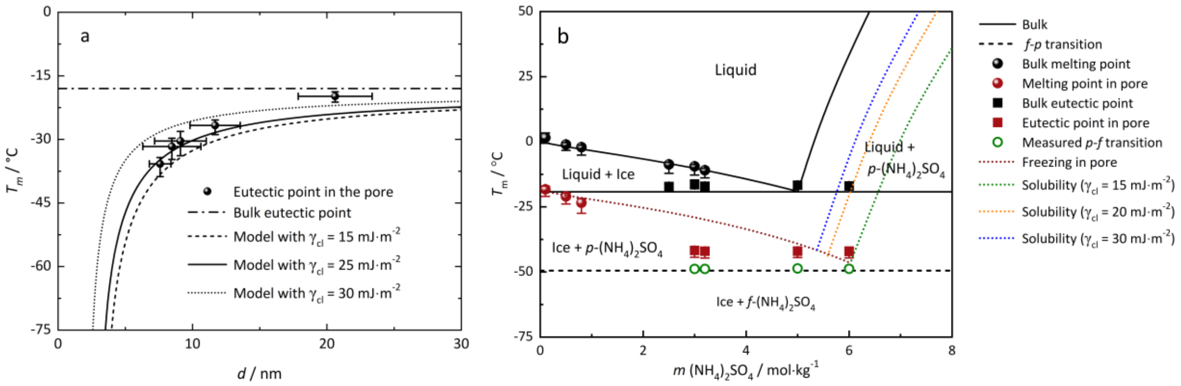

Figure 8–12. Comparison of experimental data and calculated results using the PK model with different values of crystal–liquid interfacial energies (γ_{cl}), (a): eutectic points of $(NH_4)_2SO_4$ solution confined within nanopores ranging from 3.8 to 20.6 nm; dotted, solid, and dashed lines represent calculated results using low, average, and high γ_{cl} values, respectively. (b): Phase diagram of $(NH_4)_2SO_4$ solutions confined in 6.3 nm SBA–15, comparison of experimental results with calculated curves under varying γ_{cl}. The error bar of d represents the pore size distribution range of the host materials, while the error bar of T_m denotes the difference between peak maximum and either the onset temperature (lower limit) or the offset temperature (upper limit) of the melting peak.

8.3 Deliquescence humidity of salt nanoparticles in porous silica

8.3.1 DRH of salt nanoparticles in confinement

As measured samples in the water vapor sorption experiment were less-filled during the solution impregnation, the Laplace pressure indeed appear during the during deliquescence. Therefore, the PKL model was utilized to calculate the DRHs for salt nanoparticles confined within porous silica. The contact angle in the interface of solution curvature and pore wall was assumed to be 0 °, and surface tensions and apparent molar volumes were taken from Fig. 8–3 and Fig. 8–5. The results are presented in Fig. 8–13 and compared with experimental data. Overall, the simulated DRH values agree well with experimental data when appropriate γ_{cl} are applied: 20 mJ·m^{-2}, 60 mJ·m^{-2}, 50 mJ·m^{-2}, 30 mJ·m^{-2}, and 20 mJ·m^{-2} for KCl, $MgCl_2·6H_2O$, $NaClO_4·H_2O$, $Mg(ClO_4)_2·6H_2O$, and $Ca(ClO_4)_2·4H_2O$, respectively. Among these, the DRH of $Ca(ClO_4)_2·4H_2O$ was detected only in 20.6 nm pore, and it aligns most closely with the calculated DRH curve assuming γ_{cl} = 20 mJ·m^{-2}, as marked by the purple solid curve in Fig. 8–13f.

The influence of salt–liquid interfacial energy (γ_{cl}) is not significant for KCl, only a slightly decrease in DRH is observed when γ_{cl} increases from 10 to 50 mJ·m^{-2}, as shown in Fig. 8–13a. In contrast, similar changes in γ_{cl} have a considerably larger influence on DRH of other salts, including $MgCl_2·6H_2O$, $NaClO_4·H_2O$, $Mg(ClO_4)_2·6H_2O$, and $Ca(ClO_4)_2·4H_2O$. The interfacial energy γ_{cl}

indirectly influences the water vapor pressure by enhancing the solubility of the confined salt nanoparticle, as indicated in Fig. 8−14a. However, unlike $Mg(ClO_4)_2$ and $Ca(ClO_4)_2$, the concentration increase of the weakly hygroscopic salt KCl does not substantially lower the water vapor pressure, as seen in Fig. 8−14b. Therefore, the DRH lower shift of salt in the nanopores is dominated by the curvature−induced reduction in vapor pressure at the solution−gas interface.

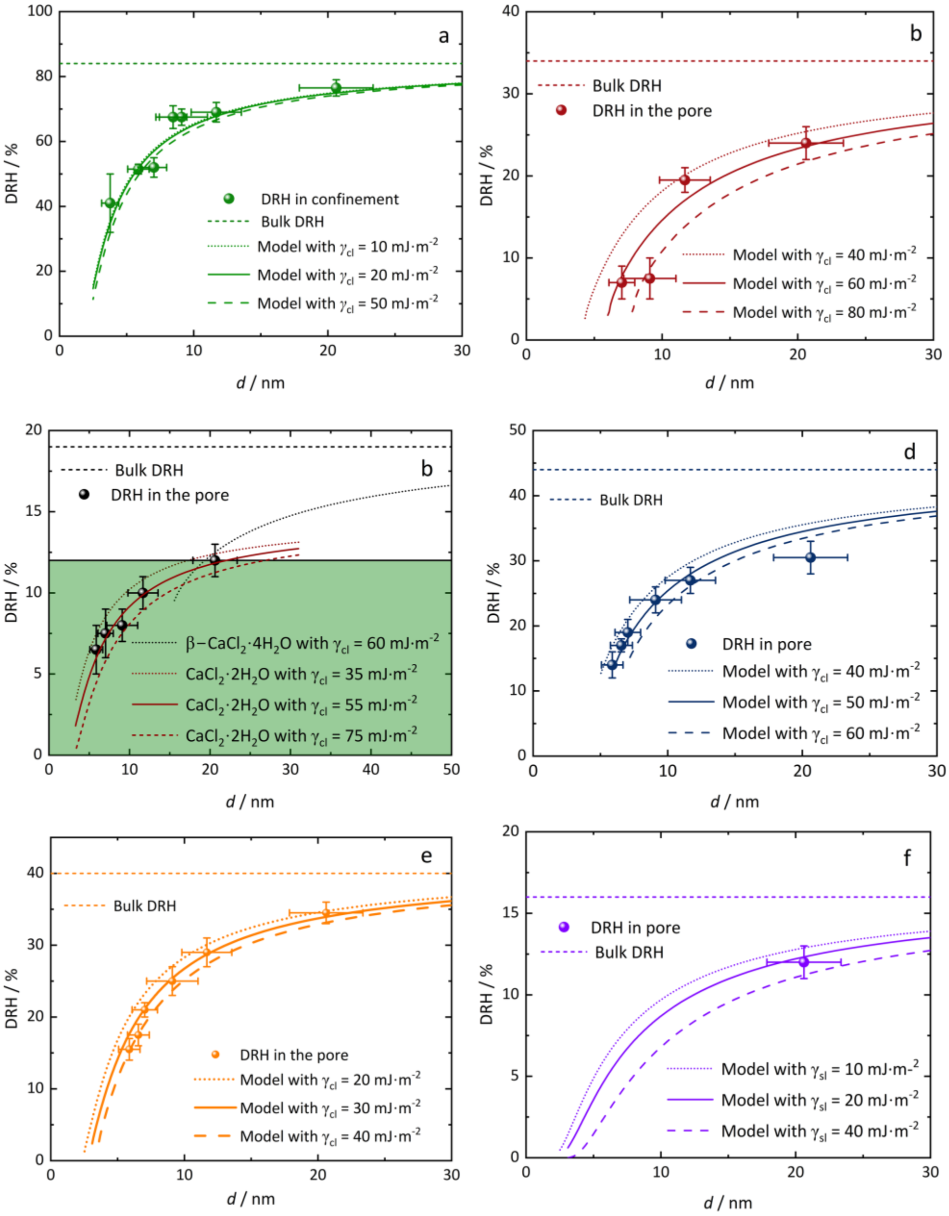

Figure 8−13. DRHs at 25 °C of chloride and perchlorate salt nanoparticles confined in porous silica with pore sizes ranging from 3.8 to 20.6 nm. Experimental data (symbols) and PKL modeled curves (lines), (a): KCl, (b): $MgCl_2\cdot6H_2O$, (c): β−$CaCl_2\cdot4H_2O$ or $CaCl_2\cdot2H_2O$, (d): $NaClO_4\cdot H_2O$, (e): $Mg(ClO_4)_2\cdot6H_2O$, (f): $Ca(ClO_4)_2\cdot4H_2O$. The error bar of *d* represents the pore size distribution range of the host materials, while the error bar of DRH or ΔDRH denotes the deviation between average value and either the onset DRH (lower limit) or the offset DRH (upper limit) of the water vapor sorption isotherm.

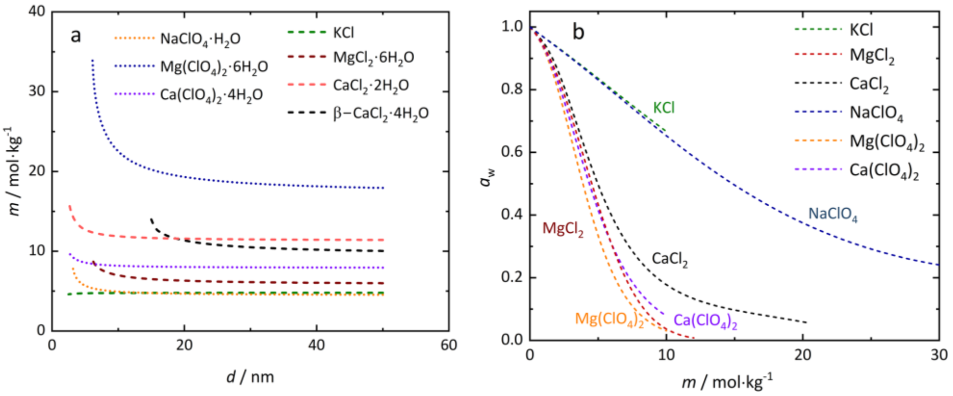

Figure 8–14. Calculated solubility of salt nanoparticles in porous silica (a), and water activity of salt solution (b) at 25 °C, obtained using PKL model.

Water vapor sorption of $CaCl_2·nH_2O$: From an experimental perspective, deliquescence is typically identified by a noticeable change in the slope of water vapor sorption isotherms, regardless the type of solid phase. However, from a modeling standpoint, it is essential to specify the solid phase in equilibrium during deliquescence. In the case of bulk $CaCl_2·nH_2O$, the water vapor sorption process involves multiple metastable phase transitions. The hydration from $CaCl_2·2H_2O$ to $β–CaCl_2·4H_2O$, followed by the deliquescence of latter, has been analyzed in detail in Chapter 5 and also in the previous publication (Wang et al., 2024). As shown in Fig. 5–8 and Fig. 5–12, the deliquescence of bulk calcium chloride hydrate occurs with $β–CaCl_2·4H_2O$, rather than the thermodynamic stable $α–CaCl_2·4H_2O$ or $CaCl_2·6H_2O$.

Herein, we assume that the deliquescence behavior of calcium chloride hydrates in porous silica follows that of the bulk phase, equilibrating with $β–CaCl_2·4H_2O$ or possibly with $CaCl_2·2H_2O$. In bulk conditions, the equilibrium hydration RH from $CaCl_2·2H_2O$ to $β–CaCl_2·4H_2O$ is approximately 12.5%. Unlike the pronounced RH depression observed for deliquescence in nanopores, hydration transitions appear to be far less sensitive to pore size, as suggested by the study from Eberbach et al., (2023). Therefore, the experimentally observed DRHs below 12.5% likely corresponds to the deliquescence of $CaCl_2·2H_2O$. The calculated DRHs for $CaCl_2·2H_2O$ and $β–CaCl_2·4H_2O$ are shown as the black dot curve and red solid curves in Fig. 8–13c, respectively. The green–shaded region indicates the RH range where deliquescence of $CaCl_2·2H_2O$ is expected. The interfacial energies (γ_{cl}) for $CaCl_2·2H_2O$ and $β–CaCl_2·4H_2O$ are roughly estimated to be 55 mJ·m^{-2} and 60 mJ·m^{-2}, respectively.

8.3.2 Limitations of the thermodynamic model

The thermodynamic model generally performs well for phase equilibrium calculations in larger pores (approximately > 5 nm), but fails to yield valid results in smaller pores. The lower limit of model applicability arises from two primary factors:

(1) The extrapolation uncertainty of thermodynamic properties at highly supersaturated solutions.

The water vapor pressure of a salt solution is dictated by its molality, which is determined by the dissolution equilibrium of the salt. Theoretically, the chemical potential of a salt nanoparticle is elevated relative to that of its bulk counterpart due to the contribution of surface energy. The chemical potential of the salt MX(aq) can be expressed as:

$$\mu_l = \mu_l^\circ + RT\ln\left(\mathrm{a}_M^{\mathrm{n}}\mathrm{a}_X^{y}\mathrm{a}_W^{z}\right) = \mu_l^\circ + RT\ln Q \qquad (8\text{–}6)$$

where Q reflects the ion activity product. In order to achieve equilibrium with a nanoparticle, the ion activity of MX(aq) in the liquid phase need to increase, implying a higher solubility than that in the bulk. As shown in Fig. 8−14a, the calculated solubility increases significantly in the pores below 10 nm. However, in PKL or PK model, the value of ln$Q$ tends to plateau (e.g., for KCl and $NaClO_4 \cdot H_2O$) or even decline (e.g., for $CaCl_2 \cdot 4H_2O$) at molalities far beyond bulk solubility limits (Fig. 8−15a), indicating an inability to achieve dissolution equilibrium regardless of further increase in salt molality. This plateau or decrease in ln$Q$ is physically unreasonable and limits the model's applicability in strongly confined space (< 5 nm), where the solubility product salt is significantly larger than in bulk. This issue stem from the limitation of parameter extrapolation. Like other semi−empirical models, the Pitzer model parameters are obtained through regression of experiment data, (e.g., water activity and activity coefficient) and are reliable within the validated temperature and concentration range. However, in extrapolated regions (the green area in Fig. 8−15b), the predicted thermodynamic properties may appear plausible yet carry considerable uncertainty. The potential deviation in activity coefficient or water activity can result in unphysical ln$Q$ behavior in highly supersaturated regions.

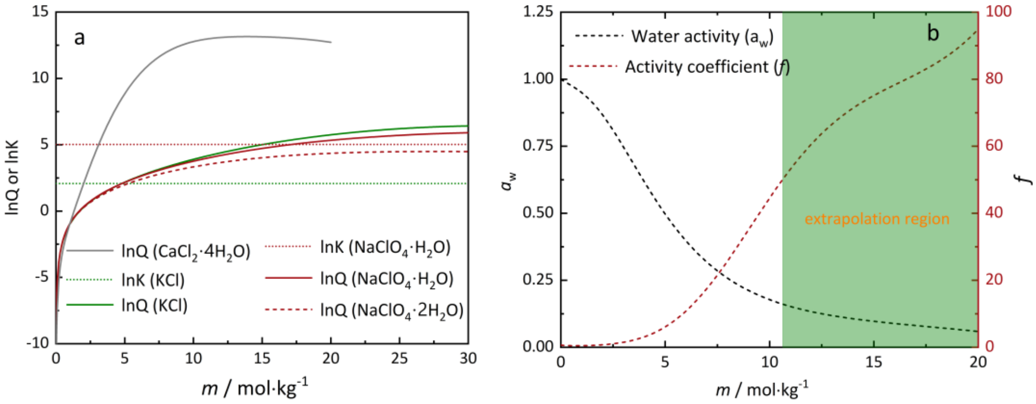

Figure 8−15. (a): Comparison of the natural logarithms of the solubility product constant (ln$K$) and the ionic activity product (ln$Q$) for KCl, $CaCl_2 \cdot 4H_2O$, and $NaClO_4 \cdot H_2O$ (or $NaClO_4 \cdot 2H_2O$) at 25 °C; (b): Water activity and mean activity coefficient of $CaCl_2$ solutions as a function of molality at 25 °C.

(2) The influence of interfacial energy in strong confinement

In smaller pores (approximately < 5 nm), the solubility of salt nanoparticle is strongly influenced by both particle size and salt–solution interfacial energy (γ_{cl}). Unlike bulk system, where thermodynamic variables depend solely on temperature and pressure, the confined solution is influenced by additional interfacial forces. During deliquescence, the solution is trapped between the salt crystal and the pore wall. When these interfaces are in close proximity, the interaction of two interfaces significantly alters the chemical potential of the confined solution, contributing an additional interfacial energy term $\Delta\gamma$ (Wang et al., 2025). For computational simplicity, the γ_{cl} was assumed constant across all concentrations and pore sizes in this study. Although this assumption facilitates modeling, it introduces inaccuracies under strong confinement, leading to poor predictive performance.

In summary, while extrapolation is a known limitation of empirical models, it also highlights the exploratory power of modeling in extreme conditions, such as nanoscale confinement. The key question is how far such model can be extended beyond the available experimental data while retaining physical relevance.

8.3.3 Modeling of water vapor sorption isotherm

Deliquescence refers to the phase transition from a crystalline solid to a saturated salt solution, typically characterized by a sharp increase in water uptake at a critical relative humidity (known as DRH) in the water vapor sorption measurements. For a bulk crystal, this transition at well–defined relative humidity values. In contrast, for confined salt particles, deliquescence occurs gradually over a broader humidity range, as illustrated in Fig. 7–30 and Fig. 7–33. A representative example is the water vapor sorption behavior of KCl in the 7.0 nm pore silica, as presented in Fig. 8–16a. Unlike the sharp sorption profile of bulk KCl, the confined system shows initial water uptake at very low humidity, increasing progressively before a more abrupt rise near the DRH. The gradual uptake at low humidity is attributed water adsorption on the pore walls, while the continuous increase near 60% RH corresponds to the deliquescence of KCl within the nanopores.

The finite slope in the vapor sorption curve at the deliquescence step reflects the influence of pore size distribution of the host material, which was presented in Fig. 4–1. The SBA-15 silica with pore size maximum at 7.0 nm exhibits a distribution primarily spanning from 5 nm to 10 nm, resulting in a range of DRH from approximately 47% to 65%. The volume fraction of porous material (Ø) at each pore size was calculated using the expression:

$$\emptyset = \frac{\mathrm{d}v\times(d_{\mathrm{p(i+1)}}-d_{\mathrm{p(i)}})}{\sum_i^j \mathrm{d}v\mathrm{d}d_{\mathrm{p}}} \qquad (8\text{–}7)$$

Where dv is the differential pore volume at each pore diameter, $d_{\mathrm{p(i)}}$ and $d_{\mathrm{p(j)}}$ denote the starting and ending pore diameters of integrated area, respectively, within the range from 0 to 50 nm. It is assumed that, at each RH, the water uptake arises solely from the deliquescence of the KCl confined within the pores of the corresponding size, where saturated KCl solution is formed and completely fills pore volume. Based on this assumption, the adsorbed water content as a function of RH and pore size was calculated using PKL model. To enable a direct comparison with the water vapor sorption behavior of the KCl-loaded 7.0 nm SBA-15, the calculation was restricted to the same pore size distribution and volume fraction as in the experiment. The resulting water uptake is plotted against RH in Fig. 8–16b, together with the experimental data (red sphere), which were obtained from the differential of the water vapor sorption curve shown in Fig. 8–16a.

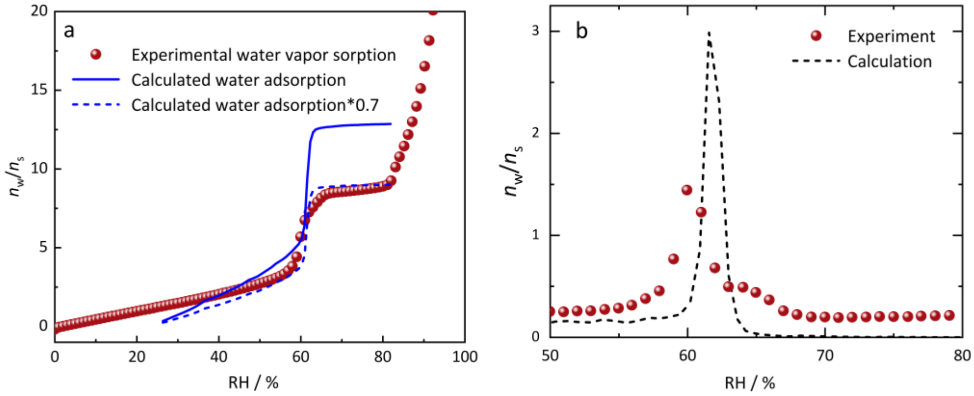

Figure 8–16. (a): water uptake of KCl in porous silica as a function of relative humidity; (b): the water vapor sorption isotherm of KCl nanoparticle in 7.0 nm porous silica at 298.15 K.

The calculated water uptake curve (black dashed line) is narrower and reaches a higher maximum than the experimental derivative data (red sphere), yet the primary region of water uptake corresponds well with the experimental observation. The blue solid curve in Fig. 8–16a, obtained by integrating the black dashed curve from Fig. 8–16b, represents the total calculated water uptake as a function of relative humidity. This curve aligns closely with the experimental data (red sphere) in the initial adsorption region (prior to deliquescence), but significantly overestimate the uptake during the deliquescence transition. To account for this, a scaled curve (blue dashed line, 70% of the calculated value) is also plotted, demonstrating improved agreement with the experimental data. This comparison supports the conclusion that the water vapor sorption behavior of the composite is strongly inherited from the pore size distribution of the host porous silica. The apparent overestimation of the calculated water content, as evidenced by the solid blue curve in Fig. 8–16b, can primarily be ascribed to the substantial uncertainty associated with the solubility-equilibrium calculations. Since the concentration of KCl solutions exhibit only a week dependence on water activity, even larger derivations in the calculated solubility exert little influence on the predicted DRH values within the nanopores. As a result, the measured uptake falls below the theoretically predicted values derived from the PKL model.

8.4 Conclusion

In this Chapter, the phase equilibria of confined salt solutions, including NaCl, KCl, $MgCl_2$, $CaCl_2$, $NaClO_4$, $Mg(ClO_4)_2$, $Ca(ClO_4)_2$, and $(NH_4)_2SO_4$, were systematically investigated through modeling of ice melting points, eutectic points, and deliquescence relative humidities. Available surface tension of salt solutions and apparent molar volumes at infinite dilution were critically evaluated, and physically reasonable extrapolations were performed to extend the model lower temperatures and higher concentrations. Two modeling scenarios were introduced, PK (Pitzer–Kelvin) and PKL (Pitzer–Kelvin–Laplace), to examine the influence of Laplace pressure on the ice melting and salt dissolution equilibria. These simulations showed good agreement with the experimental data when appropriate values for the ice–solution (γ_{cl}) and the salt–solution (γ_{cl}) interfacial energies were applied. Furthermore, the limitation of the model under strong nanoconfinement (< 5 nm), were analyzed from the perspective of solution activity coefficient and interfacial energy (γ_{cl}). Additionally, the influence of pore size distribution of silica host materials on the vapor sorption was also addressed. The major findings are summarized below:

(1) Depression of ice melting and eutectic temperatures

Both the melting and eutectic points of aqueous solutions confined in nanopores shift downward with decreasing pore size. This depression arises primarily from two factors: the interfacial energy between the crystal and the solution, and the Laplace pressure imposed by the concave solution–vapor interface. To disentangle these effects, two thermodynamic frameworks were compared: the PK model, which combine Pitzer theory with the Kelvin equation, and the PKL model, which further incorporates the contribution of Laplace pressure. PKL model compensates for salting-out effects induced by negative Laplace pressure through enhanced crystal-solution interfacial energy (γ_{cl}). This correction become especially important for salts that undergo substantial volume change upon dissolution, and it provides a consistent explanation for the shifts and boundary displacement observed in the confined phase diagrams.

(2) Deliquescence in confinement

The depression of the deliquescence relative humidities in confined salts arises from the combined effect of concave solution–vapor interface and the presence of dissolved ions. The curvature of the confined meniscus lowers the vapor pressure, while ion–solvent interactions further reduce the equilibrium humidity. Within the framework, the interfacial energy (γ_{cl})

between the salt nanocrystal and the surrounding solution is accounted for, leading to enhanced solubility and a corresponding decrease in water activity. At same time, the negative Laplace pressure introduced in confined pores is incorporated as a counteracting factor in the model, which may reduce solubility and increase water activity. Beyond shifting DRHs to lower humidity, confinement can also alter solid-phase stability. The PKL model captures this behavior, for example in multi-hydrate systems such as $CaCl_2 \cdot nH_2O$, where confinement not only depresses DRHs but also stabilizes lower hydrates as the equilibrium solid phase.

(3) Water uptake behavior

In contrast to the sharp deliquescence step characteristic of bulk salts, confined systems exhibit a progressive water uptake. This continuous increase reflects the pore size distribution with in the host material, where smaller pore deliquescence at lower relative humidities while larger pores contribute at higher humidities. As a result, the overall sorption profile becomes broadened, directly linking the confinement-induced shift of DRHs to the heterogeneity of the pore network.

In summary, the thermodynamic model that integrates Pitzer theory, the Kelvin equation, and Laplace pressure successfully captures phase equilibria shifts in larger pores (> 5 nm), including ice melting, salt dissolution, and deliquescence. However, its applicability diminishes in smaller pores (< 5 nm). The primary limitations of the model stem from the lack of reliable thermodynamic data, such as surface tensions, activity coefficients, and solution molar volumes, under supercooled and highly supersaturated conditions. Moreover, the assumption of a constant crystal–solution interfacial energy breaks down at strong confinement, further undermining model accuracy. These constraints highlight the limitation of semi–empirical model in extreme nanoscale environments. Coupling with molecular simulations may offer a promising pathway to overcome these challenges, providing physically grounded insights in regimes where empirical model struggle.

Chapter 9. Water film: the motor of phase transitions of salt mixtures

The presence of water film on the crystal surface induces the deliquescence of soluble electrolytes and causes powder agglomeration (Dupas–Langlet et al., 2015), it also facilitates solid–solid reactions of salt particles, such as hydration reactions (Steiger et al., 2008b; Houben et al., 2022). This process involves the dissolution of the educt phase and nucleation of the product phase within the nano- or microscale water film. In multicomponent systems, phase transitions or chemical reactions are frequently observed when exposed to water vapor. These processes, such as mutual deliquescence of salt mixtures, the formation of double salts or solid solutions, and other chemical reactions are facilitated by the water film compared to direct solid–solid reactions. Numerous studies investigated nanoscale interfacial reactions in various systems using advanced techniques. These studies have primarily focused on microscale salt–water interfacial interactions in binary salt–water systems. However, in multicomponent systems, exposure to water vapor often leads to more complex phase transitions and chemical reactions, such as mutual deliquescence of salt mixtures, the formation of double salts or solid solutions, and other water film-facilitated chemical reactions. The underlying mechanisms driving these processes remain insufficiently understood. Although capillary condensation has been proposed to explain the mutual deliquescence of salt mixtures in contact with water vapor, direct experimental evidence on the specific role of a water film in this process is still lacking. Therefore, it is essential to experimentally elucidate the initiation and progression of these reactions in salt mixtures upon exposure to water vapor.

In this Chapter, dynamic water vapor sorption, Raman spectroscopy, and environmental scanning electron microscopy (ESEM) were used to probe the role of the water film in phase transitions of a reciprocal quaternary salt systems, Na^+–Cl^-–K^+–NO_3^-//H_2O. Our goal was to elucidate the contribution of the water film to the mutual deliquescence of the ternary salt mixtures, and, for the first time, to understand its role in the transformation of the metastable salt pair according to $KCl + NaNO_3 \rightarrow NaCl + KNO_3$ and $NaCl + (NH_4)_2SO_4 \rightarrow NH_4Cl + Na_2SO_4$. The influence of relative humidity of the latter solid-state reaction is particularly interesting as water is not involved in the reaction equation. The findings provide a detailed explanation of the mechanisms of vapor–solid and solid–solid reactions in analogous systems.

9.1 Experiments

9.1.1 Water vapor sorption

Water vapor sorption isotherms of two reciprocal quaternary systems: Na^+–Cl^-–K^+–NO_3^- (ten samples: NaCl, KCl, $NaNO_3$, KNO_3, NaCl + KCl, NaCl + $NaNO_3$, KNO_3 + KCl, KNO_3 + $NaNO_3$, KCl + $NaNO_3$, and NaCl + KNO_3), and Na^+–Cl^-–NH_4^+–SO_4^{2-} (nine samples: NH_4Cl, Na_2SO_4, $(NH_4)_2SO_4$, NH_4Cl + NaCl, NH_4Cl + Na_2SO_4, NH_4Cl + $(NH_4)_2SO_4$, $(NH_4)_2SO_4$ + NaCl, $(NH_4)_2SO_4$ + Na_2SO_4, and Na_2SO_4 + NaCl) were measured using an SPSx−1μ moisture sorption analyzer (ProUmid GmbH). In the SPSx−1μ up to 23 samples are placed in dishes in a temperature and relative humidity (RH) controlled chamber. The dishes are automatically positioned on the load cell of a microbalance and the samples are weighed at predefined time intervals (30 min in this study). Samples of approximately 50 mg were used in each measurement and all mixtures had a molar ratio of 1:1. Isotherms were collected at 25 °C by increasing the RH from 0−95% in 2% steps and a hold time of 10 h at each humidity step. A detailed investigation of the hold time in deliquescence measurements was carried out recently (Stahlbuhk et al., 2025b). The measurement conditions selected in the present study (50 mg sample size and 10 h hold time) are sufficient to detect the deliquescence step in the water uptake curves reliably while still keeping the measurement times acceptable (Stahlbuhk et al., 2025b).

9.1.2 Environmental scanning electron microscopy

Phase transformations on crystal surfaces or at crystal interfaces of salt mixtures were investigated using environmental scanning electron microscopy coupled with energy−dispersive X-ray spectroscopy (ESEM−EDX, EVO system, Carl Zeiss Microscopy GmbH). Measurements aimed to observe *in-situ* topology changes and variations of the elemental composition. To achieve a broad relative humidity range in the high-vacuum chamber, ESEM was performed at 3 °C with the chamber containing only water vapor. Relative humidity was derived from the chamber pressure by $RH = (p/p_{sat}) \times 100$, with $p_{sat} = 758$ Pa at 3 °C. Thus, for example, the working range was 1.3% RH at $p = 10$ Pa and 82.5% RH at $p = 625$ Pa. Pressures were incremented between minimum and maximum pressures of 10 Pa and 625 Pa, respectively. Each setpoint was held constant until pressure stability and stage temperature drift < 0.1 °C were achieved before imaging. Other experimental parameters include an accelerating voltage (Extra High Tension, EHT) of 20.00 kV, a LaB6 (lanthanum hexaboride) cathode filament, and an NTS BSD detector (nano Technology Systems BackScattered). Unless otherwise specified, all micrographs were captured at a magnification of 208×.

ESEM experiments were conducted with a self-grown NaCl single crystal, a NaCl + KCl salt mixture, a mixture of self-grown single crystals of NaCl and KCl and a mixture of $NaNO_3$ and KCl. Prior to SEM imaging, the samples were dried at 50 °C and 1% RH for 30 minutes to remove the adsorbed water accumulated during sample preparation

9.1.3 Time–lapse microscopy

The deliquescence behavior of NaCl, KCl, and their mixture was documented using time–lapse micrographs captured with a 3D–digital microscope (HIROX) with the following setting: 100× to 200× magnification, lens MXG–2500REZ; KH–8700, with a view field diameter of 2079.49 µm and 1.30 µm resolution. The experiments were conducted in a climate–controlled chamber equipped with a glass window, where the relative humidity in a 0.2 $L \cdot min^{-1}$ constant gas flow of nitrogen was controlled using a humidity generator GenRH/Mcell (ProUmid GmbH) with a HC2–IC 102 humidity probe (Rotronic). All observations were performed at room temperature (20 ± 1 °C).

9.1.4 Raman spectroscopy

Raman reference spectra of $NaNO_3$ and KNO_3 were collected on a Senterra Raman dispersive microscope (Bruker Optics GmbH). The laser was operated at 532 nm and 20 mW with an integration time of 10 s and spectra were recorded in the 20–2500 cm^{-1} spectral range. Additional *in-situ* Raman spectra were collected during the water vapor sorption experiments using a WP 785 nm laser (Wasatch Photonics) operated at 450 mW and 200 ms integration time (two scan average). Spectra were recorded in the range 270–2000 cm^{-1} with 7 cm^{-1} resolution and a working distance of 50 mm. The Raman probe was positioned on the glass-top cover of the SPSx-1µ instrument (ProUmid GmbH, Germany). Spectra were recorded during the water vapor sorption of the $NaNO_3$ + KCl mixture, humidity was increased in 2% increments in the range 28–73% RH with a hold time of 5 h at each step.

9.2 Results and Discussion

9.2.1 Water adsorption on a NaCl surface

Micrographs of a NaCl single crystal were collected across a range of relative humidity from 1.3% to 82.5% RH at 3 °C and elemental mapping using energy-dispersive X-ray spectroscopy (EDX) was conducted at each RH step, selected images are shown in Fig. 9–1. Although water was not observed visually on the crystal surface at 1.3% RH, elemental analysis revealed a few oxygen-rich regions, as highlighted by the orange circle in Fig. 9–1c. Given that neither NaCl nor the carbon substrate contains oxygen, these areas are attributed to water molecules either as newly adsorbed water or as residual water after drying. EDX micrographs (Fig. 9–1c to Fig. 9–1f) demonstrate the variation in oxygen density on the NaCl surface with changing relative humidity. At 75% RH, just below the DRH of NaCl (76% at 3 °C), oxygen (green spots) almost uniformly covers the surface. At 82.5% RH, the crystal surface is dominated by oxygen indicating the formation of the bulk solution film. Quantitative analysis at 1.3% RH yields weight fractions of 1.6% (oxygen), 54.0% (chlorine), 37.1% (sodium) and 5.6% (carbon substrate). The weight fraction of oxygen increases to 52.8% at 82.5% RH. Figure 9−1b illustrates the increasing amount of surface water with increasing RH as measured by the oxygen weight fraction, and an EDX elemental mapping image of oxygen is shown in Fig. 9−2. Notably, a change of the slope above 60% RH suggests the beginning of ion mobilization and the formation of a solution film.

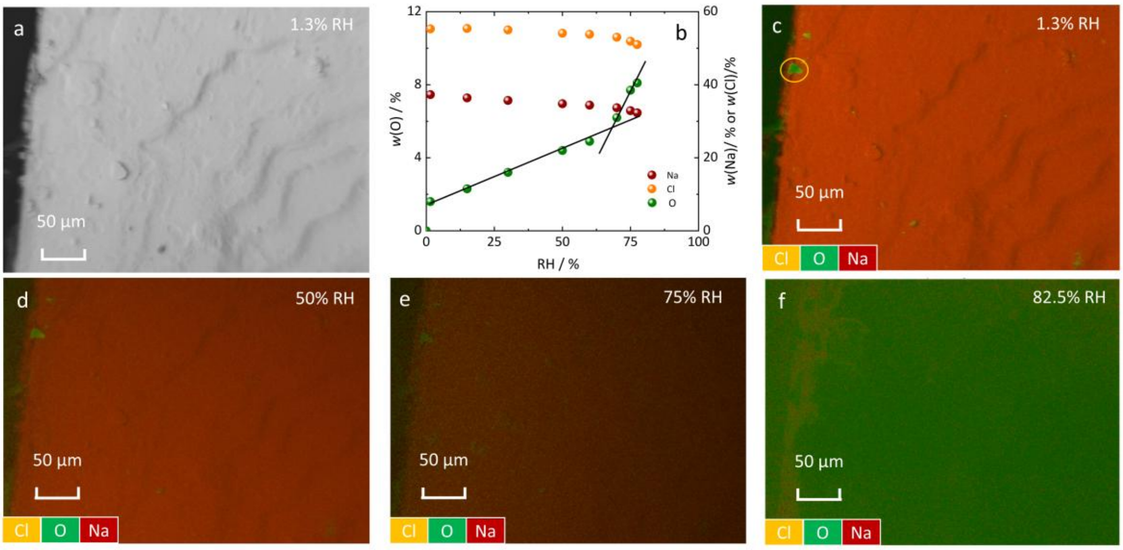

Figure 9−1. Illustration of the crystal surface topology (ESEM images a) and elemental distribution (EDX images c, d, e, f) with changing RH; EDX elemental mapping: sodium (red) chlorine (orange), and oxygen (green); (b) weight fractions of oxygen $w(\mathrm{O})$ (H_2O), sodium $w(\mathrm{Na})$ and chlorine $w(\mathrm{Cl})$ on NaCl surface vs. relative humidity. Black lines in Figure 9−1b are drawn to guide the eyes.

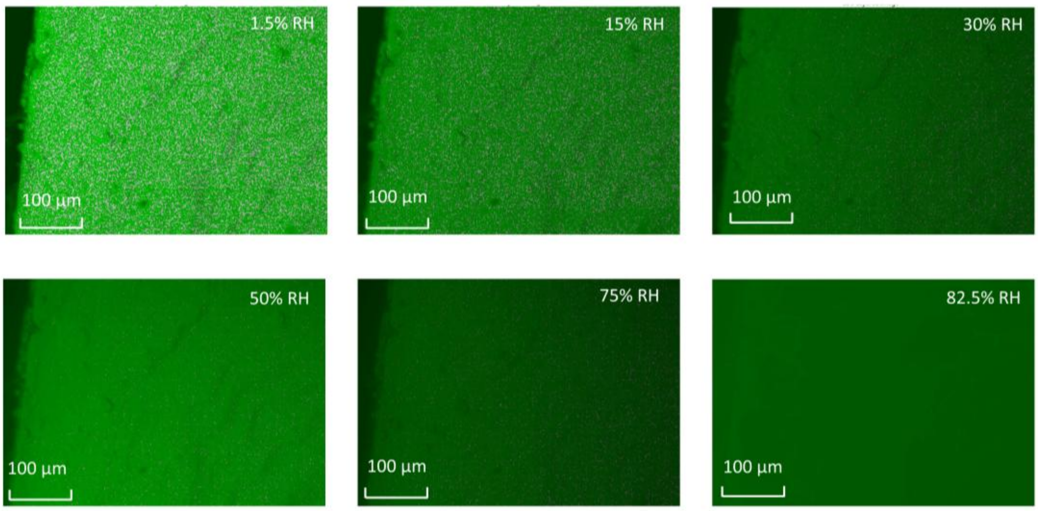

Figure 9−2. EDX elemental mapping of oxygen distribution on the NaCl surface as the relative humidity increases from 1.3% to 82.5% RH.

Unlike water condensation in the atmosphere or on hydrophobic surfaces, the formation of an adsorbed water film on the NaCl crystal surface helps to bypass the nucleation barrier for the water liquefaction. Instead, condensation at higher humidity is driven by the reduced water activity in the brine on the crystal surface rather than by the solid–gas interaction. These results are in line with infrared spectroscopy and X-ray photoelectron spectroscopy studies (Peters and Ewing, 1997a; Verdaguer et al., 2008; Dai et al., 1997), in which the water adsorption on a NaCl surface has been categorized into three stages: (1) adsorption of isolated water molecules (0–30% RH), (2) multilayer water adsorption (30%−50% RH), (3) bulk−like water film formation (50% to DRH). Ion solvation and ion mobility begin below 50% RH, corresponding to approximately two to three water layers on the crystal surface, allowing for the formation of a three-dimensional structure around hydrated ions (Peters and Ewing, 1997a; Verdaguer et al., 2008; Dai et al., 1997). Enhanced ion mobility facilitates the formation of hydrated ion clusters, increasing the amounts of available sites for further water adsorption, and enhancing water vapor sorption above 60% RH. According to a previous study (Bruzewicz et al., 2011), the thickness of this film reaches approximately 5 nm at 75% RH, which is close to the DRH of NaCl at 25 °C. This film thickness is sufficient for ion solvation, thus, it is best considered as a brine film as supported by both experimental observations (Verdaguer et al., 2008; Lin et al., 2021; Dai et al., 1997; Verdaguer et al., 2005; Bruzewicz et al., 2011) and thermodynamic considerations (Bruzewicz et al., 2011). The investigation in ESEM and EDX elemental mapping offers a new insight into the water adsorption behavior on NaCl crystal surfaces.

9.2.2 Mutual deliquescence of ternary salt mixtures

Water vapor sorption isotherms for pure NaCl, KCl, $NaNO_3$, KNO_3, and their ternary mixtures are shown in Fig. 9−3. It is evident that the mutual deliquescence relative humidity (MDRH) of the four salt mixtures (indicated by the black dots in pictures from Fig. 9−3a to Fig. 9−3d) is lower than the deliquescence humidities (DRH) of the pure salts in all four cases. The depression in MDRH was also confirmed through time−lapse optical microscopy observations of the NaCl + KCl system, as shown in Fig. 9−3e and Fig. 9−3f. In this setup, adjacent NaCl and KCl crystals simulate a salt mixture, while isolated NaCl and KCl crystals serve as pure salt references for comparison. As illustrated in Fig. 9−3f, the NaCl + KCl mixture begins to transform into a droplet at a certain humidity level, indicating the onset of deliquescence, while the isolated NaCl and KCl crystals still remain stable.

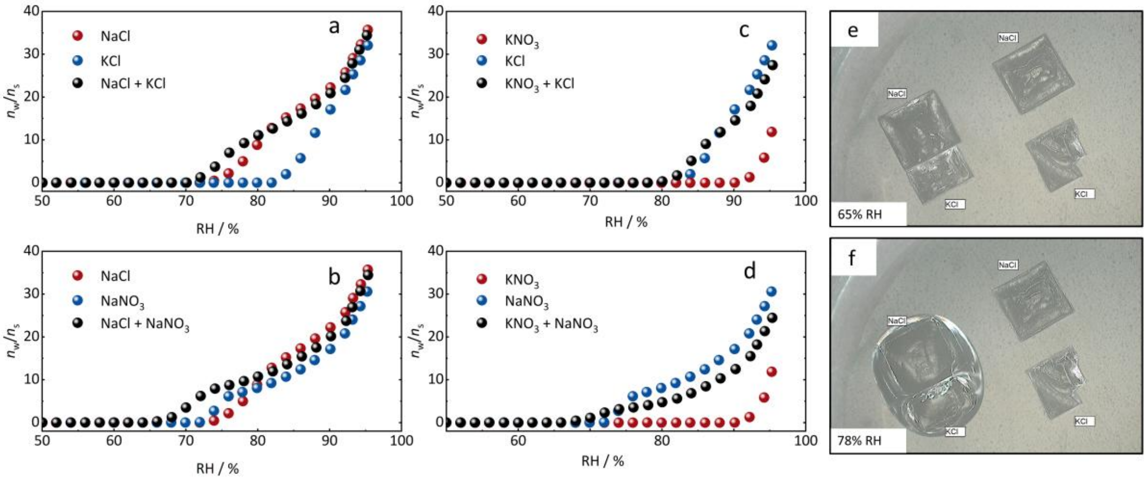

Figure 9−3. Water vapor sorption curves of pure NaCl, KCl, $NaNO_3$, KNO_3 and their ternary mixtures at 25 °C. e−f: micrographs of the NaCl + KCl at 65% RH (e) and 78% RH (f).

This shift agrees with both theoretical considerations as discussed below and with model calculated MDRH of the four mixtures provided in the Figs. 9−4 and 9−5. The solubility diagrams of the ternary systems NaCl–KCl–H_2O, NaCl–$NaNO_3$–H_2O, $NaNO_3$–KNO_3–H_2O, KCl–KNO_3–H_2O have been calculated using the same thermodynamic model used to calculate the phase diagram of the reciprocal system. This model has been validated using experimental solubility which are reproduced to within experimental data by the model calculations (Steiger et al., 2008a).

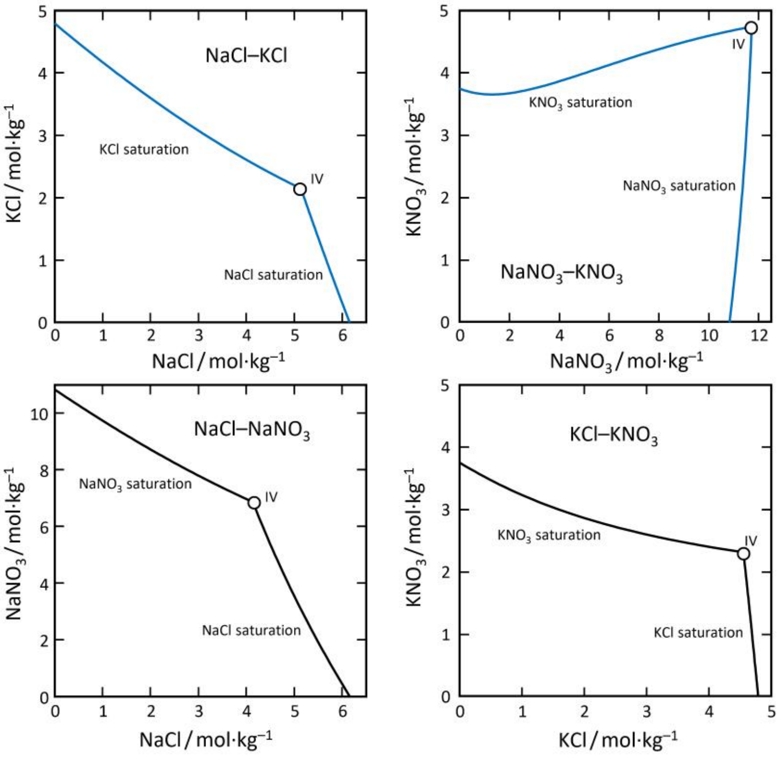

Figure 9−4. Solubilities in the four ternary systems, solid phases as indicated (symbols represent invariant points, IV).

The solubilities in the four ternary systems are presented in Fig. 9–4. Each line represents the solubility of one salt upon increasing the concentration of the second salt. The intersection of the two curves represent the invariant points (IV), i.e., the solutions saturated with respect to both salts. Figure 9–5 presents the water activities of the saturated solutions shown in Fig. 9–4 versus the mole fraction composition, i.e., the relative humidity in equilibrium with these solutions. Again, the intersection of two respective curves is the equilibrium humidity (water activity) of the solutions that are saturated with respect to both solids. At lower relative humidities, a solution is not stable and both salts are in the crystalline state. Therefore, the water activity of the solution saturated with both salts equals the mutual deliquescence humidity (MDRH) of the respective mixture, i.e., the relative humidity at which deliquescence starts. In agreement with theory, it is obvious the saturation water activities decrease with increasing concentration of the second salt such that the MDRH is always lower than the DRH of both single salts. The calculated values of the MDRH are in good agreement with the experimental data shown in Fig. 9–3, in particular, if it is considered that the water vapor sorption measurements are dynamic rather than equilibrium measurements.

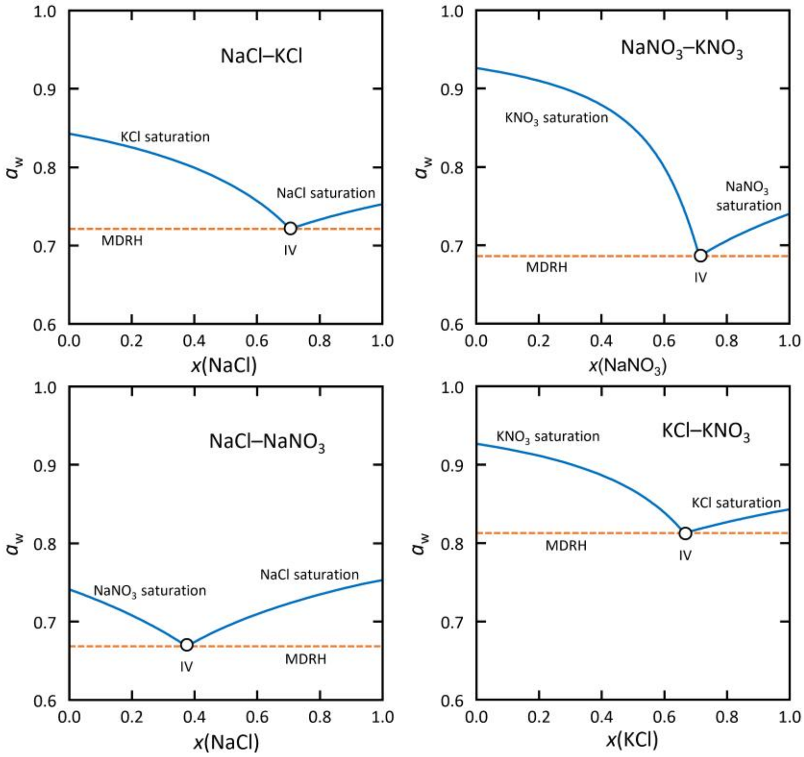

Figure 9–5. Water activities aw of saturated and mutual deliquescence humidities (MDRH), a_w at the invariant points.

To further explore this process on a smaller scale, water adsorption in a NaCl + KCl mixture was observed in the ESEM imaging mode at various RHs. Figure 9–6a shows the initial morphology of two crystals, KCl (top) and NaCl (bottom), connected by a narrow bridge. The EDX elemental mapping in Fig. 9–6b reveals that certain areas of each crystal were contaminated by the other during sample preparation, visible as red shading on the KCl and the green strip (highlighted by the orange circle) on the NaCl surface. The shape of these contaminated areas, indicated by variable brightness in the SEM micrograph (Fig. 9–6a, orange circle), aligns well with the EDX image in Fig. 9–6b. Upon exposure to water vapor, the liquid droplet first appears in the contaminated areas at 79% RH, as indicated by the orange circle in Fig. 9–6e. This droplet formation results from the mutual deliquescence between contaminant KCl and NaCl substrate. However, the droplet remained localized, unable to spread across the entire crystal, as the limited amount of contaminant KCl was quickly depleted, preventing further deliquescence. At the NaCl–KCl interface, the salt bridge begins to become liquid at 80% RH, as highlighted by the green cricle in Fig. 9–6f. As time progressed and humidity increased, ions from both KCl and NaCl continuously diffuse into the liquid bridge, leading to its expansion and, eventually, to the liquefaction of the entire system.

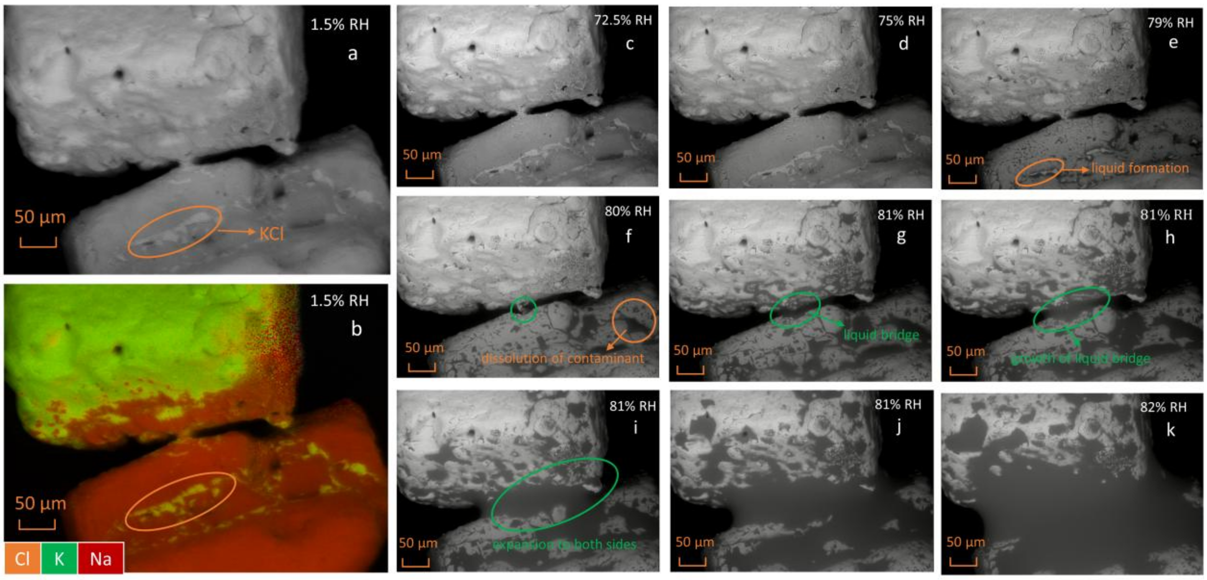

Figure 9–6. SEM micrograph (a) and EDX elemental mapping (b) of two adjacent NaCl and KCl crystals at 1.5% RH (green: potassium, red: sodium, orange: chloride); (c)–(k): SEM micrographs of the two crystals at various RHs and 3 °C.

To better assess the process at the interface, a pair of NaCl and KCl crystals with smoother surfaces were grown and placed next to each other (Fig. 9–7). These crystals allow for a closer contact area than the standard commercial crystals used before (Fig. 9–6). Water vapor sorption and deliquescence in the interfacial area as observed by SEM is presented in Fig. 9–7 within a humidity range of 75% to 77%. The results indicate that a liquid film forms along the edge of microcrystal on the crystal surface at 75% RH, seen in the orange circle in Fig. 9–7a. It is assumed that a liquid film, just as observed in Fig. 9–6 on the crystal surfaces, also forms in the contact area of the crystals though it is not visible in the micrographs. At 77% RH, the formation of liquid in the interface region is evident and at constant RH the deliquescence process continues.

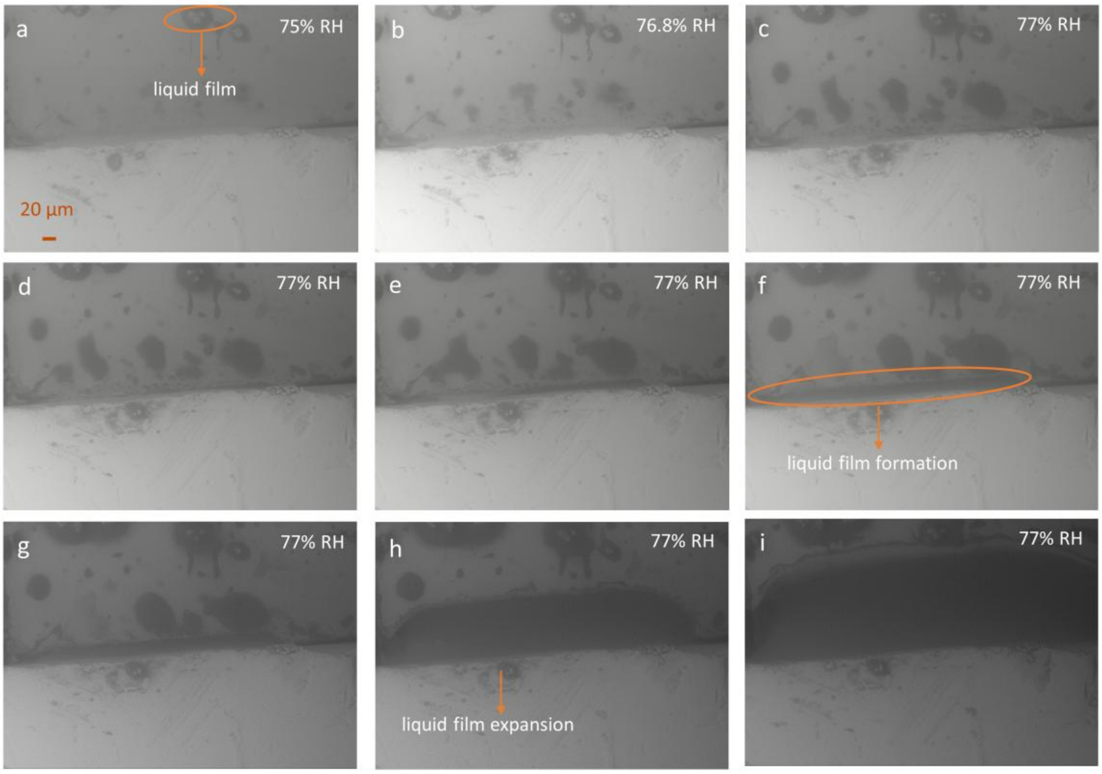

Figure 9−7. SEM micrographs during the formation of a liquid film at the interface between two crystals of NaCl (top) and KCl (bottom).

To understand why salt mixtures exhibit a lower mutual deliquescence relative humidity compared to the respective pure components, it is necessary to interpret this phenomenon from both thermodynamic and dynamic perspectives, focusing on the conditions for equilibrium and the onset of liquefaction at lower humidity. Thermodynamically, deliquescence represents an equilibrium between the crystalline solid, the saturated solution and water vapor. Thus, the relative humidity equals the water activity of the saturated solution. In this equilibrium, the aqueous solution acts as a bridge that facilitates interaction between water vapor and salt crystal, maintaining the balance of salt dissolution−crystallization and water evaporation−condensation. Wexler and Seinfeld (1991) demonstrated on thermodynamic grounds, using the Gibbs−Duhem equation, that the water activity of a solution saturated with respect to a solid is always lower in the presence of a second solute. To illustrate this, we consider a saturated aqueous solution of an electrolyte 1 (e.g., NaCl) to which a second electrolyte 2 (e.g., KCl) is added. The Gibbs−Duhem equation for this solution is:

$$n_1 d\mu_1 + n_2 d\mu_2 + n_w d\mu_w = 0 \qquad (9\text{−}1)$$

The chemical potential of NaCl(aq) does not change and equals the chemical potential of NaCl(cr) as long as the solution is saturated. At the same time, the chemical potential of KCl(aq) increases with increasing concentration slowly approaching the chemical potential of the second solid phase KCl(cr). Thus, the first term in eq 9–1 vanishes as $d\mu_1 = 0$, the second term is always positive and, consequently, the third term must be negative. Since $\mu_w = \mu_w^{\circ} + \mathrm{R}T\ln a_w$, $d\mu_w$ is only negative if the water activity a_w decreases upon addition of the second electrolyte at saturation of the first one. The same applies if NaCl is added to a saturated solution of KCl. In effect, for both solids, the water activities of saturated solutions decrease with increasing concentration of the second electrolyte. At the intersection of the two curves, both solids are saturated and the water activity now equals the MDRH (see in Fig. 9–5). Thus, the water activity of the solution saturated with respect to two solids is always lower than the DRH of the respective pure compounds.

Regarding the mechanism of liquefaction at a RH below the MDRH, despite liquid water being thermodynamically unfavorable on a pure salt surface, it is hypothesized that the adsorbed water film acts as a catalyst. As previously explained, the deliquescence of NaCl commences with the formation of a water film. Similarly, the water adsorption occurs at the interface of NaCl and KCl. Due to the surface roughness, two crystals are unable to form a perfect contact, likely leaving a slit in the interfacial area, as depicted Fig. 9–8. With increasing humidity, the adsorbed water layers on both sides converge, forming thicker layers as shown in the ESEM micrographs in Fig. 9–6 and Fig. 9–7. The merged solution film facilitates ion exchange and diffusion between NaCl and KCl. Notably, this merged film contains both $\mathrm{Na^+}$, $\mathrm{K^+}$, and $\mathrm{Cl^-}$ ions, whereas the initial adsorbed water layers on the pure salt surface contains only a single solute. An alternative interpretation suggests that the initial liquid film is formed directly by capillary condensation between two particles (Kwok et al., 2010). In porous silica materials, water condensation pressure can drop below 60% RH at 25 °C when the pore diameter is reduced to 2.5 nm (Rother et al., 2022), and this threshold decreases further in the presence of salt (Talreja–Muthreja et al., 2022). Although it is unlikely that such a small pore was present in our SEM investigation, nanoscale irregularities likely exist in the contact area of two surface, as shown schematically in Fig. 9–8. Thus, the formation of a nanodroplet is essential for connecting two surfaces at the atomic level, regardless of how the droplet was generated. The ion diffusion results in a solution film that is saturated with respect to both salts, exhibiting a lower water vapor pressure than a solution with a single solute. The growth of the solution film is controlled by the humidity and it remains confined to the interfacial area until the RH in the environment reaches the MDRH. At this point, the solution spreads over the bulk crystals, leading to macroscopic dissolution. Microscopic water adsorption or capillary condensation also exist at the grain interface of a pure salt, as shown in the upper schematic diagram of Fig. 9–8. This process acts as a trigger for the transition from water vapor to solution but it remains confined in the interface below the DRH, as the bulk dissolution process is governed by the multiphase thermodynamic equilibrium between gas, liquid and solid phase.

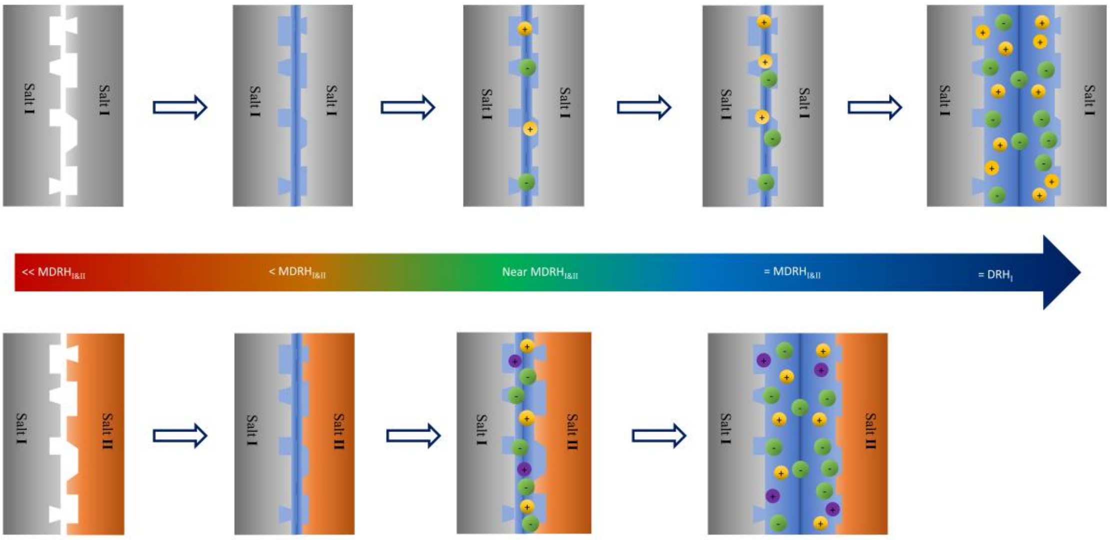

Figure 9−8. Schematic diagram of the deliquescence of a single salt (upper) and a salt mixture (bottom).

9.2.3 The transformation of metastable salt pair

The system $Na^+–K^+–Cl^-–NO_3^-//H_2O$ is a simple reciprocal quaternary system. It consists of four solid-phase regions corresponding to $NaNO_3$, NaCl, KCl, and KNO_3, along with five two-phase co-saturated lines and two invariant points (Fig. 9−9). Each pair of salt regions shares a common phase boundary except $NaNO_3$ and KCl, which are separated by NaCl and KNO_3. Thus, the crystalline phases $NaNO_3$ and KCl cannot coexist in equilibrium with a saturated aqueous solution. Instead, they transform into the NaCl + KNO_3 pair. Consequently, NaCl + KNO_3 is the thermodynamically stable pair, while $NaNO_3$ + KCl is the metastable pair in this reciprocal system. This raises the question of whether this stability preference of the NaCl + KNO_3 pair is maintained in the absence of liquid water, particularly when the metastable pair $NaNO_3$ + KCl is exposed to water vapor.

The phase diagram of the reciprocal system $Na^+–Cl^-–K^+–NO_3^-//H_2O$ consists of four solid-phase regions corresponding to $NaNO_3$, NaCl, KCl, and KNO_3, along with five two-phase co-saturated lines and two invariant points, as illustrated in Fig. 9−9. Each pair of salt regions shares a common phase boundary except $NaNO_3$ and KCl, which are separated by NaCl and KNO_3. This separation means that the crystalline phases $NaNO_3$ and KCl cannot coexist in equilibrium with a saturated aqueous solution. Instead, they spontaneously transform into the NaCl + KNO_3 pair according to the phase diagram. Consequently, NaCl + KNO_3 is the thermodynamically stable pair, while $NaNO_3$ + KCl is the metastable pair in this reciprocal system. This raises the question of whether this stability preference of the NaCl + KNO_3 pair is maintained in the absence of liquid water, particularly when the metastable pair $NaNO_3$ + KCl is exposed to water vapor. The model calculated relative humidities in equilibrium with the two invariant points are 62.5% RH (IV1) and 67.2% RH (IV2), respectively.

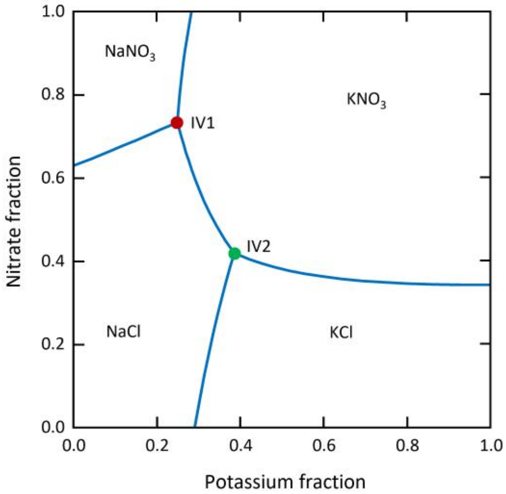

Figure 9–9. Jänecke diagram of the Na^+–K^+–Cl^-–NO_3^-–H_2O reciprocal system at 25 °C calculated with a thermodynamic equilibrium model based on Pitzer type ion interaction equations (Steiger et al., 2008a). Symbols represent invariant points (IV1 and IV2); the model calculated relative humidities in equilibrium with the two invariant points are 62.5% RH (IV1) and 67.2% RH (IV2), respectively.

The water vapor sorption isotherms of the equimolar mixtures of NaCl + KNO_3 and $NaNO_3$ + KCl, respectively, are depicted in Fig. 9–10a. Notably, the onset of water adsorption for both NaCl + KNO_3 and $NaNO_3$ + KCl mixtures occurs at 68% RH, which is lower than the DRHs of the individual pure components but aligns closely with the humidity of invariant point 2 (NaCl + KNO_3 + KCl, shown in the phase diagram Fig. 9–9). Additionally, in a magnification of the results in the humidity range below 68 %, a visible water uptake in the sorption curve of $NaNO_3$ + KCl is observed (Fig. 9–10b, green dots), initiating at the water activity of invariant point 1 (NaCl + KNO_3 + $NaNO_3$, shown in the phase diagram Fig. 9–9) at 62% RH. This observation suggests that partial conversion of $NaNO_3$ + KCl to NaCl + KNO_3 occurs at this stage, which is consistent with their common mutual deliquescence relative humidity in the sorption curves. The minor water uptake at 62% is likely due to a transition of the metastable to the stable pair in a dissolution–precipitation process. Similar to the deliquescence of salts and their mixture, also for this metastable salt pair, water adsorption or capillary condensation occurs at the grains at low RH, accompanied by ion solvation within a nanoscale water film or droplet. To be specific, as depicted in Fig. 9–10g, the interfacial solution films originating from both surfaces initially only contain two ions each, either Na^+ and NO_3^- or K^+ and Cl^-. With increasing humidity, the films grow in thickness, merging to form a multi–component solution containing all four ions supersaturated with NaCl and KNO_3. As a result, NaCl and KNO_3 will crystallize from the solution film until KCl is depleted. Prior to reaching a new equilibrium, all four solid phases NaCl, KNO_3, $NaNO_3$, and KCl temporarily coexist within the interfacial region. This phenomenon may explain the minor water uptake at 62% RH in the sorption curve of Fig. 9−10b, which reflects the mutual deliquescence of NaCl, $NaNO_3$, and KNO_3 mixture. The extent of mutual deliquescence is determined by the relative rates of precipitation (of NaCl and KNO_3) and dissolution (of $NaNO_3$ and KCl). In the 62%−68% RH range, the bulk solution, rather than the microscopic solution film, serves as the reaction medium facilitating interaction between the two crystals.

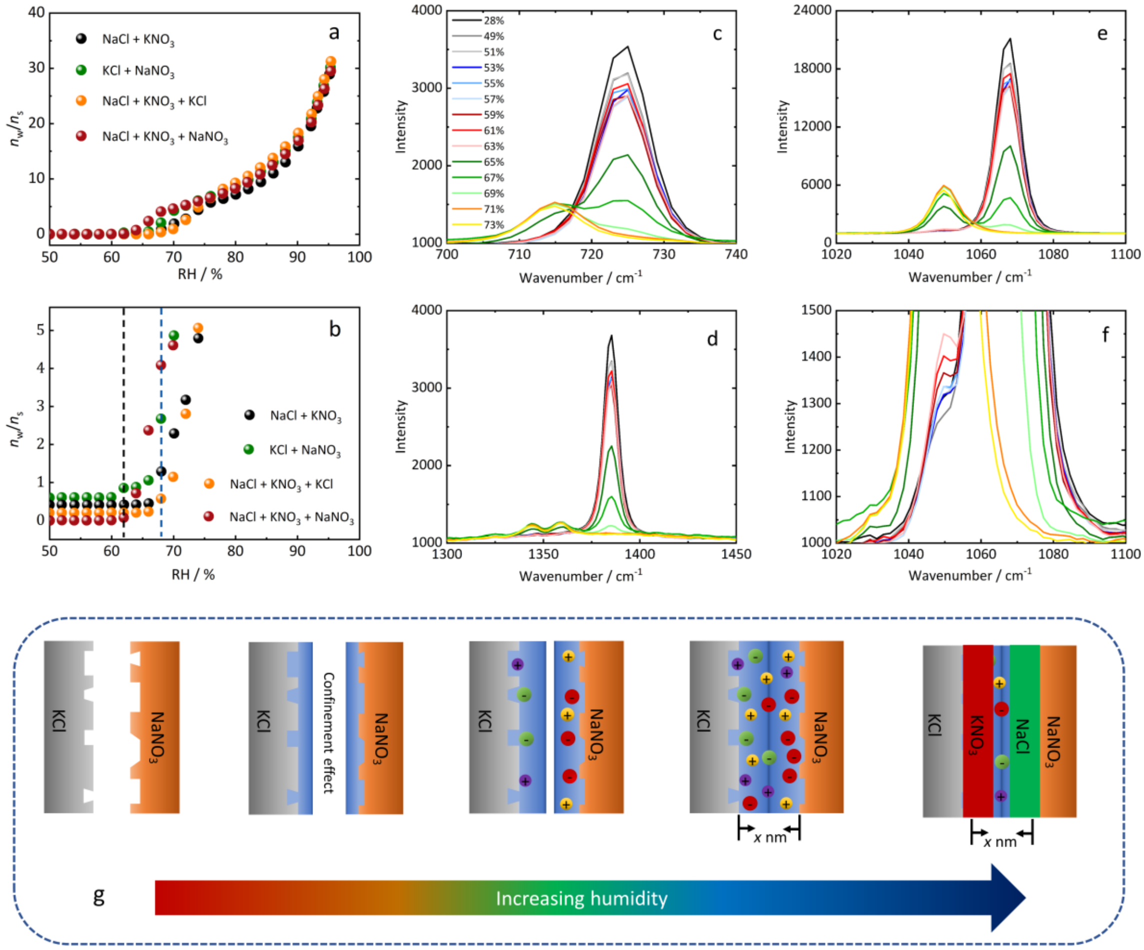

Figure 9−10. (a): Water vapor sorption curves of several binary and ternary salt mixtures of the system Na^+–Cl^-–K^+–NO_3^-//H_2O; (b): magnification of the RH range in which deliquescence occurs (data are displaced vertically for clarity by 0.2 (orange, 0.4 (black), and 0.6 (green)); (c–e): Raman spectra of the $NaNO_3$ + KCl mixture at various RH; (f): magnification of the spectra in the range of 1020−1100 cm^{-1}; (g): schematic diagram of the transition from metastable to stable pair transition.

To validate the proposed hypothesis, Raman spectra of the metastable $NaNO_3$ + KCl pair, with a molar ratio of 1:1, were recorded over a humidity range from 27% RH to 73 % RH at 25 °C. Three spectral regions, specifically 700−740 cm^{-1}, 1020−1100 cm^{-1}, and 1300−1450 cm^{-1}, are illustrated in Figs. 9−10c, d, e, and a detailed view of the Raman peak at 1050 cm^{-1} is presented in Fig. 9−10f. All observed Raman spectra are attributed to the fundamental vibrational bands of NO_3^- and exhibit notable changes above 63% RH. Indeed, a subtle shoulder appears at 1050 cm^{-1}, whose intensity slightly increases with increasing humidity, until a visible peak at approximately 65% can be observed. By comparing with the reference spectra of $NaNO_3$ and KNO_3 in Fig. 9–11, we deduce that this peak shift reflects the transformation of $NaNO_3$ into KNO_3. Although NaCl is not detectable in the Raman spectrum, it is highly probable that it precipitates as well to maintain liquid–solid equilibrium. The onset of these obvious changes in the Raman spectra falls between the MDRH of invariant point 2 and the invariant point 1 (shown in the phase diagram Fig. 9–9), in accordance with the narrow humidity window for water uptake by the $NaNO_3$ + KCl system. This supports our assumption that adsorbed water provides the necessary liquid environment for the reaction $NaNO_3 + KCl \rightarrow NaCl + KNO_3$. This transformation can be divided into two stages, the formation of a nanoscale film and the development of a bulk solution. The initial shoulder in Fig. 9–10f corresponds to the formation of a small amount KNO_3 within a thin solution film, which results in a minor increase in water uptake at 62%, as seen in the water vapor sorption curve in Fig. 9–10a. This limited water uptake occurs because the mutual deliquescence is impeded once one of the eutonic components is depleted. In the second stage, the presence of a bulk solution, following mutual deliquescence, the dissolution–precipitation reaction is significantly accelerated compared to the nanoscale film stage, leading to the pronounced Raman peak at 1050 cm^{-1}, characteristic of KNO_3.

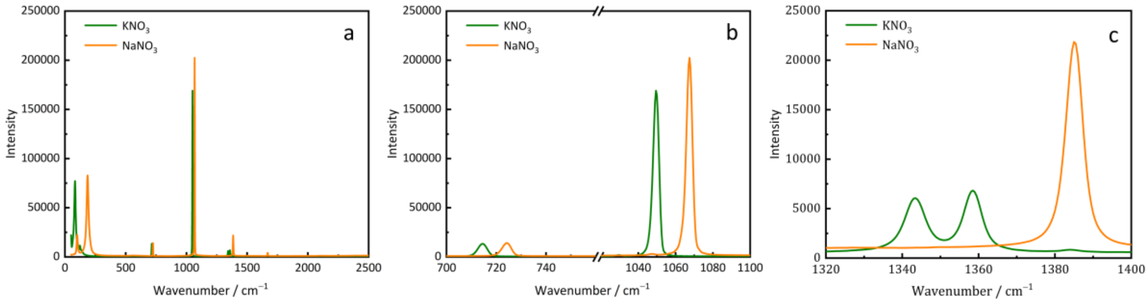

Figure 9–11. Raman reference spectra of pure $NaNO_3$ and KNO_3 (collected with the Senterra Raman microscope).

Additional Raman measurements using a Raman microscope with higher resolution and confirming the results presented in Fig. 9–10 are provided in Fig. 9–12. During collection of the Raman spectra, the laser was focused on KCl crystal in contact with $NaNO_3$ crystal. Spectra were recorded at 50% and 70% RH, respectively. By comparing the micrographs Fig. 9–12a (50% RH) and Fig. 9–12b (70% RH), it is evident that new microcrystals have formed on the KCl surface upon increasing the RH to 70%. This is confirmed by the corresponding Raman spectra shown in Figs. 9–12c and 9–12d, where characteristic Raman signals of crystalline KNO_3 only appear in the spectrum recorded at 70% RH (shown in black). Thus, these measurements confirm the *in-situ* Raman measurements shown in Fig. 9–10.

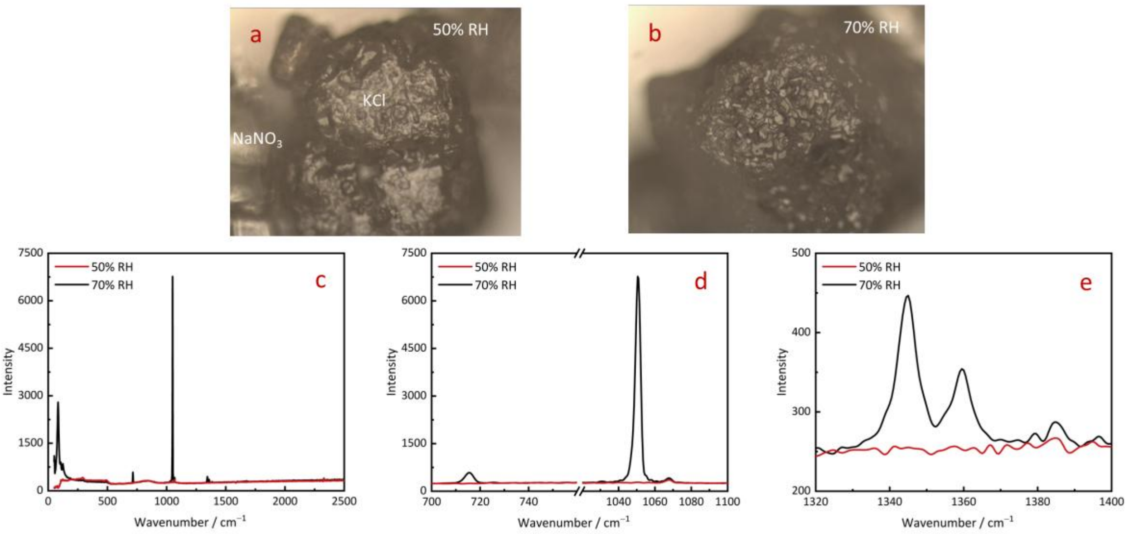

Figure 9–12. Raman spectra recorded during exposure of an initial mixture of pure $NaNO_3$ + KCl to 50% and 70% relative humidity, respectively. (a)–(b): Optical micrographs of KCl crystals during Raman measurements at the corresponding relative humidities; (c)–(e): Raman spectra recorded at 50 % RH (red) and 70% RH (black) confirming the formation of KNO_3 microcrystals on the KCl crystal surface in contact with $NaNO_3$ at 70 % RH.

The ESEM images in pictures from Fig. 9–13a to Fig. 9–13d illustrate the morphology changes occurring as water molecules adsorb onto the salt surface. It is worth mentioning that two images were captured at 62% RH within a 12–hour interval, with the later labelled as 62% RH–2 (Fig. 9–13c). It is clear from Fig. 9–13a that the $NaNO_3$ surface appears generally smooth at 5% RH, although some irregularities are visible. When the humidity reaches 62%, minimal visible changes are observed initially. However, after 12 hours, the flat surface becomes covered with microcrystals, which is likely to be KNO_3, and a liquid film is seen at the interface of the two crystals (Fig. 9–13c). According to the sodium and potassium distribution from EDX mapping (Fig. 9–13e), the KCl crystal surface is coated with sodium in several small spots. These sodium-rich spots expand into a larger area at 62% RH, marked by red zones in the Fig. 9–13f. The comprehensive elemental mapping image in Fig. 9–13h confirms that the red areas represent NaCl micro crystals, as they contain sodium and differ visibly from $NaNO_3$. The greenish surrounding of the NaCl microcrystals originate from water-related oxygen, indicating the formation of a solution film. Additionally, the dark grey regions near the interface of the two crystals, such as the area circled in orange in Fig. 9–13c, further suggest the presence of a solution film. This observation aligns with the small increase in water uptake at 62% RH shown in Fig. 9–10b. Moreover, the Raman spectra presented in Fig. 9–10 indicate the appearance of KNO_3, the second reaction product next to NaCl, which corresponds to microcrystal formation on the $NaNO_3$ surface. Over time and with increased humidity, the entire surface becomes coated with newly generated KNO_3 at 74% RH.

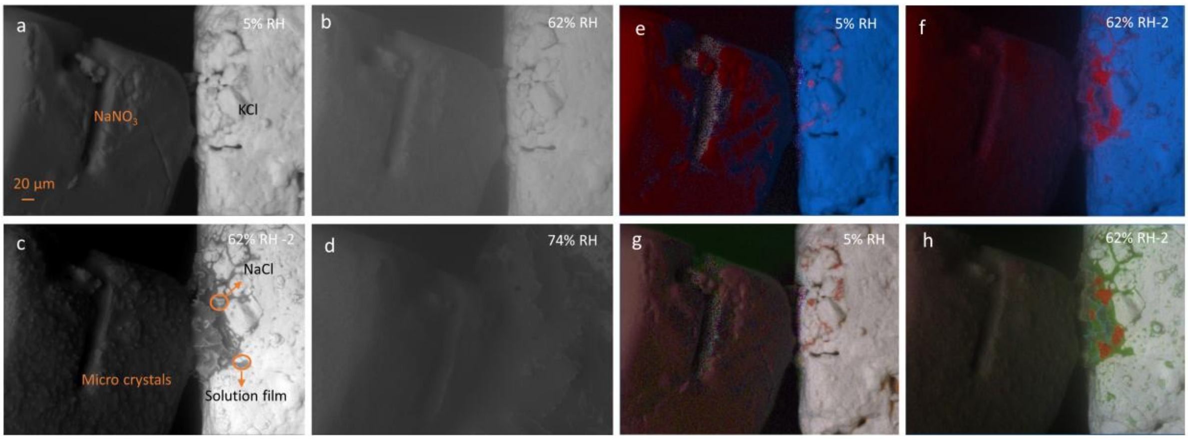

Figure 9−13. ESEM and EDX images of the $NaNO_3$ + KCl mixture at different RH. a–d: morphology of the salt crystals; e–h: elemental distributions, red: sodium, purple: nitrogen, orange: chloride, blue: potassium, green: oxygen, e–f: without oxygen, g–h: with oxygen.

9.2.4 Water vapor sorption of $Na^+–Cl^-–NH_4^+–SO_4^{2-}//H_2O$ system

Extensive studies have been carried out to investigate the water vapor sorption of the inorganic aerosol salts with various methods (Guo et al., 2019; Dong et al., 2007; Gu et al., 2017). In particular, the hygroscopic properties of NaCl + $(NH_4)_2SO_4$ mixture have been examined experimentally, revealing between discrepancies and thermodynamic predictions (Svenningsson et al., 2006; Rissler et al., 2023). The thermodynamically stable solid phase of aqueous mixture containing Na^+, Cl^-, NH_4^+, and SO_4^{2-} are NH_4Cl, $Na_2SO_4\cdot nH_2O$, and $Na_2SO_4\cdot(NH_4)_2SO_4\cdot4H_2O$. This implies that the binary salt mixture NaCl + $(NH_4)_2SO_4$ is metastable upon contact with water, leading to phase transformation into the more stable assemblage of NH_4Cl and Na_2SO_4 (Zhang et al., 2013). The water sorption process of NaCl + $(NH_4)_2SO_4$, involve not only mutual deliquescence but also the transformation to stable solid phase NH_4Cl + Na_2SO_4. Furthermore, the presence of volatile component NH_4Cl introduces additional complexity through the triple phase equilibrium among the solid, aqueous and gas phases, specifically, $NH_4Cl_{(s)}–NH_4Cl_{(aq)}–NH_{3(g)}$, resulting in significant deviations between the experimental observations and model predictions.

The water vapor sorption isotherms of binary and ternary subsystems of the reciprocal system $Na^+–Cl^-–NH_4^+–SO_4^{2-}//H_2O$ at 25 °C are presented in Fig. 9−14a. In the ternary mixtures, the mole ratio of each salt component is approximate 1 : 1. The deliquescence relative humidities (DRHs) of the individual salts, along with the mutual deliquescence relative humidity (MDRH) of the mixtures, identified by the sharp increase in water uptake in the sorption isotherms are tabulated in Table 9−1. The measured DRH values show good agreement with both the reported data from literature and the values predicted with The Extended Aerosol Inorganics Model (E−AIM). Notably, the MDRHs of the salt mixtures are consistently lower than the DRHs of the corresponding pure component.

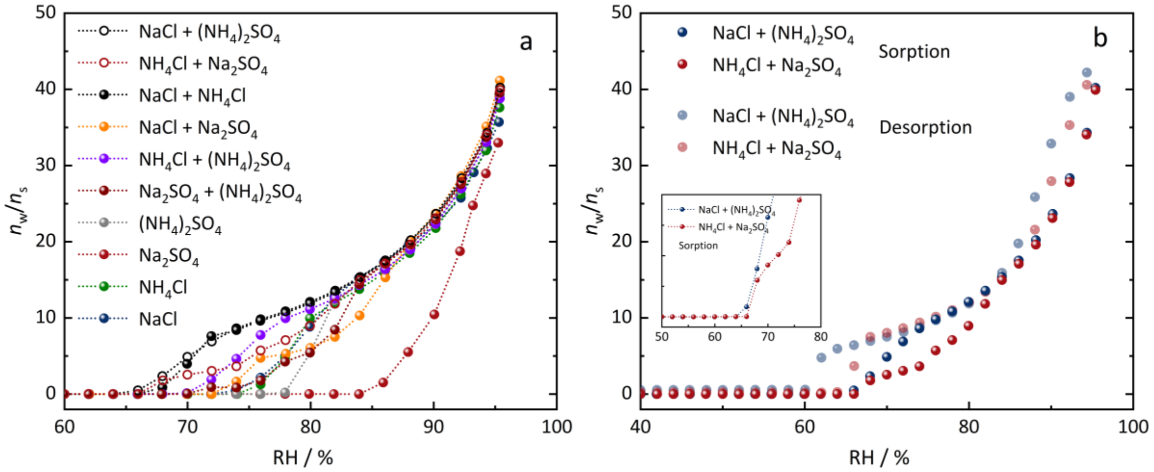

Figure 9−14. (a): Water vapor sorption isotherms of NaCl, NH_4Cl, Na_2SO_4, $(NH_4)_2SO_4$, and their ternary mixtures at 25 °C; (b): Sorption and desorption curves of NaCl + $(NH_4)_2SO_4$ and NH_4Cl + Na_2SO_4.

Table 9−1. Deliquescence relative humidity (DRH) of individual salts and salt mixtures at 25 °C.

Salt system	Our measurements	Literature	E−AIM model
NaCl	76%	76% [a]	76%
NH_4Cl	76%	77% [b]	78%
Na_2SO_4	86%	86% [c]	94% [d]
$(NH_4)_2SO_4$	80%	81% [b]	80%
NaCl + NH_4Cl	68%	68.5% [b]	70%
NaCl + Na_2SO_4	74%		75%
$(NH_4)_2SO_4$ + NH_4Cl	72%	70.1% [b]	72%
$(NH_4)_2SO_4$ + Na_2SO_4	76%		82%
Na_2SO_4 + NH_4Cl	68%		69%
$Na_2SO_4\cdot(NH_4)_2SO_4\cdot4H_2O$	Unobserved		84%

a: Talreja−Muthreja et al., 2022; b: Fong et al., 2016; c: Steiger et al., 2008c; d: $Na_2SO_4\cdot10H_2O$

Similar to the reciprocal system Na^+–Cl^-–K^+–NO_3^-//H_2O, mutual deliquescence and solid−solid transformations also occur in the Na^+–Cl^-–NH_4^+–SO_4^{2-}//H_2O system. Due to the presence of the double salt $Na_2SO_4\cdot(NH_4)_2SO_4\cdot4H_2O$ in this system (Zhang et al., 2013), the water vapor sorption behavior of the NaCl + $(NH_4)_2SO_4$ mixture follows a more complex pathway. As shown in Fig. 9−14b, the sorption isotherms of NaCl + $(NH_4)_2SO_4$ and NH_4Cl + Na_2SO_4 two pairs overlap in the high humidity range (> 85%), suggesting that the resulting solution compositions coverage during the dilution process. However, deviations are observed in the intermediate humidity range between 65% and 80%, corresponding to the mutual deliquescence and the dissolution of residual solid phase. This behavior indicates that, although the final solution compositions are identical, the liquefaction pathways of two salt pairs differ. The zoom-in inset of Fig. 9−14b shows that the NaCl + $(NH_4)_2SO_4$ pair begins to adsorb water at a slightly lower humidity (66% RH) than the NH_4Cl + Na_2SO_4 pair (68% RH), which is consistent with the calculated mutual deliquescence humidity at 67.7% (solid phase: NaCl, NH_4Cl, and $(NH_4)_2SO_4$) at 25 °C.

The water vapor sorption behavior was simulated with E−AIM model III developed by Wexler and Clegg (2002), which is based on the Pitzer thermodynamic framework. The calculated results were compared with experimental data, as shown in Fig. 9−15 and Table 9−1. Overall, the model captures the deliquescence relative humidities and subsequent dilution behavior well, except for systems containing Na_2SO_4. According to the E−AIM model, Na_2SO_4 is expected to undergo a phase transition to $Na_2SO_4 \cdot 10H_2O$ at approximately 82% RH, followed by deliquescence at around 94% RH, as represented by the orange dotted curve in Fig. 9−15b.

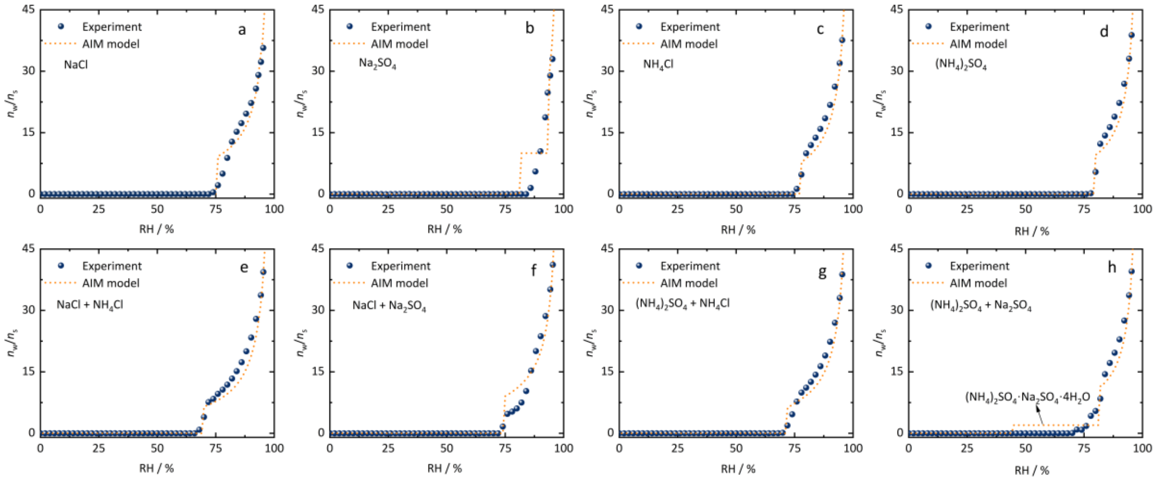

Figure 9−15. Water vapor sorption isotherms of pure salts and their ternary mixtures NaCl + NH_4Cl, NaCl + Na_2SO_4, $(NH_4)_2SO_4$ + NH_4Cl, $(NH_4)_2SO_4$ + Na_2SO_4 at 25 °C, and the calculated results with E-AIM model.

However, experimental sorption isotherms indicate direct deliquescence of Na_2SO_4 at 86% RH, consistent with the reported DRH of metastable phase Na_2SO_4(V) in the previous studies. The absence of the hydration from Na_2SO_4(V) to $Na_2SO_4 \cdot 10H_2O$ as well as the lack of transformations between Na_2SO_4(V) and Na_2SO_4(III), has been discussed in the literature (Linnow et al., 2006; Steiger et al., 2008c), suggesting that Na_2SO_4 frequently enters metastable states upon exposure to moisture. The discrepancy between measured and calculated isotherms for the NaCl + Na_2SO_4 mixture can likely be attributed to this metastable behavior of Na_2SO_4. In the case of NH_4SO_4 + Na_2SO_4 mixture, the formation of the double salt $Na_2SO_4 \cdot (NH_4)_2SO_4 \cdot 4H_2O$ is predicted to occur at approximately 45% RH, followed by deliquescence at 84% RH, as indicated by the orange dot curve in Fig. 9−15h. The formation of double salt was not observed in the water vapor sorption isotherm. This absence is most likely due to the kinetic constraints associated with the solid-gas reaction, which can hinder the transformation with the experimental timescale.

The MDRH of the NH_4Cl + Na_2SO_4 mixture was calculated to be 69% RH, which aligns well with the experimental value shown in Fig. 9−16. In contrast, for the metastable NaCl + $(NH_4)_2SO_4$ mixture, a solid−solid transformation to NH_4Cl + Na_2SO_4 is initiated at low humidity through the formation of a thin water film at the grain interface. However, due to the slow kinetics of the solid−gas reaction, the newly generated phases constitute only a minor fraction of the mixture. As a result, the metastable system primarily comprises four components: NaCl, NH_4Cl, Na_2SO_4, and $(NH_4)_2SO_4$ prior to complete deliquescence. Mutual deliquescence involving NaCl, $(NH_4)_2SO_4$, and *in-situ* formed NH_4Cl occurs at approximately at 67.7% RH. The slight water uptake observed for the NaCl + $(NH_4)_2SO_4$ mixture at 66% RH (as seen in Fig. 9−14b and Fig. 9−16) likely reflects the onset of this mutual deliquescence process. The presence of bulk solution further accelerates the NaCl + $(NH_4)_2SO_4$ → NH_4Cl + Na_2SO_4 transformation. Considering that the mutual deliquescence humidity (67.7% RH) is very close the to the MDRH of NH_4Cl + Na_2SO_4 pair (69% RH), it is plausible that solid−solid transformation, deliquescence, and dissolution occur simultaneously in a homogenous manner, leading to the deviation with stable salt pair in the sorption isotherm.

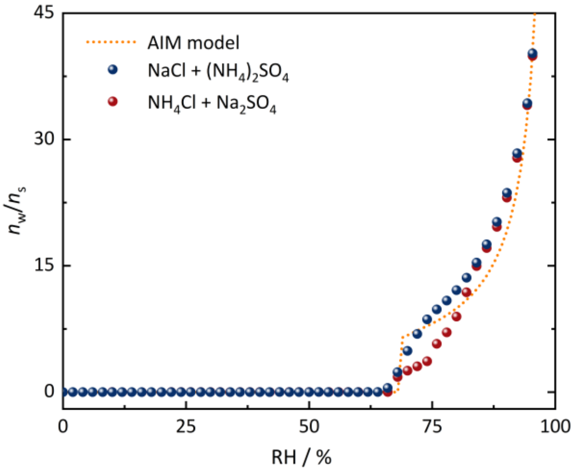

Figure 9−16. Water vapor sorption isotherms of pure salts and their ternary mixtures NaCl + NH_4Cl, NaCl + Na_2SO_4, $(NH_4)_2SO_4$ + NH_4Cl, $(NH_4)_2SO_4$ + Na_2SO_4 at 25 °C, and the calculated results with E−AIM model.

9.3 Conclusions

In this study, the interactions between water vapor and salts or salt mixtures have been investigated using water vapor sorption, optical microscopy, environmental SEM, and Raman spectroscopy. Two quaternary reciprocal systems Na^+−Cl^-−K^+−NO_3^-//H_2O, Na^+−Cl^-−NH_4^+−SO_4^{2-}//H_2O and their respective subsystems, which involve various types of reactions with moisture, was selected for this investigation. Using ESEM and EDX elemental mapping, the formation and evolution of a water film on a NaCl surface was confirmed in response to increased humidity as observed previously using other experimental techniques (Peters et al., 1997; Foster and Ewing, 2000; Ewing, 2004; Verdaguer et al., 2008; Lin et al., 2021; Dai et al., 1997; Verdaguer et al., 2005; Bruzewicz et al., 2011). Subsequently, the shift of the mutual deliquescence humidity of salt mixtures to below the DRH of the pure salts was observed using dynamic water vapor sorption. This shift is in an agreement with previous experimental results and with theoretical considerations (Mauer, 2022; Salameh and Taylor, 2005; Wexler and Seinfeld, 1991); it is also validated by model calculations. Using ESEM and optical microscopy, the findings indicate that it is the direct contact of adsorbed water films on two adjacent crystal surfaces or the capillary condensation in void spaces at grain interfaces that lead to a mixed electrolyte solution film with lower water activity serving as the initiator for mutual deliquescence.

The transition from the metastable salt pair $NaNO_3$ and KCl to the thermodynamically stable pair NaCl and KNO_3 in the quaternary reciprocal system occurs in two steps upon exposure to water vapor: (1) dissolution of $NaNO_3$ and KCl in the interfacial water film; (2) the precipitation of NaCl and KNO_3. It is important to note that this transition provides an example of a solid-state reaction that is significantly accelerated by the formation of a nanoscale water film, although water is not involved in the reaction equation. Overall, the water film plays a crucial role at solid-water vapor interfaces and as an ion diffusion media. Given the ubiquitous presence of water vapor in natural and industrial environments, it is likely that such a water film forms on the surface of most materials leading to mutual deliquescence, caking, or chemical reactions. On the Martian surface, for instance, the presence of such water films within the soil may facilitate the mutual deliquescence of salt mixtures under low humidity conditions. Furthermore, it could provide a liquid medium conducive to potential microbial survival of life and mineral reactions. In earth's atmosphere, water films on aerosol particles initiate cloud nucleation and contribute to chemical transformations in aerosol mixtures. A notable example is the transformation from $NaCl-(NH_4)_2SO_4$ to NH_4Cl, Na_2SO_4, $NH_{3(g)}$, and $HCl_{(g)}$ upon exposure to water vapor (Rissler et al., 2023). Similarly, water adsorption among particulate grains significantly impacts the stability of pharmaceuticals and food products during manufacturing and storage, particularly due to the presence of highly soluble components (Li et al., 2016a). These phenomena underscore the essential role of water films in phase transitions of salt mixtures, and these universally existing interactions between water vapor and soluble electrolytes warrant further explorations.

Chapter 10. Summary and Outlook

10.1 Summary

This dissertation presents a comprehensive study on the phase behavior of salt solution in confined environments, focusing on ice melting, eutectic transitions, deliquescence, and the formation of thin water films. Both experimental investigations and thermodynamic modeling are employed to examine the shifts in phase transition conditions under confinement, such as eutectic temperature and deliquescence relative humidity (DRH). These findings have direct implications for understanding the water cycle among solid, liquid, and gas phases on the Martian surface, as well as hygroscopic properties of inorganic mineral aerosol nanoparticles, where the deliquescence and eutectic melting at the nanoscale remain underexplored. Furthermore, the role of adsorbed water film in initiating the process of mutual deliquescence of salt mixture and solid−solid transformation is addressed with various methods.

In **Chapter 2**, the research context is established, covering water phase behavior in Martian environments, nanoconfinement, surface area, and supercooling conditions. It is found that water vapor condensation pressure and ice melting point are depressed in nanoconfinement. Studies on the stability of chloride and perchlorate solutions, which are primarily formed via eutectic melting and deliquescence, suggest that the highly hygroscopic salts may allow liquid water to transiently exist on the Martian surface. These phenomena underscore the motivation to explore the phase behaviors of brines under confinement, where the stability region of liquid water is expanded relative to the bulk phase. The introduction of interfacial water films and the anomalous properties of water in the supercooled regime aids in understanding water adsorption and cryogenic solution behavior.

In **Chapter 5**, water vapor sorption analysis and Raman measurements on $CaCl_2{\cdot}2H_2O$ and $CaCl_2{\cdot}6H_2O$ and their dehydration products were conducted. The results indicate two possible hydration sequences from lower hydrates to deliquescence at 298.15 K: (1) Hydration of the monohydrate to the dihydrate, followed by the formation of $\beta{-}CaCl_2{\cdot}4H_2O$, ending with its deliquescence at 18.5% RH; (2) Hydration of the monohydrate to the dihydrate, followed by the formation of $\alpha{-}CaCl_2{\cdot}4H_2O$ and of the hexahydrate, ending with its deliquescence at 29% RH. It was observed that the transition from pure dihydrate to $\beta{-}CaCl_2{\cdot}4H_2O$ occurs spontaneously, instead of hydration to the thermodynamically stable $\alpha{-}CaCl_2{\cdot}4H_2O$. The latter phase is only formed in the presence of crystal seeds of $\alpha{-}CaCl_2{\cdot}4H_2O$ that remained after dehydration. Additionally, direct deliquescence of $\beta{-}CaCl_2{\cdot}4H_2O$ and thus absence of hydration to hexahydrate at 298.15 K is reported for the first time, which could be explained by the more similar lattice structure of $CaCl_2{\cdot}2H_2O$ (orthorhombic) and $\beta{-}CaCl_2{\cdot}4H_2O$ (monoclinic) than $\alpha{-}CaCl_2{\cdot}4H_2O$

(triclinic). Apart from that, an explanation for the observed transformation sequence is proposed, considering the impact of the enhanced solubility of β−$CaCl_2·4H_2O$ compared to the α−$CaCl_2·4H_2O$. The resulting water to salt ratio below six may contribute to the absence of $CaCl_2·6H_2O$ formation. A Raman spectrum of $CaCl_2·H_2O$ not reported previously is also provided.

In **Chapter 6**, Systematic calorimetric measurements were conducted with $CaCl_2$ and NaCl solutions to investigate the absence of eutectic transition in confined dilute solution. The results demonstrate that the occurrence of the eutectic transition is controlled by three main factors, salt concentration, pore size, and pore filling degree. In confined solutions with insufficient supply with ions, the interfacial layer remains unsaturated, leading to the crystallization of solely ice in the core and the absence of a eutectic transition. Conversely, in more concentrated solutions or if supply with ions is sufficient, the interfacial layer becomes saturated, and the presence of excess bulk−like ions in the core facilitates simultaneous salt and ice crystallization at the eutectic point. Supply for the complete saturation of the interfacial layer can either stem from a sufficiently large core volume, thus, in large pores, or from diffusion of a reservoir from outside of an overfilled pore. we propose that the preferential accumulation of dissolved ions in the interfacial layer and the resulting depletion of the ions in the core of the pore are the key factors contributing to the absence of salt crystallization at the eutectic point. These findings highlight the critical role of interfacial layers influencing the ion distribution and phase behavior of electrolyte solutions in nanoconfinement, specifically, confirming sorption and strong enrichment of ions in the interfacial layer.

In **Chapter 7**, experimental measurements of ice melting and eutectic points were carried out for a range of salt solutions under confinement, including NaCl, $MgCl_2$, $CaCl_2$, $NaClO_4$, $Mg(ClO_4)_2$, $Ca(ClO_4)_2$, and $(NH_4)_2SO_4$. DRHs of these salts in nanopores were also measured using water vapor analyzer. Results show systematic depression of melting and eutectic points relative to the bulk phase, with values decreasing as pore size decreases. Notably, eutectic transitions were not observed in dilute solutions for all any systems, consistent with literature reports. The lowest eutectic temperatures for all systems were approximately −70 °C, though the minimum detectable pore size for first−order phase transitions varied by salt. For perchlorates $Mg(ClO_4)_2$ and $Ca(ClO_4)_2$, eutectic transitions were often undetectable due to strong supercooling effects. Instead, the ice melting behavior of less concentrated perchlorate solutions in porous silicas was probed, showing lower melting temperatures than bulk counterparts. Furthermore, significant depression for the DRHs of salt nanoparticles in nanopores were observed as well, such as KCl, $MgCl_2·6H_2O$, β−$CaCl_2·4H_2O$ or $CaCl_2·2H_2O$, $NaClO_4·H_2O$, $Mg(ClO_4)_2·6H_2O$, and $Ca(ClO_4)_2·4H_2O$. Additionally, the water vapor sorption isotherm of confined KCl nanoparticle contains three steps, deliquescence in the pore, curvature filling, and bulk solution dilution.

In **Chapter 8**, a thermodynamic model incorporating Pitzer theory, Kelvin equation, and Laplace pressure, was developed to simulate ice and eutectic points, as well as DRHs, under confinement. The modeled results show good agreement with experimental data when appropriate values of crystal–solution interfacial energy were used. To assess the role of Laplace pressure, two scenarios, PKL (Pitzer–Kelvin–Laplace) and PK (Pitzer–Kelvin) model, were proposed. PKL model compensates for salting-out effects induced by negative Laplace pressure through enhanced crystal-solution interfacial energy (γ_{cl}). In addition, simulated water vapor sorption isotherm of KCl in porous silica also reflects the pore size distribution of the host material. Nonetheless, the model is limited by the extrapolation uncertainties in the supercooled and supersaturated regions, and by the anomalous thermodynamic properties of pure water at low temperatures.

In **Chapter 9**, we employed a new method to investigate the moisture uptake behavior on the NaCl crystal surface under varying humidity levels using environmental scanning electron microscopy coupled with energy–dispersive X–ray spectroscopy (ESEM–EDX). Additionally, water vapor sorption, ESEM, and Raman microscopy are used to examine the role of water films in facilitating phase transitions and chemical reactions of salt mixtures. Our results indicate that the water uptake on a NaCl crystal surface initiates early and increases with rising humidity. A sudden increase in the condensation rate above 60% RH suggests the ion solvation in the water film. In ternary mixtures, the water film occurs by water vapor adsorption or capillary condensation at the interface between two crystals in the early stage, where ions from both sides dissolve into the interfacial water film to form a nanoscale brine film. This process initiates the mutual deliquescence of a NaCl−KCl mixture at a relative humidity lower than the deliquescence humidity of either of the two single salts. For the solid–solid reaction $NaNO_3 + KCl \rightarrow NaCl + KNO_3$, the process involves the dissolution of reactants and the precipitation of products, where the interfacial water film acts as a liquid bridge, promoting the ion diffusion and exchange between the two reactants. Additionally, the water vapor sorption behavior of quaternary reciprocal $Na^+–Cl^-–NH_4^+–SO_4^{2-}//H_2O$ system was examined and compared with the results calculated using the E–AIM model. The observed derivations from the modeled sorption isotherms are likely attributed to the unexpected metastable transformation of Na_2SO_4.

10.2 Outlook

This dissertation advances our understanding of phase equilibria and multiphase transformations in salt systems under nanoscale confinement, offering insights directly relevance to Martian geochemistry, atmospheric aerosols, and cryogenic chemical processes. The observed depression in eutectic melting temperatures and DRHs under confinement broaden our horizon on the phase behavior of water in cold and arid environments, such as Arctic and Martian surface. The pore−size−dependent deliquescence of confined salt nanoparticles enhances the design flexibility of thermal energy storage materials in their operational humidity range. Furthermore, the experimentally supported mechanism of mutual deliquescence in salt mixtures, along with solid−solid transition induced by water vapor exposure, provides a bridge between the macroscopic thermodynamic phenomena and the molecular−scale interfacial interactions. As an extension of this concept, eutectic melting may also proceed via a comparable process, medicated by a pre-melted water film on the ice surface.

Despite these advances, further effects are needed to refine the thermodynamic model, particularly to improve its predictive performance under highly supercooling and supersaturated conditions. Given the experimental challenges associated with accessing these regimes, molecular simulation may offer a promising alternative for to generating physically consistent thermodynamic data. Additionally, incorporating interfacial heterogeneities, such as the ion accumulation behavior and the effects of disjoining pressure into model will enhance its reliability when applied to nanoscale systems. While the current studies focus primarily on binary and simple multicomponent systems, natural environments like aerosol nanoparticles and Martian regolith typically contain more complex mixture. Therefore, future investigations into multicomponent mixture are essential to increase the applicability to real world scenarios.

In conclusion, this dissertation demonstrates how confinement, interfacial structuring, and phase metastability co−govern the phase behavior of salt solutions. These findings have significant implications for understanding thermodynamic process of salt solution in extreme conditions, offering a robust framework for future interdisciplinary investigations, particularly in planetary science and aerosol chemistry.

References

Abramzon and Gaukhberg, 1993a. Surface tension of salt solutions. *Russ. J. Appl. Chem. 66*(8),1473–1480.

Abramzon and Gaukhberg, 1993b. Surface tension of salt solutions. *Russ. J. Appl. Chem. 66*(6),1315–1320.

Abramzon and Gaukhberg, 1993c. Surface tension of salt solutions. *Russ. J. Appl. Chem. 66*(6),1139–1146.

Acheson, D.T., 1965. Vapor pressure of saturated aqueous salt solutions. *Humidity and moisture*, *3*, 521.

Akin, M., Huang, J., Shi, X., Veneziano, D. and Williams, D., 2013. *Snow removal at extreme temperatures* (No. Project 99085/CR11–04). Minnesota Department of Transportation, Research Services.

Ali, K., Bilal, S. and Siddiqi, S., 2006. Concentration and temperature dependence of surface parameters of some aqueous salt solutions. *Colloids and Surf., A*, *272* (1–2), 105–110.

Ally, M.R. and Braunstein, J., 1996. Activity coefficients in concentrated electrolytes: a comparison of the Brunauer–Emmett–Teller (BET) model with experimental values. *Fluid Ph. Equilib*. *120* (1–2), 131–141.

Angell, C.A., 2002. Liquid fragility and the glass transition in water and aqueous solutions. *Chem. Rev. 102* (8), 2627–2650.

Angell, C.A. and Sare, E.J., 1970. Glass-forming composition regions and glass transition temperatures for aqueous electrolyte solutions. *J. Chem. Phys*. *52* (3), 1058–1068.

Antoniou, A.A., 1964. Phase transformations of water in porous glass. *J. Phys. Chem.*, *68* (10), 2754–2763.

Archer, D.G. and Carter, R.W., 2000. Thermodynamic properties of the NaCl + H_2O system. 4. Heat capacities of H_2O and NaCl(aq) in cold-stable and supercooled states. *J Phys. Chem. B*, *104* (35), 8563–8584.

Archer, D.G. and Wang, P., 1990. The dielectric constant of water and Debye-Hückel limiting law slopes. *J. Phys. Chem. Ref. Data*, *19* (2), 371–411.

Argyris, D., Cole, D.R. and Striolo, A., 2010. Ion-specific effects under confinement: the role of interfacial water. *ACS Nano*, *4* (4), 2035–2042.

Aristov, Y.I., Tokarev, M.M., Cacciola, G. and Restuccia, G.J.R.K., 1996a. Selective water sorbents for multiple applications, 1. $CaCl_2$ confined in mesopores of silica gel: sorption properties. *React. Kinet. Catal. Lett. 59*, 325−333.

Aristov, Y.I., Tokarev, M.M., Restuccia, G. and Cacciola, G.J.R.K., 1996b. Selective water sorbents for multiple applications, 2. $CaCl_2$ confined in micropores of silica gel: Sorption properties. *React. Kinet. Catal. Lett. 59*, 335−342.

Aristov, Y.I., Di Marco, G., Tokarev, M.M. and Parmon, V.N., 1997. Selective water sorbents for multiple applications, 3. $CaCl_2$ solution confined in micro- and mesoporous silica gels: Pore size effect on the "solidification-melting" diagram. *React. Kinet. Catal. Lett. 61*, 147−154.

Artemov, V.G., Uykur, E., Kapralov, P.O., Kiselev, A., Stevenson, K., Ouerdane, H. and Dressel, M., 2020. Anomalously high proton conduction of interfacial water. *J. Phys. Chem. Lett. 11* (9), 3623−3628.

Bakhuis Roozeboom, H.W., 1889. Experimentelle und theoretische Studien über die Gleichgewichtsbedingungen zwischen festen und flüssigen Verbindungen von Wasser mit Salzen, besonders mit dem Chlorcalcium. *Z. Phys. Chem*. *4* (1), 31−65.

Baidakov, V.G., Protsenko, S.P. and Tipeev, A.O., 2013. Temperature dependence of the crystal-liquid interfacial free energy and the endpoint of the melting line. *J. Chem. Phys*. *139*, 224703.

Barati Farimani, A. and Aluru, N.R., 2016. Existence of multiple phases of water at nanotube interfaces. *J. Phys. Chem. C*, *120* (41), 23763−23771.

Barraclough, P.B. and Hall, P.G., 1974. The adsorption of water vapor by lithium fluoride, sodium fluoride and sodium chloride. *Surf. Sci. 46* (2), 393−417.

Barreneche, C., Fernández, A.I., Cabeza, L.F. and Cuypers, R., 2015. Thermophysical characterization and thermal cycling stability of two TCM: $CaCl_2$ and zeolite. *Appl. Energy*, *137*, 726−730.

Bartels−Rausch, T., Jacobi, H.W., Kahan, T.F., Thomas, J.L., Thomson, E.S., Abbatt, J.P., Ammann, M., Blackford, J.R., Bluhm, H., Boxe, C. and Dominé, F., 2014. A review of air-ice chemical and physical interactions (AICI): liquids, quasi-liquids, and solids in snow. *Atmos. Chem. Phys*. *14* (3), 1587−1633.

Batchelor, R.W. and Foster, A.G., 1944. The freezing point of adsorbed liquids. *Trans. Faraday Soc*. *40*, 300−305.

Bertram, A.K., Koop, T., Molina, L.T. and Molina, M.J., 2000. Ice formation in $(NH_4)_2SO_4$−H_2O particles. *J. Phys. Chem. A*, *104* (3), 584−588.

Baumgartner, M. and Bakker, R.J., 2009. $CaCl_2$–hydrate nucleation in synthetic fluid inclusions. *Chem. Geol. 265* (3–4), 335–344.

Bellouin, N. and Yu, H., 2022. Aerosol-radiation interactions. In *Aerosols and Climate,* 445–487. Elsevier.

Beyer, K.D., Bothe, J.R. and Burrmann, N., 2007. Experimental determination of the $H_2SO_4/(NH_4)_2SO_4/H_2O$ phase diagram. *J. Phys. Chem. A*, *111* (3), 479–494.

Beyer, R. and Steiger, M., 2010. Vapor pressure measurements of NaHCOO+ H_2O and KHCOO+ H_2O from 278 to 308 K and representation with an ion-interaction (Pitzer) model. *J. Chem. Eng. Data*, *55* (2), 830–838.

Bibring, J.P., Langevin, Y., Poulet, F., Gendrin, A., Gondet, B., Berthé, M., Soufflot, A., Drossart, P., Combes, M., Bellucci, G. and Moroz, V., 2004. Perennial water ice identified in the south polar cap of Mars. *Nature*, *428* (6983), 627–630.

Boyle, R., 1660. New Experiments Physico-Mechanical touching the Spring of the Air. Oxford, England: H. Hall, 265–270. Available on-line at: Echo (Max Planck Institute for the History of Science; Berlin, Germany)

Brillouin, L., 1922, Diffusion of light and X-rays by a transparent homogeneous body. *Annu. Phys.* 17 (2), 88–122.

Bruzewicz, D.A., Checco, A., Ocko, B.M., Lewis, E.R., McGraw, R.L. and Schwartz, S.E., 2011. Reversible uptake of water on NaCl nanoparticles at relative humidity below deliquescence point observed by noncontact environmental atomic force microscopy. *J. Chem. Phys. 134*, 044702.

Burba, C.M. and Janzen, J., 2015. Confinement effects on the phase transition temperature of aqueous NaCl solutions: The extended Gibbs–Thomson equation. *Thermochim. Acta*, *615*, 81–87.

Cabrol, N.A. and Grin, E.A., 1999. Distribution, classification, and ages of Martian impact crater lakes. *Icarus*, *142* (1), 160–172.

Cabrol, N.A. and Grin, E.A., 2010. Searching for lakes on Mars: Four decades of exploration. *Lakes on Mars*, 1–29.

Caro, R., Hnedkovsky, L., del Río, J.M. and Hefter, G., 2020. Molar volumes and heat capacities of aqueous solutions of $Mg(ClO_4)_2$. *J. Chem. Eng. Data*, *65* (7), 3735–3743.

Carter, R.L., 1976. Single-crystal Raman spectra of paraelectric $(NH_4)_2SO_4$. *Spectrochim. Acta A*, *32*(3), 575–579.

Caupin, F. and Anisimov, M.A., 2019. Thermodynamics of supercooled and stretched water: Unifying two-structure description and liquid-vapor spinodal. *J. Chem. Phys. 151,* 034503.

Čeleda, J. and Žilková, J., 1977. Surface tension as evidence for complex formation in strongly concentrated electrolyte solutions. *Coll. Czech. Chem. Commun*. *42* (9), 2728–2736.

Chen, C., Wang, X., Binder, K., Pöschl, U., Su, H. and Cheng, Y., 2024. Convergence of dissolving and melting at the nanoscale. *Faraday Discuss*. *249*, 229–242.

Chen, J., Guo, J., Meng, X., Peng, J., Sheng, J., Xu, L., Jiang, Y., Li, X.Z. and Wang, E.G., 2014. An unconventional bilayer ice structure on a NaCl (001) film. *Nat. Commun. 5* (1), 4056.

Chen, M., Wu, S., Xu, S., Yu, B., Shilbayeh, M., Liu, Y., Zhu, X., Wang, J. and Gong, J., 2018. Caking of crystals: Characterization, mechanisms and prevention. *Powder Technol. 337*, 51–67.

Cheng, Y., Su, H., Koop, T., Mikhailov, E. and Pöschl, U., 2015. Size dependence of phase transitions in aerosol nanoparticles. *Nat. Commun*. *6* (1), 5923.

Chevrier, V.F., Hanley, J. and Altheide, T.S., 2009. Stability of perchlorate hydrates and their liquid solutions at the Phoenix landing site, Mars. *Geophys. Res. Lett. 36*, L10202.

Chevrier, V.F. and Rivera–Valentin, E.G., 2012. Formation of recurring slope lineae by liquid brines on present-day Mars. *Geophys. Res. Lett. 39*, L21202

Chevrier, V.F., Fitting, A., Elsenousy, A. and Rivera–Valentín, E.G., 2022. Thermodynamic modelling of perchlorate/chloride and perchlorate/chlorate deliquescence at Mars–relevant temperatures. *Geochim. Cosmochim. Acta*, *333*, 56–74.

Chin, M. and Kahn, R., 2009. *Atmospheric aerosol properties and climate impacts* (Vol. 2). US Climate Change Science Program.

Clark, B.C., Baird, A.K., Weldon, R.J., Tsusaki, D.M., Schnabel, L. and Candelaria, M.P., 1982. Chemical composition of Martian fines. *J. Geophys. Res. Solid Earth*, *87* (B12), 10059–10067.

Clegg, S.L. and Brimblecombe, P., 1995. Application of a multicomponent thermodynamic model to activities and thermal properties of 0–40 mol kg^{-1} aqueous sulfuric acid from < 200 to 328 K. *J. Chem. Eng. Data*, *40* (1), 43–64.

Clegg, S.L. and Wexler, A.S., 2011. Densities and apparent molar volumes of atmospherically important electrolyte solutions. 1. The solutes H_2SO_4, HNO_3, HCl, Na_2SO_4, $NaNO_3$, NaCl, $(NH_4)_2SO_4$, NH_4NO_3, and NH_4Cl from 0 to 50 °C, including extrapolations to very low temperature and to the pure liquid state, and $NaHSO_4$, NaOH, and NH_3 at 25 °C. *J. Phys. Chem. A*, *115* (15), 3393–3460.

Cohen, M.D., Flagan, R.C. and Seinfeld, J.H., 1987. Studies of concentrated electrolyte solutions using the electrodynamic balance. 1. Water activities for single-electrolyte solutions. *J. Phys. Chem*. *91* (17), 4563–4574.

Collins, E.M. and Menzies, A.W., 2002. A comparative method for measuring aqueous vapor and dissociation pressures with some of its applications. *J. Phys. Chem*. *40* (3), 379–397.

Collins, G.C. and Goodman, G.C., 2007. Enceladus' south polar sea. *Icarus*, *189*(1), 72–82.

Conde, M.M., Vega, C. and Patrykiejew, A., 2008. The thickness of a liquid layer on the free surface of ice as obtained from computer simulation. *J. Chem. Phys. 129*, 014702.

Conde, M.R., 2004. Properties of aqueous solutions of lithium and calcium chlorides: formulations for use in air conditioning equipment design. *Int. J. Therm. Sci. 43* (4), 367–382.

Coolidge, A.S., 1924. The adsorption of vapors by charcoal. *J. Am. Chem. Soc*. *46* (3), 596–627.

Coriell, S.R., Hardy, S.C. and Sekerka, R.F., 1971. A non-linear analysis of experiments on the morphological stability of ice cylinders freezing from aqueous solutions. *J. Cryst. Growth*, *11* (1), 53–67.

Corradini, D. and Gallo, P., 2011. Liquid-liquid coexistence in NaCl aqueous solutions: a simulation study of concentration effects. *J. Phys. Chem. B*, *115* (48), 14161–14166.

Corradini, D., Rovere, M. and Gallo, P., 2010. A route to explain water anomalies from results on an aqueous solution of salt. *J. Chem. Phys. 132*, 134508.

Corti, H.R., Appignanesi, G.A., Barbosa, M.C., Bordin, J.R., Calero, C., Camisasca, G., Elola, M.D., Franzese, G., Gallo, P., Hassanali, A. and Huang, K., 2021. Structure and dynamics of nanoconfined water and aqueous solutions. *Eur. Phys. J. E*, *44*, 136.

Craig, A. and McIntosh, R., 1952. The preparation of sodium chloride of large specific surface. *Can. J. Chem. 30* (5), 448–453.

Cziczo, D.J. and Abbatt, J.P.D., 1999. Deliquescence, efflorescence, and supercooling of ammonium sulfate aerosols at low temperature: Implications for cirrus cloud formation and aerosol phase in the atmosphere. *J. Geophys. Res. Atmos*. *104* (D11), 13781–13790.

Dai, L., Guo, X., Zhang, F., Du, Y., Ke, X., Li, Y., Cao, G., Li, Q., Lin, L., Shu, K. and Peng, G., 2019. Seasonal dynamics and controls of deep soil water infiltration in the seasonally-frozen region of the Qinghai–Tibet plateau. *J. Hydrol. 571*, 740–748.

Dai, Q., Hu, J. and Salmeron, M., 1997. Adsorption of water on NaCl (100) surfaces: Role of atomic steps. *J. Phys. Chem. B*, *101* (11), 1994–1998.

Debenedetti, P.G. and Stanley, H.E., 2003. Supercooled and glassy water. *Phys. Today*, *56* (6), 40–46.

Desarnaud, J., Bonn, D. and Shahidzadeh, N., 2016. The pressure induced by salt crystallization in confinement. *Sci. Rep. 6* (1), 30856.

Dohm, J.M., Baker, V.R., Boynton, W.V., Fairén, A.G., Ferris, J.C., Finch, M., Furfaro, R., Hare, T.M., Janes, D.M., Kargel, J.S. and Karunatillake, S., 2009. GRS evidence and the possibility of paleooceans on Mars. *Planet. Space Sci*. *57* (5−6), 664−684.

Dong, J.L., Li, X.H., Zhao, L.J., Xiao, H.S., Wang, F., Guo, X. and Zhang, Y.H., 2007. Raman Observation of the Interactions between NH_4^+, SO_4^{2-}, and H_2O in Supersaturated $(NH_4)_2SO_4$ Droplets. *J. Phys. Chem. B*, *111* (42), 12170−12176.

Donkers, P.A.J., Sögütoglu, L.C., Huinink, H.P., Fischer, H.R. and Adan, O.C.G., 2017. A review of salt hydrates for seasonal heat storage in domestic applications. *Appl. Energy*, *199*, 45−68.

Döppenschmidt, A. and Butt, H.J., 2000. Measuring the thickness of the liquid-like layer on ice surfaces with atomic force microscopy. *Langmuir*, *16* (16), 6709−6714.

Dore, J., 2000. Structural studies of water in confined geometry by neutron diffraction. *Chem. Phys*. *258* (2−3), 327−347.

Dupas−Langlet, M., Benali, M., Pezron, I., Saleh, K. and Metlas−Komunjer, L., 2015. The impact of deliquescence lowering on the caking of powder mixtures. *Powder Technol. 270*, 502−509.

Dutcher, C. S., Wexler, A. S. and Clegg, S. L., 2010. Surface tensions of inorganic multicomponent aqueous electrolyte solutions and melts. *J. Phys. Chem. A*, 114 (46), 12216−12230.

Dyson, J.E., Whalley, L.K., Slater, E.J., Woodward−Massey, R., Ye, C., Lee, J.D., Squires, F., Hopkins, J.R., Dunmore, R.E., Shaw, M. and Hamilton, J.F., 2023. Impact of HO_2 aerosol uptake on radical levels and O_3 production during summertime in Beijing. *Atmos. Chem. Phys.* 23, 5679−5697.

Eberbach, M.C., Huinink, H.P., Shkatulov, A.I., Fischer, H.R. and Adan, O.C., 2023. The effect of nanoconfinement on deliquescence of $CuCl_2$ is stronger than on hydration. *Cryst. Growth Des.* 23 (3), 1343−1354.

Ediger, M.D., Angell, C.A. and Nagel, S.R., 1996. Supercooled liquids and glasses. *J. Phys. Chem. 100* (31), 13200−13212.

Erko, M., Findenegg, G.H., Cade, N., Michette, A.G. and Paris, O., 2011. Confinement−induced structural changes of water studied by Raman scattering. *Phys. Rev. B, 84*, 104205.

Ervens, B., 2015. Modeling the processing of aerosol and trace gases in clouds and fogs. *Chem. Rev*. *115* (10), 4157−4198.

Estel, J., Hoinkes, H., Kaarmann, H., Nahr, H. and Wilsch, H., 1976. On the problem of water adsorption on alkali halide cleavage planes, investigated by secondary ion mass spectroscopy. *Surf. Sci*. *54* (2), 393−418.

European Space Agency (ESA). Water at Martian South Pole. Available online: http://www.esa.int/Our_Activities/Space_Science/Mars_Express/Water_at_Martian_south_pole (accessed on 17 March 2004).

Ewing, G.E., 2004. Thin film water. *J. Phys. Chem. B*, *108* (41), 15953−15961.

Ewing, G.E., 2005. H_2O on NaCl: From single molecule, to clusters, to monolayer, to thin film, to deliquescence. *Intermolecular Forces and Clusters II*, 1−25.

Ewing, G.E., 2006. Ambient thin film water on insulator surfaces. *Chem. Rev*. *106* (4), 1511−1526.

Extended AIM Aerosol Thermodynamics Model: https://www.aim.env.uea.ac.uk/aim/model3/model3a.php

Fang, C., Sun, S. and Qiao, R., 2021. Dynamics of ion depletion in thin brine films. *Fuel*, *306*, 121758.

Fanghänel, T. and Grjotheim, K., 1990. Thermodynamics of aqueous reciprocal salt systems. III. Isopiestic determination of osmotic and activity coefficients of aqueous $MgCl_2$, $MgBr_2$, KCl and KBr at 100.3 °C. *Acta Chem. Scand*, *44*, 892−895.

Farmer, C.B., Davies, D.W., Holland, A.L., LaPorte, D.D. and Doms, P.E., 1977. Mars: Water vapor observations from the Viking orbiters. *J. Geophys. Res*. *82* (28), 4225−4248.

Fauré, N., Chen, J., Artiglia, L., Ammann, M., Bartels−Rausch, T., Li, J., Liu, W., Wang, S., Kanji, Z.A., Pettersson, J.B. and Gladich, I., 2023. Unexpected behavior of chloride and sulfate ions upon surface solvation of Martian salt analogue. *ACS Earth Space Chem. 7* (2), 350−359.

Fernanders, M.S., Gough, R.V., Chevrier, V.F., Schiffman, Z.R., Ushijima, S.B., Martinez, G.M., Rivera−Valentín, E.G., Archer Jr, P.D., Clark, J.V., Sutter, B. and Tolbert, M.A., 2022. Water uptake by chlorate salts under Mars-relevant conditions. *Icarus*, *371*, 114715.

Fernandez, R. and Barduhn, A.J., 1967. The growth rate of ice crystals. *Desalination*, *3*(3), 330−342.

Findenegg, G.H., Jähnert, S., Akcakayiran, D. and Schreiber, A., 2008. Freezing and melting of water confined in silica nanopores. *ChemPhysChem*, *9* (18), 2651−2659.

Finlayson−Pitts, B.J., 2003. The tropospheric chemistry of sea salt: A molecular-level view of the chemistry of NaCl and NaBr. *Chem. Rev*. *103* (12), 4801−4822.

Fischer, E., Martínez, G.M., Elliott, H.M. and Rennó, N.O., 2014. Experimental evidence for the formation of liquid saline water on Mars. *Geophys. Res. Lett*. *41* (13), 4456−4462.

Fischer, E., Martínez, G.M. and Rennó, N.O., 2016. Formation and persistence of brine on Mars: experimental simulations throughout the diurnal cycle at the Phoenix landing site. *Astrobiology*, *16* (12), 937−948.

Fölsch, S. and Henzler, M., 1991. Water adsorption on the NaCl surface. *Surf. Sci. 247* (2–3), 269–273.

Fong, B.N., Kennon, J.T. and Ali, H.M., 2016. Mole ratio dependence of the mutual deliquescence relative humidity of aqueous salts of atmospheric importance. *J. Phys. Chem. A*, *120* (20), 3596–3601.

Foote, H.W. and Saxton, B., 1916. The effect of freezing on certain inorganic hydrogels. *J. Am. Chem. Soc. 38* (3), 588–609.

Foote, H.W. and Saxton, B., 1917. The effect of freezing on certain inorganic hydrogels. II. *J. Am. Chem. Soc. 39* (6), 1103–1125.

Foster, M.C. and Ewing, G.E., 2000. Adsorption of water on the NaCl (001) surface. II. An infrared study at ambient temperatures. *J. Chem. Phys. 112* (15), 6817–6826.

Freund, J.B., 2002. Electro-osmosis in a nanometer-scale channel studied by atomistic simulation. *J. Chem. Phys. 116* (5), 2194–2200.

Fumagalli, L., Esfandiar, A., Fabregas, R., Hu, S., Ares, P., Janardanan, A., Yang, Q., Radha, B., Taniguchi, T., Watanabe, K. and Gomila, G., 2018. Anomalously low dielectric constant of confined water. *Science*, *360* (6395), 1339–1342.

Gallagher, P.K. and Brown, M.E., 2003. Handbook of thermal analysis and calorimetry.

Gallo, P., Amann–Winkel, K., Angell, C.A., Anisimov, M.A., Caupin, F., Chakravarty, C., Lascaris, E., Loerting, T., Panagiotopoulos, A.Z., Russo, J. and Sellberg, J.A., 2016. Water: A tale of two liquids. *Chem. Rev*. *116* (13), 7463–7500.

Garvin, D., Parker, V.B. and White Jr, H.J., 1987. CODATA thermodynamic tables.

Gellert, R., Rieder, R., Anderson, R.C., Bruckner, J., Clark, B.C., Dreibus, G., Economou, T., Klingelhofer, G., Lugmair, G.W., Ming, D.W. and Squyres, S.W., 2004. Chemistry of rocks and soils in Gusev Crater from the Alpha Particle X-ray Spectrometer. *Science*, *305* (5685), 829–832.

Gibbard, H.F. and Fong, S.L., 1975. Freezing points and related properties of electrolyte solutions. III. The systems $NaCl-CaCl_2-H_2O$ and $NaCl-BaCl_2-H_2O$. *J. Solution Chem. 4*, 863–872.

Glein, C.R., Baross, J.A. and Waite Jr, J.H., 2015. The pH of Enceladus' ocean. *Geochim. Cosmochim. Acta*, *162*, 202–219.

Gough, R., Chevrier, V., Baustian, K., Wise, M. and Tolbert, M., 2011. Laboratory studies of perchlorate phase transitions: Support for metastable aqueous perchlorate solutions on Mars. *Earth Planet. Sci. Lett*. *312*, 371–377.

Gough, R.V., Chevrier, V.F. and Tolbert, M.A., 2014. Formation of aqueous solutions on Mars via deliquescence of chloride-perchlorate binary mixtures. *Earth Planet. Sci. Lett. 393*, 73–82.

Gough, R., Chevrier, V. and Tolbert, M., 2016. Formation of liquid water at low temperatures via the deliquescence of calcium chloride: Implications for Antarctica and Mars. *Planet. Space Sci*. *131*, 79–87.

Gough, R.V., Primm, K.M., Rivera–Valentín, E.G., Martínez, G.M. and Tolbert, M.A., 2019. Solid-solid hydration and dehydration of Mars-relevant chlorine salts: Implications for Gale Crater and RSL locations. *Icarus*, *321*, 1–13.

Gough, R.V., Nuding, D.L., Martínez, G.M., Rivera–Valentín, E.G., Primm, K.M. and Tolbert, M.A., 2023. Laboratory studies of brine growth kinetics relevant to deliquescence on mars. *Planet. Sci. J. 4* (3), 46.

Greenspan, L., 1977. Humidity fixed points of binary saturated aqueous solutions. *J. Res. Natl. Bur. Stand. A, Phys. Chem*. *81* (1), 89.

Grjotheim, K., Voigt, W., Haugsdal, B. and Dittrich, D., 1988. Isopiestic determination of osmotic coefficients at 100 °C by means of a simple apparatus. *Acta Chem. Scand., Ser. A, 42* (8–9), 470–476.

Gruszkiewicz, M.S. and Simonson, J.M., 2005. Vapor pressures and isopiestic molalities of concentrated $CaCl_2$(aq), $CaBr_2$(aq), and NaCl(aq) to T = 523 K. *J. Chem. Thermodyn. 37* (9), 906–930.

Gu, W., Li, Y., Tang, M., Jia, X., Ding, X., Bi, X. and Wang, X., 2017. Water uptake and hygroscopicity of perchlorates and implications for the existence of liquid water in some hyperarid environments. *RSC Advances*, 7 (74), 46866–46873.

Guiné, R.P.F., Barroca, M.J., Pereira, D. and Correia, P.M.R., 2014. Adsorption isotherms of maria biscuits from different brands. *J. Food Process Eng. 37* (3), 329–337.

Guo, L., Gu, W., Peng, C., Wang, W., Li, Y.J., Zong, T., Tang, Y., Wu, Z., Lin, Q., Ge, M. and Zhang, G., 2019. A comprehensive study of hygroscopic properties of calcium- and magnesium-containing salts: implication for hygroscopicity of mineral dust and sea salt aerosols. *Atmos. Chem. Phys. 19* (4), 2115–2133.

Hamze, R., Nevoigt, I., Sazama, U., Fröba, M. and Steiger, M., 2024. Carnallite double salt for thermochemical heat storage. *J. Energy Storage*, 86, 111404.

Hanawalt, J.D., Rinn, H.W. and Frevel, L.K., 1938. Chemical analysis by X–ray diffraction. *Ind. Eng. Chem. Anal. Ed. 10* (9), 457–512.

Hanley, J., Chevrier, V.F., Berget, D.J. and Adams, R.D., 2012. Chlorate salts and solutions on Mars. *Geophys. Res. Lett. 39*, L08201.

Hanslmeier, A., 2010. *Water in the Universe* (Vol. 368). Springer Science & Business Media.

Hardy, S.C., 1977. A grain boundary groove measurement of the surface tension between ice and water. *Philos. Mag. 35* (2), 471–484.

Harkins, W.D. and Gilbert, E.C., 1926. The structure of films of water on salt solutions. II. The surface tension of calcium chloride solutions at 25 °C. *J. Am. Chem. Soc. 48* (3), 604–607.

Head III, J.W., Kreslavsky, M., Hiesinger, H., Ivanov, M., Pratt, S., Seibert, N., Smith, D.E. and Zuber, M.T., 1998. Oceans in the past history of Mars: Tests for their presence using Mars Orbiter Laser Altimeter (MOLA) data. *Geophys. Res. Lett. 25* (24), 4401–4404.

Hecht, M.H., Kounaves, S.P., Quinn, R.C., West, S.J., Young, S.M., Ming, D.W., Catling, D.C., Clark, B.C., Boynton, W.V., Hoffman, J. and DeFlores, L.P., 2009. Detection of perchlorate and the soluble chemistry of Martian soil at the Phoenix lander site. *Science*, *325* (5936), 64–67.

Hennings, E., Schmidt, H. and Voigt, W., 2014. Crystal structures of $Ca(ClO_4)_2{\cdot}4H_2O$ and $Ca(ClO_4)_2{\cdot}6H_2O$. *Acta Crystallogr. E, 70* (12), 489–493.

Henry, C. L., Dalton, C. N., Scruton, L. and Craig, V. S., 2007. Ion-specific coalescence of bubbles in mixed electrolyte solutions. *J. Phys. Chem. C*, *111* (2), 1015–1023.

Hepburn, J.R.I., 1932. The vapor pressure of water over aqueous solutions of the chlorides of the alkaline-earth metals. Part I. Experimental, with a critical discussion of vapor-pressure data. *J Chem. Soc.* 550–566.

Hillig, W.B., 1998. Measurement of interfacial free energy for ice/water system. *J. Cryst. Growth*, *183* (3), 463–468.

Hnedkovsky, L. and Hefter, G., 2021. Densities and apparent molar volumes of aqueous solutions of $NaClO_4$, $KClO_4$, and KCl at temperatures from 293 to 343 K. *J. Chem. Eng. Data*, *66* (9), 3645–3658.

Hodgson, C. and McIntosh, R., 1960. The freezing of water and benzene in porous vycor glass. *Can. J. Chem. 38* (6), 958–971.

Holmes, H.F., Baes Jr, C.F. and Mesmer, R.E., 1978. Isopiestic studies of aqueous solutions at elevated temperatures I. KCl, $CaCl_2$, and $MgCl_2$. *J. Chem. Thermodyn. 10* (10), 983–996.

Holmes, H.F., Busey, R.H., Simonson, J.M. and Mesmer, R.E., 1994. $CaCl_2$(aq) at elevated temperatures. Enthalpies of dilution, isopiestic molalities, and thermodynamic properties. *J. Chem. Thermodyn. 26* (3), 271–298.

Hong, J., Tian, Y., Liang, T., Liu, X., Song, Y., Guan, D., Yan, Z., Guo, J., Tang, B., Cao, D. and Guo, J., 2024. Imaging surface structure and premelting of ice Ih with atomic resolution. *Nature*, 630, 375−380.

Horibe, A., Fukusako, S., Yamada, M. and Fumoto, K., 1997. Surface tension of aqueous binary solutions at low temperatures. *Int. J. Thermophys. 18*, 387−396.

Houben, J., Langelaan, D., Brinkman, L., Huinink, H., Fischer, H.R. and Adan, O.C., 2022. Understanding the hydration process of salts: the relation between surface mobility and metastability. *Cryst. Growth Des. 22*(8), 4906−4916.

Huang, C., Wikfeldt, K.T., Tokushima, T., Nordlund, D., Harada, Y., Bergmann, U., Niebuhr, M., Weiss, T.M., Horikawa, Y., Leetmaa, M. and Ljungberg, M.P., 2009. The inhomogeneous structure of water at ambient conditions. *Proc. Natl. Acad. Sci. USA*, *106* (36), 15214−15218.

Hrubý, J., Vinš, V., Mareš, R., Hykl, J. and Kalová, J., 2014. Surface tension of supercooled water: No inflection point down to −25 °C. *J. Phys. Chem. Lett. 5* (3), 425−428.

Hucher, M., Oberlin Mathieu−Sicaud, A. and Hocart, R., 1967. Adsorption of water vapor on the cleavage faces of some alkali halides. *Bull. Minéral. 90* (3), 320−332.

IAPWS R1−76(2014). Revised Release on Surface Tension of Ordinary Water Substance. https://www.iapws.org/relguide/Surf−H2O.html

Israelachvili, J.N., 2011. *Intermolecular and Surface Forces*. Academic press.

Jähnert, S., Chávez, F.V., Schaumann, G.E., Schreiber, A., Schönhoff, M. and Findenegg, G.H., 2008. Melting and freezing of water in cylindrical silica nanopores. *Phys. Chem. Chem. Phys. 10* (39), 6039−6051.

Jakosky, B.M. and Haberle, R.M., 1992. The seasonal behavior of water on Mars. *Mars*, 969−1016.

Jakosky, B.M., 2021. Atmospheric loss to space and the history of water on Mars. *Ann. Rev. Earth Planet. Sci. 49* (1), 71−93.

Jantsch, E., Weinberger, C., Tiemann, M. and Koop, T., 2019. Phase transitions of ice in aqueous salt solutions within nanometer-sized pores. *J. Phys. Chem. C*, *123* (40), 24566−24574.

Jarvis, N.L. and Scheiman, M.A., 1968. Surface potentials of aqueous electrolyte solutions. *J. Phys. Chem. 72* (1), 74−78.

Jia, X., Gu, W., Li, Y.J., Cheng, P., Tang, Y., Guo, L., Wang, X. and Tang, M., 2018. Phase transitions and hygroscopic growth of $Mg(ClO_4)_2$, $NaClO_4$, and $NaClO_4{\cdot}H_2O$: implications for the stability of aqueous water in hyperarid environments on Mars and on Earth. *ACS Earth and Space Chem.* 2 (2), 159−167.

Jian, Z., Li, N., Zhu, M., Chen, J., Chang, F. and Jie, W., 2012. Temperature dependence of the crystal–melt interfacial energy of metals. *Acta Mater. 60* (8), 3590−3603.

Jiang, Q. and Lu, H.M., 2008. Size dependent interface energy and its applications. *Surf. Sci. Rep. 63* (10), 427−464.

Jones, D.R.H., 1973. The measurement of solid−liquid interfacial energies from the shapes of grain-boundary grooves. *Philos. Mag. 27* (3), 569−584.

Jones, I.D. and Gortner, R.A., 1932. Free and bound water in elastic and non-elastic gels. *J. Phys. Chem. 36* (1), 387−436.

Kallenberger, P.A. and Fröba, M., 2018. Water harvesting from air with a hygroscopic salt in a hydrogel-derived matrix. *Commun. Chem*. *1* (1), 28.

Kannan, M., 2018. Scanning electron microscopy: Principle, components and applications. *A textbook on fundamentals and applications of nanotechnology*, 81−92.

Kelly, J.T. and Wexler, A.S., 2005. Thermodynamics of carbonates and hydrates related to heterogeneous reactions involving mineral aerosol. *J. Geophys. Res. Atmos. 110*, D112001.

Ketcham, W.M. and Hobbs, P.V., 1969. An experimental determination of the surface energies of ice. *Philos. Mag. 19* (162), 1161−1173.

Kim, H., Yang, S., Rao, S.R., Narayanan, S., Kapustin, E.A., Furukawa, H., Umans, A.S., Yaghi, O.M. and Wang, E.N., 2017. Water harvesting from air with metal-organic frameworks powered by natural sunlight. *Science*, *356* (6336), 430−434.

Kim, H., Rao, S.R., Kapustin, E.A., Zhao, L., Yang, S., Yaghi, O.M. and Wang, E.N., 2018. Adsorption-based atmospheric water harvesting device for arid climates. *Nat. Commun*. *9* (1), 1191.

Kittaka, S., Ishimaru, S., Kuranishi, M., Matsuda, T. and Yamaguchi, T., 2006. Enthalpy and interfacial free energy changes of water capillary condensed in mesoporous silica, MCM−41 and SBA−15. *Phys. Chem. Chem. Phys. 8* (27), 3223−3231.

Kittaka, S., Takahara, S., Matsumoto, H., Wada, Y., Satoh, T.J. and Yamaguchi, T., 2013. Low temperature phase properties of water confined in mesoporous silica MCM−41: Thermodynamic and neutron scattering study. *J. Chem. Phys. 138*, 204717.

Kittaka, S., Ueda, Y., Fujisaki, F., Iiyama, T. and Yamaguchi, T., 2011. Mechanism of freezing of water in contact with mesoporous silicas MCM−41, SBA−15 and SBA−16: role of boundary water of pore outlets in freezing. *Phys. Chem. Chem. Phys. 13* (38), 17222−17233.

Koniorczyk, M. and Bednarska, D., 2019. Kinetics of water freezing from inorganic salt solution confined in mesopores. *Thermochim. Acta*, *682*, 178434.

Kresge, A.C., Leonowicz, M.E., Roth, W.J., Vartuli, J.C. and Beck, J.S., 1992. Ordered mesoporous molecular sieves synthesized by a liquid-crystal template mechanism. *Nature*, *359* (6397), 710–712.

Krumgalz, B.S., 2017. Temperature dependence of mineral solubility in water. Part I. Alkaline and alkaline earth chlorides. *J. Phys. Chem. Ref. Data*, *46*, 043101.

Krumgalz, B.S., Pogorelsky, R., Sokolov, A. and Pitzer, K.S., 2000. Volumetric ion interaction parameters for single-solute aqueous electrolyte solutions at various temperatures. *J. Phys. Chem. Ref. Data*, *29* (5), 1123–1140.

Kuo, M.H., Moussa, S.G. and McNeill, V.F., 2011. Modeling interfacial liquid layers on environmental ices. *Atmos. Chem. Phys. 11* (18), 9971–9982.

Kwok, K., Mauer, L.J. and Taylor, L.S., 2010. Kinetics of moisture–induced hydrolysis in powder blends stored at and below the deliquescence relative humidity: Investigation of sucrose–citric acid mixtures. *J. Agric. Food Chem. 58* (22), 11716–11724.

Kwon, S.B. and Kim, J.J., 1990. Raman studies of the 223 K phase transition in $(NH_4)_2SO_4$ single crystal. *J. Phys. Condens. Matter*, *2* (51), 10607.

La Francesca, P. and Gallo, P., 2023. Supercooled solutions of sodium perchlorate in TIP4P/2005 water: The effect of Martian solutes on thermodynamics and structure. *J. Chem. Phys. 159*, 124501.

Lad, R.A., 1968. Adsorption of water on sodium chloride: the effect of prior exposure to hydrogen chloride, carbon dioxide and water vapor. *Surf. Sci.*, *12* (1), 37–45.

Lamb, A.B. and Coolidge, A.S., 1920. The heat of absorption of vapors on charcoal. *J. Am. Chem. Soc*. *42* (6), 1146–1170.

Langlet, M., Benali, M., Pezron, I., Saleh, K., Guigon, P. and Metlas–Komunjer, L., 2013. Caking of sodium chloride: Role of ambient relative humidity in dissolution and recrystallization process. *Chem. Eng. Sci*. *86*, 78–86.

Lannung, A., 1936. Dampfdruckmessungen des systems calciumchlorid–wasser. *Z. Anorg. Allg. Chem*. *228* (1), 1–18.

Lassin, A. and André, L., 2023. A revised description of the binary $CaCl_2$–H_2O chemical system up to solution–mineral equilibria and temperatures of 250 °C using Pitzer equations. Extension to the multicomponent HCl–LiCl–NaCl–KCl–$MgCl_2$–$CaCl_2$–H_2O system. *J. Chem. Thermodyn*. 176, 106927.

Leclaire, A. and Borel, M.M., 1977a. Le dichlorure de calcium dihydraté. *Struct. Sci*. *33* (5), 1608–1610.

Leclaire, A. and Borel, M.M., 1977b. Le dichlorure et le dibromure de calciumhexahydrates. *Struct. Sci. 33* (9), 2938–2940.

Leclaire, A. and Borel, M.M., 1978. La forme β du dichlorure de calcium tétrahydraté. *Struct. Sci. 34* (3), 900–902.

Leclaire, A. and Borel, M.M., 1979. Liaisons hydrogène et coordination du calcium dans les cristaux de $CaCl_2 \cdot 4H_2O\alpha$. *Struct. Sci. 35* (3), 585–588.

Leclaire, A., Borel, M.M. and Monier, J.C., 1980. La forme γ du dichlorure de calcium tétrahydraté. *Struct. Sci. 36* (11), 2757–2759.

Lescoeur, H., 1890 Recherches sur la dissociation des hydrates salins et des composés

analogues. III. Hydrates formés par les sels haloides. *Ann. Chim. Phys. 19*, 533–556.

Li, D., Zeng, D., Yin, X., Han, H., Guo, L. and Yao, Y., 2016b. Phase diagrams and thermochemical modeling of salt lake brine systems. II. NaCl + H_2O, KCl + H_2O, $MgCl_2$ + H_2O, and $CaCl_2$ + H_2O systems. *CALPHAD*, *53*, 78–89.

Li, D., Zhao, Y.Y.S., Meslin, P.Y., Vals, M., Forget, F. and Wu, Z., 2022. Cryogenic origin of fractionation between perchlorate and chloride under modern Martian climate. *Commun. Earth Environ*. *3*, 15.

Li, N., Taylor, L.S. and Mauer, L.J., 2016a. Heat transport model for the deliquescence kinetics of crystalline ingredients and mixtures. *J. Food Eng. 169*, 298–308.

Li, T., Yan, T., Wang, P., Xu, J., Huo, X., Bai, Z., Shi, W., Yu, G. and Wang, R., 2023. Scalable and efficient solar–driven atmospheric water harvesting enabled by bidirectionally aligned and hierarchically structured nanocomposites. *Nature Water*, *1* (11), 971–981.

Lied, A., Dosch, H. and Bilgram, J.H., 1994. Glancing angle X–ray scattering from single crystal ice surfaces. *Physica B: Condens. Matter*, *198* (1–3), 92–96.

Lima, E.R.A., Boström, M., Horinek, D., Biscaia, E.C., Kunz, W. and Tavares, F.W., 2008. Co-ion and ion competition effects: ion distributions close to a hydrophobic solid surface in mixed electrolyte solutions. *Langmuir*, *24* (8), 3944–3948.

Lin, J.J., Mundoli, K.R.R., Wang, S., Kokkonen, E., Mikkelä, M.H., Urpelainen, S. and Prisle, N.L., 2021. Pre-deliquescent water uptake in deposited nanoparticles observed with *in situ* ambient pressure X-ray photoelectron spectroscopy. *Atmos. Chem. Phys. 21* (6), 4709–4727.

Lin, X., Zhang, C., Hu, S. and Chen, R., 2024. Heterogeneous ice nucleation of salt solution in porous media. *J. Chem. Phys*. *160*, 094501.

Linnow, K., Niermann, M., Bonatz, D., Posern, K. and Steiger, M., 2014. Experimental studies of the mechanism and kinetics of hydration reactions. *Energy Procedia*, *48*, 394−404.

Linnow, K., Zeunert, A. and Steiger, M., 2006. Investigation of sodium sulfate phase transitions in a porous material using humidity- and temperature-controlled X−ray diffraction. *Anal. Chem. 78* (13), 4683−4689.

Litvan, G.G., 1966. Phase transitions of adsorbates: 1. Specific heat and dimensional changes of the porous glass-water system. *Can. J. Chem. 44* (22), 2617−2622.

Liu, E., Dore, J.C., Webber, J.B.W., Khushalani, D., Jähnert, S., Findenegg, G.H. and Hansen, T., 2006. Neutron diffraction and NMR relaxation studies of structural variation and phase transformations for water/ice in SBA−15 silica: I. The over-filled case. *J. Phys. Condens. Matter*, *18* (44), 10009.

Liu, F., Zargarzadeh, L., Chung, H.J. and Elliott, J.A., 2017. Thermodynamic investigation of the effect of interface curvature on the solid–liquid equilibrium and eutectic point of binary mixtures. *J. Phys. Chem. B*, *121* (40), 9452−9462.

Longinotti, M.P., Fuentes−Landete, V., Loerting, T. and Corti, H.R., 2019. Glass transition of LiCl aqueous solutions confined in mesoporous silica. *J. Chem. Phys. 151*, 064509.

Lowenstein, A., 2008. Review of liquid desiccant technology for HVAC applications. *HVAC&R Res*. *14* (6), 819−839.

Lumme, P., Larsen, F.K., Poulsen, F.R., Christensen, A.N., Rasmussen, S.E., Sunde, E. and Sørensen, N.A., 1970. On properties of strong electrolytes II. The densities of aqueous magnesium, calcium, strontium and barium perchlorate solutions. *Acta Chem. Scand*, *24*, 1727-1734.

Malec, L.M., Gryl, M. and Stadnicka, K.M., 2018. Unmasking the mechanism of structural para−to ferroelectric phase transition in $(NH_4)_2SO_4$. *Inorg. Chem. 57* (8), 4340−4351.

Malfait, B., Pouessel, A., Jani, A. and Morineau, D., 2020. Extension and limits of cryoscopy for nanoconfined solutions. *J. Phys. Chem. Lett*. *11* (14), 5763−5769.

Malin, M.C. and Edgett, K.S., 2000. Sedimentary rocks of early Mars. *Science*, *290* (5498), 1927−1937.

Malin, M.C. and Edgett, K.S., 2001. Mars global surveyor Mars orbiter camera: interplanetary cruise through primary mission. *J. Geophys. Res. Planets*, *106* (E10), 23429−23570.

Malin, M.C. and Edgett, K.S., 2003. Evidence for persistent flow and aqueous sedimentation on early Mars. *Science*, *302* (5652), 1931−1934.

Malin, M.C., Edgett, K.S., Posiolova, L.V., McColley, S.M. and Dobrea, E.Z.N., 2006. Present−day impact cratering rate and contemporary gully activity on Mars. *Science*, *314* (5805), 1573−1577.

Marcus, Y., 2003. The sizes of molecules—revisited. *J. Phys. Org. Chem. 16*, 398–408.

Marcus, Y., and Hefter, G., 2006. Ion pairing. *Chem. Rev. 106* (11), 4585–4621.

Marion, G.M., Catling, D.C., Zahnle, K.J. and Claire, M.W., 2010. Modeling aqueous perchlorate chemistries with applications to Mars. *Icarus*, *207* (2), 675–685.

Martín–Torres, F.J., Zorzano, M.P., Valentín–Serrano, P., Harri, A.M., Genzer, M., Kemppinen, O., Rivera–Valentin, E.G., Jun, I., Wray, J., Bo Madsen, M. and Goetz, W., 2015. Transient liquid water and water activity at Gale crater on Mars. *Nat. Geosci. 8* (5), 357–361.

Materer, N., Starke, U., Barbieri, A., Van Hove, M., Somorjai, G.A., Kroes, G.J. and Minot, C., 1995. Molecular surface structure of a low-temperature ice Ih (0001) crystal. *J. Phys. Chem. 99* (17), 6267–6269.

Mauer, L.J., 2022. Deliquescence of crystalline materials: mechanism and implications for foods. *Curr. Opin. Food Sci*. *46*, 100865.

Mauer, L.J. and Taylor, L.S., 2010. Water–solids interactions: deliquescence. *Annu. Rev. Food Sci. Technol*. *1* (1), 41–63.

May, C.E. and Jayne, J.P., 1966. Dependence of surface conductivity of sodium chloride on the chemical nature of the surface. National Aeronautics and Space Administration.

Meissner, J., Prause, A. and Findenegg, G.H., 2016. Secondary confinement of water observed in eutectic melting of aqueous salt systems in nanopores. *J. Phys. Chem. Lett*. *7* (10), 1816–1820.

Millero, F.J., 1982. The effect of pressure on the solubility of minerals in water and seawater. *Geochim. Cosmochim. Acta*, *46* (1), 11–22.

Minofar, B., Vácha, R., Wahab, A., Mahiuddin, S., Kunz, W. and Jungwirth, P., 2006. Propensity for the air/water interface and ion pairing in magnesium acetate vs magnesium nitrate solutions: Molecular dynamics simulations and surface tension measurements. *J. Phys. Chem. B*, *110* (32), 15939–15944.

Mishima, O. and Stanley, H.E., 1998. Decompression–induced melting of ice IV and the liquid–liquid transition in water. *Nature*, *392* (6672), 164–168.

Molenda, M., Stengler, J., Linder, M. and Wörner, A., 2013. Reversible hydration behavior of $CaCl_2$ at high H_2O partial pressures for thermochemical energy storage. *Thermochim. Acta*, *560*, 76–81.

Momma, K. and Izumi, F., 2011. VESTA3 for three-dimensional visualization of crystal, volumetric and morphology data. *Appl. Crystallogr*. *44* (6), 1272–1276.

Morishige, K. and Nobuoka, K., 1997. X-ray diffraction studies of freezing and melting of water confined in a mesoporous adsorbent (MCM–41). *J. Chem. Phys. 107* (17), 6965–6969.

Morishige, K. and Kawano, K., 1999. Freezing and melting of water in a single cylindrical pore: The pore−size dependence of freezing and melting behavior. *J. Chem. Phys. 110* (10), 4867−4872.

Morishige, K. and Uematsu, H., 2005. The proper structure of cubic ice confined in mesopores. *J. Chem. Phys. 122*, 044711.

Mullin, J.W., 2001. *Crystallization* (Vol. 124). Butterworth−Heinemann.

Murphy, D.M. and Koop, T., 2005. Review of the vapor pressures of ice and supercooled water for atmospheric applications. *Quarterly Journal of the Royal Meteorological Society: A Journal of the Atmospheric Sciences, Applied Meteorology and Physical Oceanography*, *131* (608), 1539−1565.

Mustard, J.F., Murchie, S.L., Pelkey, S.M., Ehlmann, B.L., Milliken, R.E., Grant, J.A., Bibring, J.P., Poulet, F., Bishop, J., Dobrea, E.N. and Roach, L., 2008. Hydrated silicate minerals on Mars observed by the Mars Reconnaissance Orbiter CRISM instrument. *Nature*, *454* (7202), 305−309.

Nada, H. and van der Eerden, J.P., 2003. An intermolecular potential model for the simulation of ice and water near the melting point: A six-site model of H_2O. *J. Chem. Phys*. *118* (16), 7401−7413.

Nazari−Sharabian, M., Aghababaei, M., Karakouzian, M. and Karami, M., 2020. Water on Mars-a literature review. *Galaxies*, *8* (2), 40.

Němec, T., 2013. Estimation of ice-water interfacial energy based on pressure-dependent formulation of classical nucleation theory. *Chem. Phys. Lett. 583*, 64−68.

Newsom, H.E., Brittelle, G.E., Hibbitts, C.A., Crossey, L.J. and Kudo, A.M., 1996. Impact crater lakes on Mars. *J. Geophys. Res. Planets*, *101* (E6),14951−14955.

N'Tsoukpoe, K.E., Rammelberg, H.U., Lele, A.F., Korhammer, K., Watts, B.A., Schmidt, T. and Ruck, W.K., 2015. A review on the use of calcium chloride in applied thermal engineering. *Appl. Therm. Eng*. *75*, 513−531.

Nuding, D., Rivera−Valentin, E.G., Davis, R.D., Gough, R.V., Chevrier, V.F. and Tolbert, M.A., 2014. Deliquescence and efflorescence of calcium perchlorate: An investigation of stable aqueous solutions relevant to Mars. *Icarus*, *243*, 420−428.

Ojha, L., Wilhelm, M.B., Murchie, S.L., McEwen, A.S., Wray, J.J., Hanley, J., Massé, M. and Chojnacki, M., 2015. Spectral evidence for hydrated salts in recurring slope lineae on Mars. *Nat. Geosci. 8* (11), 829−832.

Oakes, C.S., Bodnar, R.J. and Simonson, J.M., 1990. The system $NaCl−CaCl_2−H_2O$: I. The ice liquidus at 1 atm total pressure. *Geochim. Cosmochim. Acta*, *54* (3), 603−610.

Orosei, R., Lauro, S.E., Pettinelli, E., Cicchetti, A., Coradini, M., Cosciotti, B., Di Paolo, F., Flamini, E., Mattei, E., Pajola, M. and Soldovieri, F., 2018. Radar evidence of subglacial liquid water on Mars. *Science*, *361* (6401), 490−493.

Ostwald, W., 1897. Studien über die bildung und umwandlung fester körper: 1. Abhandlung: Übersättigung und überkaltung. *Z. Phys. Chem*. *22* (1), 289−330.

Otterson, D.A., 1963. Influence of room−temperature atmospheric reaction products on the ductility of sodium chloride single crystals. *J. Chem. Phys. 38* (7), 1481−1486.

Overloop, K. and Vangerven, L., 1993. Freezing phenomena in adsorbed water as studied by NMR. *J. Magn. Reson. 101* (2), 179−187.

Papée, H.M. and Laidler, K.J., 1958. Microcalorimetry of the adsorption of water vapor on sodium chloride. *Can. J. Chem. 36* (10), 1338−1345.

Pathak, H., Späh, A., Esmaeildoost, N., Sellberg, J.A., Kim, K.H., Perakis, F., Amann−Winkel, K., Ladd-Parada, M., Koliyadu, J., Lane, T.J. and Yang, C., 2021. Enhancement and maximum in the isobaric specific−heat capacity measurements of deeply supercooled water using ultrafast calorimetry. *Proc. Natl. Acad. Sci. USA. 118* (6), e2018379118.

Patrick, W.A. and Kemper, W.A., 1937. Melting temperatures of compounds adsorbed on silica gel. *J. Phys. Chem. 42* (3), 369−380.

Pearson, R.T. and Derbyshire, W., 1974. NMR studies of water adsorbed on a number of silica surfaces. *J. Colloid Interface Sci. 46* (2), 232−248.

Peng, J., Guo, J., Ma, R., Meng, X. and Jiang, Y., 2017. Atomic−scale imaging of the dissolution of NaCl islands by water at low temperature. *J. Phys. Condens. Matter*, *29* (10), 104001.

Perin, L. and Gallo, P., 2023. Phase diagram of aqueous solutions of LiCl: A study of concentration effects on the anomalies of water. *J. Phys. Chem. B*, *127* (20), 4613−4622.

Pestova, O.N., Myund, L.A., Khripun, M.K. and Prigaro, A.V., 2005. Polythermal study of the systems $M(ClO_4)_2$−H_2O (M^{2+}= Mg^{2+}, Ca^{2+}, Sr^{2+}, Ba^{2+}). *Russ. J. Appl. Chem. 78*, 409−413.

Peters, S.J. and Ewing, G.E., 1997a. Water on salt: An infrared study of adsorbed H_2O on NaCl (100) under ambient conditions. *J. Phys. Chem. B*, *101* (50), 10880−10886.

Peters, S.J. and Ewing, G.E., 1997b. Thin film water on NaCl (100) under ambient conditions: An infrared study. *Langmuir*, *13* (24), 6345−6348.

Pitzer, K.S., 1991. Ion interaction approach: theory and data correlation. In *Activity coefficients in electrolyte solutions* (75−153). CRC Press.

Pitzer, K.S. and Oakes, C.S., 1994. Thermodynamics of calcium chloride in concentrated aqueous solutions and in crystals. *J. Chem. Eng. Data*, *39* (3), 553–559.

Poole, P.H., Sciortino, F., Essmann, U. and Stanley, H.E., 1992. Phase behavior of metastable water. *Nature*, *360* (6402), 324–328.

Poole, P.H., Sciortino, F., Grande, T., Stanley, H.E. and Angell, C.A., 1994. Effect of hydrogen bonds on the thermodynamic behavior of liquid water. *Phys. Rev. Lett. 73* (12), 1632.

Postberg, F., Schmidt, J., Hillier, J., Kempf, S. and Srama, R., 2011. A salt-water reservoir as the source of a compositionally stratified plume on Enceladus. *Nature*, *474* (7353), 620–622.

Prause, A., Meissner, J., Schomäcker, R. and Findenegg, G.H., 2020. Preparation of NiO nanoparticles in mesoporous silica via eutectic freezing and freeze–drying of aqueous precursor salts. *Micropor. Mesopor. Mater. 304*, 109136.

Price, W.C., Sherman, W.F. and Wilkinson, G.R., 1958. Infrared studies of water adsorbed on alkali halides. *Proc. R. Soc. Lond., Ser. A. Math. Phys. Sci*, *247* (1251), 467–468.

Primm, K.M., Gough, R.V., Chevrier, V.F. and Tolbert, M.A., 2017. Freezing of perchlorate and chloride brines under Mars-relevant conditions. *Geochim. Cosmochim. Acta*, *212*, 211–220.

Putnis, A. and Putnis, C.V., 2007. The mechanism of re-equilibration of solids in the presence of a fluid phase. *J. Solid State Chem. 180* (5), 1783–1786.

Putnis, C.V. and Putnis, A., 2022. A mechanism of ion exchange by interface-coupled dissolution–precipitation in the presence of an aqueous fluid. *J. Cryst. Growth*, *600*, 126840.

Qian, J., Gao, X., Pan, B., 2020. Nanoconfinement–mediated water treatment: from fundamental to application. *Environ. Sci. Technol. 54* (14), 8509–8526.

Qiao, R. and Aluru, N.R., 2003. Ion concentrations and velocity profiles in nanochannel electroosmotic flows. *J. Chem. Phys. 118* (10), 4692–4701.

Raman, C.V. and Krishnan, K.S. 1928, *Nature*, 121, 501.

Rard, J.A. and Clegg, S.L., 1997. Critical evaluation of the thermodynamic properties of aqueous calcium chloride. 1. Osmotic and activity coefficients of 0–10.77 mol· kg^{-1} aqueous calcium chloride solutions at 298.15 K and correlation with extended Pitzer ion-interaction models. *J. Chem. Eng. Data*, *42* (5), 819–849.

Rard, J.A., Clegg, S.L. and Palmer, D.A., 2000. Isopiestic determination of the osmotic coefficients of Na_2SO_4(aq) at 25 and 50 °C, and representation with ion-interaction (Pitzer) and mole fraction thermodynamic models. *J. Solution Chem. 29*, 1–49.

Raviv, U., Laurat, P. and Klein, J., 2001. Fluidity of water confined to sub-nanometer films. *Nature*, *413* (6851), 51–54.

Rennie, G.K. and Clifford, J., 1977. Melting of ice in porous solids. *J. Chem. Soc. Faraday Trans. 1: Phys. Chem. Condens. Ph. 73*, 680–689.

Rennó, N.O., Bos, B.J., Catling, D., Clark, B.C., Drube, L., Fisher, D., Goetz, W., Hviid, S.F., Keller, H.U., Kok, J.F. and Kounaves, S.P., 2009. Possible physical and thermodynamic evidence for liquid water at the Phoenix landing site. *J. Geophys. Res. Planets*, *114*, E00E03.

Richardson, G.M. and Malthus, R.S., 1955. Salts for static control of humidity at relatively low levels. *J. Appl. Chem*. *5* (10), 557–567.

Rieder, R., Gellert, R., Anderson, R.C., Bruckner, J., Clark, B.C., Dreibus, G., Economou, T., Klingelhofer, G., Lugmair, G.W., Ming, D.W. and Squyres, S.W., 2004. Chemistry of rocks and soils at Meridiani Planum from the Alpha Particle X-ray Spectrometer. *Science*, *306* (5702), 1746–1749.

Rissler, J., Preger, C., Eriksson, A.C., Lin, J.J., Prisle, N.L. and Svenningsson, B., 2023. Missed evaporation from atmospherically relevant inorganic mixtures confounds experimental aerosol studies. *Environ. Sci. Technol. 57* (7), 2706–2714.

Rother, G., Gautam, S., Liu, T., Cole, D.R., Busch, A. and Stack, A.G., 2022. Molecular structure of adsorbed water phases in silica nanopores. *J. Phys. Chem. C*, *126* (5), 2885–2895.

Ruiz–Agudo, E., Putnis, C.V. and Putnis, A., 2014. Coupled dissolution and precipitation at mineral-fluid interfaces. *Chem. Geol. 383*, 132–146.

Sahlot, M. and Riffat, S.B., 2016. Desiccant cooling systems: a review. *Int. J. Low–Carbon Technol. 11* (4), 489–505.

Salameh, A.K., Mauer, L.J. and Taylor, L.S., 2006. Deliquescence lowering in food ingredient mixtures. *J. Food Sci. 71* (1), E10–E16.

Salameh, A.K. and Taylor, L.S., 2005. Deliquescence in binary mixtures. *Pharm. Res*. *22*, 318–324.

Salis, A., Parsons, D.F., Bostrom, M., Medda, L., Barse, B., Ninham, B.W. and Monduzzi, M., 2010. Ion specific surface charge density of SBA–15 mesoporous silica. *Langmuir*, *26* (4), 2484–2490.

Sastry, S., Debenedetti, P.G., Sciortino, F. and Stanley, H.E., 1996. Singularity-free interpretation of the thermodynamics of supercooled water. *Phys. Rev. E*, *53* (6), 6144.

Schreiber, A., Ketelsen, I. and Findenegg, G.H., 2001. Melting and freezing of water in ordered mesoporous silica materials. *Phys. Chem. Chem. Phys. 3* (7), 1185–1195.

Sciortino, F., La Nave, E. and Tartaglia, P., 2003. Physics of the liquid–liquid critical point. *Phys. Rev. Lett*. *91* (15), 155701.

Seyed–Yazdi, J., Farman, H., Dore, J.C., Webber, J.B.W., Findenegg, G.H. and Hansen, T., 2008. Structural characterization of water and ice in mesoporous SBA–15 silicas: II. The 'almost–filled' case for 86 Å pore diameter. *J. Phys. Condens. Matter*, *20* (20), 205107.

Shumway, A.O., Catling, D.C. and Toner, J.D., 2021. Soils increase the stability of magnesium perchlorate brines on Mars. *Brines in the Solar System: Modern Brines*, *2614*, 6005.

Shumway, A.O., Catling, D.C. and Toner, J.D., 2023. Regolith inhibits salt and ice crystallization in $Mg(ClO_4)_2$ brine, implying more persistent and potentially habitable brines on Mars. *Planet. Sci. J. 4* (8), 143.

Slank, R.A. and Chevrier, V.F., 2024. Thermodynamic modeling of calcium or magnesium chloride, chlorate, and perchlorate ternary mixtures deliquescence at Mars-relevant temperatures. *Icarus*, *410*, 115914.

Slater, B. and Michaelides, A., 2019. Surface premelting of water ice. *Nat. Rev. Chem*. *3*(3), 172–188.

Smith, M.D., 2002. The annual cycle of water vapor on Mars as observed by the Thermal Emission Spectrometer. *J. Geophys. Res. Planets*, *107* (E11), 5115.

Sögütoglu, L.C., Birkelbach, F., Werner, A., Fischer, H., Huinink, H. and Adan, O., 2021. Hydration of salts as a two-step process: Water adsorption and hydrate formation. *Thermochim. Acta*, *695*, 178819.

Sögütoglu, L.C., Steiger, M., Houben, J., Biemans, D., Fischer, H.R., Donkers, P., Huinink, H. and Adan, O.C., 2019. Understanding the hydration process of salts: the impact of a nucleation barrier. *Cryst. Growth Des. 19* (4), 2279–2288.

Soper, A.K. and Ricci, M.A., 2000. Structures of high-density and low-density water. *Phys. Rev. Lett. 84* (13), 2881.

Speedy, R.J., 1982. Stability-limit conjecture. An interpretation of the properties of water. *J. Phys. Chem. 86* (6), 982–991.

Speedy, R.J. and Angell, C.A., 1976. Isothermal compressibility of supercooled water and evidence for a thermodynamic singularity at −45 °C. *J. Chem. Phys. 65* (3), 851–858.

Spencer, J.R. and Nimmo, F., 2013. Enceladus: An active ice world in the Saturn system. *Annu. Rev. Earth and Planet. Sci.*, *41* (1), 693–717.

Stahlbuhk, A.; Godts, S.; Steiger, M., 2025b. Dynamic water vapor sorption: a helpful tool for preventive conservation of salt contaminated built heritage. *Heritage Sci*. 13, 31.

Stahlbuhk, A. and Steiger, M., 2025a. Mixed electrolyte or single salt solution-Is there an impact of precipitating salts on the damage potential? Investigations on the $Na^+–K^+–Cl^-–NO_3^-–H_2O$ System. *Cryst. Growth Des. 25* (10), 3497–3510.

Starinsky, A. and Katz, A., 2003. The formation of natural cryogenic brines. *Geochim. Cosmochim. Acta*, *67* (8), 1475–1484.

Steele–MacInnis, M., Bodnar, R.J. and Naden, J., 2011. Numerical model to determine the composition of $H_2O–NaCl–CaCl_2$ fluid inclusions based on microthermometric and microanalytical data. *Geochim. Cosmochim. Acta*, *75* (1), 21–40.

Steiger, M., 2005. Crystal growth in porous materials–I: The crystallization pressure of large crystals. *J. Cryst. Growth*, *282* (3–4), 455–469.

Steiger, M., 2006. Freezing of salt solutions in small pores. In measuring, monitoring and modeling concrete properties: An international symposium dedicated to Professor Surendra P. Shah, Northwestern University, USA (661–668). Dordrecht: Springer Netherlands.

Steiger, M., 2018. Thermodynamic properties of $SrCl_2$(aq) from 252 K to 524 K and phase equilibria in the $SrCl_2–H_2O$ system: Implications for thermochemical heat storage. *J. Chem. Thermodyn. 120*, 106–115.

Steiger, M. and Asmussen, S., 2008c. Crystallization of sodium sulfate phases in porous materials: The phase diagram $Na_2SO_4–H_2O$ and the generation of stress. *Geochim. Cosmochim. Acta*, *72* (17), 4291–4306.

Steiger, M., Kiekbusch, J. and Nicolai, A., 2008a. An improved model incorporating Pitzer's equations for calculation of thermodynamic properties of pore solutions implemented into an efficient program code. *Constr. Build. Mater. 22* (8), 1841–1850.

Steiger, M., Linnow, K., Ehrhardt, D. and Rohde, M., 2011. Decomposition reactions of magnesium sulfate hydrates and phase equilibria in the $MgSO_4–H_2O$ and $Na^+–Mg^{2+}–Cl^-–SO_4^{2-}–H_2O$ systems with implications for Mars. *Geochim. Cosmochim. Acta*, *75* (12), 3600–3626.

Steiger, M., Linnow, K., Juling, H., Gülker, G., Jarad, A.E., Brüggerhoff, S. and Kirchner, D., 2008b. Hydration of $MgSO_4·H_2O$ and generation of stress in porous materials. *Cryst. Growth Des. 8* (1), 336–343.

Steiger, M. and Voigt, W., 2019. Solid–liquid metastable equilibria for solar evaporation of brines and solubility determination: a critical discussion. *J. Solution Chem. 48*, 1009–1024.

Stillman, D.E. and Grimm, R.E., 2011. Dielectric signatures of adsorbed and salty liquid water at the Phoenix landing site, Mars. *J. Geophys. Res. Planets*, *116*, E909005.

Stokes, D., 2008. Principles and practice of variable pressure/environmental scanning electron microscopy (VP–ESEM). John Wiley & Sons.

Sullivan, R.C., Moore, M.J.K., Petters, M.D., Kreidenweis, S.M., Roberts, G.C. and Prather, K.A., 2009. Effect of chemical mixing state on the hygroscopicity and cloud nucleation properties of calcium mineral dust particles. *Atmos. Chem. Phys. 9* (10), 3303–3316.

Suter, M.T., Andersson, P.U. and Pettersson, J.B., 2006. Surface properties of water ice at 150–191 K studied by elastic helium scattering. *J. Chem. Phys. 125*, 174704.

Svenningsson, B., Rissler, J., Swietlicki, E., Mircea, M., Bilde, M., Facchini, M.C., Decesari, S., Fuzzi, S., Zhou, J., Mønster, J. and Rosenørn, T., 2006. Hygroscopic growth and critical supersaturations for mixed aerosol particles of inorganic and organic compounds of atmospheric relevance. *Atmos. Chem. Phys*. *6*(7), 1937–1952.

Takamuku, T., Yamagami, M., Wakita, H., Masuda, Y. and Yamaguchi, T., 1997. Thermal property, structure, and dynamics of supercooled water in porous silica by calorimetry, neutron scattering, and NMR relaxation. *J. Phys. Chem. B*, *101* (29), 5730–5739.

Talreja–Muthreja, T., Linnow, K., Enke, D. and Steiger, M., 2022. Deliquescence of NaCl confined in nanoporous silica. *Langmuir*, *38* (36), 10963–10974.

Talreja–Muthreja, T. and Steiger, M., 2025. Thermodynamics of $(NH_4)_2SO_{4(aq)}$ and solubilities of $(NH_4)_2M^{II}(SO_4)_2{\cdot}6H_2O$ (M = Mg, Fe, Zn, Cu) tutton salts with implications to thermochemical storage. *J. Solution Chem*. 1–30. https://doi.org/10.1007/s10953-025-01431-w

Talreja–Muthreja, T. and Steiger, M., Water vapor sorption of $(NH_4)_2SO_4$ confined in nanoporous silica. In preparation

Tang, M., Cziczo, D.J. and Grassian, V.H., 2016. Interactions of water with mineral dust aerosol: water adsorption, hygroscopicity, cloud condensation, and ice nucleation. *Chem. Rev*. *116* (7), 4205–4259.

Taylor, F.W., 2011. Comparative planetology, climatology and biology of Venus, Earth and Mars. *Planet. Space Sci. 59* (10), 889–899.

Thanh, N.T., Maclean, N. and Mahiddine, S., 2014. Mechanisms of nucleation and growth of nanoparticles in solution. *Chem. Rev.*, *114* (15), 7610–7630.

Thommes, M., Kaneko, K., Neimark, A.V., Olivier, J.P., Rodriguez–Reinoso, F., Rouquerol, J. and Sing, K.S., 2015. Physisorption of gases, with special reference to the evaluation of surface area and pore size distribution (IUPAC Technical Report). *Pure Appl. Chem.* 87 (9–10), 1051–1069.

Thommes, M., Smarsly, B., Groenewolt, M., Ravikovitch, P.I. and Neimark, A.V., 2006. Adsorption hysteresis of nitrogen and argon in pore networks and characterization of novel micro- and mesoporous silicas. *Langmuir*, *22* (2), 756–764.

Threlfall, T., 2003. Structural and thermodynamic explanations of Ostwald's rule. *Org. Process Res. Dev*. *7* (6), 1017–1027.

Titus, T.N., Kieffer, H.H. and Christensen, P.R., 2003. Exposed water ice discovered near the south pole of Mars. *Science*, *299* (5609), 1048–1051.

Tokarev, M.M. and Aristov, Y.I., 1997. Selective water sorbents for multiple applications, 4. $CaCl_2$ confined in silica gel pores: sorption/desorption kinetics. *React. Kinet. Catal. Lett. 62*, 143–150.

Toner, J.D. and Sletten, R.S., 2013. The formation of Ca-Cl-rich groundwaters in the Dry Valleys of Antarctica: Field measurements and modeling of reactive transport. *Geochim. Cosmochim. Acta*, *110*, 84–105.

Toner, J.D., Catling, D.C. and Light, B., 2014. The formation of supercooled brines, viscous liquids, and low-temperature perchlorate glasses in aqueous solutions relevant to Mars. *Icarus*, *233*, 36–47.

Toner, J.D., Catling, D.C. and Light, B., 2015a. Modeling salt precipitation from brines on Mars: Evaporation versus freezing origin for soil salts. *Icarus*, *250*, 451–461.

Toner, J.D., Catling, D.C. and Light, B., 2015b. A revised Pitzer model for low-temperature soluble salt assemblages at the Phoenix site, Mars. *Geochim. Cosmochim. Acta*, *166*, 327–343.

Toner, J.D. and Catling, D., 2016. Water activities of $NaClO_4$, $Ca(ClO_4)_2$, and $Mg(ClO_4)_2$ brines from experimental heat capacities: Water activity > 0.6 below 200 K. *Geochim. Cosmochim. Acta*, *181*, 164–174.

Toner, J.D. and Catling, D.C., 2017a. A low–temperature thermodynamic model for the Na–K–Ca–Mg–Cl system incorporating new experimental heat capacities in KCl, $MgCl_2$, and $CaCl_2$ solutions. *J. Chem. Eng. Data*, *62* (3), 995–1010.

Toner, J.D. and Catling, D.C., 2017b. A low–temperature aqueous thermodynamic model for the Na–K–Ca–Mg–Cl–SO_4 system incorporating new experimental heat capacities in Na_2SO_4, K_2SO_4, and $MgSO_4$ solutions. *J. Chem. Eng. Data*, *62* (10), 3151–3168.

Toner, J.D. and Catling, D.C., 2018. Chlorate brines on Mars: Implications for the occurrence of liquid water and deliquescence. *Earth Planet. Sci. Lett. 497*, 161–168.

Torrie, B.H., Lin, C.C., Binbrek, O.S. and Anderson, A., 1972. Raman and infrared studies of the ferroelectric transition in ammonium sulphate. *J. Phys. Chem. Solids*, *33* (3), 697–709.

Tu, S., Lobanov, S.S., Bai, J., Zhong, H., Gregerson, J., Rogers, A.D., Ehm, L. and Parise, J.B., 2019. Enhanced formation of solvent–shared ion pairs in aqueous calcium perchlorate solution toward saturated concentration or deep supercooling temperature and its effects on the water structure. *J. Phys. Chem. B*, *123* (45), 9654–9667.

Tu, Y., Wang, R., Zhang, Y. and Wang, J., 2018. Progress and expectation of atmospheric water harvesting. *Joule*, *2* (8), 1452–1475.

Tuckermann, R., 2007. Surface tension of aqueous solutions of water-soluble organic and inorganic compounds. *Atmos. Environ. 41* (29), 6265–6275.

Uriarte, L.M., Dubessy, J., Boulet, P., Baonza, V.G., Bihannic, I. and Robert, P., 2015. Reference Raman spectra of synthesized $CaCl_2 \cdot nH_2O$ solids (n = 0, 2, 4, 6). *J. Raman Spectrosc. 46* (10), 822–828.

Ushak, S., Suárez, M., Véliz, S., Fernández, A.G., Flores, E. and Galleguillos, H.R., 2016. Characterization of calcium chloride tetrahydrate as a phase change material and thermodynamic analysis of the results. *Renew. Energy*, *95*, 213–224.

Varasova, E.N., Mishchenko, K.P. and Frost, O.I., 1937. Thermodynamic properties of aqueous solutions saturated with salt systems. I. Specific heat and vapor pressure of the system $BaCl_2$–$CaCl_2$–H_2O at 25 °C (in Russian). *Zh. Obsh. Khim. 7*, 1284–1291.

Verdaguer, A., Sacha, G.M., Luna, M., Frank Ogletree, D. and Salmeron, M., 2005. Initial stages of water adsorption on NaCl (100) studied by scanning polarization force microscopy. *J. Chem. Phys. 123*, 124703.

Verdaguer, A., Segura, J.J., Fraxedas, J., Bluhm, H. and Salmeron, M., 2008. Correlation between charge state of insulating NaCl surfaces and ionic mobility induced by water adsorption: a combined ambient pressure X–ray photoelectron spectroscopy and scanning force microscopy study. *J. Phys. Chem. C*, *112* (43), 16898–16901.

Vincent, O., Zhang, J., Choi, E., Zhu, S. and Stroock, A.D., 2019. How solutes modify the thermodynamics and dynamics of filling and emptying in extreme ink-bottle pores. *Langmuir*, *35* (8), 2934–2947.

Voigt, W., 2015. What we know and still not know about oceanic salts. *Pure Appl. Chem. 87* (11–12), 1099–1126.

Voigt, W., Haugsdal, B. and Grjotheim, K., 1990. Thermodynamics of reciprocal salt systems. III. Isopiestic determination of the osmotic and activity coefficients of the system Li^+, $Na^+//Cl^-$, NO_3^-–H_2O at 100.3 °C. *Acta Chem. Scand*, *44*, 311–316.

Voigt, W. and Zeng, D., 2002. Solid-liquid equilibria in mixtures of molten salt hydrates for the design of heat storage materials. *Pure Appl. Chem. 74* (10), 1909–1920.

Wagner, W. and Pruss, A., 1993. International equations for the saturation properties of ordinary water substance. Revised according to the international temperature scale of 1990. Addendum to *J. Phys. Chem. Ref. Data* 16, 893 (1987). *J. Phys. Chem. Ref. Data*, *22* (3), 783–787.

Wagner, W. and Pruß, A., 2002. The IAPWS formulation 1995 for the thermodynamic properties of ordinary water substance for general and scientific use. *J. Phys. Chem. Ref. Data*, *31* (2), 387–535.

Wang, G., Zhou, Y., Yamaguchi, T., Yoshida, K., Ikeda, K., Chai, K., Liu, Z. and Wu, Z., 2023b. Atomic insights into the heterogeneity and the interface interactions of nanoconfined aqueous electrolyte solution. *J. Mol. Liq. 388*, 122746.

Wang, J., Wu, H. and Wang, F., 2025. Refined kelvin theory for capillary condensation under extreme confinement. *Phys. Fluids*, *37*, 032011.

Wang, M., Zhu, Y., Mao, W., Ye, M. and Yang, J., 2023a. Chemical characteristics and reactive transport of soil salt ions in frozen soil during the freeze and thaw period. *J. Hydrol. 621*, 129580.

Wang, P., Pitzer, K.S. and Simonson, J.M., 1998. Thermodynamic properties of aqueous magnesium chloride solutions from 250 to 600 K and to 100 MPa. *J. Phys. Chem. Ref. Data*, *27* (5), 971–991.

Wang, S., Stahlbuhk, A. and Steiger, M., 2024. Hydration and deliquescence behavior of calcium chloride hydrates. *Fluid Ph. Equilib. 585*, 114171.

Wang, S., and Steiger, M., 2025. Missing eutectic transition in electrolyte solutions in confinement due to ion accumulation in the interfacial layer. *J. Phys. Chem. B*, *129* (29), 7623–7630

Wang, X., Shi, G., Liang, S., Liu, J., Li, D., Fang, G., Liu, R., Yan, L. and Fang, H., 2018. Unexpectedly high salt accumulation inside carbon nanotubes soaked in dilute salt solutions. *Phys. Rev. Lett. 121* (22), 226102.

Wänke, H., Brückner, J., Dreibus, G., Rieder, R. and Ryabchikov, I., 2001. Chemical composition of rocks and soils at the Pathfinder site. In *Chronology and Evolution of Mars: Proceedings of an ISSI Workshop, 10–14 April 2000, Bern, Switzerland* (317–330). Springer Netherlands.

Washburn, E. International Critical Tables of Numerical Data, Physics, Chemistry and Technology; McGraw–Hill: New York, 1929; Vol. 5.

Wassermann, B., Mirbt, S., Reif, J., Zink, J.C. and Matthias, E., 1993. Clustered water adsorption on the NaCl (100) surface. *J. Chem. Phys. 98* (12), 10049–10060.

Wei, J., Fang, T., Wong, C., Lakey, P.S., Nizkorodov, S.A. and Shiraiwa, M., 2020. Superoxide formation from aqueous reactions of biogenic secondary organic aerosols. *Environ. Sci. Technol. 55* (1), 260–270.

Wei, X., Miranda, P.B. and Shen, Y.R., 2001. Surface vibrational spectroscopic study of surface melting of ice. *Phys. Rev. Lett. 86* (8), 1554.

Weissenborn, P.K. and Pugh, R.J., 1996. Surface tension of aqueous solutions of electrolytes: relationship with ion hydration, oxygen solubility, and bubble coalescence. *J. Colloid Interface Sci. 184* (2), 550–563.

Weitz, C.M., Milliken, R.E., Grant, J.A., McEwen, A.S., Williams, R.M.E., Bishop, J.L. and Thomson, B.J., 2010. Mars Reconnaissance Orbiter observations of light-toned layered deposits and associated fluvial landforms on the plateaus adjacent to Valles Marineris. *Icarus, 205* (1), 73–102.

Wexler, A.S. and Clegg, S.L., 2002. Atmospheric aerosol models for systems including the ions H^+, $NH4^+$, Na^+, SO_4^{2-}, NO_3^-, Cl^-, Br^-, and H_2O. *J. Geophys. Res. Atmos. 107* (D14), ACH–14.

Wexler, A.S. and Seinfeld, J.H., 1991. Second–generation inorganic aerosol model. *Atmos. Environ. A. Gen. Top. 25* (12), 2731–2748.

Yamada, M., Fukusako, S., Kawanami, T., Sawada, I. and Horibe, A., 1997. Surface tension of aqueous binary solutions. *Int. J. Thermophys. 18*, 1483–1493.

Yang, J., Su, H., Lian, C., Shang, Y., Liu, H. and Wu, J., 2020. Understanding surface charge regulation in silica nanopores. *Phys. Chem. Chem. Phys. 22* (27), 15373–15380.

Yang, K.L., Yiacoumi, S. and Tsouris, C., 2002. Monte Carlo simulations of electrical double–layer formation in nanopores. *J. Chem. Phys. 117* (18), 8499–8507.

Yoshida, K., Yamaguchi, T., Kittaka, S., Bellissent–Funel, M.C. and Fouquet, P., 2008. Thermodynamic, structural, and dynamic properties of supercooled water confined in mesoporous MCM–41 studied with calorimetric, neutron diffraction, and neutron spin echo measurements. *J. Chem. Phys. 129*, 054702.

Yu, Y.X., Gao, G.H. and Li, Y.G., 2000. Surface tension for aqueous electrolyte solutions by the modified mean spherical approximation. *Fluid Ph. Equilib. 173* (1), 23–38.

Zalba, B., Marín, J.M., Cabeza, L.F. and Mehling, H., 2003. Review on thermal energy storage with phase change: materials, heat transfer analysis and applications. *Appl. Therm. Eng. 23* (3), 251–283.

Zemplen, G. *Ann. Phys. (Berlin)* **1907**, *22*, 391–396.

Zeng, D., Zhou, H. and Voigt, W., 2007. Thermodynamic consistency of solubility and vapor pressure of a binary saturated salt + water system: II. $CaCl_2$ + H_2O. *Fluid Ph. Equilib. 253* (1), 1−11.

Zhang, S.L., 2012. Raman spectroscopy and its application in nanostructures. John Wiley & Sons.

Zhang, Y., Xu, H.B., Zhang, Y., Pei, L.L., Qing, P.H., Liu, C.L., Hong, J.H. and Liu, K.H., 2013. Phase equilibria of the Na^+, NH_4^+‖ SO_4^{2-}, Cl^-−H_2O system. *J. Chem. Eng. Data*, *58* (4), 1050−1053.

Zhao, D., Huo, Q., Feng, J., Chmelka, B.F. and Stucky, G.D., 1998. Nonionic triblock and star diblock copolymer and oligomeric surfactant syntheses of highly ordered, hydrothermally stable, mesoporous silica structures. *J. Am. Chem. Soc.* 120 (24), 6024−6036.

Zhao, L., Pan, L., Cao, Z. and Wang, Q., 2016. Confinement−induced vitrification of aqueous sodium chloride solutions. *Chem. Phys. Lett. 647*, 170−174.

Appendix

A1. Supplementary material to Chapter 5

A1.1 Pitzer model parameters for the $CaCl_2$–H_2O system

The model reported here has been used in all calculations with $CaCl_2$ in Chapter 5, thus in the calculations of freezing and eutectic temperatures, and in calculations of the phase diagram of the system $CaCl_2$–H_2O including all stable and metastable hydrates (Chapter 5). Values of the Debye–Hückel parameter, A_ϕ, used here are those determined by Archer and Wang (1990). For the purpose of the present model, the pressure dependence of A_ϕ is not required. Therefore, it is convenient to express the temperature dependence of A_ϕ at 0.1 MPa using the following simple equation (Steiger et al., 2008a):

$$A_\phi = a_1 + a_2/(T - 222\ K) + a_3/T^2 + a_4 T + a_5 T^2 + a_6 T^4 \tag{A1–1}$$

with a_1=−0.817653 $kg^{1/2}\cdot mol^{-1/2}$, a_2=−0.8685276 $kg^{1/2}\cdot mol^{-1/2}\cdot K$, a_3=1.9251·10^4 $kg^{1/2}\cdot mol^{-1/2}\cdot K^2$, a_4=0.5251284·10^{-2} $kg^{1/2}\cdot mol^{-1/2}\cdot K^{-1}$, a_5=−7.149397·10^{-6} $kg^{1/2}\cdot mol^{-1/2}\cdot K^{-2}$ and a_6=9.338559·10^{-12} $kg^{1/2}\cdot mol^{-1/2}\cdot K^{-4}$. Equation (A1–1) is valid at temperatures ≥ 245 K and at 0.1 MPa (to 373.15 K) and at saturation pressure above 373.15 K. At lower temperatures, a linear extrapolation was used (Beyer and Steiger, 2010).

Determination of model parameters: The model used for $CaCl_2$(aq) is based on the comprehensive reviews of the thermodynamic properties of $CaCl_2$(aq) by Holmes et al., (1994) Rard and Clegg (1997) and Gruszkiewicz and Simonson (2005). Holmes et al. (1994) used a Pitzer type model to represent the available experimental data to molalities of 4.6 $mol\cdot kg^{-1}$ and to high temperatures. For the present study, however, due to the very high solubilities in $CaCl_2$ solutions, a model is required that is valid to much higher concentrations. The comprehensive treatment of Rard and Clegg (1997) yields very accurate osmotic and activity coefficients at 298.15 K to 10.8 $mol\cdot kg^{-1}$. Gruszkiewicz and Simonson (2005) report further experimental osmotic coefficients from 323–523 K and to 22 $mol\cdot kg^{-1}$.

The equation of Holmes et al. (1994) was used to generate a database of osmotic and activity coefficients from dilute solution (m = 0.001 $mol\cdot kg^{-1}$) to 4 $mol\cdot kg^{-1}$ and from 273–373 K. Additional data used were the tabulated osmotic and activity coefficients of Rard and Clegg (0.001–10.8 $mol\cdot kg^{-1}$), the experimental osmotic coefficients of Holmes et al. (1994 and 1978) at high temperature (0.4–4.8 $mol\cdot kg^{-1}$), the osmotic coefficients of Gruszkiewicz and Simonson (2005), the accurate isopiestic vapor pressure data at 373.15 K (Grjotheim et al., 1988; Voigt et al., 1990; Fanghänel and Grjotheim, 1990) and freezing temperature data (Gibbard and Fong, 1975; Oakes, 1990). Finally, additional water activities for highly concentrated solutions were calculated using the BET model (Ally and Braunstein, 1996; Zeng et al., 2007) for extrapolation (298.15, 323.15, 373.15, 393.15, 413.15, 433.15, 453.15, 473.15, 498.15, 523.15 K).

The final database consisted of 776 osmotic coefficients and 172 activity coefficients covering the temperature range from 222 to 423 K and molalities from 0.001 mol·kg^{-1} to 19 mol·kg^{-1} (at 298 K) and to 35 mol·kg^{-1} at 523 K. The database was then used in one simultaneous least-squares fit to determine the parameters of Equation (2−11) that represent the temperature dependence of the ion interaction parameters $\beta^{(0)}$, $\beta^{(1)}$, $\beta^{(2)}$, $\beta^{(3)}$ and C^{ϕ}. Values of $\alpha_1 = 1.2$ kg$^{1/2}$·mol$^{-1/2}$, $\alpha_2 = 0.7$ kg$^{1/2}$·mol$^{-1/2}$ and $\alpha_3 = 0.4$ kg$^{1/2}$·mol$^{-1/2}$ were fixed in trial calculations. The final model parameters are summarized in Table A1−1. Considering the large temperature range and, in particular, the high concentrations, the reproduction of the experimental values is very satisfactory. Standard deviations of the fit are $s(a_w) = 0.0034$, i.e. 0.34 % RH.

Using the model parameters listed in Table A1−1, values of the solubility product of $CaCl_2{\cdot}6H_2O$ were calculated using available experimental data as compiled by Krumgalz (2017). The coefficients of Equation 2−11 to represent the temperature dependence of $\ln K_6$ were then determined in a least square fit and are listed in Table A1−2.

Table A1−1. Parameters for the temperature dependent model parameters in Equation A2−11 for $CaCl_2$(aq) (to 523 K).[a]

	$\beta^{(0)}$ kg·mol^{-1}	$\beta^{(1)}$ kg·mol^{-1}	$\beta^{(2)}$ kg·mol^{-1}	$\beta^{(3)}$ kg·mol^{-1}	C_{ϕ} kg^2·mol^{-2}
q_1	−4.202538E−01	1.049697E+01	−1.399681E+01	7.096695E+00	8.612767E−03
q_2	1.312490E+03	0	5.735410E+04	−2.788168E+04	0
q_3	1.036722E+01	0	3.949181E+02	−1.885200E+02	−8.065966E−02
q_4	−1.556215E−02	−2.396205E−01	−5.621165E−01	2.650600E−01	1.630800E−04
q_5	0	2.431974E−04	0	0	0

[a] $\alpha_1 = 1.2$ kg$^{1/2}$·mol$^{-1/2}$, $\alpha_2 = 0.7$ kg$^{1/2}$·mol$^{-1/2}$ and $\alpha_3 = 0.4$ kg$^{1/2}$·mol$^{-1/2}$

Table A1−2. Parameters for the temperature dependence of the solubility products.

	q_1	q_2	q_3	q_4	q_5
$CaCl_2{\cdot}6H_2O$	9.066105E+00	4.592084E+04	2.889852E+02	−4.336224E−01	0
α−$CaCl_2{\cdot}4H_2O$	1.223477E+01	1.566068E+04	4.758397E+01	0	0
β−$CaCl_2{\cdot}4H_2O$	1.262944E+01	2.050895E+04	5.932049E+01	0	0
γ−$CaCl_2{\cdot}4H_2O$	1.271130E+01	1.843347E+04	5.331032E+01	0	0
$CaCl_2{\cdot}2H_2O$	1.682412E+01	1.295776E+05	1.082282E+03	−3.034403E+00	1.343033E−03
$CaCl_2{\cdot}H_2O$	2.003408E+01	1.234845E+05	1.027150E+03	−2.889931E+00	1.278696E−03
$CaCl_2{\cdot}1/3H_2O$	2.498334E+01	−4.822391E+03	−4.688070E+01	0	0

Then, according to Equation (2–13) and Equation (2–17), both solubility data and equilibrium relative humidities for the hydration equilibria are suitable for the calculation of the thermodynamic solubility products of $CaCl_2 \cdot 4H_2O$ ($\ln K_4$), $CaCl_2 \cdot 2H_2O$ ($\ln K_2$), $CaCl_2 \cdot H_2O$ ($\ln K_1$) and $CaCl_2 \cdot 1/3H_2O$ ($\ln K_{1/3}$) as described in detail in Steiger (2018). Solubility data (Krumgalz, 2017) and equilibrium humidities for the $CaCl_2 \cdot 6H_2O$–$CaCl_2 \cdot 4H_2O$ phase boundary (Lannung, 1936) were used to determine the coefficients of Equation (A1–11) for $\ln K_4$ which are listed in Table A1–2. Subsequently, the coefficients for the solubility products of $CaCl_2 \cdot 2H_2O$, $CaCl_2 \cdot H_2O$ and $CaCl_2 \cdot 1/3H_2O$ were determined accordingly (Table A1–2), thus, using solubility data of these solids and equilibrium humidities for the respective phase boundaries, i.e. $4H_2O$–$2H_2O$ (Lannung, 1936; Collins and Menzies, 1936), $2H_2O$–$1H_2O$ (Lannung, 1936; Pitzer and Oakes, 1994) and $1H_2O$–$1/3H_2O$ (Pitzer and Oakes, 1994).

The phase boundary $CaCl_2 \cdot 1/3H_2O$–$CaCl_2$ could not be calculated using the same approach as the solution model is only valid to 523 K such that solubility products of the anhydrous salt are not accessible. Therefore, the latter phase boundary has to be approximately calculated from thermodynamic standard data assuming a constant enthalpy of hydration:

$$\ln(p/p^{\circ})_T = \ln(p/p^{\circ})_{T_{\mathrm{R}}} + (\Delta_{\mathrm{r}}H^{\circ}/\mathrm{R}\Delta n)/(T_{\mathrm{R}} - \tfrac{1}{T}) \qquad \text{(A1–2)}$$

with p°=0.1 MPa, T_{R}=298.15 K, $\Delta n = n_{\mathrm{A}} - n_{\mathrm{B}} = 2/3$ and

$$\ln(p/p^{\circ})_{T_{\mathrm{R}}} = (\Delta_{\mathrm{r}}G^{\circ})/(RT_{\mathrm{R}}\Delta n) \qquad \text{(A1–3)}$$

In Equation (A1–2) and Equation (A1–3) $\Delta_{\mathrm{r}}H^{\circ}$ and $\Delta_{\mathrm{r}}G^{\circ}$ are the standard enthalpy and standard Gibbs energy of reaction. These quantities can be calculated from enthalpies and Gibbs energies of formation of the crystalline salts (anhydrous and 1/3 hydrate) and were taken from Pitzer and Oakes (1994) ($\Delta_{\mathrm{r}}G^{\circ}$) and Garvin et al. (1987) ($\Delta_{\mathrm{r}}H^{\circ}$).

A calculated phase diagram involving the stable hydrates $CaCl_2 \cdot 6H_2O$, α-$CaCl_2 \cdot 4H_2O$, $CaCl_2 \cdot 2H_2O$ and $CaCl_2 \cdot H_2O$ is shown in Fig. 5–1 (Chapter 5).

A1.2 Phase diagram of $CaCl_2$–H_2O system including metastable hydrates

Using the model parameters listed in Tables A1–1 and A1–2, the complete phase diagram of the $CaCl_2$–H_2O system depicted in Fig. 5–1 (Chapter 5) was calculated. The calculated phase boundaries (DRH and hydration equilibria) are in excellent agreement with experimental data where available. Fig. A1–1 shows the solubilities, deliquescence humidities and the dissociation (hydration–dehydration) equilibria in the $CaCl_2$–H_2O system in the temperature range relevant to the experiments reported in Chapter 5.

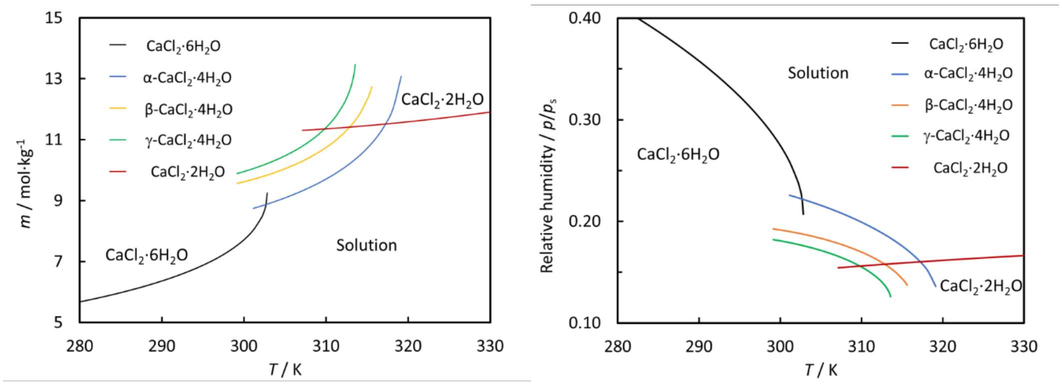

Figure A1−1. $CaCl_2$–H_2O System from 280–330 K; left: solubilities; right: deliquescence humidities.

A1.3 Deliquescence humidity of $CaCl_2·6H_2O$ at 298.15 K

The available experimental deliquescence humidities of $CaCl_2·6H_2O$ at 298.15 K shows significant scatter. A selection of the more consistent data is tabulated in Table A1−3. But even after removal of the less reliable data, the scatter is still quite large and the data cover a range from 28.2−29.5 % RH.

Table A1−3. Available experimental deliquescence humidities of $CaCl_2·6H_2O$ at 298.15 K.

Source	DRH / %
Bakhuis Roozeboom, H.W., 1889	28.2
Lescoeur, H., 1890	28.4
Hepburn, J.R.I., 1932	29.5
Lannung, A., 1936	28.6
Collins, E.M., and Menzies, A.W.C., 1936	28.4 29.2
Varasova, D.T., et al. 1937	29.1
Richardson, G.M., and Malthus, R.S., 1955	28.8
Acheson, D.T., 1965	29.0
Guo, L., et al., 2019	28.5

The experimental determination of deliquescence humidities is affected by two main sources of error, firstly, the uncertainty in the vapor pressure determination itself. Apart from that an additional error arises from the fact that the solution may not always be fully equilibrated with the solid phase resulting in an undersaturated solution (yielding too high values of DRH) or supersaturated solution (resulting in low values). In contrast, there is a large dataset of critically evaluated water activity data of $CaCl_2$ solution from large dilution to high supersaturation (Rard and Clegg, 1997). Using these data together with the best available solubility data, the water activity of a saturated solution can be determined by interpolation. From the solubility compilation of Krumgalz (2017) the molality of the saturated solution at 298.15 K was determined as m_{sat}= 7.33±0.06 mol·kg^{-1}. With the water activities of Rard and Clegg (1997) this yields a DRH of 29.1 ± 0.4 % which is considered as the most reliable value available. The value calculated with the present model (see Appendix A1.2) is 29.5 % RH.

A2. Supplementary material to Chapter 8

A2.1 Pitzer model parameters for the NaCl–H$_2$O system

Based on the model framework described in a previous paper of our group (Steiger et al., 2008a), a modified heat capacity function for liquid water was incorporated to optimize model predictions in the low temperature region. As the freezing temperatures in confinement are significantly lower than in bulk solutions, the planned calculations required significant extrapolation to temperatures below that of available experimental data in bulk solutions. Since the heat capacity of liquid water affects both, the calculation of freezing temperatures and the temperature dependence of ion the interaction parameters (via the equations for the apparent molar enthalpies), different approaches were tested to represent the complex behavior of the heat capacity of undercooled water down to very low temperatures. First, equations provided by Murphy and Koop (2005) predicting a heat capacity maximum at 225 K were used. Their equations agree with experimental data which are available only at temperatures above 236 K due to the homogeneous ice freezing limit. At lower temperatures, their treatment is based on the assumption that the structure of undercooled liquid water slowly approaches the structure of amorphous ice. Thus, also the heat capacity slowly approaches that of amorphous ice. This treatment results in the heat capacity maximum at 225 K.

The second approach to extrapolate the heat capacity of liquid water is similar to the treatment of Clegg and Brimblecombe (1995). They simply extrapolated an equation of state below 273.15 K by using the first and second temperature differentials of the heat capacity. Using their treatment together with a more recent IAPWS-95 equation of state for liquid water (Wagner and Pruß, 2002) yields the following simple equation at 0.1 MPa:

$$C_{\mathrm{p}}(\mathrm{H_2O_{(l)}}) = C_{\mathrm{p,T_r}} + \left(\frac{dC_p}{dT}\right)_{p^\circ}(T - T_0) + \left(\frac{d^2C_{\mathrm{p}}}{dT^2}\right)(T - T_0)^2 \qquad \text{(A2-1)}$$

where T_0=273.15 K. Values of C_p =75.9983 J·K^{-1}·mol^{-1}, dC_p/dT = –0.0551735 J·K^{-2}·mol^{-1}, and d^2T/dT^2 = 0.00316525 J·K^{-3}·mol^{-1} are those of Wagner and Pruß (2002).

Test calculations did not show that any one of the two heat capacity models to be superior. Therefore, the much simpler treatment of equation (A2–1) was used in the final parameterization. Another modification tested, was a new expression for the extrapolation of the Debye–Hückel parameter A_ϕ to very low temperatures. The treatment follows a similar approach as described for the heat capacity of liquid water, thus, using the first and second temperature differential of the Debye–Hückel parameter for the osmotic coefficient. This is the same approach as used by Clegg and Brimblecombe (1995), however, they used Debye–Hückel parameters of Archer and

Wang (1990) whilst, in the present treatment, the Debye–Hückel parameters of Voskov and Kovalenko (2020) were used, which are based on the most recent equation of state of water. First, their values of A_ϕ were represented by Chebychev series polynomal. In the temperature range 273–523 K and at 0.1 MPa (to 373.15 K) and saturation pressure above 373.15 K, their values of A_ϕ can be represented by the following equation and the coefficients listed in Table A2–1:

$$A_\phi = q_0 + q_1 x + q_2 x^2 + q_3 x^3 + q_4 x^4 + q_5 x^5 + q_6 x^6 + q_7 x^7 + q_8 x^8 + q_9 x^9 \qquad \text{(A2–2)}$$

where the x is the normalized temperature variable:

$$x = \frac{2T - T_{\max} - T_{\min}}{T_{\max} - T_{\min}} \qquad \text{(A2–3)}$$

with $T_{\max} = 523.15$ and $T_{\min} = 273.15$.

Table A2–1. Coefficients of Equation (A2–2) for calculation of the Debye–Hückel coefficient A_ϕ in the temperature range 273.15–523.15 K at 0.1 MPa (≤ 373.15 K) and saturation pressure (above 373.15 K).

q_0	4.91130922114192E-01	q_5	4.70400994663629E-03
q_1	1.68712428707736E-01	q_6	1.67375924878697E-03
q_2	6.02041571881852E-02	q_7	−1.38710368993371E-03
q_3	1.12889102406172E-02	q_8	−1.91808198233258E-04
q_4	8.25851369311408E-03	q_9	1.34892685945540E-03

The Deby–Hückel coefficient A_ϕ is related to the Debye–Hückel coefficients for enthalpy A_H and heat capacity A_C by:

$$A_\mathrm{H} = 4\mathrm{R}T^2\left(\partial A_\phi/\partial T\right)_p \qquad \text{(A2–4)}$$

$$A_\mathrm{C} = (\partial A_\mathrm{H}/\partial T)_p \qquad \text{(A2–5)}$$

The extrapolation of A_ϕ to low temperature is based on a linear extrapolation of A_C:

$$A_\mathrm{C}/R = (A_\mathrm{C} T_r)/R + (a/R)(T - T_r) \qquad \text{(A2–6)}$$

with $a = (\partial A_\mathrm{C}/\partial T)_{p,T_\mathrm{r}}$ and $T_0 = 273.15$ K. This yields for A_ϕ at temperatures below 273.15 K:

$$A_\phi = A_\phi(T_r) + \frac{1}{4}\frac{A_H(T_0)}{RT_0}\left(1 - \frac{T_0}{T}\right) + \frac{1}{4}\frac{A_C(T_0)}{R}\left(\ln\frac{T}{T_0} + \frac{T_0}{T} - 1\right) + \left(\frac{1}{8}\right)\left(\frac{a}{R}\right)\left(T - 2T_0\ln\frac{T}{T_0} - \frac{T_0^2}{T}\right) \qquad \text{(A2–7)}$$

with $A_\phi(T_0) = 0.376408371981534$ (kg/mol)$^{-1/2}$, $A_\mathrm{H}(T_0)/RT_0 = 0.545442059542246$ (kg/mol)$^{-1/2}$, and $A_\mathrm{C}(T_0)/R = 2.27754253611$ (kg/mol)$^{-1/2}$ and $a/R = 0.0822913489229$ (kg/mol)$^{-1/2}$ K^{-1}.

The model parameterization for NaCl(aq) is largely based on the previous model for NaCl(aq) but includes the heat capacities of liquid water and the Debye–Hückel coefficients as described before.

The temperature dependence of the Pitzer model parameters and the solubility products are given by Equation 2–13 and the parameters are tabulated in Table A2–2 and Table A2–3, respectively.

Table A2−2. Parameters for the temperature dependent model parameters for NaCl(aq).[(a)]

	$\beta^{(0)}$ kg·mol^{-1}	$\beta^{(1)}$ kg·mol^{-1}	$\beta^{(2)}$ kg·mol^{-1}	$\beta^{(3)}$ kg·mol^{-1}	C^{ϕ} kg^2·mol^{-2}
q_1	0.25033639	0.57172079	−0.442969465	0	−8.8735869E−03
q_2	1245.4554	0	−2629.0341	0	−110.27975
q_3	5.2887959	1.86365275	−10.965091	0	−0.45409111
q_4	0	0	0	0	0
q_5	0	0	0	0	0

(a) α_1 = 1.4 kg$^{1/2}$·mol$^{-1/2}$ and α_2 = 0.5 kg$^{1/2}$·mol$^{-1/2}$

Table A2−3. Parameters for the temperature dependence of the solubility products of sodium chloride hydrates.

	q_1	q_2	q_3	q_4	q_5
$NaCl\cdot 2H_2O$	3.62599	−2385.55	0	0	0
NaCl	3.64612	−4549.98	−13.80122	0	0

A3. Raw data of the melting point of salt solutions and DRHs of salt in confinement

The melting points of bulk pure water was determined as the onset temperature of the endothermic peak, whereas the peak maximum temperature was used to define the melting points of water confined within the pores. For salt solutions, the peak maximum temperature of the endothermic signals was taken as the ice melting point for both bulk and confined salt solutions. Similarly, for eutectic melting, the onset temperature and peak maximum temperature were used to determine the eutectic points of bulk and confined solutions, respectively.

The experimentally measured melting points of ice, eutectic points of salt solution, and the DRHs of salts in nanopores, as discussed in Chapter 7, are summarized in the following tables.

Table A3–1. Melting points of pure ice in bulk and in confinement.

Pore size /*d*	Ice melting point		
	Bulk	In pore	
nm	°C	°C	
Bulk	0.78	-	Fig. 7-2b and Fig. 7-8
20.6	0.66	−1.08	
11.7	0.77	−5.80	
10.5	−0.20	−7.22	
9.4	0.20	−7.73	
8.5	0.42	−9.57	
8.1	0.17	−10.81	
7.6	0.41	−11.74	
6.3	0.35	−16.56	
5.9	0.43	−19.82	
3.8	0.15	−44.27	

Table A3–2. Melting points of NaCl solution in bulk and in confinement.

Pore size /d	Molality	Ice melting point		Eutectic point		
		Bulk	In pore	Bulk	In pore	
nm	mol·kg^{-1}	°C	°C	°C	°C	
8.5	0	0.42	−9.57	-	-	Fig. 7-4a and Fig. 6-4b
8.5	0.1	1.13	−10.51	-	-	
8.5	0.3	0.33	−11.99	-	-	
8.5	0.5	−0.51	−13.38	-	-	
8.5	1.0	−2.71	−17.01	-	-	
8.5	2.0	−7.08	−24.99	-	-	
8.5	3.0	−11.70	-	−20.86	−31.33	
8.5	4.0	-	-	−20.72	−31.30	
8.5	4.5	-	-	−20.70	−31.04	
8.5	5.2	-	-	−20.72	−31.25	
8.5	5.5	-	-	−20.71	−31.17	
8.5	5.8	-	-	−20.74	−31.26	
8.5	6.1	3.87*	-	−20.76	−31.22	

*The temperature where salt completely dissolves

Table A3–3. Melting points of $CaCl_2$ solution in bulk and in confinement.

Pore size /*d*	Molality	Ice melting point		Eutectic point		
		Bulk	In pore	Bulk	In pore	
nm	mol·kg^{-1}	°C	°C	°C	°C	
9.4	0	1.94	−7.78	-	-	Fig. 6-4a and Fig. 7-4b
9.4	0.2	−0.47	−11.8	-	-	
9.4	0.4	−2.1	−16.12	-	-	
9.4	1.5	−11.80	-	−48.59	-	
9.4	2.2	−22.22	-	−49.91	−66.07	
9.4	3.2	−42.12	-	−49.58	−66.15	
9.4	3.8	−47.43	-	−47.33	−69.71	
9.4	4.0	-	-	−49.03	−67.08	
9.4	4.2	−30.09*	-	−49.65	−67.30	
9.4	4.5	−12.9*	-	−49.53	−67.30	
9.4	6.1	8.18*	-	−49.94	−67.25	

*The temperature where salt completely dissolves

Table A3–4. Eutectic points of NaCl solution in bulk and in confinement.

Pore size /*d*	Molality	Eutectic point		
		Bulk	In pore	
nm	mol·kg^{-1}	°C	°C	
Bulk	5.2	−20.69	-	Fig. 7-5a and Fig. 7-8
20.6	5.2	−20.43	−22.32	
11.7	5.2	−21.12	−29.94	
10.5	5.2	−21.46	−29.19	
8.5	5.2	−20.72	−31.25	
8.1	5.2	−20.88	−32.03	
7.0	5.2	−20.91	−36.04	
5.9	5.2	−20.81	−41.12	
3.8	5.2	−21.33	-	

Table A3–5. Eutectic points of $NaClO_4$ solution in bulk and in confinement.

Pore size /*d*	Molality	Eutectic point		
		Bulk	In pore	
nm	mol·kg^{-1}	°C	°C	
Bulk	9.0	−32.79	-	Fig. 7-5b and Fig. 7-8
20.6	9.0	−33.05	−36.79	
11.7	9.0	−33.96	−44.78	
9.1	9.0	−33.11	−49.42	
8.5	9.0	−33.24	−50.82	
7.6	9.0	−33.26	−55.94	
6.3	9.0	−33.30	−64.93	
5.9	9.0	−33.25	-	
3.8	9.0	−33.78	-	

Table A3–6. Eutectic points of $CaCl_2$ solution in bulk and in confinement.

Pore size /*d*	Molality	Eutectic point Bulk	Eutectic point In pore	
nm	mol·kg^{-1}	°C	°C	
Bulk	4.0	−50.24	-	Fig. 7-6a and Fig. 7-8
20.6	4.0	−50.67	−55.26	
11.7	4.0	−52.25	−63.4	
10.5	4.0	−52.81	−64.47	
9.4	4.0	−50.87	−66.97	
8.5	4.0	−50.45	−70.23	
8.1	4.0	−50.45	−70.73	
7.3	4.0	−50.78	−78.71	
5.9	4.0	−50.49	-	
3.8	4.0	−18.96*	-	

*unknown thermal signal

Table A3–7. Eutectic points of $MgCl_2$ solution in bulk and in confinement.

Pore size /*d*	Molality	Eutectic point Bulk	 In pore	
nm	mol·kg^{-1}	°C	°C	
Bulk	2.8	−32.11	-	Fig. 7-6b and Fig. 7-8
20.6	2.8	−32.83	−36.35	
11.7	2.8	−29.8	−45.22	
10.5	2.8	−33.76	−50.45	
9.4	2.8	–	−50.17	
8.1	2.8	−33.72	−53.36	
7.3	2.8	−33.76	−58.68	
5.9	2.8	−32.67	−65.74	
3.8	2.8	−21.38*	-	

*unknown thermal signal

Table A3–8. Melting points of $CaCl_2$ solutions in bulk and in confinement.

Pore size /*d*	Molality	Ice melting point		
		Bulk	In pore	
nm	mol·kg^{-1}	°C	°C	
Bulk	0.4	−0.35	-	Fig. 7-11a and Fig. 7-12a
20.6	0.4	−1.22	−5.88	
11.7	0.4	−1.41	−14.14	
9.4	0.4	−1.26	−15.77	
8.5	0.4	−0.96	−16.49	
8.1	0.4	−1.42	−17.29	
7.3	0.4	−3.27	−26.57	
5.9	0.4	−1.57	−33.07	

Table A3–9. Melting points of $CaCl_2$ solutions in bulk and in confinement.

Pore size /*d*	Molality	Ice melting point		
		Bulk	In pore	
nm	mol·kg^{-1}	°C	°C	
Bulk	0.8	−2.40	-	Fig. 7-11b and Fig. 7-12a
20.6	0.8	−2.68	−13.01	
11.7	0.8	−3.64	−19.82	
9.4	0.8	−3.84	−22.70	
8.5	0.8	−3.15	−21.97	
8.1	0.8	−5.63	−20.00	
7.6	0.8	−3.67	−25.52	
5.9	0.8	−4.85	−41.14	

Table A3−10. Melting points of Ca(ClO$_4$)$_2$ solution in bulk and in confinement.

Pore size /d	Molality	Bulk			In the pore			
		Onset	Peak	Offset	Onset	Peak	In pore	
nm	mol·kg^{-1}	°C	°C	°C	°C	°C	°C	
9.1	0.1	−0.54	0.938	1.88	−13.41	−9.79	−7.450	Fig. 7-20 and Fig. 7-22a
9.1	0.3	−2.77	−0.78	0.01	−17.03	−12.10	−9.59	
9.1	0.5	−6.09	−2.41	−1.44	−21.58	−15.45	−12.78	
9.1	0.8	−10.97	−5.57	−4.61	−26.35	−20.37	−17.63	
9.1	1	−12.75	−6.98	−5.90	−35.06	−27.66	−24.24	
9.1	1.5	−17.20	−11.47	−10.37	−49.91	−39.68	−36.25	
9.1	2	−23.53	−18.53	−17.45	−66.18	−58.09	−54.00	
7.6	0.1	−0.78	0.64	1.79	−16.23	−13.39	−12.30	
7.6	0.3	−3.04	−0.79	0.26	−20.26	−16.16	−14.74	
7.6	0.5	−6.23	−2.63	−1.83	−25.83	−20.55	−18.36	
7.6	0.8	−9.65	−5.04	−4.20	−40.81	−27.86	−24.84	
7.6	1	−12.05	−7.72	−6.82	−37.57	−34.86	−33.17	
7.6	1.5	−16.42	−12.08	−11.11	−58.24	−51.04	−44.70	
5.9	0.1	−1.25	0.65	1.76	−26.20	−22.16	−19.80	
5.9	0.3	−3.77	−1.04	−0.35	−30.89	−26.57	−23.89	
5.9	0.5	−6.62	−2.95	−2.20	−45.04	−32.86	−29.96	
5.9	0.8	−9.60	−5.69	−4.97	−51.03	−42.61	−41.27	

Table A3−11. Melting points of $Mg(ClO_4)_2$ solution in bulk and in confinement.

Pore size /d	Molality	Bulk			In the pore			
		Onset	Peak	Offset	Onset	Peak	In pore	
nm	mol·kg^{-1}	°C	°C	°C	°C	°C	°C	
11.7	0.1	−0.44	0.38	1.09	−14.11	−10.78	−9.02	Fig. 7-21 and Fig. 7-22b
11.7	0.3	−2.55	−1.03	−0.03	−18.18	−13.09	−10.78	
11.7	0.5	−5.33	−3.25	−2.56	−20.80	−15.64	−13.49	
11.7	0.8	−8.91	−6.37	−5.47	−26.63	−19.90	−16.87	
11.7	1	−13.56	−8.03	−6.77	−30.10	−26.31	−23.41	
11.7	1.8	−29.48	−19.09	−17.57	−46.41	−45.61	−42.26	
8.5	0.1	−0.44	0.38	1.09	−14.11	−10.78	−9.02	
8.5	0.3	−2.55	−1.03	−0.03	−18.18	−13.09	−10.78	
8.5	0.5	−5.33	−3.25	−2.35	−20.80	−15.64	−13.49	
8.5	0.8	−8.91	−6.37	−5.47	−26.63	−19.90	−16.87	
8.5	1	−13.56	−8.03	−6.77	−30.10	−26.31	−23.41	
8.5	1.8	−29.48	−19.09	−17.57	−46.41	−45.61	−42.26	
5.9	0.1	−1.12	0.53	1.59	−26.15	−22.09	−19.86	
5.9	0.3	−4.03	−1.26	−0.57	−32.48	−27.43	−24.35	
5.9	0.5	−6.89	−3.32	−2.63	−39.89	−35.16	−31.66	
5.9	0.8	−9.87	−5.89	−5.19	-55.354	−45.06	−42.19	
5.9	1	−12.90	−8.57	−7.67	−66.38	−63.75	−55.27	

Table A3–12. Melting points of $(NH_4)_2SO_4$ solution in bulk and in confinement.

Pore size /*d*	Molality	Ice melting point		Eutectic point		
		Bulk	In pore	Bulk	In pore	
nm	mol·kg^{-1}	°C	°C	°C	°C	
6.3	0.1	1.53	−18.29	-	-	Fig. 7-26
6.3	0.5	−1.07	−21.01	-	-	
6.3	0.8	−2.08	−23.41	-	-	
6.3	1.5	−4.67	−30.22	-	-	
6.3	2.5	−8.69	-	−17.85	-	
6.3	3.0	−9.71	-	−17.93	−41.73	
6.3	3.2	−10.95	-	−18.13	−41.99	
6.3	5.0	-	-	−18.14	−42.01	
6.3	6.0	-	-	−18.14	−42.13	
20.6	5.0			−17.69	-19.83	
11.7	5.0			−18.22	−26.67	
9.1	5.0			−18.04	−30.39	
8.5	5.0			−17.97	−31.68	
7.6	5.0			−18.07	−35.77	
5.9	5.0			−17.94	−44.75	
20.6	3.0	−9.71		−17.89	−22.99	
11.7	3.0	−11.14		−19.16	−27.06	
9.1	3.0	−11.01		−18.04	−30.49	
8.5	3.0	−9.52	-	−17.86	−31.35	
7.6	3.0	−10.57	-	−18.07	−45.41	
6.3	3.0	−9.44		−17.93	−41.73	
5.9	3.0	−12.18		−17.90	-	

Table A3–13. Deliquescence relative humidities (DRHs) of chlorides (KCl, $MgCl_2·6H_2O$, and $CaCl_2·nH_2O$) in bulk and in confinement at 25 °C.

Pore size /*d*	Salt	DRH			
		Onset	Offset	Average value	
nm		%	%	%	
Bulk	KCl	-	-	84	Fig. 7-30
20.6	KCl	74	79	76.5	
11.7	KCl	66	72	69	
9.1	KCl	65	70	67.5	
8.5	KCl	64	71	67.5	
7.0	KCl	49	55	52	
5.9	KCl	50	53	51.5	
3.8	KCl	32	50	41	
Bulk	$MgCl_2·6H_2O$	-	-	34	
20.6	$MgCl_2·6H_2O$	22	26	24	
11.7	$MgCl_2·6H_2O$	18	21	19.5	
9.1	$MgCl_2·6H_2O$	5	10	7.5	
7.0	$MgCl_2·6H_2O$	5	9	7	
6.6	$MgCl_2·6H_2O$	-	-	-	
5.9	$MgCl_2·6H_2O$	-	-	-	
Bulk	$CaCl_2·nH_2O$*	-	-	19	
20.6	$CaCl_2·nH_2O$*	11	13	12	
11.7	$CaCl_2·nH_2O$*	9	11	10	
9.1	$CaCl_2·nH_2O$*	7	9	8	
7.0	$CaCl_2·nH_2O$*	6	9	7.5	
5.9	$CaCl_2·nH_2O$*	5	8	6.5	
-	-	-	-	-	

* β–$CaCl_2·4H_2O$ or $CaCl_2·2H_2O$

Table A3–14. Deliquescence relative humidities (DRHs) of perchlorates ($NaClO_4·H_2O$, $Mg(ClO_4)_2·6H_2O$ and $Ca(ClO_4)_2·4H_2O$) in bulk and in confinement at 25 °C.

Pore size /d	Salt	DRH Onset	DRH Offset	DRH Average value	
nm		%	%	%	
Bulk	$NaClO_4·H_2O$	-	-	44	Fig. 7-33
20.6	$NaClO_4·H_2O$	28	33	30.5	
11.7	$NaClO_4·H_2O$	25	29	27	
9.1	$NaClO_4·H_2O$	22	26	24	
7.0	$NaClO_4·H_2O$	17	21	19	
6.6	$NaClO_4·H_2O$	16	18	17	
5.9	$NaClO_4·H_2O$	12	16	14	
Bulk	$Mg(ClO_4)_2·6H_2O$	-	-	40	
20.6	$Mg(ClO_4)_2·6H_2O$	33	37	34.5	
11.7	$Mg(ClO_4)_2·6H_2O$	27	31	29	
9.1	$Mg(ClO_4)_2·6H_2O$	23	27	25	
7.0	$Mg(ClO_4)_2·6H_2O$	20	22	21	
6.6	$Mg(ClO_4)_2·6H_2O$	16	19	17.5	
5.9	$Mg(ClO_4)_2·6H_2O$	14	17	15.5	
Bulk	$Ca(ClO_4)_2·4H_2O$	-	-	16	
20.6	$Ca(ClO_4)_2·4H_2O$	11	13	12	
11.7	$Ca(ClO_4)_2·4H_2O$	-	-	-	
9.1	$Ca(ClO_4)_2·4H_2O$	-	-	-	
7.0	$Ca(ClO_4)_2·4H_2O$	-	-	-	
5.9	$Ca(ClO_4)_2·4H_2O$	-	-	-	

A4. Chemicals directory

Table A4−1. List of hazardous substances according to GHS (hazard symbols H- and P)*

Substance	H-Statements	P-Statements	GHS symbols and signal words
Sodium chloride (NaCl)	-	-	-
Potassium Chloride (KCl)	-	-	-
Ammonium Chloride (NH_4Cl)	302, 319	264, 270, 280, 301+312, 305+351+338, 337+313	07 Warning
Magnesium chloride hexahydrate $MgCl_2{\cdot}6H_2O$	-	-	-
Calcium chloride dihydrate $CaCl_2{\cdot}2H_2O$	319	264, 280, 305+351+338, 337+313	07 Warning
Calcium chloride hexahydrate $CaCl_2{\cdot}6H_2O$	319	264, 280, 305+351+338, 337+313	07 Warning
Sodium perchlorate ($NaClO_4$)	271, 302, 319, 373	210, 220, 301+312, 305+351+338, 314	03, 07, 08 Danger
Magnesium perchlorate hexahydrate ($Mg(ClO_4)_2{\cdot}6H_2O$)	272, 315, 319, 335	210, 302, 305+351+338,	03, 07 Danger
Calcium perchlorate tetrahydrate ($Ca(ClO_4)_2{\cdot}4H_2O$)	272, 315, 319, 335	210, 220, 280, 332+313, 304+340+312, 301+352, 337+313, 371+380+375	03, 07 Danger
Sodium nitrate ($NaNO_3$)	272, 319	210, 305+351+338	03, 07 Warning
Potassium nitrate (KNO_3)	272	210, 220, 280, 370+378, 501	03 Warning
Sodium sulfate (Na_2SO_4)	-	-	-
Ammonium sulfate ($(NH_4)_2SO_4$)	-	-	-
Hydrochloric acid (HCl)	290, 314, 318, 335	234, 361, 271, 280, 303+361+353, 305+351+338	05, 07 Danger
Triblock copolymer Pluronic (P-123)	-	-	-
Tetraethoxysilane (TEOS)	226, 335, 332, 319	210, 261, 280, 304+340 305+351+338,	02, 07 Warning
3,3',5,5'-Tetramethylbenzidine (TMB)	302, 351, 413,	202, 264, 273, 280, 301+312, 308+313	07, 08 Warning
n-Hexane	225, 304, 315, 336, 361f, 373, 411	202, 210, 273, 301, 310+310, 303+361+353, 331	02, 07, 08, 09 Danger

**Data according to GESTIS Substance Database* (https://gestis-database.dguv.de).

List of Abbreviation

AFM: atomic force microscopy

CCD: charge-coupled device

DSC: differential scanning calorimetry

EELS: electron energy loss spectroscopy

EDX: energy−dispersive X−ray spectroscopy

ESEM: environmental scanning electron microscope

IR: inferred spectroscopy

MARSIS: Mars Advanced Radar for Subsurface and Ionosphere Sounding

SPSx−1μ: multi−sample Dynamic Moisture Sorption SPSx-1μ Advance

STM: scanning tunneling microscopy

TECP: Thermal and Electrical Conductivity Probe

UPS: ultraviolet photoemission spectroscopy

XPS: X−ray photoelectron spectroscopy

XRD: X−ray diffraction

E-AIM: Extended Aerosol Inorganics Model

FREZCHEM: freezing chemistry

PKL: model combining Pitzer theory, Kelvin effect, and Laplace pressure

PK: model combining Pitzer theory and Kelvin effect

MD: molecular simulation

NLDFT: non−local density functional theory

PB: Poisson−Boltzmann theory

RH: relative humidity

DRH: deliquescence relative humidity

ERH: efflorescence relative humidity

MDRH: mutual deliquescence relative humidity

EDL: electrical double layer

HDL: high–density liquid

LDL: low–density liquid

LLCP: liquid–liquid critical point

f–$(NH_4)_2SO_4$: ferroelectric ammonium sulfate

p–$(NH_4)_2SO_4$: paraelectric ammonium sulfate

MCF: siliceous mesostructured cellular foam

PSSC: porous silica salt composites

List of Figures

List of Tables

Dissemination

Publications

Wang, S., Stahlbuhk, A., Steiger, M. Water hydration and deliquescence of calcium chloride hydrates. *Fluid Ph. Equilibr*. **2024**, 114171.

Wang, S., Steiger, M. Missing eutectic transition in electrolyte solutions in confinement due to ion accumulation in the interfacial layer. *J. Phys. Chem. B,* **2025**, 129 (29), 7623–7630.

Wang, S., Godts, S., Stahlbuhk, A., Steiger, M. Water film: the motor of the phase transitions of salt mixture. *Langmuir*. Under review

Conference contributions

1. Oral talk

(1). The role of water film in the phase transitions of salt mixtures. Centre of Molecular Water Science (CMWS) Graduate Workshop. ***Freiberg, Germany***. 22–24, September, ***2025***.

(2). Water vapor sorption of salt nanoparticles in porous silica: experimental insights and thermodynamic modelling. 27th IUPAC International Conference on Chemical Thermodynamics (ICCT2025). ***Porto***, ***Portugal***, 20–24, July, ***2025***.

(3). Deliquescence of salt mixture: from water film to bulk liquid. 21th International Symposium on Solubility Phenomena and Related Equilibrium Processes (ISSP). ***Novi Sad, Serbia***. 9–13 September, ***2024***.

(4). The phase equilibrium of Mars–relevant brines: the influence of nanoconfinement. The 9th Young Scientist Forum on Earth Sciences. ***Xiamen, China***. 18–21, May, ***2024***.

(5). Anomalous phase transition behavior of dilute electrolyte solutions in nanoconfinement under cryogenic environment. 16th Annual International Conference on Porous Media (InterPore2024). ***Qingdao, China***. 12–16 May, ***2024***.

(6). The phase transition of aqueous electrolytes in confinement. 15th Annual International Conference on Porous Media (InterPore2023). ***Edinburgh, UK***. 21–26 May, ***2023***.

(7). The phase equilibria of aqueous electrolytes in confinement under Martian condition. 20th International Symposium on Solubility Phenomena and Related Equilibrium Processes (ISSP). ***Braganca, Portugal***. 4–9 September, ***2022***. (Online)

2. Poster presentation

(1). Moisture–induced phase transitions in reciprocal quaternary salt Mixtures. 27th IUPAC International Conference on Chemical Thermodynamics (ICCT2025). ***Porto***, ***Portugal***, 20–24, July, ***2025***.

(2). Water vapor sorption of KCl nanoparticle in porous silica. Centre of Molecular Water Science (CMWS) Water Day 2025. ***DESY, Hamburg, Germany***. 25–27 February, ***2025***.

(3). Hydration and deliquescence behavior of calcium chloride hydrates. 21th International Symposium on Solubility Phenomena and Related Equilibrium Processes (ISSP). ***Novi Sad, Serbia***. 9–13 September, ***2024***.

(4). Water films: The motor of phase transitions of salts in nature environments. Centre of Molecular Water Science (CMWS) Graduate Workshop. ***DESY, Hamburg, Germany***. 15–17, November, ***2023***.

(5). Water sorption in the interface of salt mixture. Water at interface Faraday Discussion. ***London, UK***. 20–22, September, ***2023***.

Invited Talk

Phase equilibria of aqueous electrolytes in nanoconfinement. Group Seminar of Prof. Dr. Mirjana Minceva. Technical University of Munich (TUM) ***Munich, Germany***, 28 November, ***2024***.

Declaration on Oath

I hereby declare and affirm that this doctoral dissertation is my own work and that I have not used any aids and sources other than those indicated. If electronic resources based on generative artificial intelligence (gAI) were used in the course of writing this dissertation, I confirm that my own work was the main and value–adding contribution and that complete documentation of all resources used is available in accordance with good scientific practice. I am responsible for any erroneous or distorted content, incorrect references, violations of data protection and copyright law or plagiarism that may have been generated by the gAI.

30, 9, 2025, Hamburg

Shaoheng Wang

Shaoheng Wang